Amorphous Nitridic Ceramics

Modelling, Structures, Properties and Energy Landscapes

A Computer Simulation Study with Special Focus on the $Si_3B_3N_7$ - System

Dissertation zur
Erlangung des Doktorgrades (Dr. rer. nat.)
der Mathematisch-Naturwissenschaftlichen Fakultät
der
Rheinischen Friedrich-Wilhelms-Universität Bonn vorgelegt von

Alexander Hannemann
aus
Emmerich/Rhein

Bonn 2003

Angefertigt mit Genehmigung der Mathematisch-Naturwissenschaftlichen Fakultät der Rheinischen Friedrich-Wilhelms-Universität Bonn.

1. Referent: Privatdozent Dr. J.C. Schön

2. Referent: Professor Dr. J. Beck

Tag der Promotion:

Dedicated my wife and my son:

Sandra and Felix Justus Hannemann,

and my parents:

Dieter and Gisela Hannemann

for all their support,
patience and understanding.

This thesis would not have been possible without the support from many people. I would like to thank:

- My Ph. D. advisor: **PD. Dr. J.C. Schön**, for his never ending patience, his enthusiasm for the topic, and for guiding me through the many possible research paths.
- **Prof. Dr. J. Beck** (University of Bonn), for taking the burden of being the second referee of this thesis.
- **Prof. Dr. M. Jansen** (MPI for Solid State Research), for providing me with the necessary financial support and equipment, as well as his interest for my research and his critical remarks.
- **Prof. Dr. P. Sibani** (University of Odense, Denmark), for his introduction to aging phenomena.
- **Prof. Dr. C. Oligschleger** (Fachhochschule Rhein-Sieg), for her very fruitful comments and introduction to the molecular dynamics methods.
- **Prof. Dr. T. Lengauer** (MPI for Computer Science, Saarbrücken) for his introduction to graph optimization techniques.
- **Drs. H. Putz, M. Berndt† and K. Brandenburg** for the great atmosphere during our work in Bonn, and Dr. H. Putz for providing me with the RMC program.
- **Dr. M. Wevers** and **M.Sc. Z. Cancarevic** for fruitful discussions.
- **Prof. Dr. C.M. Marian** (University of Düsseldorf) and her coworkers Dr. M. Gastreich and Dr. S. Reinhard, for providing me with the interaction potentials for the Si-B-N system prior to publication.
- All the members of Prof. Jansen's group at the University of Bonn and at the Max-Planck-Institute in Stuttgart for the constructive and critical discussions, which helped me to stay in contact with the experimentalists.
- The **DFG**, for financial support via SFB408, and the **Max-Planck-Society**, for a stipend.

Contents

List of Figures

List of Tables

Part I

Introduction

Chapter 1

Introduction and Outline

1.1 Introduction

Amorphous nitridic ceramics are fascinating new substances for possible technical application in aircraft and engine construction, due to their high temperature stability and their excellent mechanical properties.[76, 11, 77] In recent years, one focus of research in this field have been those ceramics that contain silicon, boron, nitrogen and carbon. Furthermore for optical applications, ceramics containing silicon, oxygen and nitrogen are being investigated.[88]

Quite generally, amorphous substances can be prepared by a large number of different synthesis routes:[35] melting and cooling, chemical vapor deposition, ion bombardment, grinding, just to name a few. Thus, it is surprising that these new materials are typically synthesized by only one procedure: the sol-gel route.[1] Therefore it is natural to ask what the (possibly different) properties of such materials would be, if they were synthesized by some other route. However, few attempts to synthesize these new ceramics via alternative routes have been been reported (see [77] for a review) and it appears that these synthesis routes do not lead to the desired products.

In contrast, computer simulations are not limited by experimental constraints and, in principle, allow one to study a chemical system under an almost unlimited number of 'experimental' conditions corresponding to different synthesis routes. Furthermore, these computer simulations offer unlimited opportunities, in principle, to study a multitude of amorphous compounds for varying compositions of the elements Si, B, C, N, O .... Such a full exploration of the field of the amorphous ceramics is clearly desirable, and would open up the possibility of designing amorphous ceramics with specific physical properties. A prerequisite for such an ability, however, is a fundamental understanding of a new class of materials such as the amorphous nitrides. Thus, in this thesis, the main focus will be on a representative prototypic material, amorphous silicon boron nitride (a-$Si_3B_3N_7$), and to a lesser extent on the $SiO_{2-z}N_{2z/3}$-system.

A first step to an understanding of a chemical system is the determination of its microscopic structure. However, amorphous ceramics lack translational symmetry and thus structural properties cannot fully be determined by conventional X-ray and neutron diffraction as is the case for crystalline materials. In the past six years a-$Si_3B_3N_7$ has been characterized by different experimental techniques with surprising results. The material exhibits an unusual low density,[78] the element distribution is homogenous down to the nanometer length scale, no vacancies exist on the length scales larger than a nanometer.[30] Below the nanometer length scale cationic islands of silicon and cationic islands of boron exist inside an anionic nitrogen matrix.[167, 166] On the Angstrøm length scale SiN_4 tetrahedra and BN_3 triangles are observed.[64, 113] Especially the formation of cationic islands is counterintuitive and thus one may wonder about the influence of the synthesis route on the structure formation in a-$Si_3B_3N_7$. To answer these questions, a microscopic view of the structure formation is necessary. Experimental information being scarce computer simulations offer a way to understand these issues.

Ideally, one would like to answer these questions, by solving the time dependent

[1] In the SiON system a synthesis via the classical melt route is also possible at low nitrogen contents[88].

Schrödinger equation for a large number of atoms. However, it is practically impossible to do so, and one has to resort to a classical description of the material, and 'only' integrate Newton's equation of motion. But in that classical description, the time scales $\tau_{sim} = 10^1 - 10^2$ ns that can be reached are very short compared to the experimental time scales τ_{exp} of days ($\tau_{exp} = 10^{13}$ ns) even if one simulates only relatively small system sizes of about $10^3 - 10^4$ atoms (compared to macroscopic samples containing 10^{23} atoms). Thus, in order to study the synthesis route of an amorphous system, such as e. g. a-$Si_3B_3N_7$, additional approximations are necessary, resulting in phenomenological models that still capture the essential processes involved in the synthesis.

As mentioned, a-$Si_3B_3N_7$ is synthesized by a sol-gel synthesis in which single source precursor molecules, (Trichlorosilylamino)dichloroborane (TADB), are crosslinked by ammonia to form a polymer, and the polymer is subsequently pyrolized. Thus, a reasonable approach is to first study the sol-gel process and then later concentrate on the pyrolysis step using straight forward simulation methods. However, no well-established methods treating the sol-gel process exist, since theoretical research in the sol-gel science has concentrated on the fundamental questions like the universality class of the sol-gel transition [154, 155]. Furthermore the kinetics of the sol-gel process itself have only been studied for organic polymers in the context of the kinetic gelation model[70, 71, 98, 99, 12], but no algorithm and application to the study of network formation during the sol-gel synthesis for more complex materials such as amorphous nitridic ceramics exist. Apart from the possibility to mimic the synthesis route of a-$Si_3B_3N_7$, a successful 'synthesis' will allow one to get a clearer understanding of the influence of the precursor molecules on the final properties of the material. Furthermore the influence of different re-activities of the constituting atoms will hopefully become clear, and finally it may be possible to explain the very low density of the materials.

Returning to the other possible synthesis paths and the dependence of the structural properties of amorphous materials on the routes chosen, we note that the effects of process parameters are typically studied within the classical glassmaker approach: heating and melting crystalline substances accompanied by subsequent cooling using different cooling rates. In computer simulations, these kind of studies have mostly been focussed on the SiO_2[169] as well as Lennard-Jones[170] and soft-sphere systems[119], the latter two serving more as simple generic models that are meant to represent a larger class of materials. Of course, experimentally the effects of cooling rates and temperature schedules have been studied for many years. However, for a-$Si_3B_3N_7$, experimental studies are impossible at ambient pressure, since the material does not form via melting a mixture of the binary components BN and Si_3N_4[171]. Clearly, this makes the computer simulation approach even more attractive for investigating a possible route to a-$Si_3B_3N_7$ via a glass transition.

Focussing on the structural properties of inorganic nitridic ceramics, it may also be possible to disregard the actual synthesis and construct models from a limited amount of experimental data. This approach is used in the very popular 'molecular modelling' approach, where one builds up clusters comprising a few thousand atoms in a step by step fashion.[55, 173] However, this methods suffers from severe drawbacks. For one, in the nitridic systems, contrary to SiO_2 and GeO_2, the generation algorithm stop at about 1000 atoms, and thus the clusters generated have a high number of surface atoms. The second drawback is that these algorithms do not seem to work when applied to periodically repeated unit cells, which are needed to take the effectively infinite size of the system into account. Thus, to study the more complex nitridic systems, an alternative approach for the generation of structural models is needed. Furthermore, to be advantegous, these methods should also be faster than conventional computer simulation methods, like molecular dynamics or Monte Carlo methods typically used in the study of amorphous materials.

Remembering that the structures of simple crystalline compounds can be successfully described by packings of spheres of anions, which occupy most of the volume of the unit cell, while the cations reside in the voids or holes of the packings, the transferability of

these concepts to amorphous covalent networks is clearly an interesting question. If succesful, it would offer an additional way to quickly generate structural models of amorphous ceramics, and allow the properties of the materials to be explored.

After these structural models have been generated by a variety of methods, one can compare the properties of the models among each other and those systems with the most interesting properties can serve as experimental synthesis goals for promising new materials. Furthermore, the comparison of the different models to experimental data allows one to understand the unusual properties especially of a-$Si_3B_3N_7$.

Earlier, we mentioned that a-$Si_3B_3N_7$ is prototypic for a new class of materials, that are expected to be of great future technological importance in high temperature applications. However, only the behaviour of the system at ambient pressure and at comparatively moderate temperatures has been explored experimentally. Thus it is clearly important to know how the system will behave at other even more extreme conditions. Apart from these technologically important questions, answers to the more fundamental question about the phase diagram of these nitridic ceramics are needed. Unfortunately, the phase diagrams of these materials have not yet been studied experimentally, but again computer simulations can clarify the situation.

Another puzzling experimental observation is that nitridic ceramics like a-$Si_3B_3N_7$ do not exhibit a glass transition at ambient pressure, in contrast to the well-studied silica systems. Since the system is amorphous, one would expect such a transition to occur. Furthermore the glassy properties of a-$Si_3B_3N_7$ are interesting from a fundamental point of view. Do these properties show similarities to the properties of typical glass formers or do they differ significantly from those of typical glass formers ? If these properties are not very different from those typical glass formers, it is highly interesting to test the applicability of old and new theoretical approaches to the glass transition.

The old insight of Goldstein[57], that the glassy behaviour of a system is related to its potential energy landscape has become quite popular again. The computational prescription of Stillinger and Weber [161] has been widely employed to study the energy landscape approach. Extending Goldstein's approach, Cavagna[26] has suggested that above the glass transition temperature T_G a second temperature T_X exists above which the dynamics of the glassy system is not governed by minimum hopping as in the original Goldstein approach, but by hopping along saddle points of the energy landscape.

Landscape studies of structural glasses investigating these features of the glass transition have only been extensively performed for simple Lennard-Jones and soft-sphere systems,[128] but no exhaustive investigation of complex systems like the amorphous nitridic ceramics exists.[2] Thus, we would expect that an analysis of the energy landscape of the new class of materials represented by a-$Si_3B_3N_7$ adds to an understanding of the glass transition in terms of the energy landscape approach.

Furthermore, contrary to e. g. the mode-coupling theory (MCT)[58] of the glass transition, the energy landscape approach has a wider applicability, since it can also be applied to the treatment of the system's properties below the glass transition temperature T_G. In that temperature regime, one typically observes *aging* phenomena, e.g. the properties of a material depend on the way and the time system has been thermally treated. Studies of aging in spin-glass systems, both experimentally[115] and in computer simulations,[6] have shown that the fluctuation-dissipation theorem (FDT) is violated in these systems in a very peculiar manner. Furthermore for spin-glass systems, the violation of the FDT were related to properties of model energy landscapes.

Clearly, an analysis of the energy landscape of more complex systems is highly desirable to test theoretical concepts derived from spin-glass systems, and from simple Lennard-Jones systems. Furthermore, the possible existence of aging phenomena in technically important materials is an important piece of information !

[2] The investigations of the energy landscape of amorphous silica are quite scarce and focus on some special aspects of the energy landscape.[91, 133]

1.2 Outline of thesis

First, we review some aspects of the phenomenology and theoretical approaches to glassiness. Next, we describe the methods employed in this thesis for the generation and the analysis of structural models generated by classical Monte-Carlo and molecular dynamics computer simulation techniques. Next, we present two new approaches for the generation of structural models of amorphous substances. The first of these approaches is the *random close packing* (RCP) approach for the generation of structural models, and it is tested for a variety of different chemical systems in chapter 5. The second approach is a separation of time scale approach to simulate the sol-gel synthesis of amorphous nitridic ceramics and is applied to a-$Si_3B_3N_7$ in chapter 6. After these methods have been presented, we investigate the structural properties of $SiO_{2-z}N_{2z/3}$-system (z=0...,2) by the RCP-approach, and then proceed to study the structural properties of a-$Si_3B_3N_7$, in chapters 7 and 8, respectively. For a-$Si_3B_3N_7$, we compare the structural and dynamical properties of the models that were generated by different methods, each representing possible distinct physical or chemical synthesis routes to the a-$Si_3B_3N_7$-system.

After the structural properties have been investigated, we analyze the (metastable) phase diagram of the $Si_3B_3N_7$-system (chapter 9) and then turn to the glassy properties of the system. In chapter 10 we show that a-$Si_3B_3N_7$ exhibits a glass transtion at a temperature T_G = 2250 K and in the subsequent chapter, we analyze the energy landscape of a-$Si_3B_3N_7$ both above and below T_G. As part of the analysis of the energy landscape, we also perform an in-depth analysis of the vibrational properties of a-$Si_3B_3N_7$ and compare these to available experimental data. Closing our analysis of the energy landscape, we show in chapter 12 that a-$Si_3B_3N_7$ exhibits aging behaviour and these aging phenomena are closely related to its energy landscape.

Chapter 2

Glassiness

The phenomenology of glass forming materials has many facets that cannot be completely treated in this thesis, and we have selected only the most important aspects. More details can be found in the monographs by e.g. Gutzow and Schmelzer[62] or Elliot[35] or in a recent review by Angell et al.[9]. A full theory of the glass transition has not yet been established and we will present different theoretical approaches to glassiness after the discussion of the glass phenomenology.

2.1 Phenomenology

Usually, a liquid of fixed composition solidifies at its melting temperature T_M upon cooling to form a crystalline compound. The solidification is accompanied by a discontinuous change of extensive thermodynamic variables like the energy or the volume. However, if the system is cooled rapidly enough, the liquid does not crystallize at T_M but becomes supercooled with respect to its melting point. The properties of the supercooled liquid then smoothly follow the liquid's properties above T_M down to a temperature interval, centered at a temperature $T_G < T_M$,[1], and at T_G, the properties of the supercooled liquid change rapidly but still continously. Below T_G the liquid has turned into an amorphous solid called a *glass*. Note that since the system is amorphous, no Bragg reflections typical for crystals are observed.

Since the cooling rate γ employed in the cooling procedure leads to different values for $T_G(\gamma)$, it is clear that the glass transition is not an equilibrium second order phase transition. In the latter case one would expect a sharply defined transition temperature. Furthermore, the properties of a glassy system upon heating from below T_G depend on the times the system has been kept below T_G[62] and/or on the heating rates. Thus, below T_G the glass is not in an equilibrium state, in which one would expect to measure time-independent properties, but rather in a non-equilibrium state. The transition from a supercooled liquid to a glass occurs at the temperature, at which the system falls out of equilibrium. However showing that a system is in equilibrium on all relevant experimental time scales t_{exp} in computer experiments is quite difficult, since equilibration implies that the ergodicity hypothesis holds for the system, and proving ergodicity is far from trivial. For practical purposes, certain equations must be fulfilled to call a system ergodic and thus the equilibrium to non-equilibrium transition or ergodic to non-ergodic transition can simply be observed by checking the validity of these equations during the computer experiment.

2.1.1 Above T_G

The equilibrium to non-equilibrium transition temperature is not the only criterion that can be used to determine the glass transition temperature T_G. Another commonly employed criterion for the glass transition temperature T_G, is that viscosity η of the liquid increasing up to 10^{13} Poise (= $10^{12}\ Pa \cdot s$) at T_G. For such highly viscous liquids (water at room temperature has a viscosity of 10^{-2} Poise), the liquid does hardly flow on laboratory time scales and thus the liquid is considered to have turned into solid. An estimate for the time scales τ_r on which e. g. irreversible structural changes happen, can be derived from rate-

[1] Even though T_G is not a well defined temperature, we will often write 'at T_G', implying that we mean 'in the interval around T_G'

theory [56]: Assuming that the viscosity is related to an elementary jump of length Δr, that the diffusion coefficient D_0 is related to the viscosity via[2] $D_0 = \frac{k_B T}{\eta d_0}$, and that the Einstein-Smoluchowski equation $D_0 \approx \frac{\Delta r}{2t}$ holds, then the time τ_R during which no structural changes occur is given by

$$\tau_R = \frac{d_0^3}{k_B T}\eta, \tag{2.1}$$

where d_0 is a typical interatomic distance. Thus the relaxation times are closely related to the viscosity. At 1000 K ($\approx$ 0.1 eV), the above formula leads to relaxation times of the order of 10^6 s for a viscosity of 10^{13} Poise. Thus one would not measure any flow for about ten days and the system can treated as a solid. [3]

Concerning the temperature dependence of the viscosity $\eta(T)$, we note that this temperature dependence can often be described e. g. by either an Arrhenius law

$$\eta(T) = A_1 \cdot \exp\left(\frac{\Delta E}{T}\right), \tag{2.2}$$

where ΔE is an experimentally observed activation energy. Note that throughout the thesis we will use units of temperatures such that $k_B = 1$. In contrast to the Arrhenius-like dependence typical for so-called strong glass formers, the temperature dependence of viscosity of the fragile glass formers is often described by the purely empirical Vogel-Fulcher-Tamman (VFT) equation,

$$\eta(T) = A_2 \cdot \exp\left(\frac{B}{T - T_C^{VFT}}\right). \tag{2.3}$$

Finally, the mode-coupling theory (MCT)[58] of the viscous slow down describes the temperature dependence of the viscosity by a power-law

$$\eta(T) = A_3 \cdot \left(T - T_C^{MCT}\right)^{-\gamma} \tag{2.4}$$

These functions are depicted in figure 2.1 in an Arrhenius plot ($\log(\eta)$ vs. 1/T), where one observes the straight line typical of the Arrhenius law, and the super-Arrhenius temperature dependence of the viscosity as the critical temperatures T_C^{VFT} and T_C^{MCT} are approached. Note, that the formal activation energies of the VFT and the MCT equations, $\frac{d\eta}{d(1/T)}$, increase the closer one gets to the critical temperatures.

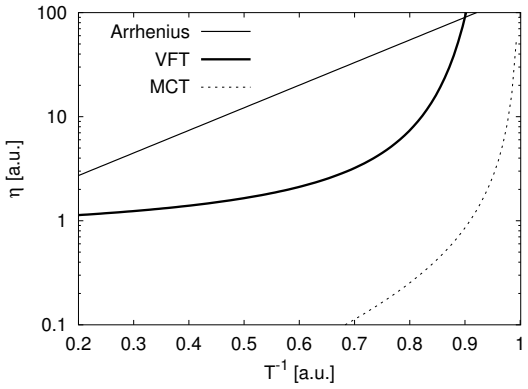

Figure 2.1: Temperature dependences of the viscosities $\eta(T)$ according to an Arrhenius law, the VFT equation, and the power-law suggested by mode-coupling theory with $A_1 = A_2 = 1$, $A_3 = 0.5$, $T_C^{MCT} = T_C^{VFT} = 1000$ and $\Delta E = 1000$ and $B = 0.5 \cdot \Delta E$.

The glass transition is not only accompanied by an exponential increase of the viscosity at T_G, but other observables characterizing different dynamical processes also change significantly. These dynamical processes, spanning a frequency range of 10^{-6} Hz to 10^{15} Hz (corresponding to relaxational time scales of days to picoseconds), can be measured by broadband dielectric spectroscopy (DES).[103] When doing DES, one probes the response of a material's polarizability to an applied frequency dependent electric field over a range of frequencies. In the liquid phase one observes a single peak relaxation frequency, and as one reaches the supercooled regime, the single peak relaxation function splits into different peaks. One observes a strong α-peak with an average frequency $\langle\nu_\alpha\rangle$ corresponding to a time scale of the α-relaxation, $\tau_\alpha = \frac{1}{2\pi\langle\nu_\alpha\rangle}$, followed by a shoulder corresponding to the slow β-relaxation processes. In the THz-regime of the frequency spectrum, the so-called Boson peak shows up in many glass forming materials.[102] Between the $\alpha-$peak and the boson peak, a minimum exists on top of which the fast β-processes have recently been determined experimentally.[102]. For fragile glass formers, the temperature de-

[2] Note that this is *not* the Stokes-Einstein relation.

[3] Sometimes the ratio of the experimental time scales t_{exp} and the relaxational time scale τ_R is called Deborah's number.

pendence of the α-relaxation times τ_α (in the range of seconds) is typically described by a VFT-equation diverging at the glass transition temperature T_G[4], whereas the slow β-relaxation follows an Arrhenius law even below T_G, thus indicating two different relaxational processes.

2.1.2 Below T_G

The properties of glassy materials below T_G are difficult to characterize, since one is dealing with a non-equilibrium situation. Experimentally, one observes that the properties of the materials do not only depend on the temperature $T < T_G$ at which the experiments are performed, but also on thermal history of the samples. The location of the peak of the specific heat shifts to higher temperatures with increasing heating rate,[62] differently cooled glasses show different glass transition temperatures when heated.[62] It has also been shown, that the location of the specific heat and the intensity of the peak strongly depend on the time and temperature the system has been kept below T_G.[156] Furthermore experiments on spin-glasses have shown that one observes *aging* effects, i. e. the properties of the system not only depend on the waiting time t_w the system has been kept at a given temperature but also on the observation time t_{obs} with which one performs a measurement.[115]

2.2 Theoretical approaches to glassiness

Even though glasses have been produced for millenia, our understanding of the glass transition is far from complete, and different theoretical approaches to the glass transition exist. Most of the theoretical approaches to the glass transition study it from the 'liquid-side' above T_G and treat the glass transition assuming that the system is in equilibrium. The theories of Gibbs and DiMarzio[54] and Adam and Gibbs,[1] which are based on a statistical mechanical approach, or the very complex Mode-Coupling theory,[58, 59] based on a dynamic view, have been extensively discussed in the literature[22],[58], and we will not present them in detail. Here, we focus on the description of the glass transition in terms of the *energy landscape* picture.

2.3 Energy landscape approach to glassiness

The potential energy landscape approach provides a phenomenologically convenient framework for treating the complex behaviour of glassy materials both above and below the glass transition temperature T_G.

The potential energy landscape (PEL)[5] of a glassy system of N atoms in a volume V, is a 3N-dimensional surface defined by the potential energy function $E(\vec{r}_1, \ldots, \vec{r}_N)$ of the N three dimensional position vectors $\vec{r}_i$. The most interesting properties of the energy landscape are the distributions of minima, also called inherent structures, the saddle points or barrier regions and the local density of states surrounding a given minimum. The minima represent mechanically stable configurations and the saddle points connecting minima and the densities of states are responsible for the dynamical properties of the system. Note that minima are points of the PEL, where the gradient vanishes, and the Hessian matrix of the second derivatives has only positive eigenvalues. Saddles of order n are points where the gradient vanishes and the Hessian matrix has n negative eigenvalues.

More than thirty years ago Goldstein [57] proposed, that the dynamical and static properties of a material are connected to its energy landscape. He assumes, that below a temperature T_X, the system spends most of its time vibrating around local minima and occasionally jumps between minima occur. Above T_X, this scenario breaks down, because a distinction between vibrations inside a minimum and the hopping between minima becomes impossible. Note that T_X is just the limiting temperature for validity that the vibrations inside minima and jumps between minima can be kept dynamically separate. To be more specific we repeat Goldstein's assumptions:

[4] Actually, the α-relaxation is difficult to detect below T_G due to the time scales involved.

[5] We use the term potential energy surface (PES), synomously.

1. A glass at low temperatures, like a crystal, is at or near a potential energy minimum.

2. The portion of the potential energy surface that represents the liquid or glassy region has, unlike the portion associated with the crystalline solid, a large number of minima of varying depths.

3. As temperature is raised, sufficient thermal energy ($1/2k_BT$ per classical kinetic degree of freedom) will become available to allow transitions to take place over potential energy barriers, even though they are large compared to the thermal energy.

4. A transition over the potential energy barrier is in some sense 'local', in that in the rearrangement process leading from one minimum to a 'near-by' one, most atomic coordinates change very little, and only those in a small region of substance change by appreciable amounts.

5. For temperatures below and around the glass transition temperature, the system will *always* be in a process of transition, but always near a minimum, in that sense that a sudden cooling will drop it into a minimum with relatively small changes of most of the coordinates.

6. The description of viscous flow in terms of energy barriers will be appropriate at low temperatures, but become less useful as temperature is raised and the liquid becomes very fluid.

In the PEL description the postulated rearrangements involve only few atoms, and it is not clear how these re-arrangements would lead to viscous flow or macroscopic mass transport. According to Goldstein, the viscous flow will only occur, if a large number of different localized re-arrangements occur that move the system 'far away' from its original minimum, and thus erase its memory. This large number of different localized rearrangements for viscous flow is necessary, because a localized rearrangement that brings a region A of the system to a region B, if a force is applied to macroscopic sample, will snap back from B to A, once the force is removed, and thus this single localized re-arrangements will *not* contribute to viscous flow. Thus a viscous flow only occurs, if either cooperative or consecutive re-arrangements have occurred. As already pointed out by Goldstein, the barriers of the energy landscape do not necessarily resemble experimentally determined activation energies, but are generic properties of the energy landscape.

2.3.1 Understanding glassy behaviour starting from the liquid state

Based on Goldstein's assumptions, Stillinger et al. [160, 157], developed a scheme to study the energy landscape of liquid and glassy materials by computer simulations, from which the material's thermodynamic properties can be determined. Furthermore, Stillinger has suggested that the dynamic properties, e.g. diffusion and viscosity can be derived from a thorough analysis of the energy landscape.[158]

Instead of treating the whole energy landscape, one maps the instantenuous configurations along the trajectories to the underlying minima using a steepest descent path. All configurations leading to the same minimum M_i belong the same basin B_i. The thermodynamic properties of the system can then be studied by breaking the conventional partition function into separate contributions from each basin yielding the equilibrium free energy at temperature T in terms of the potential energy E_i of basin i and the number of minima $\Omega(E_i)$ with energy E_i.

$$F(V,T) \propto \int_{E_{glass}} \Omega(E_i) \exp\left(-\frac{E_i + N f_{basin}(E_i;T)}{k_BT}\right) dE, \tag{2.5}$$

where $f_{basin}(E_i;T)$ is the free energy per particle of the basin surrounding minimum E_i. Typically $f_{basin}(E_i,T)$ is calculated via the classical harmonic approximation, yielding

$$N \cdot f_{basin}(T) = N \cdot k_BT \sum_{v=1}^{3N-6} \ln\left(1 - \exp\left(-\frac{E_v}{k_BT}\right)\right), \tag{2.6}$$

where the sum is over all 3N-6 normal vibrations v with energy $E_v = h\nu_v$, ν_v being the

eigenfrequencies of vibration v. Note, that for high temperature ($E_v \ll k_BT$), the exponential can be expanded into a power series, resulting in

$$N \cdot f_{basin}(T) = N \cdot k_BT \sum_{v=1}^{3N-6} \ln\left(\frac{E_v}{k_BT}\right) \quad (2.7)$$

Finally, defining the configurational entropy at energy E_i via the number of accessible basins $\Omega(E_i)$

$$S_C(E_i) = k_B \ln \Omega(E_i), \quad (2.8)$$

equation 2.5 becomes[129]

$$F(V,T) \propto \int_{E_{glass}} \exp\left(-\frac{E_i + N f_{basin}(E_i;T) - TS_C(E_i)}{k_BT}\right) dE. \quad (2.9)$$

Note that this treatment leads to a thermodynamic treatment of the equilibrium properties of the supercooled liquid state in terms of the distribution of minima, and that this approach heavily relies on the usefulness of the assumption, that the system spends most of its time inside the basins, and occasionally jumps between minima occur. To support this view, Sastry et. al. showed that different dynamical regimes in the energy landscapes of simple glass formers can be distinguished upon cooling.[130, 131] In these MD-simulations of the $Ni_{80}P_{20}$-system[6] modelled by a simple Lennard-Jones potential, it was shown that down to a certain temperature $T = 1$,[7] the average energy of the minima, periodically determined during cooling, is constant, and upon further cooling the energy of the sampled minima decreased and leveled off at about $T = 0.45$. Note, that $T = 0.45$ is just the mode-coupling temperature T_C^{MCT} determined for this systems. Furthermore it was shown, that the dynamical properties derived from the inherent structures were similar to the ones observed from the instantenuous configurations of the glass, thus indicating that the dynamics of the glasses is closely related to the properties of the energy landscape.

Even though these results are strong indications for the influence of the energy landscape on the dynamics, the direct connection between barrier crossing on the energy landscape and the dynamical properties of the supercooled liquid has not been achieved. Nevertheless, Stillinger et al. speculated that slow relaxations are due to meta-basin changes. A meta-basin consist of many basins, and fast relaxations occur within a meta-basin.[32] The inter-meta-basin changes involve consecutive re-arrangements of few atoms, leading to an overall displacement of almost all atoms, whereas the intra-meta-basin relaxations are fast and involve only very few atoms. In the Goldstein/Stillinger view, the glass transition occurs when the system gets trapped in deeper and deeper minimum regions of the energy landscape as the temperature is lowered, since the kinetic energy is not sufficient to overcome the barriers on the time scale of the experiments or simulations.

The Goldstein/Stillinger view of the energy landscape suffers from some drawbacks. Firstly, it is not yet known how the dynamics on the energy landscape is related to the macroscopic dynamics. Secondly, the applicability of the minimum hopping scenario is limited to temperatures where the system spends most of its time inside the basins. Thirdly, the analysis is restricted to those temperatures at which the system is in equilibrium. Therefore alternative approaches have been proposed.

Cavagna has suggested that, besides minimum hopping, a second mechanism for diffusion, the saddle hopping scenario, is responsible for the motion across the energy landscape.[26] In that view, the dynamics above T_X is governed by the number of imaginary modes N_{imag}, allowing the system to escape 'downhill' from a saddle (and thus take longer steps on the energy landscape), and then ending up at another saddle of comparable energy. This approach is related to the instantenuous normal mode approach (INMA) of Keyes and coworkers[150, 105, 81]. In the INMA, the diffusion coefficients depend only on the fraction of imaginary modes of the instantenuous configurations sampled at a temperature T. The original INMA approach, has

[6] The $Ni_{80}P_{20}$ system is one of the favourite test cases in computer simulation of fragile glass formers.

[7] In these LJ-systems, data is commonly given in reduced units.

been criticized[52] for some limitations: not all imaginary modes (the so-called shoulder modes) lead to basin changes due to anharmonic contributions in the interaction potentials, secondly some of the re-arrangements on leaving the instantenuous configurations are localized, and thus do not contribute to a collective motion of all atoms. The INMA approach and the saddle-ruled scenario have been supported by a number of computational studies in which the diffusion coefficients could be related to number of imaginary modes or the fraction of imaginary modes showed a temperature dependence similar to other properties of the investigated glassy materials. [149, 18, 25, 60, 8] However it is not clear, why the saddle-ruled scenario works, and if it is applicable to other systems. If it is valid, the dynamics of the system could be described on an effective landscape restricted to N_{imag} dimensions, and thus the complexity of the problem could be reduced significantly.

2.3.2 Understanding glassy behaviour starting from the solid state

Another point of view of the glass transition, has put the focus on the approximately exponentially growing density of states within a pocket on the energy landscape, present on length and time scales beyond the vibrational properties of the system.[143] Within that approach, it was shown that above a critical temperature, proportional to the inverse growth rate of the local density of states, the system spends most of the time on top of the pocket and the minimum regions are invisible and the effective barriers to neighbor basins are very small and easily surmounted. In contrast, below the trapping temperature, the system drops to the bottom of the basin, and moves to neighboring basins are greatly impeded by the full barriers now encountered.[143] In the same context, we note that the complex dynamics on energy landscapes can be described by tree- and trap-models[74, 110] which incorporate an exponentially growing density of states as one of the key assumptions. Within these models, it is possible to recover not only the equilibrium behaviour of a complex system, but also the non-equilibrium properties of the system.

Below their glass transition temperature T_G, glassy materials exhibit aging effects. The dependence of the material's properties on both the time t_w, one has waited before a measurement of an observable $O(t)$ begins, and on the observation time t_{obs}, is particularly interesting since in technical applications they are usually unwanted, and furthermore in theoretical work these phenomena are not well understood. Within the aforementioned tree and trap models, aging has been shown to exist, due to the existence of an exponentially growing density of states and minima. Furthermore, activation barriers of transition have been included in these models.

An alternative view of the properties of the energy landscape of amorphous materials in the solid state has been the extension of the ideas of Cavagna to temperatures below T_G[7]. It was found that the system explores deep-lying saddle regions of the energy landscape as time progresses after the system had been brought to non-equilibrium conditions in a typical aging experiment. In this non-equilibrium situation it was also found that the index of saddles underlying a given holding point decreased logarithmically with time.

Part II

Techniques

Chapter 3

Computer simulation methods

3.1 Introduction

Computer simulations allow one to study the properties of many-particle systems. In this chapter details of classical Monte-Carlo (MC), the molecular dynamics (MD) simulation techniques used in the thesis will be given together with a very short introduction to the statistical mechanical basis of these methods. The books by Allen and Tildesley[4], by Landau and Binder [92] and by Frenkel and Smit [42] are excellent references that contain a wealth of information about computer simulations.

3.2 Statistical mechanics

Statistical mechanics allows one to study the average properties of many-body systems containing N atoms in three dimensions from a microscopic perspective. These N particles are classically described by their velocity vectors $\vec{v}_i$ and the position vectors $\vec{r}_i$. Thus the total system can be described *microscopically* by the 6N-dimensional vector $\vec{\Gamma}$, whose components are the velocities $\vec{v}_i$ and the position vectors $\vec{r}_i$. A distinct set k of three-dimensional position vectors $\{\vec{r}_i\}$ constitutes a configuration and is commonly represented by the 3N-dimensional configuration vector $\vec{X}_k = (\vec{r}_1, \vec{r}_2, \ldots, \vec{r}_N)$. Similarly the velocities of the particles can be written as $\vec{V}_k = (\vec{v}_1, \vec{v}_2, \ldots, \vec{v}_N)$. The set of vectors $\vec{X}_k$ constitutes the configuration or state space of the system.[1] Note that the N vectors $\vec{r}_i$ are sufficient to describe the arrangement of the particles. Different particle arrangements (configurations), $\vec{X}_k$ and $\vec{X}_l$, will have different potential energies $E_k^{pot}(\vec{X}_k)$ and $E_l^{pot}(\vec{X})$ and have different kinetic energies $E_k^{kin}(\vec{V}_k)$ and $E_l(\vec{V}_l)$. The total energy of a configuration space point k is

$$E^{total}(\vec{X}_k, \vec{V}_k) = E^{pot}(\vec{X}_k) + E^{kin}(\vec{V}_k) \quad (3.1)$$

It is well known that in thermodynamic equilibrium, the macroscopic state of a system of N atoms can be described by three independent thermodynamic variables, e. g. (N, V, E), (N, V, T), (N, P, T), etc. . Thus for a system with constant number of particles N enclosed in a volume V, either the total energy E or the temperature T can be chosen as the third variable. For constant total energy E, the description is called *microcanonical* and the system is represented in the so-called *NVE*-ensemble, while for constant temperature the description is called *canonical* or the *NVT*-ensemble representation. Experimentally it is difficult to keep a system at constant volume and thus the *isothermal-isobaric* description is used and the system is represented by the so-called *NPT*-ensemble. Here an ensemble means a set of different microscopic realizations of the system that comply with the ensemble conditions, e. g. in the NVE-ensemble the different microscopic realizations have the same total energy E and the same number of particles N inside the same volume V.

The partition function Z connects the microscopic and the macroscopic properties of a system of N atoms inside a volume V at temperature T via the Helmholtz free energy

$$F = -k_B T \ln Z_{NVT}, \quad (3.2)$$

[1] In this thesis, capital letters represent configurations. Particle based vectors are written as small letters.

where

$$Z_{NVT} = \int_{\{\vec{X},\vec{V}\}} \exp(-(E(\vec{X},\vec{V})/k_BT)d\vec{X}d\vec{V} \tag{3.3}$$

is the partition function of the system in the canonical ensemble and the integral is over the set of permissible vectors $\{\vec{X},\vec{V}\}$ of the system. For velocity independent forces the kinetic energy part in equation 3.3 can easily be integrated out, and the average value $\langle A\rangle$ of an observable A that only depends on $\vec{X}$ is found to be:

$$\langle A\rangle_{ens} = \frac{\int_{\{\vec{X}\}} A(\vec{X})\exp(-E^{pot}(\vec{X})/k_BT)d\vec{X}}{\int_{\{\vec{X}\}}\exp(-E^{pot}(\vec{X})/k_BT)d\vec{X}}. \tag{3.4}$$

The partition function can be written as a product $Z = Z'\cdot Z''$, with

$$\begin{aligned} Z'' &= \int_{\{\vec{V}\}} \exp\left(-\frac{E_{kin}(\vec{V})}{k_BT})\right) d\vec{V} \\ &= \int_{\{\vec{V}\}} \exp\left(-\frac{\sum_i^N \frac{1}{2}m_i\vec{v}_i^2}{k_BT}\right) d\vec{V} \\ &= \prod_{i=1}^{n_t}\left(\frac{2\pi m_i k_BT}{h^2}\right)^{\frac{3N_i}{2}}\frac{1}{N_i!}, \end{aligned} \tag{3.5}$$

where the integration was performed over all possible velocities $\vec{V}$. m_i and N_i are the masses and the number of particles of the n_t different species found in the sample, respectively. h is Planck's constant, and the factors $N_i!$ account for the indistinguishability of the N_i particles. The configuration space part Z', the so-called configurational integral, reads:

$$Z'_{NVT} \propto \int_{\{\vec{X}\}} \exp(-E^{pot}(\vec{X})/k_BT) \tag{3.6}$$

where the integration is over all permissible configurations $\vec{X}_i$. Since this integration in general cannot be performed analytically for real systems, one has to resort to other methods of evaluating the partition function Z and the expectation values of observables. One way to perform this integration scheme is the Monte-Carlo method that is discussed in section 3.3.

As mentioned, the partition function Z_{NVT} suffices to describe the thermodynamic behaviour of the system. However, while *all* configurations $\{\vec{X},\vec{V}\}$ contribute to the partition function, for a given temperature only some of them are important, since the probability of finding a system in a state $\vec{X}_i,\vec{V}_i$ in thermodynamic equilibrium is given by the *Boltzmann factor*:

$$p(\vec{X}_i,\vec{V}_i;T) = \frac{\exp\left(-\frac{E^{total}(\vec{X}_i,\vec{V}_i)}{k_BT}\right)}{Z} \tag{3.7}$$

or restricting to only $\vec{X}_i$,

$$p(\vec{X}_i;T) = \exp\left(-\frac{E^{pot}(\vec{X}_i)}{k_BT}\right)/Z' \tag{3.8}$$

Note that the macroscopic phase (gas, liquid, solid) present is unimportant for the evaluation of the partition function Z', since only microscopic configurations $\vec{X}_i$ enter its definition.

Until now, the thermodynamic and statistical mechanical properties of a system have been described by the ensemble approach of Gibbs [53], where one investigates the average behaviour of a large number of similarly prepared systems. A different approach is given by concentrating on the time evolution of a configuration $\vec{X}(t)$, which visits different points in configuration space at a temperature T in subsequent time steps. In the long time limit $t\to\infty$, the system visits all possible configurations and the average properties are governed by the Boltzmann factor given in equation 3.8. If a system can visit all possible configurations, the system is called *ergodic* and the time averages

$$\langle A\rangle = \lim_{t_{obs}\to\infty}\frac{1}{t_{obs}}\int_0^{t_{obs}} A(\vec{X}(t),\vec{V}(t))dt \tag{3.9}$$

calculated along the trajectory (for a time span t_{obs}) equal the ensemble averages $\langle A\rangle_{ens}$. If a system is ergodic, the system is in thermodynamic equilibrium. However, achieving equilibrium in computer simulations of disordered or amorphous systems is in no way straightforward. Since the treatment of non-equilibrium systems is rather involved, we postpone a discussion of the special features to the appropriate sections.

3.3 Monte-Carlo methods (MC)

In the preceding section, general statements about thermodynamic equilibrium, configurations and trajectories have been made, but no recipe has been given how to generate these configurations in such a way that thermodynamic equilibrium can be achieved, at least in principle. As already mentioned, to determine the free energy F, one has to evaluate the partition function Z_{NVT}, which requires the determination of a multi-dimensional integral. But in thermodynamic equilibrium, only those configurations $\vec{X}$ with large Boltzmann factors $p(\vec{X};T)$ are important.

3.3.1 The basic algorithm

Metropolis et al. [109] showed, that the following recipe allows one to evaluate the important parts of the partition function $Z'(V,T)$ and thus one can calculate the thermodynamic properties of the system. In the *Metropolis* algorithm one generates a starting configuration $\vec{X}(t=0)$ at a time $t=0$ and proceeds as follows:

1. **Generation of trial configuration**
   At each step t of the algorithm one randomly modifies the configuration to generate a trial configuration $\vec{X}_{trial}$ and calculates the difference of the potential energy

$$\Delta E = E^{pot}(\vec{X}_{trial}) - E^{pot}(\vec{X}(t)). \quad (3.10)$$

2. **Metropolis criterion**
   If $\Delta E < 0$ the configuration $\vec{X}(t+1)$ is set to the trial configuration $\vec{X}_{trial}$, i. e. energy gains are always accepted. If $\Delta E > 0$, a random number $rand$ is drawn, and if $rand < \exp(-\Delta E/k_BT)$, the trial configuration is also accepted as the new configuration. Otherwise the old configuration $\vec{X}(t)$ is kept as the new configuration $\vec{X}(t+1)$.

The algorithm is repeated for a total number of steps t_{run} and at each step, the *Metropolis criterion* is employed.

The Metropolis Monte-Carlo algorithm generates a sequence of configurations $\vec{X}(t)$ and in the limit of long run times t_{run} the configuration space will be sampled according to the correct Boltzmann weight at the temperatures at which the simulations are performed. Note that for very high temperatures the Metropolis criterion $rand < \exp(-\Delta E/k_BT)$ is almost always fulfilled, and almost all changes are accepted. For low temperatures, the acceptance criterion is hardly ever fulfilled and the necessary number of steps to achieve a satisfactory sampling of configurations can become prohibitively large and thus equilibrium properties may be hard to study. Further details of the 'time scale' problem one encounters in computer simulations will be discussed in chapters 9-12.

3.3.2 Implementations

Our NVT-ensemble MC-simulations are performed similar to the original work by Metropolis et al. In each Monte-Carlo move, we shift a randomly selected atom m from its original position $\vec{r}_m^{trial} = \vec{r}_m(t) + \vec{s}$ to generate the trial vector $\vec{X}_{trial}$. The shift vector

$$\vec{s} = rand \cdot \vec{e} \cdot d_{max} \quad (3.11)$$

is calculated by randomly selecting a vector $\vec{e}$ on the unit sphere and shifting in that direction by an amount of $rand \cdot d_{max}$ Å. Here $rand$ is a random number between zero and one. In all simulations, the maximum displacement d_{max} was adjusted to achieve an acceptance ratio of the Monte Carlo moves of 50 %, as suggested in the literature.[4] The acceptance ratios were typically recalculated every 10 Monte Carlo Cycles (MCC), where one MCC corresponds to N individual atom moves. In all MC simulations, we use the two body interaction potential A (see section 3.9) to evaluate the potential energy $E^{pot}(\vec{X})$. Since interaction potential A is a short-ranged two-body interaction potential, we can also use neighbor or Verlet list[168] to save computer time. Note also that in the Metropolis algorithm, the only relevant quantity is the difference of the potential energies of the trial configuration $\vec{X}_{trial}$ and the actual configuration $\vec{X}(t)$, and if only single atom moves of an atom m are involved and the potential energy is given by a two-body interaction potential, the difference of the potential energies equals

$$\Delta E^{pot} = \sum_{i=1}^{N} V(|\vec{r}_i - \vec{r}_m|) - V(|\vec{r}_i - \vec{r}_m^{trial}|) \tag{3.12}$$

where r_m and r_m^{trial} are position vectors of the atoms in the original and the trial configurations, respectively. Note that in equation 3.12, the sum runs only over N atoms, and not over N^2 pairs of atoms, as is required for the calculation of the total potential energy by a two-body potential of a single configuration

$$E^{pot} = 1/2 \sum_{i}^{N} \sum_{j}^{N} V(r_{ij}). \tag{3.13}$$

We construct Verlet lists[168] for each atom i, i. e. a list of neighboring atoms j, that are only a distance $r_{ij} < R_V \equiv R_c + \Delta R$ apart. For interaction potential A, $R_c = 6$ Å and the extra distance ΔR was set to 2 Å. Each time an atom has moved more than $1/2\Delta R$ Å, the neighbor lists are updated. Using these neighbor list, one saves approximately 30% computer time for dense systems, since the atoms do not move very far and the sum in equation 3.12 runs only over the atoms in the neighbor list of each atom. However, for dilute systems, we calculate the energy change ΔE by equation 3.13, since the frequently necessary updates of the Verlet lists actually lead to an increased computional burden.

In the NVT-simulations, the cell volume is kept constant, but in experiments the volume usually is free to adapt to the external pressure P_{ext}. Similar to the free adaption of the cell volume, one studies the system at an external pressure P_{ext} by allowing both the atomic positions and the cell volume to vary. Similar to the random displacement of the atoms, the cubic cell volume $V = a^3$ of the (periodically repeated) simulation cell, was varied isotropically by changing the volume $V(t)$ to a trial volume

$$V^{trial} = V(t) + (rand - 0.5) \cdot \Delta V_{max}, \tag{3.14}$$

and calculating the change in potential energy of the trial configuration $\vec{X}^{trial}$ in which the position of all atoms are changed by rescaling the cell length $a' = (V^{trial}/V)^{1/3} \cdot a$. A trial configuration was accepted as a new configuration, if the energy change

$$\begin{aligned} \Delta E = E_{trial}^{pot}(V^{trial}) - E^{pot}(V(t)) \\ + P_{ext} \cdot (V^{trial} - V(t)) \end{aligned} \tag{3.15}$$

was acceptable according to the Metropolis criterion.

Note that for the calculation of the change in potential energy, the potential energy for the trial configuration must be calculated according to equation 3.13. Thus, the computional cost for a volume move τ_{vol} is proportional to the square of the number of atoms. Similar to the maximum atomic displacement, the maximum volume change ΔV_{max} was adapted to reach an acceptance ratio of 50 % in ten MCCs. Again, $rand$ is a random number between zero and one. After a volume change it is plausible to adjust the atomic positions to the new volume/cell constants and thus the volume was only changed in one to ten percent of the performed MCCs. Note that for a-$Si_3B_3N_7$ neither the average cell volume nor the time series of volumes $V(t)$ depended significantly on the choice of the ratio atom moves to volume changes.

3.4 Molecular dynamics simulations

In a molecular dynamics (MD) simulations in the NVE-ensemble, one solves Newtons equations of motion (EOM) for the classical motion of a system of N atoms, to study the microscopic time evolution of a many-body system. After initialization of the velocities $\vec{v}_i, i = 1, \ldots, N$ and assignment of initial atom positions $\vec{r}_i$, we use the velocity form of the Verlet-algorithm[4] for the integration of the EOM. The atoms are placed on randomly selected places inside the cubic simulation cell or loaded from an external source, and the velocities are initialized in such a way, that the total linear momentum of the atom is zero and that the kinetic temperature $T_{kin} = \frac{2 \cdot E_{kin}}{3Nk_B}$ equals a initial temperature T_0. After these initializations the velocity-Verlet algorithm proceeds as follows:

1. Predict the values of the positions of the atoms $\vec{r}_i(t + \Delta t)$ at time $t + \Delta t$ and the

velocities $\vec{v}_i(t+\frac{1}{2}\Delta t)$ at half time $t+\frac{1}{2}\Delta t$ by

$$\vec{r}_i(t+\Delta t) = \vec{r}_i(t) + v_i \cdot \Delta t + \frac{1}{2}a_i(t)\Delta t^2$$

and

$$\vec{v}_i(t+\frac{1}{2}\Delta t) = \vec{v}_i(t) + \frac{1}{2}a_i(t)\Delta t \tag{3.16}$$

2. Calculate the accelerations $\vec{a}_i = \frac{\vec{F}_i}{m_i}$ using the new positions $\vec{r}_i$ and the forces $\vec{F}_i = -\nabla_i E^{pot}$.

3. Correct the velocities $\vec{v}_i(t+\frac{1}{2}\Delta t)$ by

$$\vec{v}_i(t+\frac{1}{2}\Delta t) = \vec{v}_i(t)+\frac{1}{2}\vec{a}_i(t+\Delta t)\Delta t \tag{3.17}$$

For the a-$Si_3B_3N_7$system we chose a time step of 1 fs for the Velocity Verlet integration scheme and typical simulations lasted $10^6 - 10^7$ time steps corresponding to real times of 1-10 nanoseconds. Note that in the NVE-ensemble, the kinetic energy and the potential energies as well as the pressure and the kinetic temperature T_{kin} fluctuate around their mean values. To simulate a system in the constant temperature NVT-ensemble, we rescaled the magnitude of the velocities $\vec{v}_i' = \alpha \cdot \vec{v}_i$ by a factor

$$\alpha = \sqrt{\frac{\langle T_{kin}\rangle_t}{T}} \tag{3.18}$$

where the kinetic temperature $\langle T_{kin}\rangle_t$ was averaged over ten time steps prior to rescaling. Note that other methods exist, that employ an extended Lagrangian formalism to keep the temperature or other prescribed variables like the pressure constant (see the book by Frenkel and Smit [42] for an exhaustive discussion of these methods), but these methods have not been used in this thesis.

3.5 Thermodynamic properties from computer simulations

In sections 3.3 and 3.4, we showed how it is possible to generate configurations according to the laws of statistical mechanics. Now we show how experimentally accessible data can be determined from a sequence of N_{conf} configurations $\vec{X}_t$, $(t = 1, \ldots, N_{conf})$. Here the index t serves two purposes, to distinguish configurations and also to indicate the simulation time. Note that in the Monte-Carlo simulations there is no real time unit Δt like in MD simulations, and the time scale can only be set by comparison to MD-simulations.

The simplest quantity to measure is the average potential energy[2]

$$\langle E^{pot}\rangle = \frac{1}{N_{conf}}\sum_{i=1}^{N_{conf}} E_i^{pot} \tag{3.19}$$

and the fluctuations of the potential energy

$$\sigma^2[E^{pot}] = \left(\frac{1}{N_{conf}}\sum_{i=1}^{N_{conf}}[E_i^{pot}]^2\right) - \langle E^{pot}\rangle^2 \tag{3.20}$$

The specific heat $C_V = \left(\frac{\partial E}{\partial T}\right)_V$ can serve as an indicator for a phase transition (PT) between two equilibrium phases of a system. We determine the specific heat by numerically differentiating the temperature dependence of the average potential energy E^{pot}:

$$C_V(T) = \frac{\Delta\langle E^{pot}\rangle}{\Delta T}. \tag{3.21}$$

From the raw data of a computer simulation it is often not clear whether a system has really attained equilibrium, e.g. the configurations have been sampled according to the correct Boltzmann weight. Furthermore simple criteria like 'the potential energy shows no drift for successive configuration' may lead to errorrenous conclusions. Therefore we used the fluctuation-dissipation theorem (FDT) to distinguish between equilibrium or non-equilibrium simulations. For the potential energy the FDT relates the fluctuations in the potential energy to the change in potential energy accompanying a change in temperature

$$\frac{\Delta\langle E^{pot}\rangle}{\Delta T} = \frac{\sigma^2[E^{pot}]}{k_B T^2} \tag{3.22}$$

Thus, if the systems is simulated in equilibrium, the equal sign must hold at least approximately. Otherwise the system is not in

[2] In this chapter, we focus on the Monte-Carlo method and the kinetic energy E_{kin} is simply $E_{kin} = 3/2Nk_BT$.

equilibrium and measured properties in general become time dependent, since the system is *aging*.

Since computer simulations are frequently performed in the NVT-ensemble one important quantity to measure is the average pressure $\langle P \rangle$. For each configuration $\vec{X}_t$ of volume V, one determines the internal virial $\mathcal{W}$ to calculate the pressure P_t.

$$P_t = P_{id} + P_{vir} = \frac{N k_B T}{V} + \frac{\mathcal{W}}{V} \tag{3.23}$$

as the sum of the ideal gas contribution P_{id} and the virial contribution P_{vir}.

For two-body interaction potentials, the internal virial $\mathcal{W}$ can be written as:

$$\mathcal{W} = -\frac{1}{3} \sum_{i<j}^{N} \sum_{j=1}^{N} \vec{r}_{ij} \cdot \vec{F}_{ij}, \tag{3.24}$$

where $\vec{r}_{ij}$ is difference vector $\vec{r}_i - \vec{r}_j$ between the positions of the atoms i, j and $\vec{F}_{ij}$ is the force acting on atom i from atom j. The average pressure $\langle P \rangle$ of a set of configurations k is $\langle P \rangle = 1/N_{conf} \sum_{k=1}^{N_{conf}} P_k$.

3.6 Transport properties

In the study of liquids, supercooled liquids and glasses, the coefficient of self-diffusion D and the viscosity η are used to distinguish between liquids and glasses. The diffusion coefficient $D(T)$ can be obtained from the mean squared distance (MSD) between the atoms of two configurations $\vec{X}(t_1)$ and $\vec{X}(t_2)$ sampled at simulation times $t_1 < t_2$ at temperature T,

$$\begin{aligned} MSD(t_1, t_2) &= MSD(\vec{X}(t_1), \vec{X}(t_2)) \\ &= \sum_{i=1}^{N} \left(\vec{x}_i(t_2) - \vec{x}_i(t_1)\right)^2 \\ &= \left(\vec{X}(t_1) - \vec{X}(t_2)\right)^2, \end{aligned} \tag{3.25}$$

by using the Einstein-Smoluchowski relation[34]

$$D = \lim_{\Delta t \to \infty} \frac{MSD(t_1, t_2)}{6(\Delta t)}. \tag{3.26}$$

Note, that the diffusion coefficient can only be determined, if the MSD is proportional to the time interval $\Delta t = t_2 - t_1$.

Since in Monte-Carlo simulations the viscosity η can only be determined from the Stokes-Einstein relation[34]

$$\eta = \frac{k_B T}{D} \frac{1}{6\pi a}, \tag{3.27}$$

and the validity of the relation cannot be taken for granted,[75] we mostly use the diffusion coefficient D directly, to discriminate between glasses and supercooled (liquids) instead of the macroscopically accessible viscosity η.

For amorphous covalent networks, transport mechanism can also be studied by the bond-survival probabilities ($BSP(t_1, t_2)$) of bonds in the network[75]. With a given definition of a bond between two atoms (see section 4.1), we calculate the probability finding a bond $b(i, j)$ between two atoms i, j at a time t_2 provided that this bond was present at an earlier time t_1.

For equilibrium situations, the bond survival probabilities depend only on the time difference $\Delta t = t_2 - t_1$. Note that, apart from insights into transport mechanisms, the BSPs allow one to study the topological similarity between two configurations, and high values of the BSP indicate that the amorphous network is mostly preserved. In a-$Si_3B_3N_7$ one can furthermore distinguish between Si-N and B-N bonds and this distinction allows one to study the relative stability of the respective bonds. Finally, for temperatures below the glass transition temperature, the BSP will also show aging behaviour.

3.7 Global optimization

Local optimization techniques usually lead the system to the closest local minimum of the energy landscape, which is usually not the minimum with the lowest energy. To find the global minimum, or at least to get close to it, one usually employs global optimization algorithms. One of these algorithm is simulated annealing.[84] In the simulated annealing algorithm, one mimics the slow cooling of a liquid to form a solid. Typically, this is done by first equilibrating the system at a temperature T_0 using the Monte-Carlo algorithm (see section 3.3) using the energy as the cost function. After equilibration, one lowers the system's temperature to zero by a cooling sched-

ule. Frequent choices for the cooling schedule are linear cooling $T(t) = T_0 - \gamma \cdot t$ or geometric cooling schedules $T(t) = T_0 \cdot a^t$ $(a < 1)$. Between the temperature updates, the system evolves at the current temperature for, typically short, relaxation times τ_{relax}^{SA}. In this thesis, we employ the linear cooling schedule in our global optimizations, and typical choices for the relaxation times τ_{relax}^{SA} are 100 MCC.

3.8 Local optimization

Local minima of the potential energy surface are characteristic points of the energy surface and can be determined by different numerical techniques. In this thesis the conjugate gradient method and the MC-quench method have been used for the determination of these local minima. [3]

3.8.1 Conjugate gradient method

The conjugate gradient method uses the gradient of the potential energy E^{pot}

$$\nabla E^{pot} = \begin{pmatrix} \frac{\partial E^{pot}}{\partial x_1} \\ \vdots \\ \frac{\partial E^{pot}}{\partial x_{3N}} \end{pmatrix} \tag{3.28}$$

to determine a local minimum of the potential energy surface. $\frac{\partial E^{pot}}{\partial x_i}$ is the derivative of the potential energy with respect to the coordinate i of the configuration vector $\vec{X}$. Starting from an initial configuration vector $\vec{X}(0)$ one performs an initial step (of step width λ) down the steepest descent path, i. e. in the direction of gradient at configuration space point $\vec{X}(0)$, on the potential energy landscape. New steps in directions $\vec{g}(n+1)$ from point $\vec{X}(n)$ towards the minimum are calculated from combining the gradient at previously visited configuration space point $\nabla E^{pot}(\vec{X}(n-1))$ and the gradient $\nabla E^{pot}(\vec{X}(n))$ at the configuration space point $\vec{X}(n)$ using various formulae. The result of this combination is a useful approximation of the matrix of the second partial derivatives by first partial derivatives. For more technical specification, we refer the reader to the 'Numerical Recipes' by Press et. al. [175] for a detailed account of the conjugate gradient method. Here we note that we used the gradient norm $|\nabla E^{pot}| < 0.0001$ eV as the halting criterion for the determination of the minima of the local conjugate gradient search.[4]

[3] The conjugate gradient optimization were performed using the very powerful GULP program. [44]

3.8.2 MC-quench

The MC-quench method is a $T = 0$ K Monte-Carlo method. After generation of a trial configuration $\vec{X}^{trial}$ only those trial configurations are accepted, that lower the potential energy. We only used atom displacement moves for the quench procedure and the quench converged, if the net atomic displacements had fallen below 0.001 Å/atom. Note that the MC-quench procedure does not necessarily brings the system to the true minimum, where the gradient vanishes, but only very close to it. In fact, it has been shown that the time to bring the system to a minimum increases logarithmically the closer one gets to the minimum.[23] However with the MC-quench method, one can determine different minima that are accessible from the same starting configuration.

Reverse Monte-Carlo (RMC)

After the local optimizations using empirical interaction potentials, a refinement by the reverse Monte-Carlo (RMC) method of the structural models was useful to remove non-critical potential effects, that left the initial topology of the amorphous network essentially unchanged.[5] In the RMC method [107], we did not optimize the potential energy but the cost function $C(\vec{X}_i; \lambda)$, that was given as a linear combination of the difference between the computed and experimentally measured (via X-ray (X) or neutron scattering (n), if available) pair correlation functions $(\Delta D_{X/n}(\vec{X}_i))^2$, and the potential energy $E_{pot}(\vec{X}_i)$ of the configuration $\vec{X}_i$.

[4] One should note that in principle the gradient search can also stop at a saddle point ($\nabla E = 0$ for a saddle, too). However, the conjugate gradient method usually avoids these traps.

[5] The RMC-program was written by Dr. H. Putz (Crystal Impact GBR, Bonn) and was used with permission.

$$C(\vec{X}_i;\lambda) = \lambda(\Delta D_{X/n}(\vec{X}_i))^2 + (1-\lambda)E_{pot}(\vec{X}_i). \tag{3.29}$$

Note that the deviations from the experimental pair correlation function $D_X^{exp}(R)$ and $D_n^{exp}(R)$

$$(\Delta D_{X/n})^2 = (\Delta D_X)^2 + (\Delta D_n)^2 \tag{3.30}$$

were weighted equally.[6] In the optimization of the cost function $C(\vec{X}_i;\lambda)$, only random atom displacements were accepted that lowered the cost function. Thus the reverse Monte-Carlo method is similar to a MC-quench procedure in which the potential energy is substituted by the cost function $C(\vec{X}_i;\lambda)$.

3.9 Interactions potentials for the Si-B-N system

The potential energy is a key to an understanding of the thermodynamic behaviour of every many-body system. Ideally one would like to determine the potential energy of any arrangement of atoms by solving Schrödinger's equation for the electronic and nuclear part of the wave function. However, this is only possible for rather small system sizes and only on very small time scales. An alternative way to study many-body systems is to neglect the electronic effects and to treat the system classically, using an appropriate interaction potential $V(\vec{X})$. Typically these interaction potentials include two-, three- and possibly four-body interactions for the description of the interactions between the atoms.

$$V(\vec{X}) = \sum_i^N \sum_j^N V(r_{ij}) \; + \; \sum_i^N \sum_j^N \sum_k^N V(r_{ij}, r_{ik}, \Theta_{ijk}) \; + \; \text{four-body terms} \tag{3.31}$$

Thus two-body interactions require a double sum for the evaluation of the potential energy and the potential energy depends on the interatomic distance r_{ij}. Similarly, three body terms depend on the two interatomic distances and the angle Θ_{ijk} between the three atoms i, j, k. Note that the computational cost for the calculation of the potential energy depends on the squared number of atoms ($\propto N^2$) for two-body potentials and on the cube of the number of atoms $\propto N^3$) for three body interactions. Thus practically treatable computer simulations of large systems with long simulation times require a two-body potential, and only for sophisticated interactions and special situations one should use three- and four-body interaction terms.

Thus in this thesis two classical interaction potentials are employed for the modelling of a-$Si_3B_3N_7$.[7] These interaction potentials have been fitted and extensively tested by Gastreich et. al [47] and are not part of this thesis. The first one, $V_A(r_{ij})$, is a pure two-body potential, that contains no Coulomb terms and is computationally very fast. The second interaction potential, $V_B(r_{ij}, r_{ik}, \Theta_{ijk})$, which contains two- and three-body terms as well as Coulomb terms is computationally very expensive, and therefore has only been used in the local optimizations.[8] Details of the functional forms and the parameters of the potentials A and B are given in tables 3.2 and 3.3, respectively. For a detailed analysis, we refer the reader to the original publications[48, 49] and M. Gastreich's thesis[47]. In table 3.1, we summarize the potential energies and the densities of crystalline polymorphs of the $Si_3B_3N_7$-system, as determined from the interaction potentials A and B. We note that the interaction potential A favors phase separation into the binary phases $\beta-Si_3N_4$ and h-BN, whereas for potential B, the ternary crystalline phase are more stable.[9]

[6] The calculation of the pair correlation function of a configuration $\vec{X}$ is discussed in section 4.1.1.

[7] The functional form and the parameters of the interaction potential for the Si-O-N system are given in section 7.2 of chapter 7.

[8] Interaction potential B is a preliminary version of the potential published in [49], but reproduces experimental properties of the Si/B/N-system.[46]

[9] Ab-initio calculations for possible ternary crystalline modifications indicate that the binary phases should be slightly favored over the ternary phase, in agreement with potential A.[89]

System	E_A	E_B	$E(QM)$	ρ_M
β-Si_3N_4	-5.02	-17.54	-5.31	3.19
h-BN	-5.75	-15.67	-6.41	2.29
β_2-$Si_3B_3N_7$	-5.43	-16.59	x	2.79
sj-$Si_3B_3N_7$ [144]	-5.41	-16.53	x+0.09	2.77
mix (3·h-BN + β-Si_3N_4	-5.56	-16.14	-6.13	2.83
E(sj-$Si_3B_3N_7$) - E(mix)	+0.14	-0.39	+0.22	
E(β_2-$Si_3B_3N_7$) - E(mix)	+0.15	-0.45	+0.13	

Table 3.1: Potential energies and densities of crystalline polymorphs in the $Si_3B_3N_7$-system. The potential energies E_A and E_B are calculated using interaction potentials A and B and are given in eV/atom, the densities are given in g/cm^3. The crystal structures of so-called the β_2-$Si_3B_3N_7$-polymorph and for the sj-$Si_3B_3N_7$-polymorph were taken from refs. [89] and [144], respectively.The quantum mechanically calculated energies $E(QM)$ are taken from refs. [89] and [47], respectively. The quantum-mechincally calculated energy of the β_2-$Si_3B_3N_7$-polymorph is x = -189.85 eV/atom.[89]

Name	Analytical Form	Parameters	Units
Morse	$E = D_e \cdot \left\{(1 - e^{-a(r-r_0)})^2 - 1\right\}$	D_e, a, r_0	eV, Å^{-1}, Å
general 1	$E = \frac{A}{r} \cdot e^{-r/\rho}$	A, ρ	eV·Å, Å
damped dispersion	$E = -\frac{C_6}{r6} \cdot \left(1 - e^{-b_6 r} \cdot \sum_{k=0}^{6} \frac{(b_6 r)^k}{k!}\right)$	C_6, b_6	eV·Å^6, Å^{-1}
two-body Taper	$P_5 = (x_o - x_i)^{-5}$ $\cdot \left\{-6 \cdot r^5 \quad +15(x_i + x_o) \cdot r^4 \right.$ $-10(x_i^2 + 4x_i x_o + x_o^2) \cdot r^3$ $+30(x_i^2 x_o + x_i x_o^2) \cdot r^2$ $-30 x_i^2 x_o^2 \cdot r$ $\left. +10 x_i^2 x_o^3 + x_o^5 - 5 x_i x_o^4 \right\}$	x_i, x_o	Å, Å

(a) Functional form

Interaction Partners	Type of Potential	Parameter	Value
N–B	Morse	D_e	5.50007
		a	2.84990
		r_0	1.32521
N–Si	Morse	D_e	3.88461
		a	2.32660
		r_0	1.62136
N–N	damped	C_6	16691.4
	dispersion	b_6	0.50328
N–N	general 1	A	2499.01
		ρ	0.36029
B–B	general 1	A	1231.52
		ρ	0.36119
Si–Si	general 1	A	177.510
		ρ	0.63685
B–Si	general 1	A	643.332
		ρ	0.43302
Two-body taper		x_i	4.30000
		x_o	5.80000

(b) Parameter set

Table 3.2: Functional forms and parameters of the two-body potential $V_A(r)$ of Gastreich et al. [50].

Name	Analytical Form	Parameters	Units
Buckingham	$E = A \cdot \exp(-r/\rho)$	A, ρ	eV, Å
Damped Dispersion	$E = -\frac{C_6}{r6} \cdot \left(1 - e^{-b_6 r} \cdot \sum_{k=0}^{6} \frac{(b_6 r)^k}{k!}\right)$	C_6, b_6	eV·Å^6, Å^{-1}
Two-body Taper	$P_5 = (x_o - x_i)^{-5}$ $\cdot\{-6 \cdot r^5 + 15(x_i + x_o) \cdot r^4$ $-10(x_i^2 + 4x_i x_o + x_o^2) \cdot r^3$ $+30(x_i^2 x_o + x_i x_o^2) \cdot r^2$ $-30 x_i^2 x_o^2 \cdot r$ $+10 x_i^2 x_o^3 + x_o^5 - 5 x_i x_o^4\}$	x_i, x_o	Å, Å
Stillinger-Weber three-body	$E = A \cdot exp\left(\frac{\rho}{r_{12} - r_{max12}} + \frac{\rho}{r_{13} - r_{max13}}\right) \cdot (\cos(\Theta) - \cos(\Theta_0))^2$	A, ρ, r_{max12}, r_{max13}, Θ_0	eV·rad^{-2}, Å, Å, Å, deg

Table 3.3: Functional form of the three-body potential $V_B(r_{ij}, r_{ik}, \Theta_{ijk})$.

	Type of Potential	Param.	Value
N–B	Buckingham	A	29685.43
		ρ	0.137782
N–Si	Buckingham	A	10959.748
		ρ	0.190292
N–N	damped dispersion	C_6	20.4
		b_6	1.23
B–B	Buckingham	A	451.46
		ρ	0.29467
Two-body damping		x_i	3.55
		x_o	4.55

(a) Two-body part. Charges are: q(Si)=+1.995085, q(B)=+1.49631375, and q(N)=-1.49631375.

	Param.	Val.
B-N-B	A	9.047
	ρ	3.705
	Θ_0	120.0
	$r_{max12/13}$	3.750
N-B-N	A	9.047
	ρ	3.705
	Θ_0	120.0
	$r_{max12/13}$	3.750
N-Si-N	A	65.36
	ρ	3.9068
	Θ_0	109.47
	$r_{max12/13}$	3.750
Si-N-Si	A	65.36
	ρ	3.9068
	Θ_0	120.00
	$r_{max12/13}$	3.750

(b) Three-body part. Stillinger-Weber type functional form.

Table 3.4: Parameter set of the three-body potential B $V_B(r_{ij}, r_{ik}, \Theta_{ijk})$.

Chapter 4

Properties of configurations

4.1 Structural properties

4.1.1 Pair correlation functions

We calculate the X-ray and neutron scattering pair correlation functions $D_{X/n}(R)$ for each model/configuration via

$$D_{X/N}(R) = \sum_{A,B} \frac{c_A c_B f_A^{X/N} f_B^{X/N}}{\langle f^2 \rangle} D^{AB}(R) \tag{4.1}$$

where the partial pair correlation functions are:

$$D_{X/N}^{AB}(R) = \frac{4\pi r}{c_B} \left[\rho_{AB}(R) - \rho_0\right]. \tag{4.2}$$

In equation 4.1 c_A and c_B are the concentrations of the atom types A and B and $f_A^{X/N}$ and $f_B^{X/N}$ are the scattering factors/lengths of the atoms A and B for X-ray and neutron scattering, respectively. Note, that the scattering factors for X-rays depend on the wavelength of the incident X-ray beam. In equation 4.2, $\rho_0 = \frac{N}{V}$ is the number density and ρ_{AB} is the number of B-type atoms per unit volume at distance R from an A-type atom at the origin.

4.1.2 Topology and local geometry

We determine the topology of the amorphous network from the bonding graph $\mathbf{G}$.[1] The bonding graph $\mathbf{G}$ contains the atoms as the vertices of the graph and the bonds $e_{ij} \equiv b(i,j)$ between atoms i, j form the edges of the graph. We drew bonds between two atoms i, j of types t_i, t_j, respectively, if the interatomic distance fell into an interval $[r_{min}(t_i,t_j), r_{max}(t_i,t_j)]$. Note that two connected atoms were nearest neighbors. In the Si-B-N system only Si-N and B-N nearest neighbor distances are observed experimentally and thus we chose r_{min}(Si-N)=r_{min}(B-N) = 1.0 Å and r_{max}(B-N) = 1.8 Å and r_{max}(Si-N) = 2.1 Å as the distances that defined the connectivity of the bonding graph $\mathbf{G}$.[2] The nearest neighbor atoms j of an atom i defined the first coordination sphere $CS1(i)$ of atom i. The first coordination number $CN1(i)$ is the number of nearest neighbors of atom i. The mean coordination number

$$MCN1(t_i) = \frac{1}{N(t_i)} \sum_{i=1}^{N(t_i)} CN1(i), \tag{4.3}$$

is the average number of atoms surrounding an atom of type t_i. To distinguish between different coordination numbers of the atoms we calculated the distributions of first coordination spheres $h_{t_i}^{(1)}(z)$ for types t_i = Si, B or N. For silicon and boron we determined the occurrences of SiN_z-($z = 1 \ldots 6$) and BN_z-($z = 1 \ldots 6$) coordination spheres and for nitrogen we considered the $N(Si_xB_{z-x})$ ($z = 1 \ldots 6$, $x \leq z$) coordination spheres and the distributions $h_N^{(1)}(z,x)$. Note that in the case of nitrogen 36 different coordination spheres were considered. We analyzed the geometry of the different coordination spheres $CS(t_i,z)$ using

[1] See Cormen [29] for a introduction to graph theory and graph algorithms.

[2] For the other chemical systems, that were investigated in this thesis, the minimum and maximum distances employed are given at the appropriate places; in this section details for the Si-B-N system are given.

Pair	$r^{(2)}_{min}$	$r^{(2)}_{max}$
B-B	2.0	2.9
B-Si	2.0	3.2
Si-Si	2.0	3.2
Si-B	2.0	3.2
N-N	2.0	2.9

Table 4.1: Distances used in the determination of the second coordination spheres of atoms of type t_i surrounded by next nearest neighbors of type t_j in a-$Si_3B_3N_7$. All distances are given in Å.

the angular distribution functions,

$$ADF(\Theta, z) = \frac{1}{N(t_i) \cdot z^2} \sum_{i=1}^{N(t_i)} \sum_{j \in CS(t_i,z)}^{z} \sum_{k \in CS(t_i,z)} \delta(\Theta - \Theta_{ijk}). \tag{4.4}$$

We used two different procedures for the determination of the second coordination sphere of next nearest neighbors. In the *topological procedure*, we determined these next nearest neighbors of atom i from the neighbors $k \in CS1(j)$ of the neighbors $j \in CS1(i)$ of atom i. In the *geometrical* procedure we determined the next nearest neighbors of atoms i by counting all atoms j, with interatomic distances r_{ij} falling into intervals $[r^{(2)}_{min}, r^{(2)}_{max}]$. Table 4.1 summarizes the distance criteria employed.[3] Note that the geometrical and the topological procedure gave similar results.

Ring determination

We determined the rings in the structure from the bonding graph **G** by finding the shortest path from neighbor $j \in CS1(i)$ to neighbor $k \in CS1(i)$ of atom i, where atom i was excluded from the shortest path search. We searched for rings containing at most $R_{max} = 48$ atoms and excluded those rings of size R_2, whose vertices where already found in a ring of smaller size $R_1 < R_2$. Next we describe the details of the ring determination algorithm (RDA) and ring counting procedures used in the thesis.

[3] B-N and Si-N next nearest neighbors were not observed in our simulations.

The RDA uses the bonding graph **G** of the configuration as input. Note that **G** is an undirected graph. For each vertex $v_i \in \mathbf{G}$, we determine the shortest path $P(v_j, \ldots, v_k)$[4] of length $n = R(t)$ from neighbors $v_j \in CS1(v_i)$ to other neighbors $v_k \in CS(v_i) \neq v_j$. Here $CS(v_i)$ is the coordination sphere of vertex/atom v_i. In the RDA, we set the initial maximum ring size $R(0) = 3$ and increase the maximum ring size to $R(max) = 48$ in unit steps. For a fixed ring size $R(t)$, we determine for each vertex v_i, the shortest path from v_j to v_k by a breadth first search, omitting v_i from the search procedure, of course. Each time, we find a shortest path $P(v_j, \ldots, v_k)$, we check whether an already existing ring $R(v_1, ...v_n)$, $n < R(t)$, does not contain *all* vertices $v_p \in P(v_j, v_k)$. If we find that all vertices $v_p \in P(v_j, v_k)$ are not contained in a smaller ring, we add the path $P(v_j, \ldots, v_k)$ to the list of known rings. After the maximum ring size has been reached, the number of known rings N_{rings}, is the number of smallest rings in the structure. Since we are analyzing a ternary chemical system, we additionally assign to each vertex v_i a 'color' c_i according to the element type of atom v_i, and characterize the structure by

1. the total number of rings.
2. the number $N_R(n)$ of rings of size n.
3. the composition of the rings $C_n(Si)$, $C_n(B)$ and $C_n(N)$, where $C_n(X)$ is the number of atoms of element X in a ring of size n.

Since the structural models contain different numbers of vertices/atoms, we normalize our data to the number of smallest rings in the structure, and thus show:

$$h_R(n) = \frac{N_R(n)}{N_{rings}}, \tag{4.5}$$

the relative number of rings of size n and

$$h^C_R(n) = \frac{N^C_R(n)}{N_R(n)} \tag{4.6}$$

the relative number of rings of size n with a specified composition $\vec{C}$ with respect to total number of rings $N_R(n)$ of size n.

[4] A shortest path $P(v_1, \ldots, v_n)$ between to vertices v_1 and v_n is the minimum number of edges one has to traverse to get from vertex v_1 to vertex v_n.

Identification of Si-N-B building units

In a-$Si_3B_3N_7$, the interesting question arises, whether the models could be synthesized from Si-N-B building units, which represent the precursor molecule TADB. We determined the maximum number of Si-N-B building block by mapping this problem to the *maximum cardinality matching* (MCM) problem. In the MCM problem one wants to find the maximum number of edges of a graph $\mathbf{G}$ that do not share a common vertex. In our case, the graph $\mathbf{G}$ is the graph containing only silicon and boron atoms as vertices, and we drew edges between a silicon and a boron atom, if these atoms were connected by a common nitrogen atom. Note that no edges between two silicon or two boron atoms are drawn. Below we will show that the above mapping to the MCM problem allows us to determine the maximum number of Si-N-B building units within the Si-B graph. Note, that the problem can be conveniently solved using the LEDA library function *MAX_CARD_MATCHING* [108].

Above, we mentioned that the maximum number of Si-N-B building units from which a structural model can be generated in principle, can be calculated from the maximum matching of the cation connectivity graph $\mathbf{G}_{AB}$. In the graph $\mathbf{G}_{AB}$, silicon atoms are vertices with color A and boron atoms are vertices with color B. The edges of the graph $\mathbf{G}_{AB}$ are drawn from A to B colored vertices, that are connected via a common nitrogen atom. Note that the nitrogen atoms are not considered anymore and that no $A-A$ or $B-B$ edges are drawn, since these edges cannot be generated by Si-N-B in the first place (see figure 4.1). A maximum matching of an *uncolored* graph $\mathbf{G}$ is the largest set of edges e, where no two edge share a common vertex. What has to be shown now, is that from a matching M of $\mathbf{G}$, the same maximum matching in the colored graph $\mathbf{G}_{AB}$ can be reproduced. We focus on connected graphs $\mathbf{G}_{AB}$, and note that for each connected graph $\mathbf{G}_{AB}$ the coloring of this graph is uniquely determined by the color of a single node, since by definition edges are only drawn between differently colored vertices. Thus, the graph $\mathbf{G}$ can be colored to produce the graph $\mathbf{G}_{AB}$ by keeping one color fixed. We proceed in two steps now, first showing that from a maximum matching M^* of the uncolored graph $\mathbf{G}$, a matching M'_{AB} is induced. In the second step, we show that M'_{AB} is a maximum matching M^*_{AB}.

Consider a maximum matching M^* of $\mathbf{G}$, that should is recolored. Every edge e of M^*, is, due to its generation of $\mathbf{G}$ from $\mathbf{G}_{AB}$, either a A-B or a B-A edge, that is allowed in a matching M_{AB} of $\mathbf{G}_{AB}$. Since a matching M is a subset of the edges of $\mathbf{G}$, the edges of M are also a subset of the colored graph $\mathbf{G}_{AB}$, and the recolored edges are also a matching M'_{AB} of $\mathbf{G}_{AB}$.

To show that M'_{AB} is a maximum matching, we note that a maximum matching M^*_{AB} becomes a matching M'' of the graph $\mathbf{G}$ after uncoloring, since only constraints are removed. Thus M'' is a matching of $\mathbf{G}$ but not necessarily a maximum matching of M. Thus,

$$|M^*_{AB}| = |M''| \leq |M^*|, \tag{4.7}$$

where $|X|$ denotes the cardinality (the number of elements) of the set X. On the other hand, M'_{AB} is an allowed matching of $\mathbf{G}_{AB}$, and M^*_{AB} is by assumption a maximum matching. Thus

$$|M^*| = |M'_{AB}| \leq |M^*_{AB}|, \tag{4.8}$$

but the two inequalities: $|M^*| \leq |M^*_{AB}|$ and $|M^*_{AB}| \leq |M^*|$, are only valid if $|M^*_{AB}| = |M^*|$, and thus a recoloring of the maximum matching M^* of the uncolored graph $\mathbf{G}$ generates a maximum matching M^*_{AB} of the graph $\mathbf{G}_{AB}$.

Void determination

Our void determination algorithm has been adapted from [10]. To identify a void inside a given structural model, we proceed in two steps. First we divide the cubic unit cell into cubic sub-cells of size $a << L$, where L is the box length of the unit cell and determine for each sub-cell whether it is occupied by an atom or not. The cubic sub-cells constitute a graph $\mathbf{G}_S$, that contains the sub-cells as vertices and we drew edges from each sub-cell to its 26 ($3 \cdot 3 \cdot 3 - 1$) adjacent sub-cells. The n_{cc} connected components C_i of size s_i of the graph G_S, which contain the connected vacancies of the structure, are determined by a

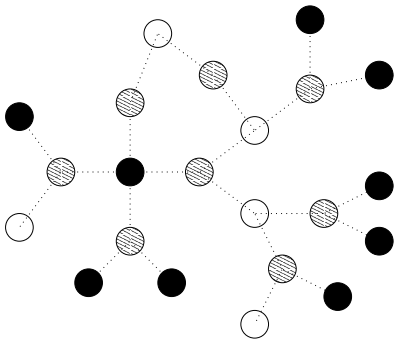

(a) Bonding graph

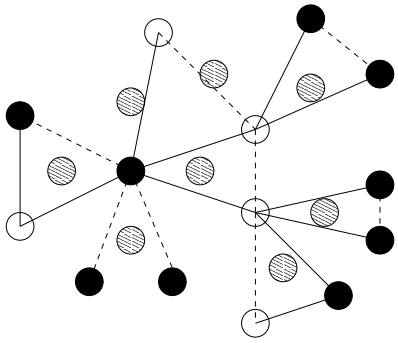

(b) Second coordination sphere graph with Si-B depicted as full lines and Si-Si/B-B edges depicted as dashed lines.

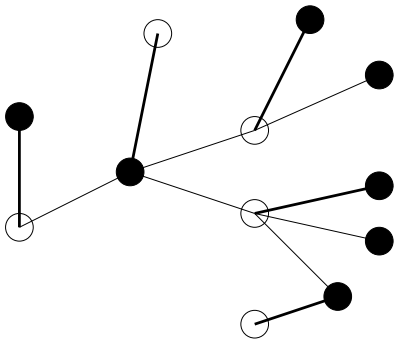

(c) Graph G_{AB} serving as input for maximum matching algorithm. A possible maximum matching is indicated by bold lines.

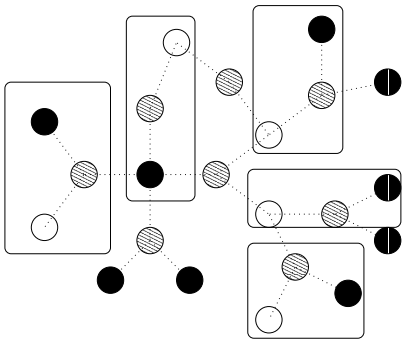

(d) Bonding graph with the maximum matching indicated by rectangular boxes.

Figure 4.1: Mapping to maximum cardinality matching. Construction of cation graph G_{AB} from bonding graph and results of maximum matching procedure. Filled/open symbols represent silicon and boron atoms, respectively, and nitrogen atoms are depicted as hatched circles.

depth-first search. Note that with the above mentioned procedure, no information about the shapes of the vacancies is given. With these definitions, the free volume of the structure is $V_f = a^3 \sum_{i=1}^{n_{cc}} s_i$ and the occupied volume is $V_{occ} = L^3 - a^3 \sum_{i=1}^{n_{cc}} s_i$. Since we also wanted to get some measure for the size of the voids inside the structure, we calculated the average size $\langle V_{cc} \rangle$ of the connected components of the vacancy graph.

Global connectivity

The existence of molecular crystals shows, that the atomistic structure of solid compounds is not restricted to 'fully connected' arrangements of atoms. Furthermore, in gases different molecules exist as stable arrangements of atoms. Deciding from a given arrangement of atoms, whether small molecules, medium sized clusters or a solid exist, is not straightforward. Therefore we analyze the global connectivity of an arrangement of atoms with the help of the bond graph $\mathbf{G}$ of the configuration. We determine the connected components of the bond graph $\mathbf{G}$ by a depth first search[29] and identify these connected components as the clusters/molecules C_i that occur in the arrangement of atoms. Note that for covalent amorphous networks at solid densities one usually finds one cluster that contains all atoms.

From the different clusters found inside a given structure, we derive some useful quantities: The distribution of cluster sizes $h(S_{cl})$, $(S_{cl} = 1, \ldots, N_{atom})$. From $h(S_{cl}; t)$, we extracted the average cluster size of a configuration containing N_{cl} clusters

$$S_{mean} = \frac{1}{N_{cl}} \sum_{i=1}^{N_{cl}} S_{cl}, \tag{4.9}$$

the size of the largest cluster present $S_{max}(t)$, and the number of clusters at time t, $N_{cl}(t)$.

From $\langle h(S_{cl}) \rangle_t$, the average over a large number of configurations, one can derive the likelihood $\langle L(S_{cl})$ of an atom to be found as part of a cluster of size S_{cl},

$$\langle L(S_{cl}) \rangle_t = \frac{S_{cl} \cdot \langle h(S_{cl}) \rangle_t}{N_{atom}}. \tag{4.10}$$

4.2 Bulk properties

The pair correlation functions and the topology of structural models of amorphous substances are frequently used to validate the 'correctness' of a structural model with respect to experimental data. However other (bulk) properties are also important. The simplest one and very often the most difficult one to reproduce by computer simulations [21] is the mass density ρ_m of the amorphous material. In computer simulations that employ periodic boundary conditions, the density is simply $\rho_m = \frac{M}{V_{cell}}$, where M is the mass of the atoms and V_{cell} is the volume of the simulation. For open boundary or cluster models, the determination of the volume $V_{cluster}$ requires additional effort. We determined the density from the average number of atoms inside spheres of increasing radii r and plotted the densities of the spheres vs the radius r. After some initial oscillations, the density fluctuates around an average value up to a distance r_{max}, above which the density decreases, due to the finite size of the cluster. We used the observed average value of the density as the density of the cluster.

For technical applications, the elastic properties of materials are very important and thus we have used the GULP program[44] to compute the Bulk module

$$B = V_0 \cdot \left(\frac{\partial^2 E^{pot}(V)}{\partial^2 V} \right)_{V_0} \tag{4.11}$$

of the structural models, in order to estimate the mechanical strength of the structural models. The bulk module B is the inverse of the compressibility $\left(\frac{\partial V}{\partial p}\right)_T$ at constant temperature, and high values of the bulk module indicate that the volume does change only slightly, when high pressures are applied to the system. Even though no experimental data is available for the a-$Si_3B_3N_7$ system and thus a comparison with the experimental data was impossible, the bulk module serves as a very important measure for the 'stiffness' of the material. Note that, these properties of the structural models may depend on their location on the energy landscape.

4.3 Vibrational properties

The vibrational properties of amorphous substances are interesting for several reasons.

In glasses one observes strong deviations of the T^3 dependence of the specific heat at temperatures $T < 10$ K,[5] which have been explained in terms of strongly localized low frequency modes in the context of the soft potential model[45].

In the context of computer simulation, these localized modes have been studied for soft-sphere glasses[138], amorphous selenium[118, 116] and amorphous silica [17, 18]. One has found that localized low frequencies exist a agreement with the soft-potential model. Recently it has been shown that the so-called Boson peak in glasses can be attributed to these localized low-frequency modes.[61]

From the chemist's point of view, one uses the vibrational properties to identify vibrations associated with typical building groups. Of course, this becomes difficult if the experimental vibrational spectra are not well resolved. Computational studies can help to clarify the assignment of the various peaks or in general to study the contributions of building units. Finally, vibrational and imaginary modes have been used to discuss relaxations and diffusion of (supercooled) liquids and glasses (see chapter 2).

In the harmonic approximation, the vibrational properties of a structural model can be calculated by diagonalizing the Hessian matrix D_{ij},

$$D_{ij}^{\alpha\beta}(\vec{X}) = \frac{1}{\sqrt{m_i m_j}} \frac{\partial^2 E}{\partial x_i^\alpha \partial x_j^\beta}, \qquad (4.12)$$

of the configuration. The elements of the dynamical matrix $D_{ij}^{\alpha\beta}$ are the mass-weighted second derivatives of the potential energy E with respect to atomic positions x_i^α, x_j^β of atoms i, j. If the Hessian is calculated at a minimum of the potential energy landscape, the 3N positive eigenvalues λ_i of the Hessian matrix are the squared phonon frequencies ω_i^2. For points on the energy landscape that are not minima, negative eigenvalues and thus *imaginary* frequencies exist, which are written as negative frequencies $\omega_i \equiv -1 \cdot \omega_i$, by convention. The phonon or vibrational density of states

$$DOS(\omega) = \frac{1}{3N} \sum_{i=1}^{3N} \delta(\omega - \omega_i) \qquad (4.13)$$

is a histogram of the frequencies of the vibrational modes observed in the structure, and can be compared to experimental inelastic neutron scattering data, after a re-weighting of the intensities with the neutron scattering cross sections. However, since no experimental data is available for a-$Si_3B_3N_7$, we only discuss the phonon density of states, without re-weighting.

4.3.1 Properties of phonons

We studied the degree of localization of modes i with frequency ω_i of the vibrational densities of states using the participation ratio

$$\rho_R(\vec{X})(\omega_i) = \left(N \sum_{j=1}^{N} (\vec{e}_j^{\,i} \cdot \vec{e}_j^{\,i})^2 \right)^{-1}. \qquad (4.14)$$

Here $\vec{e}_j^{\,i}$ is the (3-dimensional) contribution of atom j to the normalized $3N$ dimensional eigenvector $\vec{e}_i$. For extended modes, $\rho_R(\vec{X})(\omega_i)$ is of order unity and for (quasi-) localized modes, $\rho_R(\vec{X})(\omega_i)$ scales inversely with the system size.

The joint contribution of elements of type α (α = B, N, Si) to a vibrational mode i of frequency ω_i was characterized by the projected density of states

$$PDOS_\alpha(\omega_i) = \sum_{j}^{N} \left[\vec{e}_j^{\,i}(\omega_i) \right)^2] \, \delta_{t_j,\alpha}, \qquad (4.15)$$

where t_j was the type of atom j.

Since in a-$Si_3B_3N_7$ well-defined first coordination spheres exist for each silicon, boron and nitrogen atom i, we first characterized the coordination spheres by the number of neighbors $CSP_i^{t,nt}$ of type nt. These number of neighbors $CSP_i^{t,nt}$ served as an index β, for the calculation of the coordination sphere projected density of states

$$CDOS_{t,nt}(\omega) = \sum_{i=1}^{N} \left[\vec{e}_i(\omega) \right]^2 \delta_{CSP_i^{t,nt},\beta}. \qquad (4.16)$$

Note that for a given atom type t_1,

$$\sum_{j=1}^{N(CS(t_1))} CDOS_{t_1,j}(\omega) = PDOS_{t_1}(\omega), \quad (4.17)$$

where $N(CS(t_1))$ is the number of coordination spheres of type t_1. The coordination sphere projected density of states is an estimate for the contribution of local coordination spheres to a vibrational mode with frequency ω_i.

4.3.2 Imaginary modes

As already mentioned, imaginary modes are believed to be important for relaxations in glasses and (supercooled) liquids. We characterize the imaginary modes, which are present only for non-minimum configurations, by the fraction of imaginary modes

$$f_{imag}(\vec{X}) = \frac{N_{imag}(\vec{X})}{3N-6} \quad (4.18)$$

of the configurations $\vec{X}$. Furthermore, we determine the densities of states and the different projected densities of states as well as the participation ratios $\rho_R(\omega_i)$ of the instantenuous configurations, in order to study both the possible localization of these imaginary modes as well the atomic and coordination sphere contributions to these modes. A knowledge of the latter quantities would allow to find those parts of the amorphous network, that contribute most strongly to relaxational processes.

Part III

Structural Modelling

Chapter 5

A random close packing based algorithm for the generation of amorphous covalent networks

5.1 Introduction

In this chapter we will describe a newly developed method,[67] which allows us to generate amorphous covalent networks with the help of random close packings of spheres. These spheres mimic the anionic partial structure which occupies most of the volume of the solid. Our approach is inspired by the observation that many simple ionic/covalent crystalline compounds can be formally described as a dense packing of the "anions", with "cations" occupying those voids in the anionic partial structure, which agrees best with their preferred local ionic/covalent bonding requirements [112]. This method can be applied to large systems, is relatively fast, implements the boundary conditions, and can be adapted to a variety of covalent systems without significant problems.

In the next section, we will describe our approach, followed by an optimization of the algorithms in section 5.3. Finally, applications of the method to several example systems, a-SiO_2, a-Si_3N_4, a-$SiO_{3/2}N_{1/3}$, and a-B_2O_3, will be given.

5.2 Method

5.2.1 Outline

The goal of our approach is the generation of structural models for continuous random networks of a given chemical system with specified composition. An important aspect that distinguishes covalent compounds from metallic ones is the fact that usually all metal atoms can be nearest neighbors in the structure, while the stronger polarity of the covalent bond usually requires nearest neighbors to be of opposite charge. In order to take these preferred local environments of the atoms into account, we proceed in several steps, as shown on the flowchart (fig. 5.1). As a first step, we generate random close packings (RCP) of the anions, using a modification of an algorithm by Frost et al. [43] for periodic boundary conditions. Next, we identify those voids in the structure, which possess the appropriate topology and geometry to host the cations. Placing the cations into these voids is a global optimization problem, which can be mapped onto the task of determining the cost-optimal subgraph of a certain graph. One should note that this approach is a natural extension of the packing paradigm of crystal chemistry [112] to amorphous systems. Finally, we adjust the bond lengths and bond angles using an (empirical) interaction potential and/or a reverse Monte Carlo (RMC) procedure[80, 107] while leaving the topology essentially unchanged.

5.2.2 Input

In general, the chemical system consists of N_{atom} atoms, which belong to N_{type} atom types t. $N(t)$ is the number of atoms of type t ($N_{atom} = \sum_t N(t)$). Furthermore one assumes that the atoms can be divided into anions and cations, belonging to the types t_a and t_c, respectively. Thus, $N_a = \sum_{t_a} N(t_a)$ and $N_c = \sum_{t_c} N(t_c)$ are the total number of an-

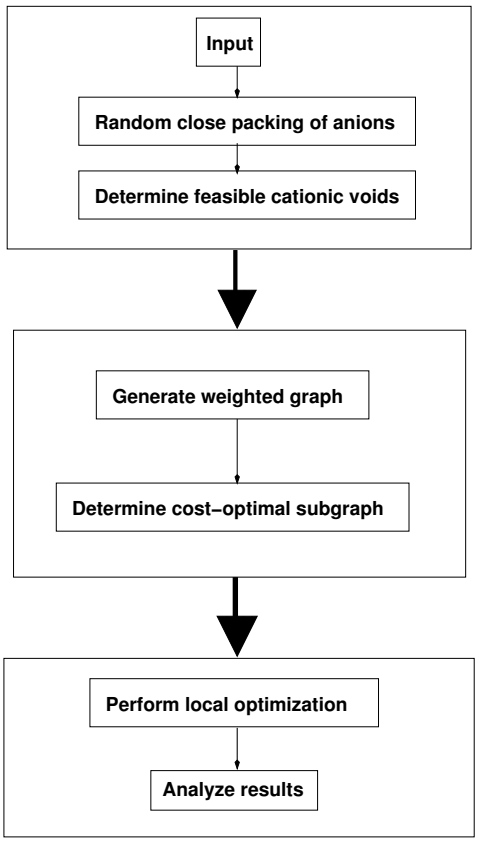

Figure 5.1: Flowchart of RCP algorithm.

ions and cations, respectively. In addition, we usually have experimental information about the typical distances between (nearest) neighbor ions i and j of type s and t, $d^{st}_{exp}(i,j)$, about feasible local coordinations of cations of type s by anions of various types t characterized by the coordination numbers $n^t(s)$ and the anion-anion distances within the coordination polyhedra, and preferred connectivities among these polyhedra. The choice of tolerances about the ideal values depends on the specifics of the algorithm. We employ

$$d^{st}_{max}(i,j) > d^{st}_0(i,j) \approx d^{st}_{exp}(i,j) > d^{st}_{min}(i,j) \tag{5.1}$$

and

$$r^{st}_{max}(i,j) > r^{st}_0(i,j) \approx d^{st}_{exp}(i,j) > r^{st}_{min}(i,j) \tag{5.2}$$

as parameters for the identification of feasible voids, and for the optimal placing, respectively. Note that r_0, r_{min} and r_{max} need not be equal to d_0, d_{min} and d_{max}, although they must be chosen compatible with each other, of course, since both reflect the local bonding of the covalent compound. Usually, we choose d_{max} and d_{min} equidistant to d_0,

$$d^{st}_{max}(i,j) - d^{st}_0(i,j) = d^{st}_0(i,j) - d^{st}_{min}(i,j) = \Delta d^{st}. \tag{5.3}$$

Since we still have to add the cations to the anion structure, for most systems the goal is not to achieve the highest packing density for random close packing (RCP- limit [178]), $\phi^{max} \approx 64\%$. Instead, we usually stop upon reaching a prescribed (stable) packing density $\phi^* \approx 52\% - 58\% < \phi^{max}$ (see below).

Finally, we need appropriate energy functions for the final adjustments of the structure candidates. Since realistic model systems are too large to allow the use of ab initio energy calculations, one employs various empirical interaction potentials that are usually fitted to crystalline modifications or to results of ab initio calculations on small related systems.

5.2.3 Generation of random close packings of anions

The generation of random close packings of anions is an adaptation of the algorithm by Frost et al.[43] to periodic boundary conditions. Initially all N_A anions are placed at random positions $\vec{r}_i$ in a periodically repeated large cubic box of volume V_I with an initial packing density $\phi_I = (N_{anion}V_{anion})/V_I \approx 0.3$. Subsequently, the cell is isotropically compressed, leading to an eventual overlap among some of the anions,

$$r_{ij} = |\vec{r}_{ij}| = |\vec{r}_j - \vec{r}_i| < d^{st}_0(i,j). \tag{5.4}$$

The next step is to reduce the overlap by moving every atom i by a vector $\vec{v}_{shift}(i)$: [1]

$$\vec{v}_{shift}(i) = -\frac{1}{2}\sum_{j=1}^{N_A} \frac{\vec{r}_{ij}}{r_{ij}}(\Delta R_{ij}). \tag{5.5}$$

Here,

$$\Delta R_{ij} = \begin{cases} d^{st}_0(i,j) - r_{ij} & \text{if} \quad r_{ij} < d^{st}_0(i,j) \\ 0 & \text{if} \quad r_{ij} \geq d^{st}_0(i,j) \end{cases} \tag{5.6}$$

[1] For many atoms, these shifts may lead to new overlaps, of course. For a single pair of anions this vector shifts the anions until mutual tangency is reached.

Next, this shifting is repeated (up to N_{shift} times), until the overlap OV vanishes within some predefined tolerance OV_{tol},

$$OV = \frac{1}{2N_A} \sum_{i=1}^{N_A} \sum_{j=1}^{N_A} \Delta R_{ij} \leq OV_{tol}. \qquad (5.7)$$

This compression and minimization-of-overlap scheme defines a compression cycle. The compression cycle is repeated, until the desired packing density is reached, $\phi = \phi^*$, or the algorithm fails to reduce the overlap to zero within N_{shift} attempts. In the latter case, the algorithm performs a decompression cycle which consists of a volume expansion accompanied by a subsequent overlap reduction. If the new overlap equals zero, the cell is compressed again, otherwise the decompression cycles proceed until the overlap vanishes. Subsequently the simulation cell is compressed again until the packing criterion is fulfilled or the permitted maximum number of decompression cycles has been attempted.

Since both the final packing densities and the efficiency with which such a packing is achieved, may depend on the way the cell is compressed, we have used both a linear and a geometrical volume schedule, $V(n+1) = V(n) - \beta V_I$ and $V(n+1) = \beta \cdot V(n)$, respectively.

5.2.4 Determination of feasible voids for cations

Usually, the anion structure with the highest packing density is used for the subsequent determination of voids appropriate for the various cations. For each cation type t_c the algorithm determines those sets of $n(t_c)$ anions j that define coordination polyhedra, which correspond within some tolerances to the preferred local environment around the cation. Starting from any anion, we first determine all neighbor anions within a given distance. Within this neighborhood, all sets $I = \{\vec{r}_j\}$ of $n(t_c)$ anions are generated that contain the starting anion, where $n(t_c)$ is the coordination number preferred by the cation. The center of gravity of these anions

$$\vec{r}_I = \frac{1}{n(t_c)} \sum_{j \in I} \vec{r}_j \qquad (5.8)$$

defines the spatial location, where a cation i of type t_c is to be placed, $\vec{r}_i = \vec{r}_I$.

Next, we check for each such polyhedron, whether the cation-anion and anion-anion distances $d^{st}(i,j) = |\vec{r}_i - \vec{r}_j|$ are within the prescribed tolerances,

$$d^{st}_{min}(i,j) \quad \leq \quad d^{st}(i,j) \leq d^{st}_{max}(i,j). \qquad (5.9)$$

This procedure is repeated for each anion as a starting point. Finally, duplicates are eliminated by a comparison of the cation locations $\vec{r}_i$. One should note, that many of the voids might be appropriate for several types of cations, which are of similar size and prefer the same coordination number.

5.2.5 Mapping to a weighted graph

After all voids for all cation types t_c have been determined, the algorithm proceeds with the generation of a weighted graph. Usually, there are more voids than cations of type t_c to be placed, $N_{void}(t_c) > N(t_c)$. However, the possible placements of the $N(t_c)$ cations are not equivalent once we take the actual local geometry of the coordination polyhedra and their connectivity into account. Thus, we have to find that subset of the set of voids that is optimal for the geometrical and topological constraints of the chemical system.

Mathematically, this task can be formulated as the determination of the cost-optimal subgraph of a certain weighted graph.[2] We construct this graph as follows: All anions and voids are chosen as vertices of various types v_i^t. We define edges e_{ij} between two vertices i and j of types s and t, respectively, if the interatomic distances $d(i,j)$ are shorter than the maximum distance allowed, $r^{st}_{max}(i,j)$,

$$d(i,j) \leq r^{st}_{max}(i,j). \qquad (5.10)$$

Finally, we define a weight function $W(e_{ij})$ for each edge e_{ij}:

[2] Graph theoretical notation [29]: A weighted graph $\mathbf{G}$ is composed of a set of vertices $v_i \in \mathbf{V}$, a set of edges $e_{ij} = (v_i, v_j) \in \mathbf{E}$ and a set of weights (costs) $W(e_{ij})$. Two vertices are called connected, if an edge $e_{ij} = (v_i, v_j)$ exists. A graph $\mathbf{G}_S$ is called a subgraph of $\mathbf{G}$, if $\mathbf{V}_S \subseteq \mathbf{V}$ and $\mathbf{E}_S \subseteq \mathbf{E}$ where $\mathbf{V}_S$, $\mathbf{E}_S$ are the vertex and edge sets of subgraph $\mathbf{G}_S$, respectively. Additionally we assign a type t to each vertex v_i^t. The degree (topological coordination number) $q^t(v_i^s)$ of a vertex v_i^s is the number of vertices v_j^t of type t connected to vertex v_i^s of type s.

$$W(e_{ij}) = \begin{cases} \epsilon^{st}(i,j) \text{ if } d(i,j) \leq r^{st}_{min}(i,j) \\ f^{st}_1(d(i,j)) \text{ if } r^{st}_{min}(i,j) \leq d(i,j) \leq r^{st}_0(i,j) \\ f^{st}_2(d(i,j)) \text{ if } r^{st}_0(i,j) \leq d(i,j) \leq r^{st}_{max}(i,j) \\ 0 \text{ if } d(i,j) > r^{st}_{max}(i,j) \end{cases} \tag{5.11}$$

Note that $W(e_{ij})$ only depends on the interatomic (vertex) distance $d(i,j)$ of the edge e_{ij}. The parabolic functions $f^{st}_i(x) = a_i x^2 + b_i x + c_i$ $(i = 1, 2)$ account for deviations from the ideal distance between atoms of type s and type t.[3] The choice of the values for ϵ^{st} has proven to be important for efficiently achieving an optimal ion distribution. If the anion distribution is kept fixed, we can use $\chi = \frac{\epsilon^{tctc}}{\epsilon^{tatc}}$ as a measure for the relative importance attached to the cation-cation and cation-anion distance requirements.

In order to achieve an efficient cost function, the edge costs are normalized to the interval [0,1].

$$W_n(e_{ij}) = \frac{W(e_{ij}) - \min_{e_{kl}} W(e_{kl})}{\max_{e_{kl}} W(e_{kl}) - \min_{e_{kl}} W(e_{kl})}. \tag{5.12}$$

Summing $W_n(e_{ij})$ over all those edges, whose vertices are both occupied, yields the geometric cost of the subgraph:

$$\mathbf{E}_{geo}(\mathbf{G}_S) = \sum_{e_{ij} \in \mathbf{G}_S} W_n(e_{ij}) \tag{5.13}$$

To this, we can add the topological cost of the graph,

$$\mathbf{E}_{top}(\mathbf{G}_S) = \sum_{t}^{t_C} \sum_{i}^{N_a} G(q^t(v^s_i)), \tag{5.14}$$

where

$$G(q^t(v^s_i)) = \alpha_t \cdot \left(\frac{q^t(v^s_i) - q^{ts}_0}{q^{ts}_0} \right)^2. \tag{5.15}$$

Here, q^{ts}_0 are the desired degrees of a vertex of type s (analogous to the preferred coordination numbers of cations and anions), and α_t is an adjustable parameter (c.f. section 5.3). Summing $\mathbf{E}_{geo}$ and $\mathbf{E}_{top}$ yields the total cost of a subgraph,

$$\mathbf{E}(\mathbf{G}_S) = \mathbf{E}_{geo}(\mathbf{G}_S) + \mathbf{E}_{top}(\mathbf{G}_S). \tag{5.16}$$

Note that the full graph and the various subgraphs contain anion-anion, anion-cation and cation-cation edges. In the examples presented in section 5.4, we have kept the distribution of the anions over the anion subgraph fixed. In that case, one can simplify the subsequent optimizations by assigning a zero weight to the anion-anion edges, thereby eliminating them from the calculations.

5.2.6 Determination of cost-optimal subgraphs

The number of possible subgraphs is given in general by a complicated expression (involving sums and products of binomial coefficients), indicating that the number of possible placements grows at least exponentially with the size of the system[4]. As a consequence, typical deterministic graph-optimization routines will fail for realistic problem sizes (see section 5.2.6) and finding good cost-optimal subgraphs requires the use of global optimization methods. We have chosen simulated annealing for this task [84].

Simulated annealing

Key ingredients of simulated annealing are the moveclass, i.e. the rule according to which new configurations are generated, and the control-parameter schedule $C(n)$. Starting from a random occupation of void vertices by cations (represented as a dynamically changing list $L_v(N_{atom})$) we generate a new subgraph (configuration) by randomly replacing a vertex v^t_{old} of the list L_v by a new vertex $v^t_{new} \in \mathbf{V}_S$, for a randomly chosen cation type t.[5] Note that both vertices have to be of the same type. The new subgraph is accepted according to the standard Metropolis criterion [109]. Subsequently, the control parameter C

[3] We calculate the parameters a_1, b_1, c_1 and a_2, b_2, c_2 from the constraints: $f^{st}_{1,2}(r^{st}_0) = 0$, $\frac{\partial f^{st}_{1,2}}{\partial x}(r^{st}_0) = 0$, $f^{st}_1(r^{st}_{min}) = \epsilon^{st}$ and $f^{st}_2(r^{st}_{max}) = 0.5\epsilon^{st}$.

[4] E.g., for the simple case of only one type of cations, we have $N_{\mathbf{G}_S} = \binom{N_{void}}{N(t_c)}$.

[5] If the distribution of different anion species over the anion vertices also needs to be optimized, appropriate moves can be included in the moveclass, of course.

is changed according to the chosen schedule $C(n)$. Since the result of a simulated annealing run usually depends on $C(n)$, we have compared two different cooling schedules, a linear and a geometrical one, $C(n) = C(0) - \gamma \cdot n$ and $C(n+1) = \gamma \cdot C(n)$, respectively (c.f. section 5.3.2).

Integer programming

In this section we describe how the determination of the cost-optimal subgraph can be transformed to an integer programming problem. Let the weighted graph $\mathbf{G}$ be defined by its vertex set $\mathbf{V} = \{v_i^t\}$ of N_V vertices, its edge set $\mathbf{E} = \{e_{ij}\} \equiv \{e_k\}$ of N_E edges and its weight set $\mathbf{W} = \{W(e_{ij})\} \equiv \{\omega_k\}$. We describe the vertex set $\mathbf{V}$ and the edge set $\mathbf{E}$ by boolean variables $\{0,1\}$ σ_i^t and ϵ_k, where $\sigma_i^t = 1$, if the vertex v_i^t of type t is occupied in the subgraph $\mathbf{G_S}$ and $\sigma_i^t = 0$ else. Similarly, $\epsilon_k = 1$, if both vertices of the edge e_k are occupied, and $\epsilon_k = 0$ else. With these variables the mixed integer problem reads:

$$\text{Maximize: } -\mathbf{E}_{geo} = \sum_k^{N_E} \epsilon_k \omega_k \tag{5.17}$$

Subject to the boundary conditions:

$$\sum_i^{N_v} \sigma_i^t = N^t \tag{5.18}$$

for all occuring vertex types t (N^t=number of ions of type t), and

$$\sigma_i^t - \epsilon_k \geq 0 \tag{5.19}$$

$$\sigma_j^t - \epsilon_k \geq 0 \tag{5.20}$$

$$\epsilon_k - \sigma_i - \sigma_j \geq -1 \tag{5.21}$$

for all edges $e_k = e_{ij}$ and vertices v_i^t.
Equation 5.17 corresponds to equation 5.13. Equation 5.18 ensures that the number of occupied vertices N_v^t for each type t equals the number of atoms N^t required by composition. Equations (5.19, 5.20, 5.21) ensure that the boolean variables $\epsilon_k = 1$, if and only if σ_i and σ_j both equal one. In other words: the last three equations "activate" edge $e_k = e_{ij}$, if both vertices, v_i and v_j, are "switched on". For a typical optimization in which about 400 cations should be placed among 800 anions, the whole graph $\mathbf{G}$ typically contains about 2000 vertices and about 40000 edges yielding a total of about 42000 boolean variables to be optimized. Clearly the number of possible configurations precludes the use of a branch & bound algorithm[29], if one is interested in good results in a short time, and thus we employ the simulated annealing procedure described in the previous paragraph for the determination of the cost-optimal subgraph.

5.2.7 Local optimizations of structure candidates

Typically, the configurations generated by the algorithm described above tend to be slightly distorted, and it is necessary to relax the structure candidates in the final step of our approach. In particular, the anion-anion pair correlation function are always δ-functions of the nearest neighbor distance by construction, and similarly the nearest neighbor peaks in that cation-anion pair correlation function are too broad. The local relaxation removes these anomalies, while keeping the topology of the network essentially intact: Depending on the choice of the cost functions for the relaxation, between 85% and 99% of the bonds persist during the relaxation, and the broken bonds essentially result in dangling bonds with very minor structural rearrangements, if any at all. Figure 5.2 shows a "before" and "after" picture of the pair correlation function for the relaxation of a-SiO_2 using a simple cost function with 96% percent of the bonds preserved.

Usually, one chooses the potential energy as the cost function for the local optimization involved, using e.g. the conjugate gradient method. Since realistic systems are too large for optimizations based on ab initio energy calculations, we employ either interaction potentials based on fits to ab initio calculations on small systems related to the chemical system of interest, or simple empirical potentials, where we fit the parameters to related binary or ternary crystalline structures.

If experimental data of sufficient quality are available, one can also perform the relaxation using the reverse Monte Carlo method

(RMC) [107]. Here, the cost function consists of the difference between the computed and measured radial distribution functions, plus penalty terms that prevent unphysical atom-atom distances.

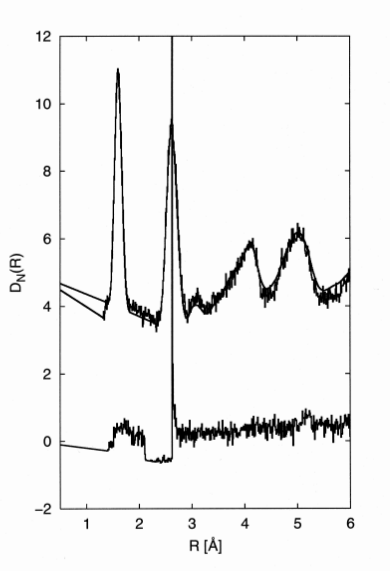

Figure 5.2: Comparison of pair correlation function $D_N(R)$ calculated from the structural models of a-SiO_2 before and after the local refinement. The upper curves show both the experimental data (smooth curve) and the calculated pair correlation function after refinement, the lower curve is the pair correlation function before refinement. Note that 96% of the cation-anion bonds are identical in the 'before' and 'after' structure models.

5.3 Analysis and optimization of the algorithm

In this section we analyze the characteristics of the two main parts of our algorithm. First we discuss the behaviour of the RCP-algorithm (section 5.3.1) and second we elaborate on the features of the determination of cost-optimal subgraphs (section 5.3.2). In the final subsection (section 5.3.3) we comment on the overall run-time characteristics of the whole algorithm.

5.3.1 Generation of random close packing of anions

We investigate the dependence of the RCP-algorithm on the size of the system by performing five runs each for every system size $N = 32, 64, 128, 256, 512, 1024$ and 2048 of spheres of equal size for four different values of the compression rate $\beta = 0.1, 0.01, 0.001$ and 0.0001, applying a linear compression schedule.
Fig. 5.3 shows the total number of shifts $\tau_{comp}(\phi^*)$ needed to reach a given packing density ϕ^* for several different values of β. In figure 5.4, we show, as a double logarithmic plot, the total number of shifts τ_{comp} necessary to reach the (color-coded) packing fractions ϕ_i. The results show, that a lowering in decompression rate does lead to an overall increase of calculation time. This fact is readily explained by noting that a decrease of (de-)compression rate results in an increase in the number of minimization-of-overlap cycles which is not compensated for by the reduced number of shifts required to minimize the overlap. Additionally, the straight line fits in the double-log plot ($\tau_{comp} \propto N^{\kappa}$) show that the number of shifts required to minimize the overlap depend on the number of atoms (spheres) only sublinearly ($\kappa \approx 0.3$) and that these exponents are basically independent of the applied cooling rate β. We would like to add, that the results of an investigation using a geometric compression schedule yielded almost the same results.

5.3.2 Determination of cost-optimal subgraph

We analyzed the properties of our algorithm for a test system of composition $Si_{84}O_{63}N_{70}$. Here, we treat silicon atoms as cations, and oxygen and nitrogen atoms as anions, respectively. The preferred coordinations of silicon by the anions, oxygen by silicon, and nitrogen by silicon are four, two and three, respectively. The distance parameters employed are shown in table 5.1.

Both d_0^{st} and r_0^{st} are set equal to the experimental values d_{exp}^{st}. The parameters $r_{min}^{t_a t_a}$, $r_{max}^{t_a t_a}$,

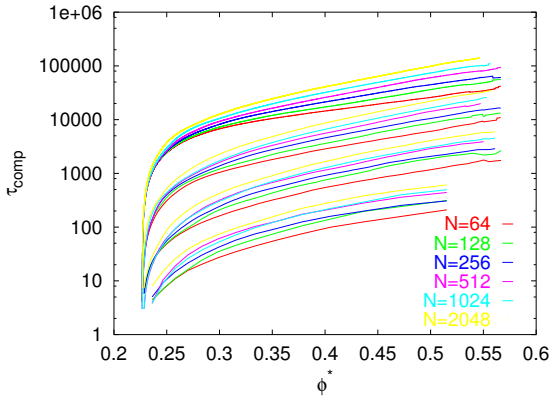

Figure 5.3: Size-scaling and compression rate dependences of RCP-algorithm. τ_{Comp} denotes the number of shifts needed to reach packing fraction ϕ^*. Compression rates are (from bottom to top): 0.1,0.01,0.001 and 0.0001. The system sizes are depicted as colors.

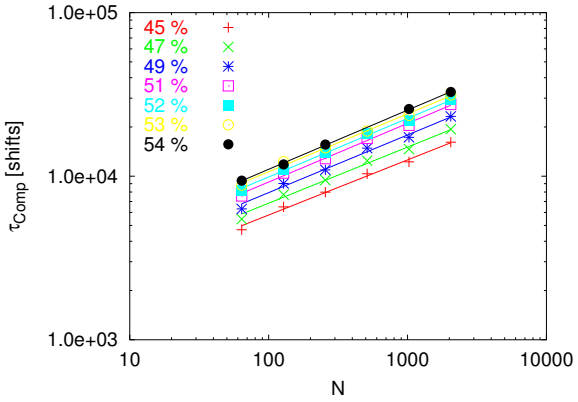

Figure 5.4: Number of shifts τ_{Comp} to reach color coded packing fractions ϕ. Straight lines are fits to a power law $\tau_{Comp} \propto N^{\kappa}$ The resulting exponent is $\kappa \approx 0.3$.

$r_{min}^{t_c t_c}$, and $r_{max}^{t_c t_c}$ are given by

$$r_{min/max}^{t_a t_a} = r_{min/max}^{t_c t_a} \sqrt{2(1 - cos(\theta_0^{t_c}))} \quad (5.22)$$

and

$$\begin{aligned} r_{max}^{t_c t_c} &= r_{max}^{t_c t_a} \sqrt{2(1 - cos(\theta_0^{t_a}))} \\ r_{min}^{t_c t_c} &= r_{min}^{t_c t_a} \sqrt{2(1 - cos(\theta_{min}^{t_a}))} \end{aligned} \quad (5.23)$$

Here, $\theta_0^{t_c} (= 109.47°)$ is the ideal bond angle at silicon, $\theta_0^{t_a}$ denotes the optimal bond angle at an anion of type t_a ($\theta_0^N (= 120.0°)$ and $\theta_0^O (= 140.0°)$), and $\theta_{min}^{t_a}$ is the minimum allowed bond angle at an anion of type t_a ($\theta_{min}^N (= 90.0°)$ and $\theta_{min}^O (= 90.0°)$).

Atoms	r_0	r_{max}	r_{min}	r_{exp}
Si-O	1.61	2.11	1.11	1.61
Si-N	1.72	2.22	1.22	1.72
O-O	2.63	3.45	1.98	2.63
N-O	2.72	3.54	2.07	2.72
N-N	2.81	3.63	1.99	2.81
Si-Si	3.00	3.97	1.20	3.00

Table 5.1: Geometric parameters for edge weights function $f_{1,2}$. All lengths are given in Å. Experimental values r_{exp} are taken as average interatomic distances from crystalline references substances α-quartz, Si_2N_2O and β-Si_3N_4.

The test runs were organized as follows: First, several volume schedules were tested concerning their efficiency in reaching the desired packing fraction ϕ^*. Next, two of these schedules were employed to generate ten different anion packings each. For each packing, three different values $\Delta d^{st} = 0.3, 0.4, 0.5 Å$ were used to identify feasible voids, followed by the generation of the void graph[6], where the weights of the edges were varied ($\chi = 1, 2, \ldots, 5$). Finally, four different annealing schedules were tested for each weighted void graph, and for each schedule twenty optimization runs were performed. In each case, the initial control parameter C_0 was set to 2.0 c.u (units of cost), and after ten Monte-Carlo cycles[7], the control parameter was updated according to the chosen cooling schedule.

In a first step, we investigated the effect of varying the criterion employed for the void identification, $\Delta d = 0.3$ Å, $0,4$ Å, and 0.5 Å. Figure 5.5 shows n_{void} as a function of packing density ϕ^* for different values of Δd. Clearly, the larger Δd and the higher the packing density ϕ^* the more suitable voids can be found. Of course, since many of the new voids will be of poor quality, it is not obvious that choosing larger values of e.g. Δd will result in better final configurations. Furthermore, while the number of voids per cation n_{void} is larger for higher tolerances and a larger number of pos-

[6] We did not vary the parameters $r_{min/max}$ in this process, since these values are essentially dictated by the chemistry of the system.

[7] One Monte-Carlo cycle (MCC) corresponds to N_{void} attempted cation exchanges.

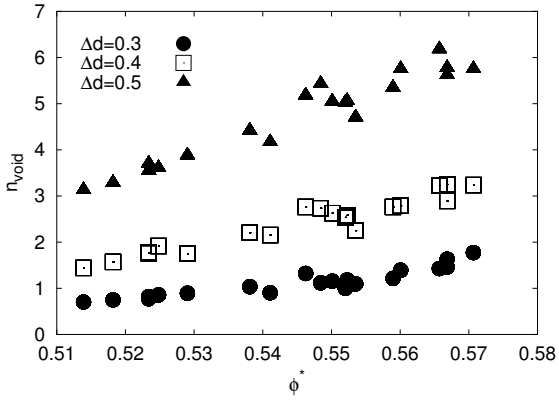

Figure 5.5: Dependence of the number of identified voids per cation n_{void} on the packing fraction ϕ^* for different tolerances Δd.

Δd	χ	D_{min}	E_{mean}	E_{best}
0.50	5.0	2.26	0.329	0.327
0.50	4.0	2.26	0.330	0.327
0.50	3.0	2.26	0.332	0.329
0.50	2.0	2.22	0.335	0.332
0.50	1.0	2.15	0.342	0.339
0.40	5.0	1.58	0.375	0.373
0.40	4.0	1.59	0.376	0.374
0.40	3.0	1.58	0.379	0.376
0.40	2.0	1.57	0.383	0.381
0.40	1.0	1.59	0.395	0.392

Table 5.2: Dependence of best energies E_{best} and corresponding minimum silicon-silicon distances D_{min} (given in Å) on Δd (given in Å) and ratio χ for the slowest geometrical cooling schedule. 200 optimization runs are included for every value of Δd and χ (10 different random packings, with 20 optimization runs each). E_{mean} is the average cost of the observed low-cost subgraphs.

sible voids should give the system more flexibility to find better solutions, an increase in n_{void} results in a considerably larger configuration space that needs to be explored and might result in very long run times of the global optimization. The analysis of the configurations produced by the subsequent simulated annealing runs (c.f. table 5.2) revealed that the best energies (lowest costs) were obtained for a slow geometrical cooling schedule, provided that the geometrical tolerance Δd is chosen suitably large: The choice $\Delta d = 0.3$Å did not produce enough useful voids ($n_{void} = 0.7 - 1.5$), to allow a placement of all cations, while $\Delta d = 0.4$Å ($n_{void} = 1.7 - 3.4$) always produced optimal graphs that still contained (highly undesirable) face-sharing tetrahedra ($E_{opt}(\mathbf{G}_S) = 0.373 - 0.400$). Finally, for $\Delta d = 0.5$Å ($n_{void} = 3.0 - 6.0$), most neighboring tetrahedra shared only corners, with the rest exhibiting edge-connectivity ($E_{opt}(\mathbf{G}_S) = 0.327 - 0.340$). Thus, the size of the graph did not pose a serious problem, and the availability of more suitable voids (even though many would only be of marginal quality) allowed us to strongly reduce the number of unfavorable polyhedra connections like face- and edge sharing.

Regarding the ratio $\chi = \frac{\epsilon(t_c t_c)}{\epsilon(t_c t_a)}$ of the ϵ-parameters used to assign weights to the edges, we find that the results also depend on the choice of this ratio. Testing $\chi = 1, 2, \ldots, 5$ (c.f. table 5.2) shows that a large ratio of $5:1$ yielded the best results.

Finally, we checked, to what degree E_{top} should contribute to the cost of an edge. We found that large contributions of E_{top} were detrimental (even $\alpha_t = 0.1$ was already "too large"), and small ones were essentially "neutral". Thus we have set $\alpha_t = 0$ in the applications described in section 5.4.

We therefore conclude that for our test system the geometrical tolerance factor Δd should lie in the range of $0.4 - 0.5$Å and that a geometrical cooling schedule should be used in conjunction with a low cooling rate γ (0.99 c.u/10MCC proved to be slightly better, on average, than 0.90 c.u/10MCC). Furthermore, very short cation-cation edges should be penalized more strongly than cation-anion edges that are too short, i.e. a large ratio χ should be used.

5.3.3 Run-time analysis

The overall run-time of the RCP-algorithm can be deduced from figure 5.6, showing that the wall-clock time t_{run} scales with system size $N = N_{atom}$ as $O(N^\lambda)$ [with $\lambda = 2.1 - 2.4$]. From our implementation we recognize that the time required to minimize the overlap scales as $O(N^2)$. The results of section 5.3.1 showed that the number of shifts required to minimize the overlap for a given fixed

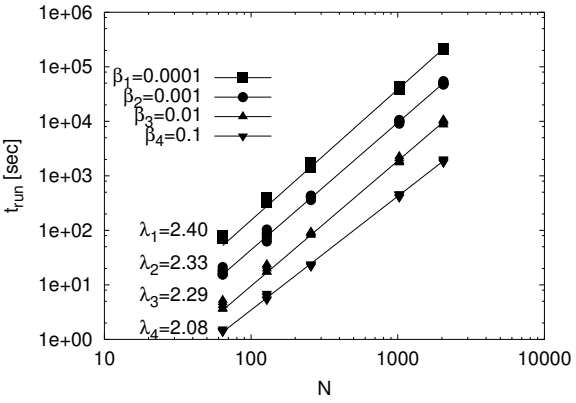

Figure 5.6: Run-time behaviour of RCP-algorithm. Wall-clock run time in seconds for different system sizes N and compression rates β needed to reach a packing fraction ϕ^*=57%. Straight lines are fits to a power law $t_{run} \propto N^{\lambda}$. The fit results in $\lambda \approx 2.3$.

volume introduced an additional size dependence $\tau_{shift} \propto N^{0.3}$. We would like to stress, that the additional exponent κ arises from the definition of the optimization problem. It is probably not related to the particular implementation but points to inherent aspects of the optimization problem.
The void determination is basically $O(N)$, and the generation of the weighted graph goes as $O(N^2)$. Finally, one MC-cycle in the simulated annealing is of order $O(N)$, and the number of MC-cycles needed to generate a satisfactory cation placement depends on the cooling rate γ. Since the determination of the cost-optimal subgraph is NP-complete, one would have to choose, in principle, a logarithmic cooling schedule in order to reach the global optimum with probability one [51].

5.4 Applications to selected chemical systems

We have applied our method to the systems a-$SiO_{3/2}N_{1/3}$, a-SiO_2 and a-Si_3N_4 and a-B_2O_3. Each system consisted of about 1000 atoms. Ten packings were generated and for each packing the best subgraph out of twenty simulated annealing runs was submitted to the local optimization procedure. The local optimizations were performed using the program GULP[44] employing an empirical interaction potential, whereas local optimizations using the reverse Monte-Carlo method were performed with the program RMC [124]. Note that our RMC-procedure is not a global search but only a quench (T=0K in terms of simulated annealing). Thus, only minute atomic displacements take place leading to the closest minimum of the cost-function employed: For the local optimizations with empirical potentials and RMC, the shifts of the atoms were below 0.03 Å/atom and 0.003 Å/atom, respectively. In the examples presented, the overall topology remained intact with 87% to 97% of the bonds being preserved throughout the relaxation.

5.4.1 a-SiO_2

The local optimizations were performed by successive application of a conjugate gradient optimization utilizing the well-known BKS potential [15] and a quench-RMC procedure using the experimental data taken from ref. [177]. Our results show, that silicon is mostly tetrahedrally coordinated by oxygen and oxygen is mostly two-fold coordinated by silicon (mean coordination numbers MCN(Si) = 3.92/MCN(O)=1.96). This is in excellent agreement with the experimental value of MCN(Si) = 3.8 - 3.9 [177]. Figure 5.7 compares the experimental pair correlation function (from neutron scattering) with the average pair correlation function derived from our models.[8] Note the remarkable agreement between simulation and experiment. Additionally we would like to point out that the average density of about 2.5 g/cm^3 is within 10% of the experimental value.[9] Very similar results were found when we employed a simple Lennard-Jones type potential for the relaxation (see chapter 7) instead of the BKS-

[8] In all figures, the correlation functions derived from the models are normalized such that the integral over the function agrees with the integral over the experimental curve.

[9] Of course, our algorithm would allow us to adjust the overall density of our models to achieve close agreement with experiment. However, one should note that a) experimentally measured densities of amorphous systems often tend to systematically underestimate the density of the "ideal" (defect-free) material, and b) the observed density often depends on the details of the generation. Thus, we have not performed a fine-tuning of the density of our models.

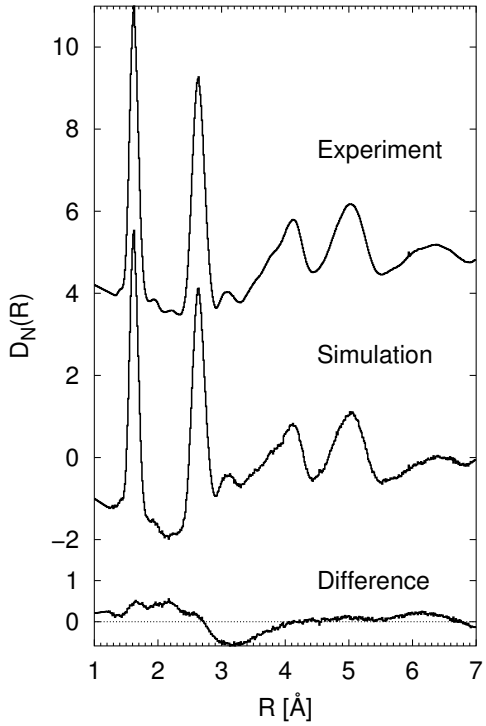

Figure 5.7: Pair correlation function for a-SiO_2. Experimental data was taken from reference [177]. Curves are shifted for clarity. Units of the y-axis are barns $\cdot$ Å^{-2} (taken from ref. [177]). The bottom curve is the plot of the difference $D_N^{sim}(R)$ - $D_N^{exp}(R)$.

potential.

5.4.2 a-$SiO_{3/2}N_{1/3}$

The local optimizations were performed using an empirical interaction potential fitted to the crystalline structures α-quartz, β-Si_3N_4 and Si_2N_2O, only[10] , followed by a RMC-quench based on the experimental data from X-ray scattering[63]. In the final structures silicon exhibited tetrahedral coordination by the anions ((MCN(Si) = 3.68), nitrogen was mostly trigonally planar coordinated by silicon atoms (MCN(N)=2.68) , and O was mostly two-fold coordinated by Si with an Si-O-Si angle of about 140°. More than 90 % of the $SiO_{4-x}N_x$ tetrahedra were connected via corners, but some edge sharing also occurred. These re-

[10]For cation-anion interaction, the potential is a combination of Coulomb and Lennard-Jones terms, and a soft sphere potential ($\propto 1/r^6$) was used for anion-anion-interactions. (For details of the potential see table 7.1 in chapter 7)

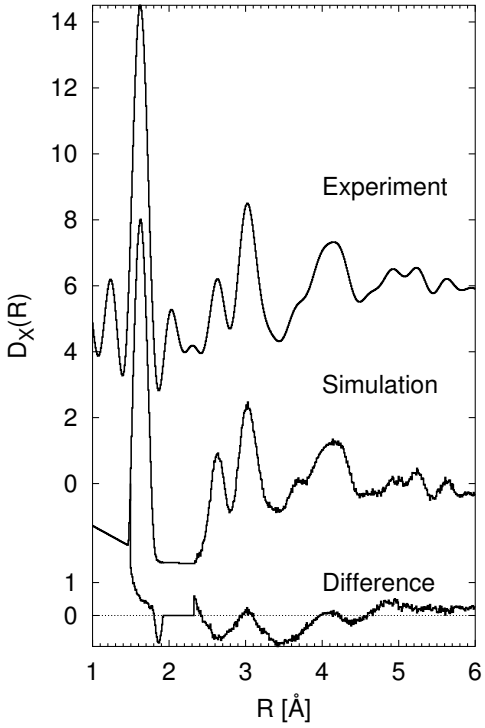

Figure 5.8: Comparison of experimental[63] and calculated X-ray pair-correlation function for a-$SiO_{3/2}N_{1/3}$. In the experimental data, the peak at 2.1 Å is clearly a ghost peak, and the same probably holds for the smaller one at 2.4 Å [63]. Curves are shifted for clarity. Units of the y-axis are Å^{-2} (taken from ref. [63]). The bottom curve is the plot of the difference $D_X^{sim}(R)$ - $D_X^{exp}(R)$, where we have excluded the range 2.1 - 2.4 Å(ghost peaks) from the difference plot.

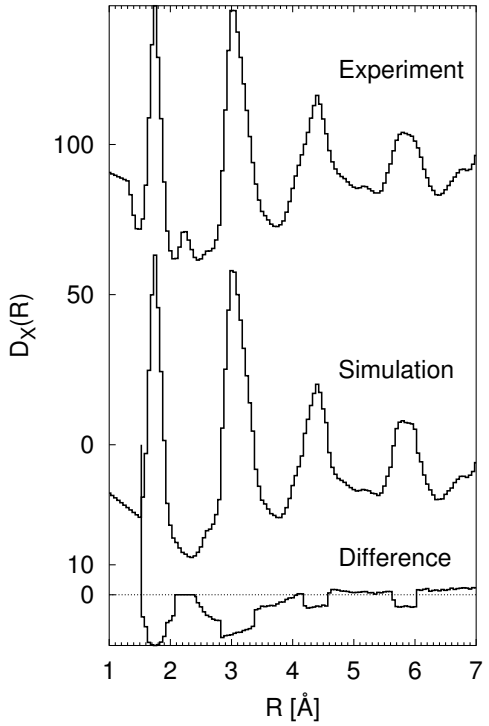

Figure 5.9: Pair correlation function for a-Si_3N_4. The experimental data was taken from [72]. The peak at 2.3 Å is supposed to be a ghost peak [3, 72]. Curves are shifted for clarity. Units of the y-axis are electronic units per unit of composition $\cdot$ μm^{-1} (taken from ref. [72]). The bottom curve is the plot of the difference $D_X^{sim}(R)$ - $D_X^{exp}(R)$, where the ghost peak at 2.3 Å has been excluded from the difference plot.

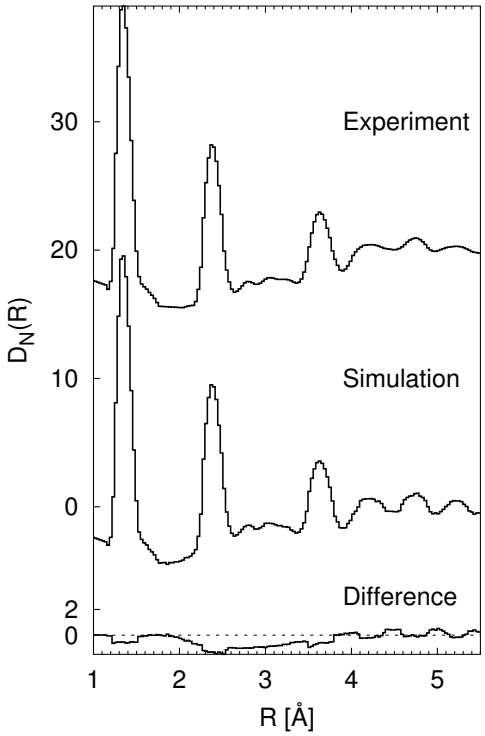

Figure 5.10: Pair correlation function for a-B_2O_3. The experimental data was taken from [153]. Curves are shifted for clarity. Units of the y-axis are barns $\cdot$ $Å^{-2}$ (taken from ref. [153]).The bottom curve is the plot of the difference $D_N^{sim}(R)$ - $D_N^{exp}(R)$.

sults are in good agreement with experimental data from NMR-spectroscopy [88].

When we compare the experimental X-ray pair correlation function of a-$SiO_{3/2}N_{1/3}$ [63] with the results from our models, we find a quite satisfactory agreement (fig. 5.8). One clearly distinguishes three peaks in the pair correlation functions D_X(R) at about 1.65, 2.6 and 3 Å, which belong to Si-O/N, O/N-O/N and Si-Si interatomic distances, respectively. The experimental pair correlation function exhibits a further broad peak at about 4.2Å, which is also present in the simulated structure and can be associated with third nearest neighbor distances Si-N/O.

5.4.3 a-Si_3N_4

The local optimizations of structural models for Si_3N_4 were performed by utilizing the interaction potential B [48] (see also section 3.9, followed by a RMC-quench based on the experimental data from X-ray scattering[72]. Analysis of the structures showed that the local environments can be classified as tetrahedral for silicon and mainly trigonally planar for nitrogen (with MCN(Si) = 3.77 and MCN(N) = 2.83), respectively.

Concerning the pair correlation function, the agreement with experimental data[72] is quite remarkable. All peaks which are observed experimentally are also found in the results of our simulations (see fig. 5.9). The relatively sharp peak at about 1.7 Å clearly refers to Si-N interatomic distances, while the slightly broader peak at 3.0 Å represents N-N and Si-Si distances. Additionally the peak at 4.0 Å is also visible in the simulation, and is dominated by third nearest neighbor Si-N distances. The small shoulder at about 2.6 Å in the pair correlation function for the simulated structure is also observed in the experimental data, and is associated with Si-Si interatomic distances stemming from edge sharing SiN_4 tetrahedra. The average density of our structural models is 2.75 g/cm^3. This agrees well with the experimental values that vary between 2.6 g/cm^3 and 2.8 g/cm^3, depending on the reaction conditions during the deposition[3].

5.4.4 a-B_2O_3

We generated five different structural models for a-B_2O_3 using for the local optimization a combined application of conjugate-gradient optimization and a quench-RMC procedure. The conjugate-gradient optimizations employed the interaction potential B1 of reference [164], and the experimental data (for the RMC) was taken from reference [153]. In figure 5.10 we show the experimental and simulated pair correlation function as obtained from neutron scattering. One clearly distinguishes three peaks at 1.35 Å, 2.6 Å and 3.8 Å in both the simulation and experimental curves. A further analysis shows, that these peaks correspond to B-O (1.35 Å), B-B/O-O (2.6 Å) interatomic distances. The peak at about 3.62 Å can be attributed to next-nearest neighbor B-O interatomic distances. Furthermore our results show, that boron is mainly trigonally planar coordinated by oxygen (MCN(B-O) = 2.82) and oxygen is two-fold coordinated by boron (MCN(O-B) = 1.91). The average density of our models is 1.78 g/cm^3, quite close to the experimental value of 1.8 g/cm^3 [104].

5.5 Discussion

As we have mentioned earlier, we do not require the packing fraction of our random close packings to be close to the RCP-limit of $\phi^{max} \approx 64$ %. Of course, in principle, our algorithm does reach this limit after sufficiently long times, and test runs with small systems show that we also find crystalline packings in the end. No stable packings (with respect to the moveclass of our algorithm) are found between 64 % and ca. 70 %, where crystallization (to bcc or fcc packings) occurs. Similar results had been obtained by Frost et al.[43] for small clusters using the analogous algorithm for clusters[11].

In the literature, several algorithms have been proposed for the generation of random sphere packings with periodic boundary conditions close to the RCP- limit[101, 100, 28]. Among these, one by Clark and Wiley[28]

[11] The first incarnation of this algorithm goes actually back to work by Stillinger[159] and Finney[38].

shows the greatest resemblance to ours, since their rescaling of the radii has the same effect as our rescaling of the simulation cell. In order to accelerate the convergence to high densities, they introduce, in addition, random displacements of the atoms, analogous to adding heat to the system. We find that such moves do improve the speed of our algorithm, too, but only for densities above the 58% range, which usually are not of interest to us.

In this context, one should note that the packing fractions in our algorithm usually reach a plateau at some point, where the packing fraction oscillates between about 52% and 58%. Interestingly enough, hard-sphere liquids in mode-coupling theory exhibit a critical density of $\phi_c^{MCT} \approx 52.5$ % [59], and Rintoul et al. [125] show that a melting/freezing range for hard spheres exists between $\phi_f \approx 49.5\%$ and $\phi_m \approx 54.5\%$. Finally, the experimentally observed transition from an (ergodic) hard-sphere liquid to a (non-ergodic) solid takes place at $\phi_c^{exp} = 57.8\%$ for a gel consisting of spherical particles (diameter ca. 200 nm) [165]. This might offer some explanation, why both the geometrical and the linear schedule for volume compression are similarly efficient in generating random close packings with $\phi^* \approx 55\%$.

Combining random packings of anions with placements of cations in feasible voids has been attempted for amorphous ionic models of yttrium iron garnet (YIG) by Lines[95]. He employed a sequential addition algorithm of anions and cations by building a cluster of anions (with open boundary conditions) while concurrently placing the cations into existing voids defined by at least three anions. The anions are added subject to the condition that they touch at least three neighboring ions. However, after the cluster size reaches several hundred atoms, the algorithm terminates, since it is no longer possible to maintain the correct composition of the system. In order to overcome this problem, one would have to introduce some "rewinding" procedure into this "depth-first"-type of algorithm - a process which becomes very quickly very time-consuming, as has been observed for similar schemes in network-building algorithms[174].

In contrast, our algorithm proceeds much more globally, since we first generate the anion partial structure, and then optimally place the cations into these resulting voids. This procedure has the great advantage that many feasible configurations are available irrespective of system size. It provides a fast method for the generation of structural models of covalent amorphous networks[12]. As the examples show, it can be adapted to a variety of chemical system where covalent bonding is dominant, as long as some information about the preferred local environment of the ions and some empirical potential is available. Thus, the algorithm adds a new tool for the generation of amorphous structures, both complementing existing methods and serving as an alternative approach in systems with non-trivial synthesis routes.

[12] On a Pentium 450 MHz PC generating a system consisting of ca. 1000 atoms takes about one or two days depending on the potential employed during the final adjustment stage.

Chapter 6

Modelling the sol-gel synthesis of a-$Si_3B_3N_7$

6.1 Introduction

From a modeller's point of view, a sol consist of a number of different monomers inside a container at medium densities. The monomers have different bonding functionalities f and can be connected via bonds to form a number of connected components of various sizes, commonly called clusters. If for a concentration of monomers p at least one cluster extends from one side of the container to the other side, the sol has turned into a gel. The concentration p_c of monomers above which this large cluster, the so-called infinite incipient cluster (IIC), exists is called the critical concentration, and p_c indicates the onset of the sol-gel transition (SGT).

Understanding this transition theoretically is far from trivial. Flory[39, 40, 41] and Stockmayer[162, 163, 180] showed that, if the monomers do not form loops, a sol-gel transition occurs as soon as the concentration of monomers p, having a single functionality f exceeds the critical value $p_c = \frac{1}{f-1}$. De Gennes[31] and Stauffer[154] showed, that the SGT is closely related to the - purely geometrical - *lattice percolation* problem. In the percolation problem one asks the simple question: how many clusters does one find on a lattice of size L^3, if a fraction of $r_L = N/L^3$ of the lattice sites are occupied and fictive bonds exist between all neighboring lattice sites. Depending on the lattice type, one finds different critical fractions r_c of occupied lattice sites above which a cluster exists, that reaches from one side of the lattice (the container) to the other side of the lattice.

The dynamic processes occuring during gelation have been studied extensively in the *kinetic gelation* model of Manneville and de Seze[106] and Herrmann et al.[70, 12]. [1]The kinetic gelation model is a lattice model for the radical polymerization of organic bi- and tetra functional monomers. Usually simulations are performed on a cubic lattice with about 50 % of the lattice sites occupied. Chemical reactions are initiated by randomly placing a small number of radicals on the lattice. These radicals move across the lattice, and bonds between monomers are created along the trace of the radicals. Within this type of modelling it was shown that a sol-gel transition exists. Furthermore, spatial correlations between pairs of tetramers exist[13], and thus the distribution of tetramers is not purely random as it would be the case in the percolation type approach. The kinetic gelation has been extended by Pandey and coworkers to include thermal motion of the monomers, effects of solvents and temperature[96, 98, 97, 99, 122].

The kinetic gelation model and its variants has been extensively investigated with special focus on the critical properties and the sol-gel-transition, but it is not clear whether such simplified models can be used for the generation of structural models of amorphous ceramics, and furthermore, if these models are capable to mimic the very complex synthesis routes that are necessary to produce these newly developed inorganic materials.

Thus we have developed a separation of time scales approach that take specific aspects of the real system (here: a-$Si_3B_3N_7$) into account. In this chapter, we first give a gen-

[1]For a review see [71].

eral outline of our separation of time scales approach, followed by details of our specific implementations. Next, the resulting structural models are analyzed with respect to the influence of various process parameters, and finally compared with geometrical and topological information gained from physical measurements.

6.2 Sol-Gel Route

6.2.1 Experimental observations

As mentioned earlier in section 1.1, a true simulation of the full sol-gel route is not yet feasible. In order to design the intermediate steps needed to construct a multi-stage model of the process, we first identify the central elements and stages of the actual synthesis route.

In the experiments, one starts with a dispersion of molecules containing (Si-N-B)-units (TADB = Cl_3Si-(NH)-BCl_2) in a medium consisting of NH_3 molecules plus a certain amount of hexane. All components are highly mobile at this stage. During polymerization, new bonds are generated among and between these and the NH_3 molecules, removing the functional parts of the TADB-molecules (the Cl atoms) and leaving only some hydrogen containing end-groups:

$$\mathrm{TADB} + \mathrm{NH_3} \longrightarrow \mathrm{polyborosilazane} + \mathrm{NH_4Cl} \tag{6.1}$$

More specifically, the following reactions at the functional groups (X-Cl), (X-NH_2), and (X-NH-Y) are likely to dominate the process:

$$\begin{aligned} \mathrm{R_1(X-Cl)} + \mathrm{NH_3} &\longrightarrow \\ \mathrm{R_1(X-NH_2)} + \mathrm{HCl}, & \end{aligned} \tag{6.2}$$

$$\begin{aligned} \mathrm{R_1(X-Cl)} + \mathrm{R_2(Y-NH_2)} &\longrightarrow \\ \mathrm{R_1(X-NH-Y)R_2} + \mathrm{HCl}, & \end{aligned} \tag{6.3}$$

$$\begin{aligned} \mathrm{R_1(X-NH_2)} + \mathrm{R_2(Y-NH_2)} &\longrightarrow \\ \mathrm{R_1(X-NH-Y)R_2} + \mathrm{NH_3}, & \end{aligned} \tag{6.4}$$

$$\begin{aligned} \mathrm{R_1(X-NH-Y)R_2} + \mathrm{R_3(Z-NH_2)} &\longrightarrow \\ \mathrm{(R_1X)(R_2Y)(R_3Z)N} + \mathrm{NH_3}. & \end{aligned} \tag{6.5}$$

Here, X, Y and Z can be B or Si, and R_1, R_2 and R_3 just denote the remainder of the molecule containing the functional group.

There exists only a limited amount of experimental and theoretical information regarding the details of these reactions. Presumably, the condensation reactions (6.4) and (6.5) are the slowest overall, while for identical R_1 and X, reaction (6.2) should be somewhat faster than reaction (6.3). Of particular interest has been the question, of how the speed of the aminolysis reactions (6.2) and (6.3) depend on the identity of X, and the details of the remainder R_1. Ab initio Car-Parrinello calculations have confirmed[127] the experimental observation/intuition that the (B-Cl) bond is more easily broken than the (Si-Cl) bond, and that the details of R_1 are not crucial compared with the B vs. Si effect.

Hexane does not appear to play any role in the actual reaction process; it only ensures that the final polyborosilazane remains soluble for the purpose of further processing (shaping, spinning, etc.) before the pyrolysis step. From the point of view of modeling the polymerization, the only effect of hexane is some reduction of the overall density of the reacting molecules.

Furthermore, we notice that this first reaction phase usually takes place in a considerable excess of NH_3, $c_{\mathrm{NH_3}}/c_{\mathrm{TADB}} = R_C \approx 100$. These conditions suggest that most of the Cl-elimination will have taken place very early in the process before the actual cross-linking begins among the TADB molecules. Noting that each TADB contains 5 Cl-atoms, one would estimate that the fraction of TADB-molecules that are involved in $n(\leq 5)$ reactions of type (6.3) is on the order of $O(R_C^{-n})$.[2]

Depending on R_C, one would expect that by the end of the Cl-elimination only relatively

[2]Most likely, this estimate is actually an upper limit, since the NH_3 molecules are much more mobile than oligomers containing more than one (Si-N-B)-unit. Thus, multiple encounters of TADB molecules needed to generate large oligomers early in the polymerization stage are even less likely once the local region around a TADB that has participated in several reactions has been depleted of TADB. Whether this effect makes a quantitative difference depends on the speed of reaction (6.2) compared to the speed of diffusion of the oligomers, of course. For a more precise analysis, the corresponding diffusion-reaction problem would need to be solved.

small oligomers containing no more than on the order of ten (Si-N-B)-units will be present.[3] Further cross-linking should then occur via NH_3-elimination according to reactions (6.4) and (6.5).

Since the temperature is relatively low, many of the (Si-N-B)-units from TADB are likely to survive intact at this polymerization stage. However, this is surely no longer going to be the case during the pyrolysis stage of the synthesis. During this pyrolysis in N_2, the remaining foreign atoms are removed while evolving NH_3, N_2 and H_2, and the structure is allowed to solidify, becoming more dense in the process. This second process will also include the wholesale destruction and rebuilding of the Si-N and B-N bonds (locally), due to the high annealing temperatures (≈ 1500 K).

We conclude from our analysis that the central elements of the process are the following:

- Initial configuration
- Cl-elimination
- Cross-linking while (X-Cl) functional groups are still present (first stage)
- Cross-linking while only (X-NH_2) and (X-NH-Y) functional groups are available (second stage)
- Annealing

6.2.2 General multi-stage approach

Initial configuration

We first note that the initial configuration can be modeled as being a random arrangement of the TADB-, NH_3- and hexane molecules in a (periodically repeated) simulation cell. Furthermore, since hexane is inert for all practical purposes, it can be eliminated from the model. Thus, the initial configuration can be simplified and should only consist of TADB and NH_3, where all effects due to hexane are incorporated as a lowering of the initial density of the system.[4]

Cl-elimination

From the ab-initio simulations, it appears that the details of the removal of the Cl-atoms are probably not critical for the overall process. Here, we are only referring to possible differences in the reaction rates for the first, second, etc. Cl-atom to be eliminated. The different reaction rates of B-Cl and Si-Cl bonds clearly need to be included in the model. For the simple model we are trying to construct, we will therefore ignore the Cl-atoms by treating them as mere placeholders for free Si- and B-valencies. Similarly, the hydrogen atoms can be modeled as placeholders for free nitrogen valencies, both in TADB and ammonia.

While it appears to be safe to discard the Cl- and similarly the H-atoms as such, a critical question is, whether there exists a preference for the removal of Cl from the B- or the Si-functional unit. Similarly, we have to wonder, whether free N-valencies prefer to react with available Si- or B-valencies. Finally, there is the issue of whether free N-valencies in TADB and oligomers (denoted N^1) react as quickly with free B- or Si-valencies as the free valencies in NH_3 (denoted N^2). Within the approach presented here, we assume that the reactivity of N^1 and N^2 are comparable.

First stage cross-linking

A first step to model this process would be to assume a very simplified interaction of molecules walking randomly inside the simulation cell: If a N with a free valency approaches a Si or B with a free valency, the two molecules link with a gain in energy $E_{Si-N} < E_{B-N}$, respectively. In the low-temperature regime of the polymerization process, we can even assume that any bond which has been formed is not going to be broken. Regarding the shape of the new molecule, we can assume that it obeys the simple model building rules for molecules, with N and B being approximately trigonally planar coordinated by cations and anions, respectively, while Si

[3] A tree graph oligomer derived from m TADB molecules, i.e. containing m (Si-N-B)-units occurs with probability $O(R_C^{-m})$. For $R_C = 100$ and $m = 10$, this leads to a probability $p = 10^{-20}$. Assuming 10^{21} TADB molecules immersed in 10^{23} NH_3 molecules leads to about 10 ($m = 10$)-oligomers.

[4] In principle, the polymerization will also take place without any hexane being present.

is tetrahedrally coordinated by N, with complete flexibility in the dihedral angles up to the point that two atoms collide within their vander-Waals radii.

We note that B-N is the stronger bond, and thus one would assume that there will be a tendency to form B-N bonds over Si-N bonds. On the other hand, with B-N bonds having perhaps formed quickly initially, they might be too stable to allow the formation of e.g. a B-N-B linkage starting with two B-N bonds.

Ideally, we would perform long-term simulations, with a realistic ratio of the diffusion- and reaction-rates, and similarly realistic energy gains and costs for creating and destroying a B-N or Si-N bond. However, such a simulation is only feasible for a highly activated system, i.e., for unrealistic temperatures. A way to address this problem is a separation of time scales approach. At the beginning of the process, we can assume that the diffusion of all reaction participants is fast enough to create a homogeneous mixture (analogous to the well-stirred reactor approximation). No spatial variation of the reaction partners is present, and we can assume that the likelihood of each TADB to react with another TADB is exactly given by $1/R_C$. From the modeling point of view, this has another advantage: we can assume that, on the density-equilibration time scale, each TADB and NH_3 molecule moves randomly with arbitrary step length, i.e., each free spot in the simulation cell has equal probability to be the next location of the molecule.

However, we quickly encounter a problem regarding the movement of the newly linked molecules containing several Si-N-B-units. Modeling the movement of these oligomers is rather expensive in computation time, in particular in a dense solution, where two such molecules are very slow to pass one another. A possible solution is to recall that the ammonia molecules are both highly mobile and present in excess. Thus we can assume that molecules consisting of more than N_{max} Si-N-B-units are essentially stationary with respect to the medium, while the NH_3 molecules are always present everywhere in the system as before. Once cross-linking has started and produced larger molecules, these serve as spatially fixed growth centers for the further adsorption of TADB and ammonia molecules.

One issue we have to address at this stage is the faster reactivity of B-Cl-functional groups. If we assume that the individual TADB molecules can quickly rotate in the NH_3 medium, the opportunity to react can be taken as equal for all functional groups, B-Cl and Si-Cl, and the likelihood that a successful reaction takes place depends on the reaction rates. Thus, free B-valencies will more quickly be saturated than the Si-valencies, both at the stationary oligomers and the still mobile TADB.

Second stage cross-linking

After all free B- and Si-valencies have been saturated, two things change. The NH_3 molecules can no longer react, and the reaction rates will presumably be slower than before, since only reactions (6.4) and (6.5) can take place. Thus, we can from now on ignore the NH_3 molecules, while continuing to move single TADB molecules and perhaps also small oligomers. Now reactions (6.4) and (6.5) will occur among the stationary oligomers and mobile TADB, where we still assume that at the low temperatures where the polymerization is performed no B-N or Si-N bond will break, at least not without being re-formed right away during the ammonolysis.

Once all TADB molecules have become part of stationary oligomers, the separation of time scales arguments cut the other way. Now the diffusion (and 'wobbling') of the oligomers will be the slow controlling time scale, while we assume that the (irreversible) reaction takes place at once after the encounter of two oligomers. In principle, we can now perform an appropriate diffusion simulation for the oligomers. However, there is a faster way: Reducing the density by rescaling the simulation cell leads for the small clusters to get within range of another, and results in the desired merger dynamics of the small oligomers.

We note that, implicitly, this model assumes that growth takes place essentially continuously without any breaking of bonds. This favors a "first seen, first bonded" approach, only modified by the special model kinetics favoring the saturation of the free B-valencies. However, for very long polymerization times in the real system, one might want to permit bond-breaking, too. In this way, the rela-

tive strengths of the B-N and Si-N bonds mentioned earlier can be taken into account, too.

Still, these statistically relevant properties of the system would not make themselves felt during the relatively short MC/MD-simulations we can perform. Annealing at low temperatures is too slow for the statistical preference to preserve B-N bonds, to have an effect compared to the influence of the initial random placement - after all, Si-N bonds are also very strong by themselves and do not break easily at low temperatures once they have formed[5]. Of course, we can take this tendency, i.e. for stronger B-N bonds to be present with a higher probability, into account by again favoring reactions (6.4) and (6.5) for X = B over X = Si during the merger dynamics.

Annealing

While at the beginning of the annealing phase we can still use the modeling procedure from the previous step, this no longer holds true for the long-time annealing at higher temperatures. Although the available simulation times are still rather short, we can now perform MC or MD simulations at the annealing temperature $T \leq 1500$ K, using satisfactory empirical potentials.

6.2.3 Procedure 1

General aspects

In the first procedure, we have decided to model polymerization and the early stage of the pyrolysis in one step, to focus on the kinetic effects. We assume that, on the long time scales we are interested in, many openings and closings of Si-N and B-N bonds can take place. Thus, concepts from statistical mechanics can be applied: We can assume that the (Si-N-B)-unit can be destroyed, and, furthermore, the addition of new atoms and the growth of the polymer clusters can be modeled by assuming an enhanced average sticking probability of B atoms at free N atom valencies.

In addition, we note that the larger the oligomers and polymers have become the less likely they are to move past each other in the solution. On the other hand, the individual molecules and atoms that attach to the larger units are still quite mobile and thus can be assumed to be homogeneously dispersed throughout the volume. The assumption of many bond-breakings and -openings allows us to model the growth of these polymers as a aggregation-growth process, where no atom that has been linked to the polymer is ever removed again[6].

Since this process will take place throughout the volume, we assume that several starting centers are present, where the growth process will be initiated. The kinetic effect makes itself felt in the preference of non-saturated N-atoms at the surface of the polymer to preferentially bond to the available B-atoms. One should also note that we are in a highly oversaturated state, and that the density is so high that the final fully linked compound is created by a merger dynamics[85, 141] of these small polymer-pieces, and not via an Ostwald-ripening process.

Algorithmic implementation

To implement this procedure, we proceeded as follows: We started with a periodic (in order to take the essentially infinite extent of the real system into account) diamond-type lattice, where the number of sites in the simulation cell was such that a prescribed density was going to be achieved upon the placement of all $N_{atom} = N_{\mathrm{Si}} + N_{\mathrm{B}} + N_{\mathrm{N}}$ atoms. The distance between two neighboring lattice sites corresponded to the average of the B-N and Si-N bond lengths. A small percentage of the (Si, N, and B) atoms were placed onto the lattice to serve as aggregation initiation sites. Next, we swept over all anions and cations already on the lattice and added one cation or anion from the reservoir, respectively, to an open neighboring lattice point of the atom under consid-

[5] Of course, in the melt at high temperatures, we clearly notice the higher strength of the B-N bond, even on short time scales (see section 10). But such high temperatures are not part of the sol-gel route we would like to model.

[6] Of course, each individual atom will be added and removed many times. But statistically, there will always be some atom present at the bonding site once an atom has been added a first time. Thus, the (pieces of the) polymer only grow and never diminish when viewed on the long time scale on which short time fluctuations have been averaged out.

eration. Of course, we ensured that the topology was correct, i.e. only up to three neighbors for B and N were allowed, and similarly no cation-cation or anion-anion nearest neighbors were permitted. This applied to both the site at which the atom was inserted and the occupied neighbor sites. The kinetic effect was taken into account by given a preference to B-atoms whenever it was a N-atom's "turn" to choose a new neighbor, while ensuring that the final composition was as desired ($N_{\mathrm{Si}} = N_{\mathrm{B}}$). After each insertion of a B or Si atom, we update the bonding probabilities $p_{(\mathrm{N-B})}$ $(= 1 - p_{(\mathrm{N-Si})})$,

$$p_{(\mathrm{N-B})}(n+1) = \frac{N^r_{\mathrm{B}}}{N^r_{\mathrm{B}} + N^r_{\mathrm{Si}}} p_{(\mathrm{N-B})}(n), \quad (6.6)$$

where N^r_{Si} and N^r_{B} are the number of silicon and boron atoms in the reservoir, respectively. The initial value of $p_{(\mathrm{N-B})}$ was denoted $p^0_{(\mathrm{N-B})}$

As long as the prescribed final density was not too high, this process only stopped after all N_{atom} atoms have been placed. Thus, we chose a density of $\rho^{init} = 1.53$ g/cm^3, which is consistent with the density at the beginning of the pyrolysis stage of the actual synthesis ($\rho = 1 - 1.4$ g/cm^3[78]). Using this procedure, we generated five structures each for two sizes of the initial atoms set (3 and 30).[7]

At this stage, we removed the strains introduced by the lattice-based growth procedure, by a constant volume local optimization followed by a constant pressure conjugate gradient local optimization and finally refined the structural models using an RMC quench-procedure to remove non-critical potential effects, that influence the precise atom-atom distances, but do not change the overall topology of the network. The optimizations employed the computationally efficient two-body interaction potential A (see section 3.9). In the Reverse Monte Carlo (RMC) stochastic quench procedure, we chose the weighting factor $\lambda = 0.20$ (see section 3.8.2). Typically, the changes in the atom positions in this final refinement step were small (< 0.001 Å).

Annealing We modelled the final annealing by Monte Carlo relaxations at different temperatures between 250 and 3000 K, in which we varied both the cell parameters and the atomic position at zero external pressure. For the MC relaxations we employed the interaction potential A. The run length of the simulations was 10^6 MCC, and we varied the cell parameters isotropically every 100 MCC on average. As mentioned, one MCC consisted of N atomic displacements. The final tempered configurations were again optimized by conjugate gradient local optimizations in which both the cell parameters and the atomic positions were simultaneously optimized and we refined the optimized models using the RMC stochastic quench procedure.

[7] For consistency checks, we also generated structures with 15 growth centers for selected values of $p_{(N-B)}$.

6.2.4 Procedure 2

General aspects

An alternative implementation places the division line between the initial network formation and the annealing phase of the pyrolysis towards the end of the polymerization step. Here, we assume that the Si-N-B-units are essentially preserved, i.e. we deal with complete Si-N-B-units placed into the simulation cell together with N-units. Nevertheless, we want to reduce the amount of computational effort needed as much as possible.

Thus, we use the separation of time scales arguments to make several simplifications. First, we note that in the first linking stage, encounters among clusters consisting of linked TADB-molecules and N-atoms, are unlikely for clusters beyond a certain size N_{max}. Thus, we postpone the actual placement into the simulation cell, and instead keep a list of the N_{TADB} Si-N-B units involved. We run through this list, and keep replacing Cl-atoms by N(H_2)-units. In a fraction of $1/R_C$ cases, we take one of the not-yet-linked TADB-molecules[8] from the list, and link it with the TADB (or a (n)-unit-oligomer) just being considered, thus creating a (n+1)-unit oligomer.[9] From a certain size (N_{max}), the oligomer is too slow to move, and will not be picked any more as the second partner in the first stage linking.

[8] In general, we can also use small oligomers containing more than one TADB-unit at this step.

[9] The choice of whether to take a TADB (= 1-unit oligomer) or a small oligomer ($n > 1$), is again made at random, where the probability is a monotonic function of the mobility of the oligomer.

The process stops once all Cl-atoms have been removed[10]. Now we are going to place the oligomers at random into the cell at a comparatively low density (taken to agree with the original density based on the amount of hexane and NH_3 still present). We now proceed by shrinking the volume of the periodically repeated simulation cell. At this stage, the only movements of the oligomers consist in rotations of the molecules. Whenever two functional N-valencies encounter one another during this process, a condensation reaction takes place, and a link is formed, creating a larger oligomer. This process continues until no more rotational movement is possible, and further shrinkage would result in massive overlap of the atoms in the oligomers.

At this point, one fully connected polymer should have been generated. From here on, the modeling of the annealing procedure follows the route outlined for procedure 1 in subsection 6.2.3.

Algorithmic implementation

Following the above outline, the algorithm is divided into four parts: generation and optimization of fragments, packing and merging of fragments, optimization of the packed oligomers, and the final annealing of the system.

Generation and optimization of fragments We distinguish two types of atoms: those that are already part of an oligomer ("fragment" atoms), and those that are still part of the reservoir ("reservoir" atoms). We assume that a reaction only takes place between a fragment atom and a reservoir atom.[11]

Furthermore non-occupied nearest-neighbor sites j of some atom a at site i can only be used for a growth step, if the following (mostly topological) constraints are fulfilled for both the lattice site j at which the reacting atom of the reservoir will be placed and the other lattice sites that will be occupied by the remainder of the inserted atom/molecule: The atom a is under-coordinated[12], and there are neighbor sites, where reservoir atoms/molecules can be inserted[13]. Finally, no two cations are permitted to be nearest neighbors on the lattice.

Initially, we select N_f^0 TADB molecules from a reservoir that contains $N^r_{(\mathrm{TADB})}$ TADB-molecules (represented as Si-N-B building units) and N^r_{N} ammonia molecules (represented as nitrogen atoms). Since the actual synthesis takes place in an excess of ammonia, we chose $R_c = N_r(\mathrm{TADB})/N_r(\mathrm{N}) \approx 0.03$ for a complete application of the algorithm. Each atom of these molecules is placed at the center of a tetrahedral lattice.[14] The distances between the points of these lattices was 1.54 Å, approximately equal to the average B-N and Si-N bond distance.

The actual growth algorithm consists of the following steps: First, one randomly selects a fragment f_s that is capable of growth, and selects the top ranked atom a_{top} of fragment f_s. Here, we rank each atom in the fragment according to

$$rk(a_i) = \Lambda \left(\frac{n - \tau(a_i)}{n} \right) + (1 - \Lambda) \cdot \left(\frac{CN_{max}(t_i) - CN(a_i)}{CN_{max}(t_i)} \right); \quad (6.7)$$

for each atom a_i, $\tau(a_i)$ is the time at which it had been inserted into a fragment.

A high value of Λ favours a 'first-in first grow' strategy producing relatively compact oligomers, while low values of Λ lead to a growth mechanism similar to the DLA (diffusion limited aggregation) approach and result

[10] Depending on the choice of parameters, we might continue, until all the mobile oligomers have become linked.

[11] Intra-fragment reactions are not supposed to occur. Of course this will happen in the later compactification phase.

[12] We call an atom a_i under-coordinated, if the number of nearest neighbors $CN(a_i)$ is smaller than the maximum coordination number $CN_{max}(t_i)$ of the type t_i of atom a_i. Here we have chosen $CN_{max}(Si) = 4$, $CN_{max}(B) = 3$ and $CN_{max}(N) = 3$ in agreement with the experimental data.

[13] Atoms that fulfill these requirements are called capable of growth. Similarly, a fragment f is called capable of growth if it contains at least one such atom.

[14] For bookkeeping, we create two lists: *frag_grow* and *atom_grow(f)*. In *frag_grow* we store the fragments that are capable of growth, and in *atom_grow(f)* we store for each fragment f the specific atoms. After initialization, *frag_grow* contains N_f entries and for each Si-B-N fragment f *atom_grow(f)* contains three entries.

in fractal-like fragments. In equation 6.7 n is the total number of growth steps performed on the selected fragment f_s and $CN(a_i)$ is the current number of nearest neighbors of atom a_i.

Next, we select the element type bt of the atom that will bind to atom a_{top}. If atom a_{top} is a silicon or boron atom, only nitrogen atoms are eligible for bonding. If a_{top} is a nitrogen atom, the selection of the element type is governed by the bonding probabilities $p_{(N-B)}$ and $p_{(N-Si)} = 1 - p_{(N-B)}$. This is followed by selecting the bonding unit bu that contains atoms of the element type bt. If bt = Si or B, only Si-N-B units are eligible, but if bt = N, we chose a Si-N-B unit or a nitrogen atom randomly with probability R_C or $1 - R_C$, respectively.

Next, one attempts to place the bonding unit bu as a nearest neighbor to atom a_{top} onto the lattice. In general, several placements that do not violate the constraints may exist. In that case we randomly chose one of these arrangements for insertion. If no insertion was possible, the bond atom a_{top} was removed from the list of atoms capable of growth.

After this growth step had been executed, the procedure was repeated, until either the reservoir or the list of fragments capable of growth were empty.[15] Finally, the resulting oligomers were optimized using the conjugate gradient method with the interaction potential A.

Packing of optimized fragments At this stage, the set of oligomers f are independent molecular species, containing an overall excess of nitrogen. The process of packing and merging these oligomers is implemented in several steps. First, we treat each fragment f as a (quasi)-independent sphere with radius:

$$R_f = \max_{i=1\ldots N_f^{atom}} (\Delta R_i), \tag{6.8}$$

where N_f^{atom} is the number of atoms in oligomer f and $|\Delta\vec{R}_i^f| = |\vec{R}_i^f - \vec{R}_0^f|$ is the distance of atom i of fragment f from the center of gravity $\vec{R}_0^f$ of fragment f.

We now assign a hard sphere radius

$$R_f^{HS} = R_f - R_{sh} \tag{6.9}$$

to each fragment f and create a random packing of these hard spheres using Monte Carlo simulations. The fragments were placed into a periodically repeated unit cell of volume V_{init} with an initial packing density of $\rho_{pack}^{frag} = 0.3$. The move class includes random displacements of the hard-spheres and compressions of the simulation cell, at a ratio of 99:1. The length of the runs was $n_{max} = 20000$ MCC, where one MCC consisted of N_f moves. Within n_{max} we reached packing densities of $\rho_{pack}^{frag} > 0.60$, where the packing densities were calculated with respect to the hard-sphere radii R_f^{HS}.[16]

Next, the optimized rotational configuration $\mathcal{R}(\phi_f^{best}, \psi_f^{best}, \theta_f^{best})$ $(f = 1 \ldots N_f)$ of the fragments for this random packing was determined by comparing $N_{rot} = 5000$ rotational configurations $\mathcal{R}(\phi_f, \psi_f, \theta_f)$. Each configuration was generated by placing all fragments f inside the cell at the position of the corresponding hard spheres and rotating each fragment f by random Eulerian angles $(\phi_f, \psi_f, \theta_f)$. The number of pairs of close nitrogen atoms ($d_{NN} < 2$ Å) belonging to neighboring fragments determined the "value" of a configuration, since the mergers among the oligomers should take place by eliminating one of the two nitrogen atoms. If no configuration that fulfilled all geometric and topological constraints was found in this step, R_{sh} was decreased ($R_{sh} = R_{sh} - \delta R$) and a new random packing of hard spheres with larger radii $R_f^{HS} = R_f - R_{sh}$ was generated. Finally, the overall composition of the system was adjusted by removing one N atom from each pair of the neighboring nitrogen atoms. However, usually, the required composition had not been reached after this step, and further under-coordinated nitrogen atoms were removed at random until the composition $Si_3B_3N_7$ was reached.

Local optimization of linked oligomers and tempering We optimized the resulting assembly of linked oligomers in two steps. First we removed the largest strains in the system by a conjugate gradient energy minimization employing potential A, where we only var-

[15] Except for extreme parameter choices the reservoir did not become empty.

[16] No packing densities exceeding 0.64 have been observed.

ied the atomic positions. Next, we relaxed the structure by varying both the cell parameters and the atomic positions, again using the conjugate gradient method. The final step of procedure 2 was the annealing of the locally optimized system with a standard Monte-Carlo (MC) algorithm at temperatures $T \leq 1500$ K at constant pressure, analogous to procedure 1. This energy optimization was again followed by a RMC-quench refinement.

6.3 Results

6.3.1 Procedure 1

Polymerization and pyrolysis

Tables 6.1(a) and 6.2(a) show the mean coordination numbers for the first and second coordination spheres of the atoms after the constant volume plus subsequent constant pressure conjugate gradient minimizations, respectively. In the first coordination spheres, boron and silicon were coordinated by $2.6-3.0$ and $3.6-4.0$ nitrogen atoms, respectively, and nitrogen was coordinated by about $2.8-2.9$ cations. We only observe a relatively small dependence on the probability to form N-B bonds, $p^0_{(\mathrm{N-B})}$, and on the number of growth centers I: Larger values of $p^0_{(\mathrm{N-B})}$ resulted in higher/lower coordination of B/Si by nitrogen, and variations in the number of starting sites did not lead to significant changes. Note that the densities of the optimized models is in all cases around 1.7 g/cm^3, close to the experimentally observed density of 1.9 g/cm^3.

The effect of $p^0_{(\mathrm{N-B})}$ is more visible in the second coordination sphere, where e.g. larger values of $p^0_{(\mathrm{N-B})}$ result in higher B-B next nearest neighbor coordinations. Again, no clear dependence on the number of the initially placed atoms I is found.

Figures 6.1(a) and 6.1(c) show the computed X-ray and neutron diffraction radial distribution functions in comparison with experiment, before a RMC-refinement. In both cases, already good qualitative agreement with experiment is observed, which improves even more once the RMC refinement is performed (c.f. fig. 6.1(b), 6.1(d)). As function of $p^0_{(\mathrm{N-B})}$, the agreement appears to be higher for higher values of $p^0_{(\mathrm{N-B})}$, both for X-ray and neutron data. As mentioned earlier, the topology of the structure does not change significantly in the RMC refinement step.

Next, we present the angle distributions at Si, B, and N. We observe only relatively small effects of the choice of $p^0_{(\mathrm{N-B})}$, mostly in the strength of the 90^o peak in the N-Si-N angle distribution which indicates the presence of edge-sharing among the SiN_4 tetrahedra. Note that this effect is less pronounced for the RMC-refined models.

Annealing

Finally, we turn to the structures of the models one finds after tempering for 10^6 MCC at various temperatures at zero external pressure. We have tempered only those models that were generated using an initial bonding probability $p^0_{\mathrm{N-B}} = 0.99$ at different temperatures T $\leq$ 4000 K.
Figures 6.3(a), 6.3(b), 6.3(c) and 6.3(d) depicting the temperature dependences of different structural and bulk properties of the tempered (squares), the constant pressure optimized (circles) and the refined models (triangles), show that these properties change significicantly once the temperature was raised above 1500 K. Below 1500K the density of the structure increased only slightly, reaching a value of 1.8 g/cm^3, close to the experimentally found value. Similarly, we find that the mean coordination numbers for the first coordination sphere are essentially preserved up to 1500 K, only an increase is observed, while the second coordination number only changes weakly up to 1500 K (figures 6.3(b)-6.3(c)). Above 1500 K, the higher number of boron boron next nearest neighbors as well as silicon silicon next nearest neighbors vanishes. We note here that neither the optimization nor the RMC refinements change the structural and bulk properties significantly, which are in agreement with the experimental data. This holds also for the pair correlation functions, which continue to show good agreement with experimental data (figure 6.4). Note that the agreement between the experimental and the pair correlation functions of the 'high temperature' models is better than for the low temperature models. In contrast, the densities and the numbers of next nearest neighbors of the

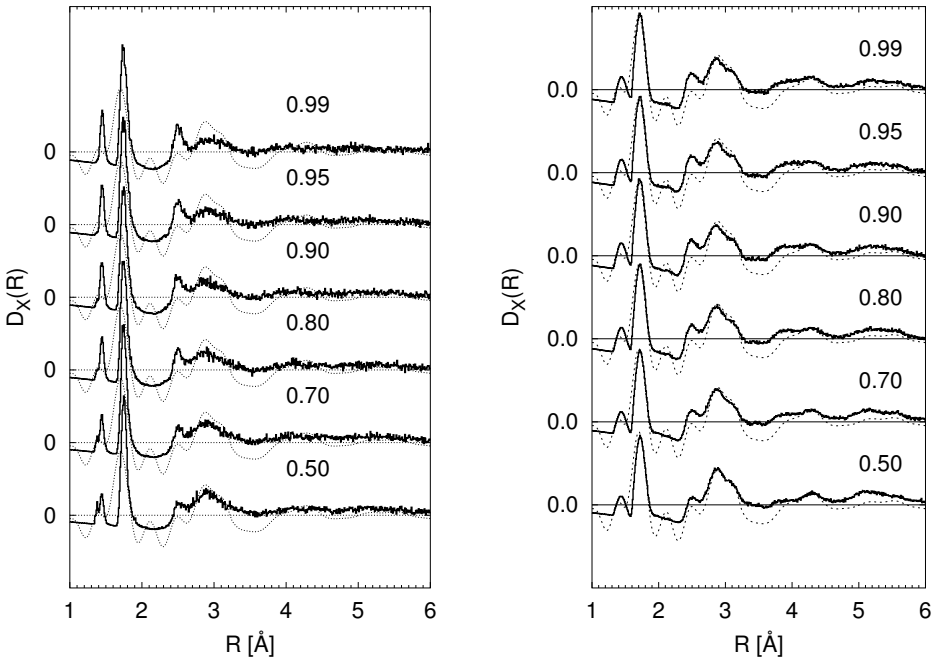

(a) X-ray (optimized)

(b) X-ray (refined)

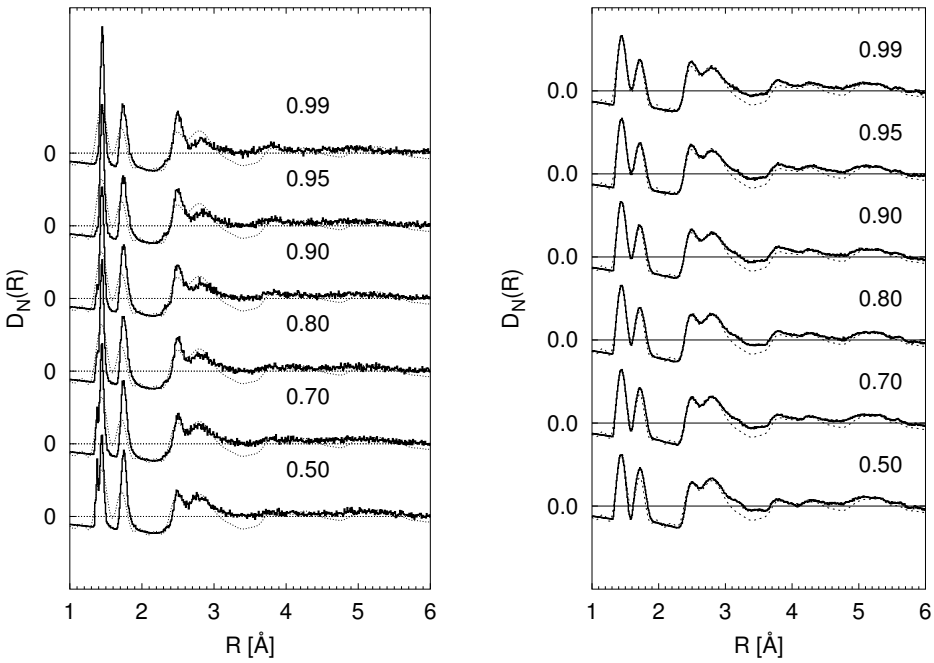

(c) neutron (optimized)

(d) neutron (refined)

Figure 6.1: X-ray (top) and neutron (bottom) pair correlation functions of the constant pressure optimized structural models (left column) and the refined models generated by procedure 1. Numbers inside the figures are the values of $p^0_{(N-B)}$. The number of initially placed atoms was 30.

p^0_{N-B}	I	Si	B	N	ρ_{opt}
0.50	30	3.97	2.58	2.81	1.65
0.50	3	4.04	2.53	2.82	1.57
0.70	30	3.91	2.70	2.83	1.68
0.70	3	3.95	2.71	2.85	1.61
0.80	30	3.86	2.80	2.85	1.72
0.80	3	3.87	2.82	2.87	1.70
0.90	30	3.77	2.87	2.85	1.72
0.90	5	3.77	2.91	2.86	1.62
0.95	30	3.74	2.95	2.87	1.74
0.95	3	3.73	2.97	2.87	1.62
0.99	30	3.70	2.97	2.86	1.79
0.99	3	3.74	2.98	2.88	1.67

(a) optimized

p^0_{N-B}	I	Si	B	N
0.50	3	3.90	2.54	2.76
0.50	30	3.79	2.58	2.73
0.70	3	3.74	2.71	2.77
0.70	30	3.73	2.70	2.75
0.80	3	3.65	2.82	2.77
0.80	30	3.63	2.80	2.76
0.90	3	3.56	2.91	2.77
0.90	30	3.56	2.87	2.76
0.95	3	3.51	2.96	2.78
0.95	30	3.49	2.94	2.76
0.99	3	3.50	2.97	2.78
0.99	30	3.46	2.95	2.76

(b) refined

Table 6.1: Mean coordination numbers of silicon (Si), boron (B) and nitrogen (N) of constant pressure optimized (left) and RMC refined models (right) generated by procedure 1. p^0_{N-B} is the initial probability to bind an nitrogen atom to a boron atom. I is the number of atoms initially placed on the lattice. ρ_{opt} is the density in g/cm^3 of the constant pressure optimized models.

p^0_{N-B}	I	Si-S	Si-B	B-B	B-Si
0.50	30	5.12	2.78	2.07	2.78
0.50	3	5.56	2.26	2.55	2.26
0.70	30	4.83	3.00	2.16	3.00
0.70	3	4.92	2.96	2.30	2.96
0.80	30	4.57	3.25	2.24	3.25
0.80	3	4.48	3.30	2.20	3.29
0.90	30	4.47	3.16	2.48	3.16
0.90	3	4.59	3.05	2.66	3.05
0.95	30	4.61	3.03	2.87	3.03
0.95	3	5.07	2.59	3.29	2.59
0.99	30	4.61	2.83	3.29	2.83
0.99	3	5.62	2.11	3.99	2.11

(a) optimized

p^0_{N-B}	I	Si-Si	Si-B	B-B	B-Si
0.50	30	4.55	2.63	2.07	2.63
0.50	3	5.13	2.16	2.56	2.16
0.70	30	4.28	2.82	2.16	2.82
0.70	3	4.31	2.77	2.30	2.77
0.80	30	3.91	3.03	2.23	3.03
0.80	3	3.89	3.06	2.20	3.06
0.90	30	3.81	2.94	2.47	2.94
0.90	3	3.93	2.85	2.66	2.85
0.95	30	3.89	2.80	2.85	2.78
0.95	3	4.29	2.43	3.28	2.42
0.99	30	3.88	2.58	3.25	2.56
0.99	3	4.76	1.93	3.96	1.92

(b) refined

Table 6.2: Mean number of next nearest neighbors of silicon (Si-Si/Si-B) and boron (B-B/B-Si) of constant pressure optimized models (left) and RMC refined models (right) generated by procedure 1. p^0_{N-B} is the initial probability to bind an nitrogen atom to a boron atom. I is the number of atoms initially placed on the lattice.

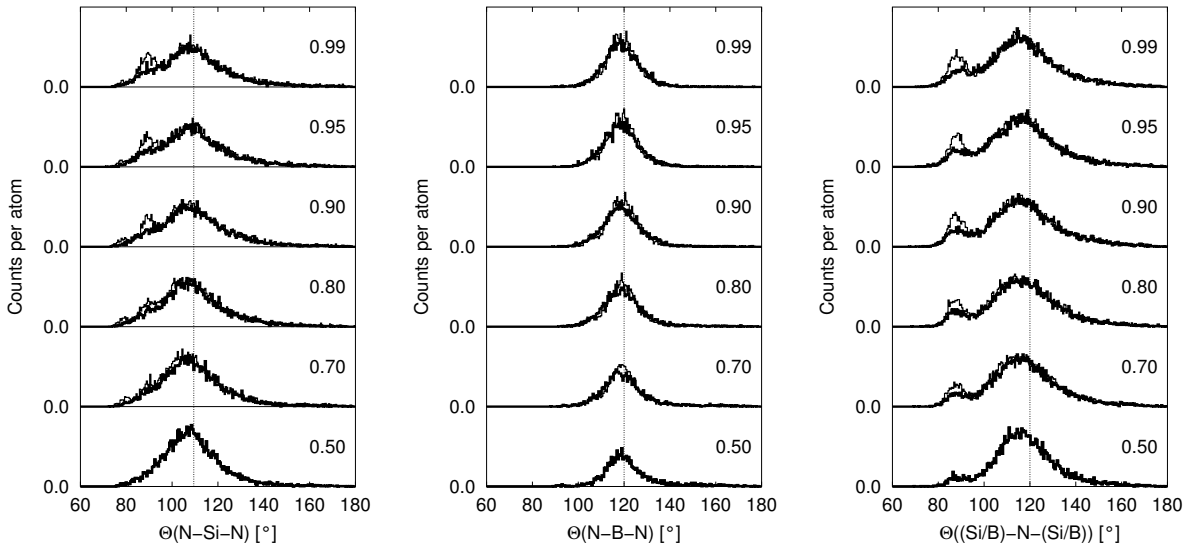

Figure 6.2: Angular distribution function of silicon (left), boron (middle) and nitrogen atoms (right) before (thin lines) and after (bold lines) RMC refinements of the constant pressure optimized models. The number of initially placed atoms was 30.

'low temperature' models agree better with the experimental data.

6.3.2 Procedure 2

Since procedure 2 is rather complex, and each step depends on several parameters, we analyzed the algorithm in three steps. First we study the effects of the system sizes S, the ratio of the number of initially placed TADB molecules to the total number of TADB molecules, the ratio of nitrogen atoms to the TADB-molecules, and the different bonding probabilities, on the properties of the 'as-generated' fragments. Secondly, we study for a system size $S = 300$ TADB molecules (1300 atoms), the dependence of the properties of the optimized fragments on different bonding probabilities and on the number of initially placed TADB-molecules for a fixed value of $R_c = 0.03$. After these investigations, we employ the remaining parts of procedure 2 to a system containing a final number of 1300 atoms, and annealed this system at different temperatures T < 2000 K.

Generation and optimization of fragments

Generation of fragments Figures 6.5(a) to 6.5(d) depict the dependence of various properties of the as-generated fragments on the mean number of atoms of the fragments $\langle N_f^{atom} \rangle$, averaged over different choices for R_c and the number of TADB molecules in the reservoir X_r(TADB)= $N(\mathrm{TADB}) - N_f^0(\mathrm{TADB})$ and system size S. For each choice of the parameters, five sets of fragments were generated. Note that the properties depended only on the fraction of TADB molecules in the reservoir and on the bonding probabilities $p_{(\mathrm{N-B})}$. The fraction of TADB molecules in the reservoir only influences the average number of atoms of the fragments, and the bonding probabilities are responsible for some structural properties.

Clearly for Λ=1 all fragments are compact. The fractal dimension D_f is approximately 3 and does not depend on the choice of the bonding probability $p_{(N-B)}$. The fractal dimension D_f was calculated by fitting a power law $R(N) \propto N^{D_f}$ to the dependence of the mean radius $R^2_{mean} = \sum_i^{n_x} (\vec{R}_i - \vec{R}_0)^2$ on the system size $N_f^{atom} = n_x$, where $\vec{R}_0$ is the center of gravity of the cluster. Note, that for $\Lambda = 0.1$, we observed rod like fragments with a fractal dimension 1.0 in three dimensions.

The effect of the bonding probability $p_{(N-B)}$ can be inferred from figure 6.5(b), in which we plot the average distance of a silicon and a boron atom from the center of gravity of the fragment vs. the fragment size. For extreme values ($p_{(\mathrm{N-B})} = 0.0001/0.9999$), sili-

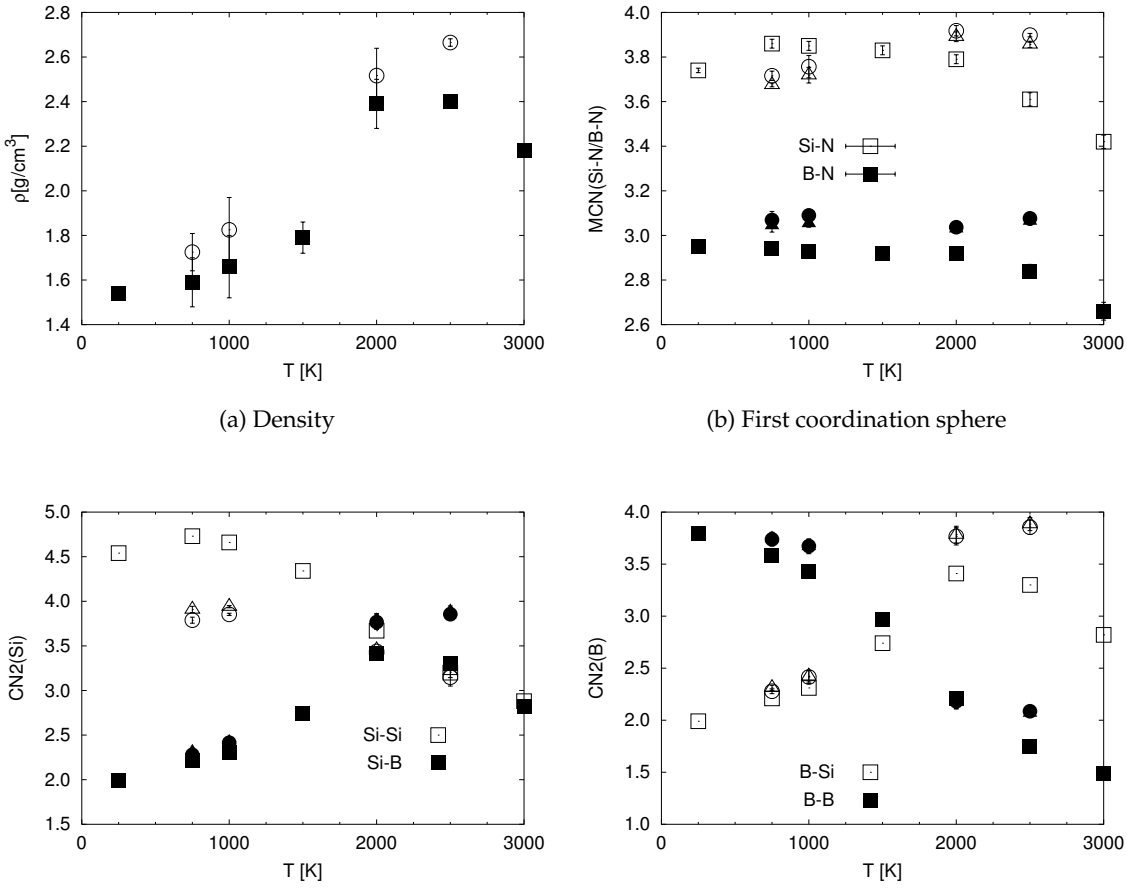

(a) Density

(b) First coordination sphere

(c) Second coordination sphere of silicon

(d) Second coordination sphere of boron

Figure 6.3: Temperature dependence of different properties of the tempered model generated by procedure 1. Squares represent the data of the instantenuous configuration, circles the data of the optimized models and triangles are the data for the RMC refined models.

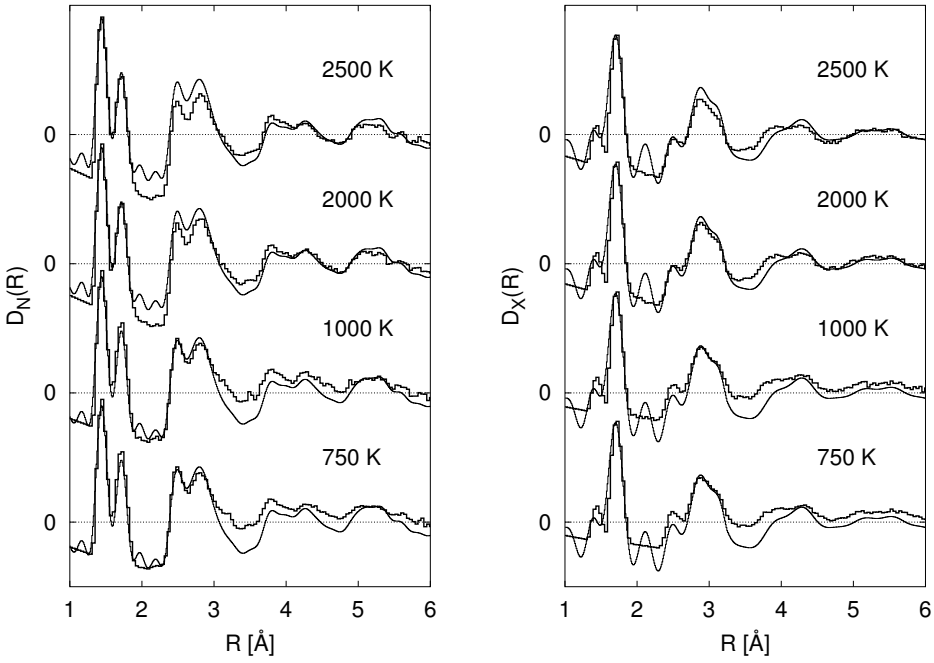

(a) neutron

(b) X-ray

Figure 6.4: Neutron (left) and X-ray (right) pair correlation functions of the tempered structural models after constant pressure local optimizations and RMC refinement. The temperatures at which the models were tempered are given inside the figures. Thin lines represent the experimental data.

con atoms are further/closer to the center of gravity of the fragments. For $p_{(\mathrm{N-B})}$ = 0.5, the distances to the center of the fragment are identical. Even though the mean distances of silicon and boron atoms are slightly different on average for different choices of the bonding probabilities, the average number of next nearest silicon-boron neighbors does not depend on the bonding probabilities for larger fragment sizes ($N_f^{atom} \geq 150$ atoms). However the average number of boron-boron and silicon-silicon next nearest neighbors depends on the choice of the bonding probability $p_{(\mathrm{N-B})}$. Low values of $p_{(\mathrm{N-B})}$ result in a higher number of silicon-silicon next nearest neighbors, contrary to the lower number of silicon-silicon next nearest neighbors observed for higher values of $p_{(\mathrm{N-B})}$. Note, that the mean number of boron-boron/silicon-silicon next nearest neighbors is always substantially lower than the experimentally observed values four/six. For larger fragment sizes, the number of next nearest neighbors become independent of the size of the fragments and independent on the choice of the bonding probabilities.

Optimization of fragments Having discussed the dependence of the properties of the "as generated" clusters/fragments on different choices of the bonding probability $P_{(N-B)}$, we now turn to the discussion of the properties of optimized fragments for two extreme values of the bonding probability $P_{(N-B)} = 0.5$ and $P_{(N-B)} = 0.9999$, weighting factor $\Lambda = 1.0$, and a total system size of 1300 atoms. Since the above analysis had shown that the properties of the fragments were basically independent of the choice of R_c, we use $R_c = 0.03$ in the forthcoming sections. The number of initially placed TADB affected the properties of the fragments and thus we initially placed 50, 30, 15 and 5 TADB molecules on the lattice, thus leaving 250 (83%), 270 (90 %), 285 (95 %) and 295 (98 %) TABD molecules in the reservoir.

Table 6.3 shows the average number of atoms inside an oligomer (fragment) for different numbers N_f^0 of initially placed TADB molecules. As expected, the number of atoms in the oligomers increases with a decreasing N_f^0. Figures 6.6(a) to 6.6(f) show the average

N_0	$\langle N_f^{atom} \rangle \pm \Delta\ N_f$
60	33 ± 13
50	38 ± 13
30	61 ± 14
15	117 ± 17
5	328 ± 20

Table 6.3: Average number of atoms $\langle N_f^{atom} \rangle$ in the fragments generated by procedure 2 using different numbers of initially placed TADB molecules N_0. The total number of TADB molecules was 300 and the bonding probability $p_{(N-B)}$ was 0.9999. Note that at this stage the total number of atoms in all oligomers exceeds the prescribed value of 1300, requiring the removal of many excess N-atoms in the merger phase.

probability of finding a boron/silicon atom among all atoms a distance $R \pm \Delta R$ away from the center of gravity of the optimized fragments for the two investigated bonding probabilities $P_{(N-B)} = 0.5$ and $P_{(N-B)} = 0.9999$. For higher values of $P_{(N-B)}$, we find a preference for boron atoms close to the center of the optimized oligomers, but we note that the fluctuations are quite large. Note also, that if we only grow one cluster, one does observe a clustering of boron atoms close to the center of the center for high values of $p_{(N-B)}$, but for larger distances the probability of finding a boron or a silicon atom are more or less equal.

Packing and merging of optimized fragments

Next we focus on the packing and merging stage of procedure 2. As already mentioned in the description of the algorithm, the generation of random packings of fragments leads to packing densities of $0.59 < \rho_{pack} < 0.64$ for more than 15 fragments. For completeness, we have summarized the packing densities in table 6.4. There we also give the fraction of undercoordinated nitrogen atoms X_m that had to be removed from the assembly of packed fragments. Note that a fraction $(1 - X_m)$ of the atoms are removed by the merging procedure. Furthermore, the shell radius R_{sh} that could be subtracted from the maximum radius of the fragments without resulting in too short

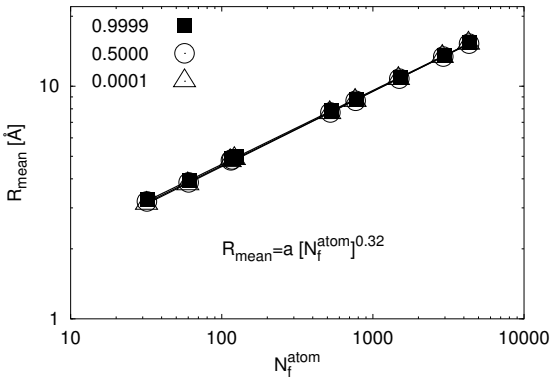

(a) Mean radial size of fragments

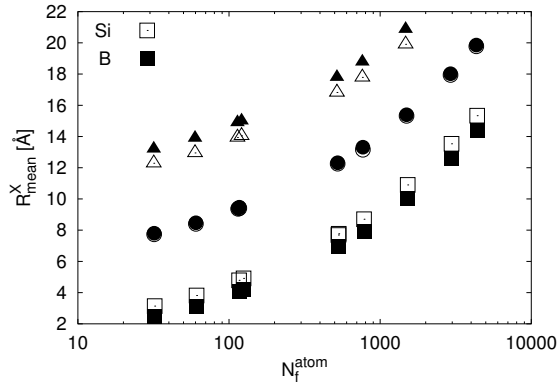

(b) Mean radial distances of silicon and boron atoms from the center of the fragments. Curves for different choices of $p_{(\mathrm{N-B})}$ are vertically shifted by ± 6 Å.

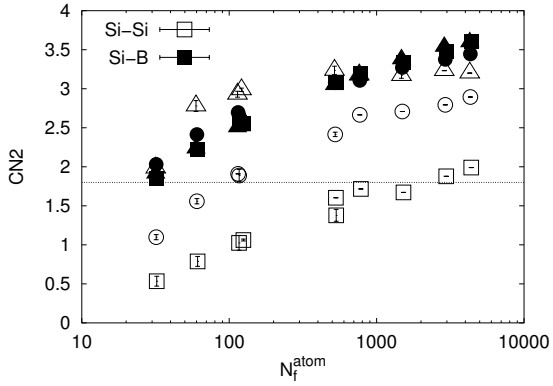

(c) Second coordination sphere of silicon

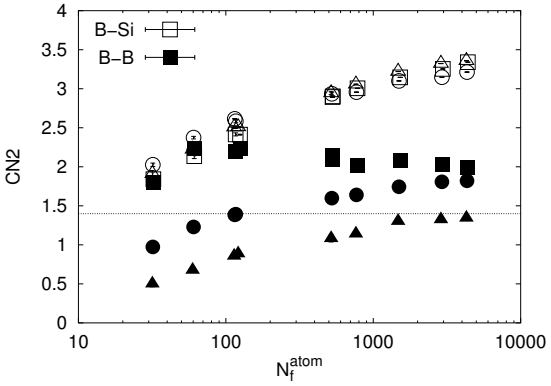

(d) Second coordination sphere of boron

Figure 6.5: Dependence of various properties of the fragments generated by procedure 2 on the number of atoms of the fragments. Filled symbols show the data for boron related properties. Squares, circles and triangles represent the data for $p_{(\mathrm{N-B})}$=0.9999, 0.5 and 0.0001, respectively. The dotted horizontal lines in figures 6.5(c), 6.5(d) are the experimental values of mean numbers of next nearest boron neighbors to silicon (Si-B) and silicon to boron atoms (B-Si), respectively.

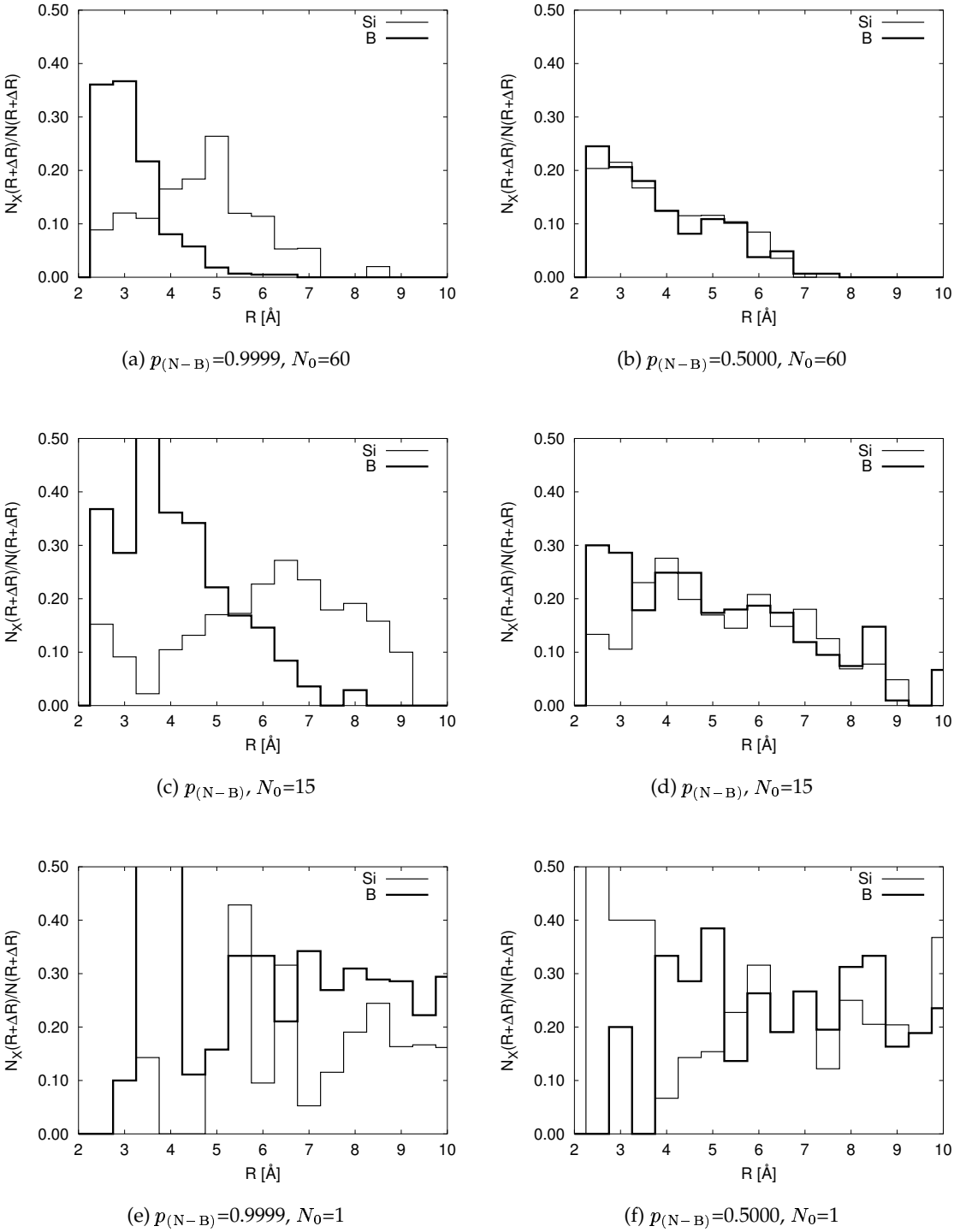

(a) $p_{(\mathrm{N-B})}$=0.9999, N_0=60

(b) $p_{(\mathrm{N-B})}$=0.5000, N_0=60

(c) $p_{(\mathrm{N-B})}$, N_0=15

(d) $p_{(\mathrm{N-B})}$, N_0=15

(e) $p_{(\mathrm{N-B})}$=0.9999, N_0=1

(f) $p_{(\mathrm{N-B})}$=0.5000, N_0=1

Figure 6.6: Average probabilities $p_{\mathrm{Si/B}}(R) = \frac{N_{\mathrm{Si/B}}(R+\Delta R)}{N(R+\Delta R)}$ of finding a boron/silicon atom at a distance $R + \Delta R$ from the center of gravity of a fragment for different numbers N_0 of initially placed TADB molecules and two bonding probabilities $p_{(\mathrm{N-B})}$. (Bold lines: boron atoms).

interatomic distances, is larger for larger fragments, indicating that the larger fragments are more 'diffuse' at larger distances. In table 6.4 we also list the size of the largest connected component and the densities both after constant volume (ρ_v and S_v^{max}) and after subsequent constant pressure conjugate gradient optimization (ρ_p and S_p^{max}), respectively, of the packed and merged fragments. After this stage there are still a few oligomers (< 5 % of the total number of atoms) that are not linked to the largest connected cluster.

Annealing

Finally, we turn to the structures of the models one finds after annealing for 10^6 MCC at various temperatures at zero external pressure. We have annealed those models, that were generated using an initial bonding probability $p_{\mathrm{N-B}} = 0.9999$ at different temperatures T $\leq$ 2000 K.

Figures 6.8(a), 6.8(b), 6.8(c) and 6.8(d), depicting the temperature dependences of different structural and bulk properties of the annealed (squares), the constant pressure optimized (circles) and the refined models (triangles), show that the structural properties change little as the temperature is increased. Only healing (increase of the number of nearest neighbor) is observable. The average number of next nearest silicon-silicon neighbor atoms is slightly higher than the number of next nearest silicon-boron neigbor atoms, but for boron the number of boron-boron next nearest neighbors is *lower* than the number of boron-silicon next nearest neighbors. We note here that neither the optimization nor the RMC refinements change the structural and bulk properties of the models very much. Furthermore, the refined pair correlation functions show good agreement with the experimental data.

The density of the structures increased at higher temperatures reaching a value of ≈ 2.4 g/cm^3 below 1250 K, and similar to the results on the stability of voids, which are discussed more thoroughly in section 9.3.4, we also observed a logarithmic time dependence of the densities (see figure 6.7). Comparing the average sizes of vacancies found in structures generated by both procedures, shows that in procedure 1, larger voids are generated, that are stable up to 1500 K, whereas in procedure 2, the voids are destroyed at lower temperatures, again showing the increased internal surface sizes, that most probably lead to much quicker reshuffling of the volume (figure 6.11). Finally, we note that most of the B-N bonds are preserved during the annealing phase, whereas more Si-N bonds are destroyed in the course of the simulation (figure 6.9).

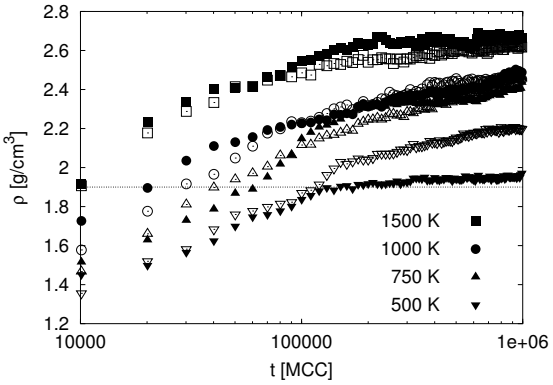

Figure 6.7: Time dependence of the density during variable atom/cell MC-relaxation at different temperatures for 30 (open symbols) and 15 (filled symbols) initially placed TADB fragments. The models were generated using a bonding probability $p_{N-B} = 0.9999$ and employing procedure 2.

6.4 Discussion

In the two previous sections two modifications of a separation of time scales approach to the modeling of a-$Si_3B_3N_7$ were presented. The agreement of the pair correlation functions derived for neutron and X-ray scattering is satisfactory. Similarly, silicon rich regions are observed in the final ceramic after annealing. Note that these silicon rich regions are observed in NMR experiments.[167, 166] The quantitative agreement is better for procedure 1, in which the densities of the generated models are very close to the experimental density. Most likely, the reason for the latter observation is that in procedure 1, the growth from one aggregation center is influenced by the growth from another aggregation center, whereas in procedure 2, oligomers grow independently and the pack and merge

N_f^0	R_{sh}	X_m	S_v^{max}	ρ_v	S_p^{max}	ρ_p	ρ_{pack}
50	1.35	0.73	1258	0.7	1266	0.94	0.63
30	1.50	0.78	1245	0.84	1281	1.12	0.61
15	2.35	0.77	1253	0.97	1274	1.22	0.59
5	2.85	0.85	1248	0.70	1249	1.00	0.51

Table 6.4: Overview over results after the packing and merging stage of procedure 2 as function of initially placed TADB molecules N_f^0. R_{sh} is the shell radius in Å at which the successfull merging could be accomplished (see equation 6.9). X_m is the fraction of under-coordinated nitrogen atoms that needed to be removed at the end of the merging stage. $S_{V,p}^{max}$ and $\rho_{V,p}$ are the sizes of the largest connected components and the density (in g/cm^3) after the local constant volume and constant pressure optimization, respectively. ρ_{pack} is the packing fraction of the hard spheres that enclose the fragments prior to merging.

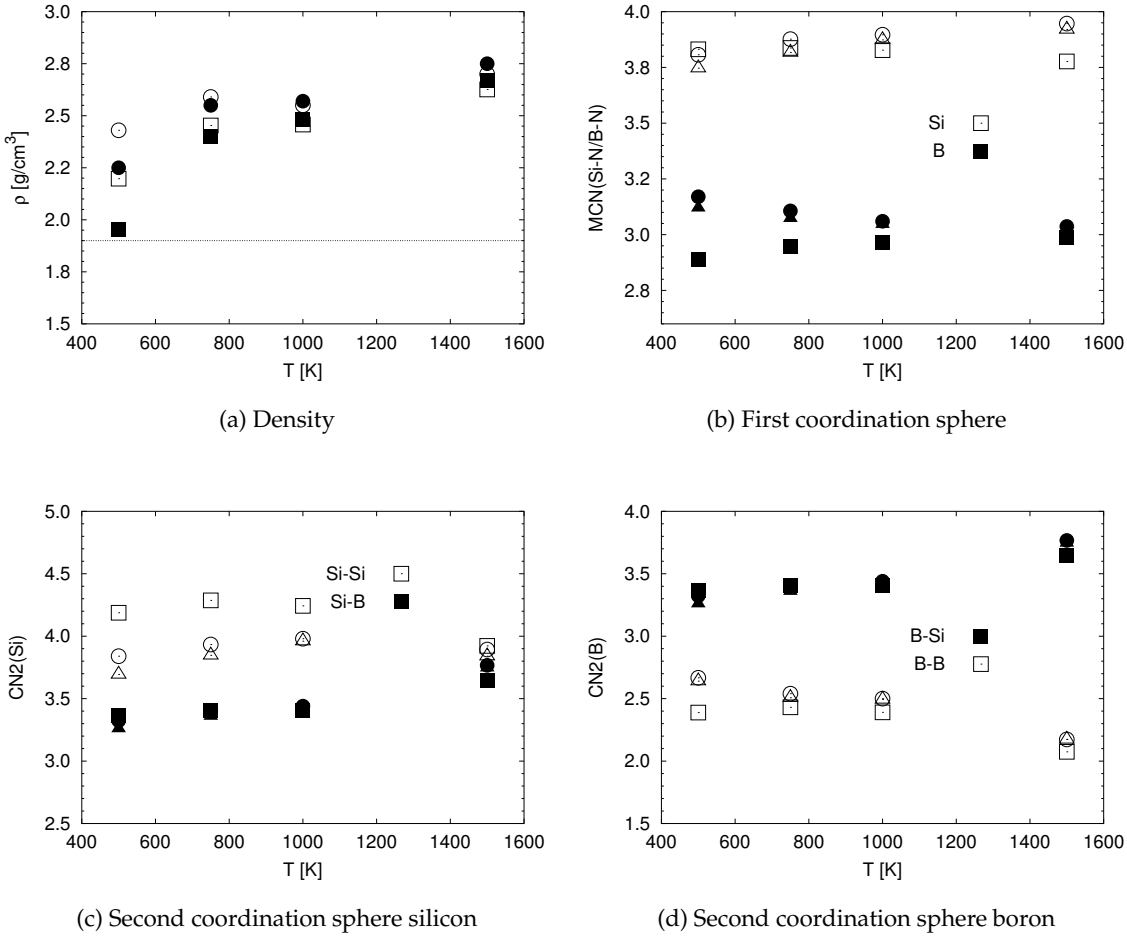

(a) Density

(b) First coordination sphere

(c) Second coordination sphere silicon

(d) Second coordination sphere boron

Figure 6.8: Temperature dependence of different properties of the annealed models generated by procedure 2. Squares depict the instantenous configurations, circles the data for the subsequently optimized model and triangles are the data for RMC-refined models. Only the data for 30 initially placed TADB molecules is shown. The dotted horizontal line in figure 6.8(a) is the experimentally observed density at 298 K after annealing. For comparison see figure 6.3.

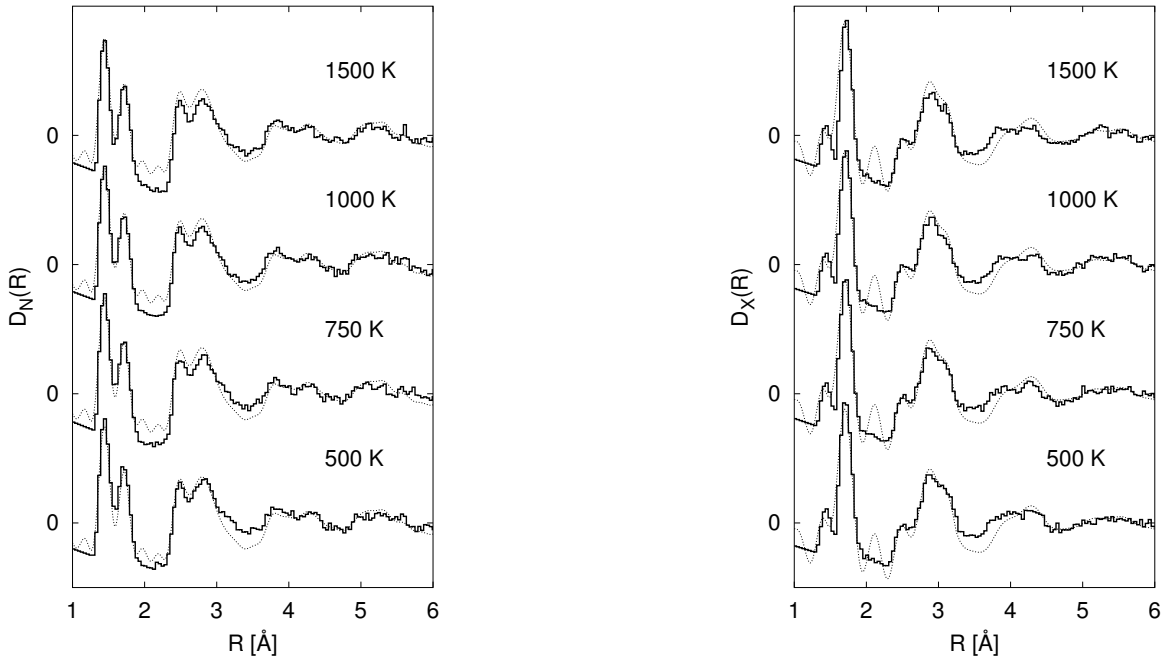

(a) neutron

(b) X-ray

Figure 6.10: Neutron (left) and X-ray (right) pair correlation functions of the annealed structural models generated by procedure 2 after constant pressure local optimizations and RMC refinement. The temperatures at which the models were annealed are given inside the figures. Thin lines represent the experimental data. For comparsion see figure 6.4.

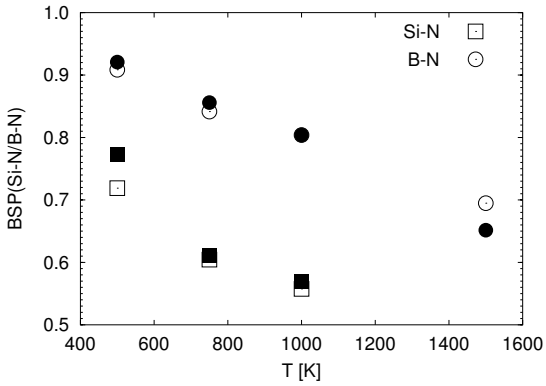

Figure 6.9: Temperature dependence of the bond survival probabilities (BSP) during variable atom/cell MC-relaxation at different temperatures for models generated by procedure 2. Initially 15 (filled symbols) and 30 (open symbols) TADB fragments were placed on the lattice. The BSPs were calculated with respect to an initial waiting time of $t_w = 10^4$ MCCs and it was averaged over the last $2 \cdot 10^5$ MCCs.

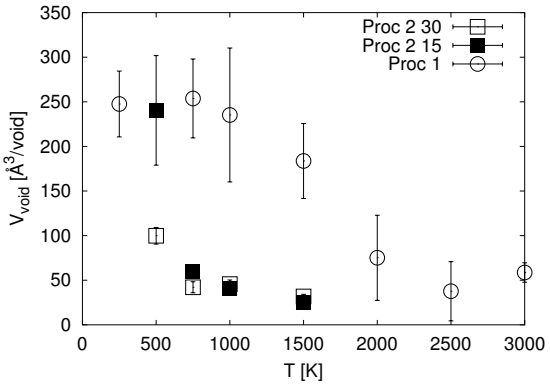

Figure 6.11: Temperature dependence of the average volume of vacancies inside structural models generated by procedures 1 and 2 during MC-NPT relaxations. For procedure 2, we show the data for 15 and 30 initially placed TADB molecules. In the void determination algorith, we used a lattice spacing Δa=2.5 Å.

stage of procedure 2 is not capable to compactify the structures, thus leading to a larger inner surface. Here one should also keep in mind, that in the experiment the overall volume can only decrease by the diffusion of voids to the surface of the material. But once a crust has formed, i. e. all voids within a few nanometers have been removed, this process stops and the density remains essentially unchanged for the remainder of the annealing. In contrast during the simulations, void space can be removed rather easily (the surface is "effectively" only about 20 Å away !). Thus the increase of the density during the annealing tends to greatly exaggerate the densification effect. Within the approach presented here, the large inner surface generated by procedure 2 can very easily move to the boundaries of the simulation cell, thus resulting in a faster densification and denser structural models.

Considering the formation of silicon rich regions, the kinetic effect incorporated by the preferred bonding probabilities $p_{(N-B)}$ is most clearly visible in procedure 1, in which the growth is performed at different growth centers in the same 'container' atom by atom, whereas in procedure 2 the aggregation centers grow independently. Furthermore the kinetic effect is much less pronounced for procedure 2 in which individual TADB molecules are used in the growth procedure. In procedure 1 both silicon and boron rich islands are formed, whereas in procedure 2 no boron rich island are produced, since the growth by TADB molecules introduces silicon atoms at random position after some initial growth steps have been performed. Procedure 2 has also shown, that the kinetics affect the structural properties only on length scales < 10 Å leading to different second coordination spheres and to a preference for the formation of surfaces that contain an excess of the 'slowly reacting' atoms, in agreement with experiment which shows a homogenous cation distribution on length scales exceeding 1 nm.[30]

However this effect is less pronounced for larger distances, casting some doubt on the special role the TADB precursor molecules play for the formation of the island like structures on intermediate length scales (< 6 Å). Maybe the TADB molecules are more important for the development of a homogenous distribution of the elements on length scale $>$ 10 Å. However, our findings are in agreement with the general line of thought of the separation of time scale approach, where the reactions among the TADB molecules and the NH_3 molecules are expected to occur throughout the solution, i. e. we do not have a standard nucleation process as one would expect

during the growth of the amorphous ceramic during the cooling from the melt.

A comparison of the final structures with those one finds when simulating alternative synthesis routes, (see section 8.3 of chapter 8), such as glass formation from the melt, sintering of nanosized crystal fragments, random packing analogous to vapor deposition) shows that the structures presented here compare favourably with those other models, both regarding the pair correlation functions and with respect to medium range order and the density[17]. Only the crystal fragment model exhibits similarly good agreement with experimental data. Furthermore, the structural properties of the annealing models are rather insensitive to the annealing at temperatures $T < 1500$ K, again showing that the synthesis route and the kinetics involved do play an important role for the structural properties of the synthesized product.

Finally, the separation of time scale approach we have presented here is more general of course, and can be easily modified to model the sol-gel synthesis of other amorphous solids. In these modifications one could also include solvent effects, concurrent growths of larger building units and thus obtain an in depth view into the genesis of inorganic polymers.

[17] Keeping the limitations of the finite size of the simulation cell and the crust formation in mind.

Chapter 7

Modelling of the amorphous Si/O/N-system

7.1 Introduction

Multi-component oxynitridic glasses are an important class of amorphous ceramics that are of great interest for technical applications[65], since they can combine the strength of oxidic/nitridic glasses with the feasibility of tuning their properties via the variation of the nitrogen/oxygen ratio. However, they share with other amorphous ceramics the dearth of information about their microscopic structure, which makes ab initio theoretical predictions about the properties of the ceramics very difficult. Furthermore, it has not been possible so far to synthesize compositions with all possible ratios of nitrogen and oxygen[88]. Thus, a rational synthesis aimed at producing an oxynitridic ceramic with well-defined mechanical, thermal, optical, and dielectric properties is handicapped in a two-fold way: the predictability of the ceramics properties remains at the empirical stage, while at the same time the full range of the possible compounds cannot be explored synthetically. Just as with silicate glasses, each chemical system will exhibit its own specific microstructure, depending on the network modifiers added. However, it is to be expected that many structural features found for simple glasses will also be found in the more complex systems. In this chapter, we focus on the simplest paradigmatic system, amorphous Si/O/N. We have employed the random close packing based algorithm[67] for the generation of amorphous covalent networks to model a-$SiO_{2-z}N_{2z/3}$ (a-SiON) for a range of z values. After briefly describing the aspects of the algorithm specific to the Si/O/N-system employed (sec. 7.2), we compare the experimental data for a-$SiO_{3/2}N_{1/3}$ with the properties of our models (sec. 7.3). Finally, we discuss the structural properties of models for the amorphous SiON compounds as a function of nitrogen content (sec. 7.4).

7.2 Generation of structural models

We apply the random close packing based algorithm described in section 5 and in [67] to the generation of network models for $SiO_{2-z}N_{2z/3}$, with different compositions z. The first subsection gives a short outline for the general algorithm, and the second subsection discusses the parameters employed.

7.2.1 Outline of the general algorithm

In this section, we outline the RCP-based algorithm for the generation of structural models of covalent networks. The details of the algorithm are described in chapter 5.
The basic idea of the algorithm employed is the observation that most of the accessible volume in a typical inorganic crystal structure is occupied by densely packed anions, while the cations reside in the voids of the anion packing. We transfer this idea to amorphous structures in a four step process: First we generate a random close packing of anions (represented by spheres of radius R_i) using a modification of the RCP-algorithm by Frost et al.[43] to periodic boundary conditions. Next we identify all N_{void} voids v in the packing, which are suit-

able locations for cations of type s[1]. The resulting set of voids [2] and the anions form the set of vertices of a graph $\mathbf{G}$. Edges are defined between pairs of vertices, with weights depending on the agreement of the ion-ion distances in the structure with typical values in crystalline compounds containing the analogous atoms. In a third step we determine the cost-optimal subgraphs $\mathbf{G}_S$[3] of the weighted graph $\mathbf{G}$. Note that the determination of a cost-optimal subgraph is a NP complete problem, which requires the application of global optimization techniques. We employ simulated annealing for this task [84]. This leads to a number of low cost subgraphs from which we derive structure candidates. Finally, these structure candidates are refined by conjugate-gradient methods utilizing an empirical interaction potential. If experimental data is available, a final fine-tuning via a Reverse Monte-Carlo (RMC) procedure is also possible.

7.2.2 Choice of parameters for a-SiON

We have investigated the chemical system $SiO_{2-z}N_{2z/3}$, for several compositions $z = 0, 0.25, \ldots, 2$. For each composition z we have generated ten random close packings of about 600 anions (oxygen and nitrogen) resulting in a total number of atoms of about one thousand inside a cubic cell of about 20 Å cell length. Table 7.1 summarizes the parameters of the random close packings and the graph generation part of the algorithm. The cooling rate γ for the simulated annealing used in the determination of the least-cost subgraphs $\mathbf{G}_S$ was set to $\gamma = 0.99$ (for a geometric cooling schedule), and 25 optimizations were performed for each packing. The potential energy was modeled as a sum of two-body terms,

$$E_{pot} = \sum_{<ij>} V(r_{ij}). \tag{7.1}$$

[1]These cations of type s have a preferred coordination number $n_s(t)$ and preferred interatomic distances to anions of type t, i.e. all distances r_{vj} of the center of gravity of the void to all of its anions j must fall into an interval $\left[r^{st}_{min}, r^{st}_{max}\right]$, thus defining the coordination sphere.

[2]Usually the number of identified voids exceeds the number of cations required by composition.

[3]The size of $\mathbf{G}_S$ is $N^v_{\mathbf{G}_S} = N_c + N_a$ vertices, where N_c and N_a are the number of cations and anions required by composition, respectively. The number of vertices in Graph $\mathbf{G}$ is $N^v_{\mathbf{G}} = N_{void} + N_a$.

s-t	r_0	Δr	d_{min}	d_{max}
O-O	2.63	0.82	11.98	3.45
N-O	2.72	0.82	1.98	3.54
N-N	2.81	0.82	1.99	3.63
Si-Si	2.98	0.94	1.20	3.97
Si-O	1.61	0.50	1.11	2.11
Si-N	1.72	0.50	1.22	2.22

Table 7.1: Random close packing parameters. Distances are given in Å. For further explanation see sec. 7.2.1.

s-t	C_{ij}
O-O	1131.0
N-O	1586.0
N-N	1425.0

s-t	ϵ_{ij}	σ_{ij}
Si-O	0.20	1.998
Si-N	0.20	2.165

Table 7.2: Interaction potential parameters for the Si/O/N-system. Parameters C_{ij}, ϵ_{ij} and σ_{ij} refer to equations 7.2.

Here, the simple two-body interaction potential $V(r_{ij})$ consisted of a Coulomb plus a Lennard-Jones term for cation-anion interaction and Coulomb plus soft-sphere term for anion-anion and cation/cation interactions:

$$V_{ca}(r_{ij}) = \frac{q_i q_j}{r_{ij}} + 4\epsilon\left[\left(\frac{\sigma_{ij}}{r_{ij}}\right)^{12} - \left(\frac{\sigma_{ij}}{r_{ij}}\right)^{6}\right],$$
$$V_{aa}(r_{ij}) = \frac{q_i q_j}{r_{ij}} + \frac{C_{ij}}{r^6_{ij}}. \tag{7.2}$$

We set the atomic charges q_i equal to the formal oxidation states of the atoms (q(Si) $= +4$, q(O) $= -2$, and q(N) $= -3$). The remaining parameters of the interaction potential were chosen in such a way that the geometrical properties (bond lengths, bond angles) of the crystalline phases SiO_2, Si_3N_4 and Si_2N_2O were reproduced under constant volume conditions and are given in table 7.2.

7.3 Comparison to experimental data

The models for the composition $z = 0.0$ (SiO_2), $z = 0.5$ ($SiO_{3/2}N_{1/3}$) and z=2 (Si_3N_4), were

generated as described in section 7.2. In order to fine-tune their structure, we performed RMC-optimization (see section 3.8.2) on all of the ten structural models obtained after the local optimizations with respect to the simple empirical energy function. In the RMC-refinements, we used a weighting parameter $\lambda = 0.80$, giving more weight to the experimental data, and employed the interaction potential described in section 7.2.2

Figure 7.1 shows the experimental and the averaged simulated pair correlation functions. One clearly notices four major peaks (1.62, 2.63, 3.02 and 4.15 Å) in both the experimental and the simulated structures. The first three peaks can clearly be attributed to Si-O/N, O/N-O/N and Si-Si interatomic distances, respectively. The last peak at about 4.15 Å corresponds to third nearest neighbor Si-N/O-Si-N/O interatomic distances. One should note that this satisfactory agreement between experiment and model is already present for the original structural models without (!) the RMC based fine-tuning (see table 7.3). As one already suspects from the small average atomic displacements during the RMC-optimization, the effect of the RMC-procedure only consisted of a smoothing of the pair correlation function - the main geometric and topological features of the models are established during the procedure described above in section 7.2.2

Our results compare well with experimental findings as shown in figure 7.2 (already shown in figure 5.7 of chapter 5), in which experimental as well simulated pair correlation functions for a-SiO_2 [177] and a-Si_3N_4 [72] are depicted. One clearly notices the good agreement between simulated and experimental data. Regarding the small peaks observed between 2.0 and 2.4 Å in the experiment, we classify them as ghost peaks arising from the Fourier transform of the structure factor $S(q)$ that lacks measurements at high q-values.

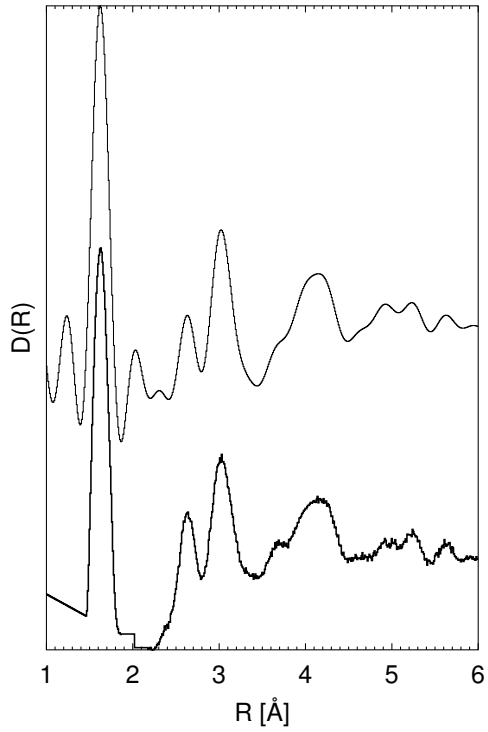

Figure 7.1: Experimental X-ray pair correlation function $D_X(R)$ (top) and average X-Ray pair correlation function of the structural models of a-$SiO_{3/2}N_{1/3}$ (bottom) after local optimization and RMC-refinement.

7.4 Structural properties of a-$SiO_{2-z}N_{2z/3}$

Since the agreement between experiment and model was quite satisfactory for $z = 0.5$ (see above), $z = 0$ (a-SiO_2) and $z = 2.0$ (a-

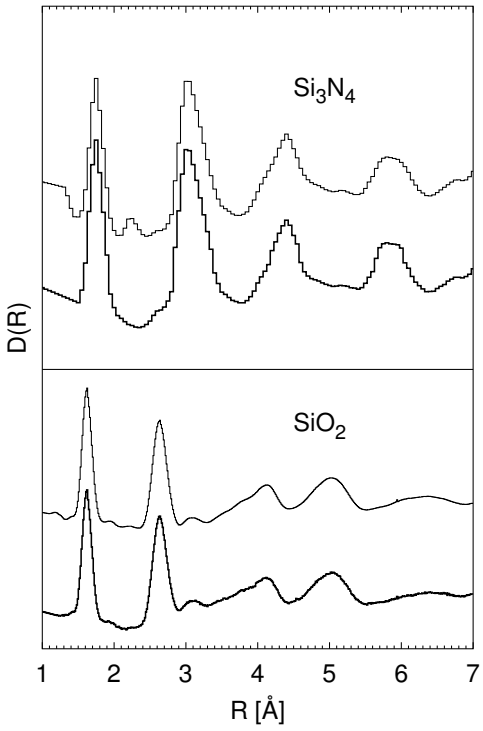

Figure 7.2: Comparison of experimental pair correlation functions $D_{N/X}(R)$ for a-SiO_2[177] (neutron) and a-Si_3N_4[72] (X-ray) with the model based pair correlation functions.

Si_3N_4) (see figures 7.1,7.2), we have generated a sequence of models for compositions $z = 0.25, \ldots, 1.75$. All data presented are averages over ten independently generated models after local optimizations with the empirical interaction potential. Since no measurements have been performed for these compositions, no fine-tuning with RMC was possible. However, since this step only resulted in very minor changes of the structures for amorphous SiO_2, a-Si_3N_4 and a-$SiO_{3/2}N_{1/3}$, we feel that the simple energy function is sufficient for a geometric and topological analysis of the models for a-SiON. Figure 7.3 shows the total pair correlation functions $D_X(R)$, for different compositions z. Here, $\rho(R)$ is the number density of atoms surrounding an atom at the origin within a spherical shell of volume $4\pi R^2 dR$ and distance R from the origin. One clearly notices three peaks at about 1.6, 2.8 and 3.0 Å in all models. In addition, broad peak(s) at about 4 Å are visible. The first peak at about 1.6 Å shifts to about 1.74 Å as the nitrogen content increases with higher z. It can be clearly attributed to Si-O ($\approx$ 1.6 Å) and Si-N interatomic distances ($\approx$ 1.7Å). This becomes obvious when one considers the de-convolution of the total pair correlation function $D(R)$ into its partial pair correlation functions $D_{ij}(R)$ for $z = 1.0$ in figure 7.4.

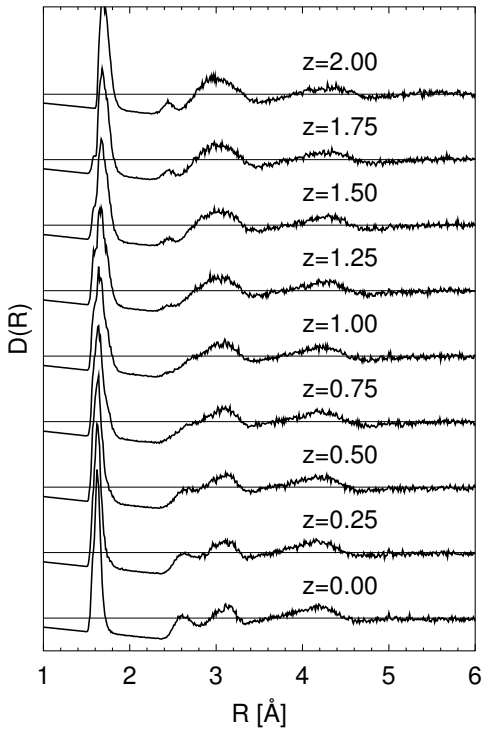

Figure 7.3: X-ray pair correlation functions $D_X(R)$ of structural models for $SiO_{2-z}N_{2z/3}$for the z values given in the figure after local optimization.

The peak(s) in the range from 2.6 to 3.0 Å correspond to O/N-O/N and Si-Si interatomic distances, respectively. The broad peak at about 4.0 Å is clearly due to Si-N/O third nearest neighbor distances as can be seen from figure 7.3. Furthermore, a peak at about 2.4 Å becomes more prominent with increasing nitrogen content. Within the models, this peak can clearly be attributed to shorter silicon-silicon inter-atomic distances (see below).
Important geometric and topological quantities of interest are the first coordination spheres of the structural models. Here, we define the first coordination sphere of an atom i to contain those atoms j, whose distance r_{ij} to i lies between 1.4 and 2.00 Å. Table 7.3 summarizes the mean coordination numbers and mean bond lengths for silicon, oxygen and nitrogen for different compositions

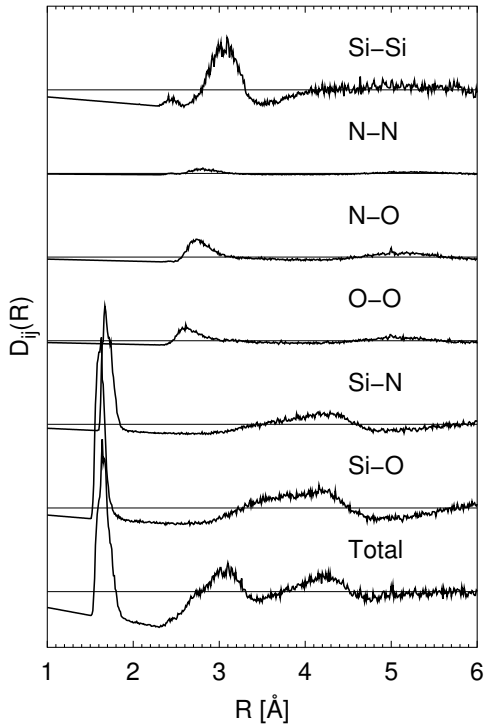

Figure 7.4: Deconvolution of the total pair correlation function D(R) into the partial pair correlation functions $D_{ij}(R)$ for $z = 1$. Pair correlation functions are calculated for X-ray scattering.

z. The silicon coordination number close to four together with the peak in the X-Si-X (X = O,N) angular distribution function (ADF) (figure 7.5) at about 109° indicate the mainly tetrahedral coordination of Si by oxygen and/or nitrogen, which is in good agreement with experimental results from NMR-spectroscopy[88]. The coordination number of oxygen is close to two and the mean bond angle (Si-O-Si $\equiv \phi(O)$) of about 142° indicates the non-linear two-fold coordination of oxygen by silicon. Again, this is in good agreement with experimental NMR results on the bond angle distribution in silica glass ($\phi_{Exp}(O) = 145°$ [36]. The coordination number of nitrogen is close to three, and the peak in the angular distribution function for Si-N-Si ($\phi(N)$) at 120° indicates the mainly trigonally planar coordination of nitrogen by silicon. A careful analysis of angular distribution functions for the X-Si-X and Si-N-Si bonding angle, also revealed an increasing peak at about 90° with increasing nitrogen content which is related to the increase in the number of edge-sharing $SiO_{4-x}N_x$ tetrahedra.

A simple geometric argument[4] shows that these additional peaks are correlated with shortened inter-atomic silicon-silicon distances of about 2.5 Å (see fig. 7.3). We would like to point out that these findings cannot be ruled out from experimental results even for a-Si_3N_4, since all reported pair correlation functions [3, 72] show a small shoulder at about 2.5 Å. In addition, the formation of edge-sharing tetrahedra can actually be favorable energetically, if this edge-sharing leads to a decrease in the number of dangling bonds[5].

Concerning the distribution of $SiO_{4-x}N_x$-tetrahedra, our results show these tetrahedra to be randomly distributed throughout the simulation cell. No phase separation occurs. Figure 7.6 compares the simulation results to the results of a mean-field model that incorporates a random distribution of tetrahedra as its key ingredient (c.f. section 7.5). The good agreement between mean-field model and simulation data yields evidence that the main characteristics (random distribution of tetrahedra) of the mean field model are also present in our simulations. Furthermore the mean coordination numbers (O-O, N-O and N-N) (c.f. table 7.4) in the ternary phases do not show any indications for phase separations on the length scale of our modeling approach.

7.5 Mean field model for distribution of $SiO_{4-x}N_x$tetrahedra in $SiO_{2-z}N_{2z/3}$

In this section we derive a formula for the number of different $SiO_{4-x}N_x$tetrahedra in a-$SiO_{2-z}N_{2z/3}$ in a mean field approach. We assume that an idealized structural

[4] $D(Si-Si) = D(Si-N)\sqrt{2(1-cos(\phi(N))} \rightarrow D(Si-Si) = 2.4$ Å with $D(Si-N) = 1.72$ Å and $\phi(N) = 90°$

[5] This edge-sharing occurs independently of the potential one chooses for the local optimization. In the case of a-Si_3N_4, where more refined interaction potentials[48] exist, we have performed additional local optimizations of the models with such a potential. We found that the optimizations yielded similar results concerning the geometric and topological properties.

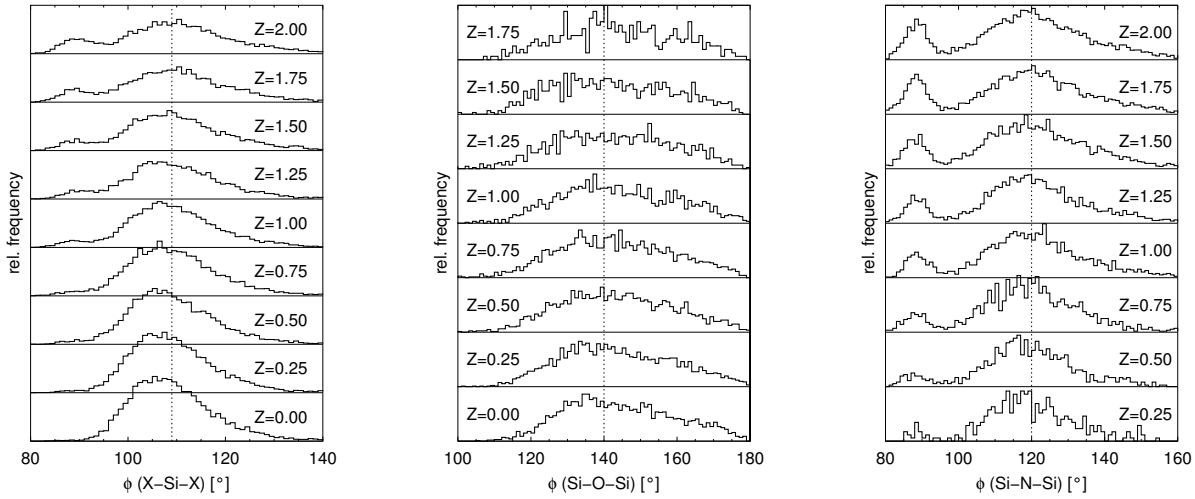

Figure 7.5: Angular distribution functions of silicon (left), oxygen (middle) and nitrogen (right) atoms for different compositions z given inside the figure.

Z	Si-X		O-Si		N-Si		ρ
	d	CN	d	CN	d	CN	
0.00	1.63	3.76	1.63	1.881			2.55
0.25	1.64	3.74	1.63	1.893	1.72	2.46	2.62
0.50	1.65	3.67	1.63	1.884	1.71	2.47	2.64
0.50*	1.65	3.62	1.63	1.879	1.71	2.41	2.64
0.75	1.66	3.66	1.63	1.895	1.72	2.552	2.67
1.00	1.67	3.59	1.63	1.868	1.72	2.56	2.58
1.25	1.68	3.54	1.63	1.857	1.71	2.56	2.58
1.50	1.69	3.57	1.63	1.874	1.72	2.62	2.63
1.75	1.71	3.53	1.64	1.825	1.72	2.63	2.58
2.00	1.72	3.54			1.72	2.65	2.59
2.00*	1.76	3.54			1.76	2.79	2.75

Table 7.3: Mean bond lengths d and mean coordination numbers CN for silicon, oxygen and nitrogen and average densities of the structural models for different compositions z after local optimization. Bond lengths are given in Å and the density is given in [g/cm^3]. Data marked by an asterix $*$ is the data for the structural models after the RMC-refinement step.

Z	Si-Si	O-O	O-N	N-O	N-N
0.00	3.54	5.28			
0.25	3.80	4.75	0.56	3.25	0.63
0.50	3.99	4.07	1.11	3.09	1.44
0.50*	3.87	4.02	1.08	3.09	1.44
0.75	4.37	3.40	1.79	3.17	2.29
1.00	4.60	2.63	2.41	3.00	3.12
1.25	4.86	1.92	2.99	2.86	3.92
1.50	5.38	1.26	3.74	2.82	4.97
1.75	5.69	0.51	4.24	2.58	5.89
2.00	6.16				6.92
2.00*	6.92				7.77

Table 7.4: Mean number of next nearest neighbors Si-Si, O-O, N-O and N-N for different compositions z. Data marked by an asterix $*$ corresponds to the data obtained after the RMC-refinement.

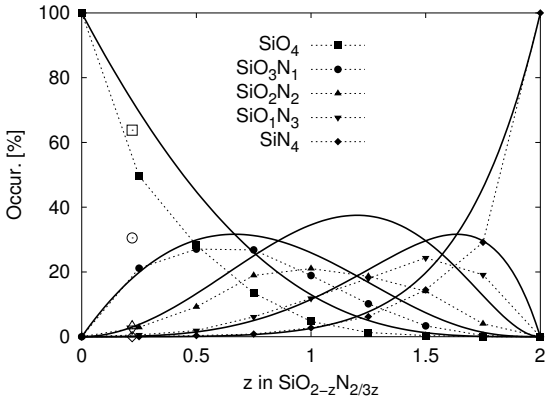

Figure 7.6: Comparison of mean-field model for the distribution of $SiO_{4-x}N_x$for different compositions z to results of computer simulations. The mean field model is depicted as full lines, data from the simulations is shown as points, dotted lines are a guide to the eye only. Experimental data for z=0.22 is depicted as open symbols[88].

model contains non-interacting $SiO_{4-x}N_x$-tetrahedra and that there are Y formula units $SiO_{2-z}N_{2z/3}$ in the structure. We would like to know the probability P($SiO_{4-x}N_x$) of finding a $SiO_{4-x}N_x$-tetrahedron, if we pick a silicon atom coordinated by four arbitrary anions randomly from a structure with given composition z.

Furthermore we assume that the anions are randomly distributed in the structure. In that case the probability of finding an oxygen atom is simply given as number of oxygen atoms divided by the total number of anions. Similarly the probability of picking a nitrogen atom is the number of nitrogen atoms divided by the total number of anions. Since the total number of anions is $Y \cdot (2 - z + \frac{2z}{3}) = Y \cdot (2 - \frac{z}{3})$ the probability of drawing a nitrogen atom is simply

$$P(\mathrm{N}) = \frac{\frac{2z}{3}}{2 - \frac{z}{3}} \tag{7.3}$$

and for oxygen

$$P(\mathrm{O}) = \frac{2 - z}{2 - \frac{z}{3}} \tag{7.4}$$

The joint probability of drawing $4 - x$ oxygen and x nitrogen atom in four draws then reads:

$$P(\mathrm{SiO}_{4-x}\mathrm{N}_x) = \binom{4}{x} \cdot P(\mathrm{O})^{4-x} \cdot P(\mathrm{N})^x$$

$$P(\mathrm{SiO}_{4-x}\mathrm{N}_x) = \frac{4!}{(4-x)!x!} \cdot \left(\frac{2 - z}{2 - \frac{z}{3}}\right)^{4-x} \cdot \left(\frac{\frac{2z}{3}}{2 - \frac{z}{3}}\right)^x \tag{7.5}$$

7.6 Summary and discussion

Using the random close packing approach for the modelling of amorphous covalent networks, we have shown that the structural properties of amorphous silicon oxynitrides are best described by a network of corner-sharing randomly distributed $SiO_{4-x}N_x$-tetrahedra. Additionally our results suggest that oxygen is two-fold coordinated and nitrogen prefers trigonal coordinations. Furthermore, we have presented evidence that with increasing nitrogen content the number of the $SiO_{4-x}N_x$tetrahedra sharing edges increases slightly.

Chapter 8

Structural Modelling of a-$Si_3B_3N_7$

8.1 Introduction

In this chapter, we present in detail five different classes of structural models for a-$Si_3B_3N_7$ based on different generation procedures, each associated with a different chemical and physical route that might, in principle, allow us to generate a-$Si_3B_3N_7$. First, we describe and shortly discuss the various techniques. Next, the resulting structural models are compared among each other and with geometrical and topological information gained from physical measurements. Finally, several physical properties such as the bulk modulus and the phonon spectra will be calculated, and compared with experimental data as far as available.

8.2 Model generation

In general, each of our modeling approaches can be divided into two steps. The first, major one, consists of the generation of the "raw" model, where the final network topology is established to over 90 %. Depending on the synthesis class, several techniques, including possibly a global optimization, might be needed. In each instance, this first stage is followed by a local (conjugate gradient) relaxation and fine-tuning of the "raw" model structures based on refined potentials and cost functions described in subsection 8.2.2.

8.2.1 Classes of model generation

Cooling from the Melt (Class A)

The procedure to generate a model for a-$Si_3B_3N_7$ via rapid cooling from the melt was as follows. First a hypothetical crystalline structure of $Si_3B_3N_7$[89] in a cubic box with side length $L = 19.1$ Å was heated to 2500 K and allowed to equilibrate for 1.0 ns, using (N,V,T)-ensemble[1] molecular dynamics (MD). The size of the system was $N_{atom} = N_{\mathrm{Si}} + N_{\mathrm{B}} + N_{\mathrm{N}} = 702$ atoms, with $N_{\mathrm{Si}} = 162$, $N_{\mathrm{B}} = 162$, and $N_{\mathrm{N}} = 378$. For the MD-simulations, we employed a velocity-Verlet integration algorithm[4], with a time step $\Delta t = 1.0$ fs. The temperature was fixed by periodic velocity rescaling, and we used the computationally efficient empirical two-body potential A to describe the potential energy of the system. For details of the complex functional form of the interaction potential see section 3.9. In order to take the essentially infinite extent of the real system into account, we have employed periodic boundary conditions. Next, the system was rapidly cooled down to zero Kelvin using molecular dynamics simulated annealing with three cooling rates $\gamma^{MD} = 2.5 \cdot 10^{12}, 2.5 \cdot 10^{11}, 2.5 \cdot 10^{10}$ K/s while keeping the volume constant. This cooling was performed for three different starting configurations taken along the 1 ns trajectory at 2500K. As an alternative, we also performed slow Monte Carlo (MC) coolings simulated annealing for the same system. First, the system was equilibrated at $T = 2500$ K for 10^6 MCC. We then employed several cooling rates $\gamma^{MC} = 2.5 \cdot 10^{-1}, 2.5 \cdot 10^{-2}, 2.5 \cdot 10^{-3}$ K/MCC again keeping the volume constant, starting at three different melt configurations. The move-class of the MC simulations consisted of single atom moves, where the atom chosen was shifted by a random vector $\vec{d}$. The step-size $|\vec{d}|$

[1] (N,V,T)- and (N,p,T)-ensemble refer to simulations with constant particle number, volume and temperature, and constant particle number, pressure and temperature, respectively (see chapter 3).

was adjusted such that for each temperature an acceptance rate of $\approx$ 50 % was achieved. Each Monte Carlo cycle (MCC) consisted of a random sweep over all atoms in the system, i.e. N_{atom} individual atom moves.

In addition, we used stochastic simulated annealing as a global optimization procedure by performing the annealing from a number of high-temperature starting points, i.e., we heated the equilibrated ($T = 2500$ K) melt to an initial temperatures $T_0 = 5000$ and 6000 K. Again, three different cooling rates $\gamma = 30, 3, 0.3$ K/MCC were used for each T_0.

For comparison, we also performed local optimizations as described in subsection 8.2.2 for each of the equilibrated high-temperature configurations, corresponding to quenches with infinite cooling rates.

At the end of each of the three processes, the topological structure of the resulting random covalent network had been established. In a final step (c.f. subsection 8.2.2), we could now fine-tune the atom positions using refined potentials for a conjugate gradient minimization. Subsequently the difference between measured and computed X-ray and/or neutron scattering data served as the cost function in the RMC-refinement via a stochastic quench.

Class	P	Explanation
A	1	Melt equilibrated with molecular dynamics (MD) followed by cooling with MD
	2	Melt equilibrated with MC followed by cooling with MC
	3	Melt equilibrated with MD followed by global optimization with simulated annealing
B	4	Simulated annealing of low density crystal fragment
	5	Constant pressure Monte-Carlo cooling of medium density crystal fragment
	6	Constant volume Monte-Carlo cooling of medium density crystal fragment
C	7	Constant pressure Monte-Carlo cooling of cluster with open boundary conditions
	8	Constant pressure Monte-Carlo cooling of periodically repeated interior of cluster
D	9	Random close packing model
E	10	Sol-gel model

Table 8.1: Overview of model classes and modelling procedures used for each of the classes A-E. Details of the modelling procedures are given in table 8.2.

Crystal Fragments (Class B)

An alternative route to a-$Si_3B_3N_7$ might be the solid state sintering of microcrystallites of BN and Si_3N_4. However, so far, such experiments do not appear to lead to a ternary Si/B/N compound. It seems that there does not exist a sufficiently strong driving force that would lead to a mixing, once we are below the melting point of the binary two end-compounds. Furthermore, ab initio energy calculations of hypothetical crystalline $Si_3B_3N_7$ structures suggest that the stable thermodynamic state at zero temperature might correspond to a phase separation into crystalline BN and Si_3N_4[89]. Similarly, the energies computed with the potential we employed for our model generation, show that the binary compounds are energetically favorable compared with the crystalline and amorphous ternary compounds. To what extent such a phase separation would occur at very high temperatures in the ternary melt is not clear, since at standard pressures decomposition is supposed to take place for $T > 2000$ K.

However, we note that we would be in a non-equilibrium situation during a rapid cooling process from the melt into the solid state. Thus, knowing or suspecting that a separation into crystalline BN and Si_3N_4 is energetically favorable compared to the ternary compound at low temperatures and pressures, is not conclusive evidence to exclude that a sufficiently rapid cooling process at high pressures would not result in an amorphous phase with a nearly homogeneous cation distribution. Furthermore, one would expect that at very high temperatures and pressures, e.g. beyond the critical liquid-gas point of the ternary melt ($p > p_c \approx 1.3$ GPa, $T > T_c \approx 8000$ K)[2], a complete mixing of the constituents

[2]The critical pressure and temperature have been es-

could take place. Nevertheless, some degree of phase separation might well occur during the quenching into the glassy state even at high pressures.

Currently, straightforward MD/MC simulations cannot resolve this issue, since the time scales involved in modeling such a separation process, if it were to take place at all, are too long. Note that e. g. the rapid cooling procedure described above produced amorphous random networks with a very homogeneous distribution of cations (c.f. table 8.6). In order to address a possible separation tendency (which might well appear during any process chosen to synthesize a-$Si_3B_3N_7$, not only via the melt route!), we have introduced such an effect by hand. We have constructed a model[66] for a-$Si_3B_3N_7$ that consists of many (≈ 15) BN and Si_3N_4 nano-crystallites ($\oslash < 1/2$ nm). The size of the system was $N_{atom} = 1144$, with $N_{\mathrm{Si}} = 264$, $N_{\mathrm{B}} = 264$, and $N_{\mathrm{N}} = 616$. The side length of the cubic box was $L = 27$ Å, resulting in an initial density of $\rho = 1.5$ g/cm^3. Besides the standard energy relaxation and fine tuning as described in subsection 8.2.2, we have also performed global optimizations using stochastic simulated annealing ($T_0 = 3, 4, 5 \times 10^3$ K and three cooling rates $\kappa = 30, 3, 0.3$ K/MCC each), where the volume was kept constant. Again, potential A was used for the energy evaluation.[3]

For comparison, we performed additional global and local optimizations at higher initial density $\rho = 2.01$ g/cm^3, re-scaling the side length for this purpose to $L = 25.03$ Å. For this starting configuration, we performed two sets of global optimizations, keeping the volume and the pressure constant, respectively. Again several starting temperatures ($T_0 = 1, 2, \ldots, 5 \times 10^3$ K) and three cooling rates ($\kappa = 10^{-1}, 10^{-2}, 10^{-3}$ K/MCC) were used.

Clearly, the model is expected to exaggerate the heterogeneity of the cation distribution by assuming fully formed nanocrystallites. Nevertheless, it constitutes a possible structure model that takes some features of the melt-route structure generation process into account that would otherwise not be accessible. Furthermore, it constitutes a limiting case for those structure models that incorporate inhomogeneities of the cation distribution.

timated from calculations of the liquid-gas region of the equation of state of the ternary system $Si_3B_3N_7$ determined in chapter 9.

[3]We note that upon heating to starting temperatures for the global optimization above 3000 K, the individual crystallites began to melt and the cation distribution started to resemble somewhat the one of the high-temperature melt employed in subsection 8.3.2.

Molecular Modeling (Class C)

A traditionally quite popular way to generate computer models for amorphous systems has been the molecular modeling approach.[16] Here, one takes some local coordination information into account and, starting with a small nucleus consisting of a few atoms, one builds the amorphous structure in an atom-by-atom or building-block-by-building-block fashion. Originally, this used to be done by hand, but nowadays one can perform this task using a computer. Typically, this procedure results in a cluster, since periodic boundary conditions are usually not part of the generation process.

Physically, this process would correspond to the slow growth of a cluster in vacuum, where small precursor molecules or individual atoms are adsorbed on the surface, followed by chemical reactions and, possibly, a reorganization of the cluster or part of it, in order to relieve tensions. Clearly, a comparison with bulk amorphous compounds is difficult as long as surface effects are relevant. However, if we can reach very large cluster sizes, perhaps exceeding millions of atoms,[111] the influence of the surface on the internal structure might vanish, and we can treat the interior of the cluster as a representative of the amorphous material. Furthermore, if we generate a large number of such clusters in the gas phase, they can be deposited on a surface, and allowed to grow into a bulk amorphous material upon solid state sintering. From the modeling point of view, amorphous network clusters containing hundreds of thousands of atoms are not easily constructed and difficult to perform e.g. dynamic calculations with. Thus, our goal was to generate a periodic model using molecular modeling. As a starting point, we have chosen to use the molecular modeling procedure originally developed by Gladden[55], and refined by Wefing[173], for clusters. But since this method does not

work well when imposing periodic boundary conditions, we have proceeded via a two-step process, in order to generate a periodic structure model. As mentioned above, starting from a few-atom nucleus, we add atoms, alternating between nitrogen and the cations (B and Si being chosen at random, with $N_{\mathrm{Si}} : N_{\mathrm{B}} \approx 1$ on average), where we make sure that the local coordinations (BN_3-triangles, SiN_4-tetrahedra, and $N(Si,B)_3$-triangles) and geometric constraints are fulfilled. Once this is no longer possible, we allow some removal of recently added atoms, in order to attempt a new line of construction. As the cluster grows, further improvements become increasingly more difficult, until the time needed to add further atoms (including the deconstruction and rebuilding time of the cluster) exceeds all practical limits[4]. For the Si/B/N clusters we have constructed, this typically takes place when the cluster reaches a size of a thousand atoms.

In a second step, we cut a cubic section from the interior, containing about 600 atoms, and use this as the periodically repeated simulation cell for the relaxation calculations. Since we end up with rather large energetically unfavorable interfaces at the boundaries of the simulation cell, careful annealing starting at relatively high temperatures is needed to reach a reasonable structure. Here, we proceeded in two stages. First, the system was allowed to equilibrate at two initial temperatures $T_0 = 1500$ and 2500 K using Monte Carlo simulations at constant pressure. For three end-configurations from different random walk trajectories, we performed the usual local optimizations (c.f. subsection 8.2.2). Furthermore, these configurations served as starting points for global optimizations with two different initial temperatures ($T_0 = 1500$ and 2500 K) and cooling rates ($\kappa = 2.5 \cdot 10^{-1}, 2.5 \cdot 10^{-2}, 2.5 \cdot 10^{-3}$ K/MCC)

For a comparison, the same annealing procedure was performed for the original cluster without periodic boundary conditions. The structural properties of the periodic structures could then be compared with those one would find for the interior of the original cluster.

In all instances, subsequent local relaxations were performed as a final step as described in subsection 8.2.2.

Random Close Packing (Class D)

Chemical vapor deposition of molecules containing (Si-N)-, (B-N)-, or (Si-N-B)-units, or atom beam deposition of the participating atoms Si, B, and N, on a substrate followed by low-temperature sintering would be another possible route to generate bulk amorphous Si/B/N-materials, in this instance, as an amorphous film. The pre-sintering structure generated in this way would be a random arrangement of Si and B atoms probably already surrounded by (and bonded to) nitrogen. One possible model describing the structures produced in this way is the so-called random close packing model adapted for the generation of covalent networks[67] (see also chapter 5). We generated five different topologies using the RCP procedure, each containing 1040 atoms. In the usual final step, we performed a conjugate gradient minimization of energy and a structural fine tuning as described in subsection 8.2.2. We note that the topology of the network had already been established to over 90 % after the cation placement step, however.

Sol-Gel Route (Class E)

While constituting reasonable structures, none of the preceding models has been generated in a fashion that corresponds to the route chosen by the experimental chemist. As mentioned above, a true simulation of the full sol-gel route is not yet feasible. Nevertheless, we have developed a separation of time scales (lattice-based) approach that allows us to investigate the effects of the kinetics of the polymerization, that appears to favor the early formation of B-N bonds, and pyrolysis during the sol-gel-process (see chapter 6).

As a reminder we briefly recall the implementation of procedure 1, detailed in section 6.2.3. We proceeded as follows: We started with a periodically repeated diamond-type lattice, where the number of sites in the simulation cell was such that a prescribed density

[4]These destruction/rebuilding processes are conceptually similar to the famous "Tower of Hanoi" problem, where each new layer doubles the time required to perform the task leading to an exponential growth in complexity with system size.

was going to be achieved upon the placement of all $N_{atom} = N_{\mathrm{Si}} + N_{\mathrm{B}} + N_{\mathrm{N}}$ atoms. The distance between two neighboring lattice sites corresponded to the average of the B-N and Si-N bond lengths. About 1 % of the atoms were placed onto the lattice to serve as aggregation initiation sites. Next, we swept over all anions and cations already on the lattice and added one cation or anion, respectively, to an open neighboring lattice point of the atom under consideration. Of course, we ensured that the topology was correct, i.e. only up to three neighbors for B and N were allowed, and similarly no cation-cation or anion-anion nearest neighbors were permitted. The kinetic effect was taken into account by giving a preference to B-atoms whenever it was a N-atom's turn to choose a new neighbor, while ensuring that the final composition was as desired ($\mathrm{N}_{Si} = \mathrm{N}_B$). This preference was implemented by employing selection or bonding probabilities ($p_{(\mathrm{N-B})}/p_{(\mathrm{N-Si})}$) for the choice of neighbors of not yet fully coordinated nitrogen atoms.

As long as the prescribed final density was not too high, this process only stopped after all N_{atom} atoms have been placed. Thus, we chose a density of $\rho^{init} = 1.53$ g/cm^3, which is consistent with the density at the beginning of the pyrolysis stage of the actual synthesis ($\rho = 1 - 1.4$ g/cm^3). Using this procedure, we generated five structures each for two numbers of aggregation sites (3 and 30) two choices for the initial bonding probabilities $p^0_{(\mathrm{N-B})}$=0.95 and $p^0_{(\mathrm{N-B})} = 0.99$. Finally, we optimized and refined the atom positions and the cell volume by the local optimization procedures described in subsection 8.2.2.

Summary of the model generation

Using the five different general approaches described above, about 200 structure models have been generated, using ten particular modeling procedures: Each of these procedures contained several parameters, and each was followed by four local optimizations procedures as described in subsection 8.2.2. The only exception were the open cluster, where constant volume minimizations did not apply, and the sol-gel process, where we always performed the second group of minimizations (constant volume followed by constant pressure). In addition, for all procedures that involved a global optimization or cooling stage we also performed these local optimizations (quenches) directly for the starting configurations of the annealing procedure, for comparison. Table 8.2 gives an overview over all the models, listing the total number of atoms involved, what kind of cooling/global optimization procedure (if any) was applied, and what specific parameters of the annealing were varied.

8.2.2 Local relaxation and structure refinement

Although at the end of each generation procedure the resulting structure already possessed the final network topology, several of these "raw" models, e.g. the models produced by the RCP procedure or the crystal-fragment based models, still exhibited a locally distorted structure. Thus, we performed in each case additional local optimizations of the energy using the conjugate gradient technique (see section 3.8). Two different potentials have been employed to calculate the potential energy, potential A, which contained only two-body terms without Coulomb contributions, and a more complex potential potential B, that contained two- and three-body as well as Coulomb terms (c. f. section 3.9). For comparison purposes, two different procedures were used for each interaction potential:

1. We proceed in two steps: First, we optimize the atom positions while keeping the simulation cell fixed (constant volume optimization), in order to remove the most egregious tensions from the system. Next, we optimize both atom positions and cell variables (constant pressure optimizations).

2. We vary atom position and cell variables concurrently to find the nearest local minimum.

This results in four different local optimization strategies, which we label I (potential A/Opt 1),II (A/2), III (B/1) and IV (B/2), respectively. We note that both potentials have been fitted to reproduce the structure and phonon spectrum of the binary end-compounds BN

Class	P	N_{atom}	ρ_0	T_0	t_{eq}	γ	Ens	N_{mod}
A	1	702	2.75	2500	10^6	$2.5 \cdot (10^{12}, 10^{11}, 10^{10})$	NVT	9
	2	702	2.75	2500	10^6	$2.5 \cdot (10^{-1}, 10^{-2}, 10^{-3})$	NVT	9
	3	702	2.75	5000, 6000, 7000	10^3	$3.0 \cdot (10^{1}, 10^{0}$	NVT	18
B	4	1144	1.54	5000, 6000, 7000	10^3	$3.0 \cdot (10^{1}, 10^{0}, 10^{-1})$	NVT	27
	5	1144	2.01	1000, 2000, 3000	10^5	$1.0 \cdot (10^{-1}, 10^{-2}, 10^{-3})$	NpT	36
	6	1144	2.01	1000, 2000, 3000	10^5	$1.0 \cdot (10^{-1}, 10^{-2}, 10^{-3})$	NVT	36
C	7	974	2.65	1500, 2500	10^6	$2.5 \cdot (10^{-1}, 10^{-2}, 10^{-3})$	NpT	18
	8	562	2.85	1500, 2500	10^6	$2.5 \cdot (10^{-1}, 10^{-2}, 10^{-3})$	NpT	18
D	9	1040	2.83	n.a.	n.a.	n.a.	n.a.	5
E	10	1300	1.57	n.a.	n.a.	n.a.	1,5.	10

Table 8.2: Details of the modelling procedures. P is the number of the procedure , introduced for later reference. N_{atom} is the number of atoms in that model. The densities ρ are given in g/cm^3 and the initial temperatures T_0 are in K. The models were kept for t_{eq} timesteps at the initial temperature T_0, before the global optimization/slow cooling began. The cooling rates γ are given in K/MCC in the MCC simulation and in K/s in the MD simulations. Similarly the equilibration times t_{eq} are given in MCC and fs for MC and MD-simulations, respectively. Ens denotes the ensemble in which the global optimizations/coolings were performed. Note, that in the NpT ensemble the external pressure was set to zero ($p_{ext} = 0$ GPa). To improve the statistics, we generated three trajectories for each set of the optimization parameters T_0, t_{eq} and γ. N_{mod} is the total number of raw models generated for the specific modelling procedure.

and Si_3N_4, and the structures of hypothetical ternary crystalline $Si_3B_3N_7$ compounds that had been optimized using ab initio methods. Furthermore, the potentials reproduce the ab initio calculations of simple molecules containing Si, B, and N.

After the local optimizations, our final step consisted of a Reverse Monte Carlo (RMC) type stochastic quench at constant volume (see section 3.8.2 for details). We chose $\lambda = 0.20$ and the structures were optimized for $5 \cdot 10^5$ MCC. Typically, the changes in the atom positions in this final refinement step were small (< 0.03 Å/atom).

8.3 Structural properties

For each of the ten modeling procedures belonging to the five classes of structure models for a-$Si_3B_3N_7$, we have analyzed various structural properties: the radial and angular distribution functions, the mean coordination numbers within the first and second neighbor spheres around the atoms, and the ring statistics. The details of the procedures/algorithms for the determination of these properties are discussed in chapter 4.1. Experimentally, direct comparisons are possible for the radial distribution function measured with X-ray and neutron scattering, for the first coordination sphere via e.g. EXAFS or NMR measurements, and for the second coordination sphere via REDOR-NMR experiments. Angular distributions are only accessible in an indirect fashion, and the same holds true for e.g. the third neighbor sphere. Finally, fingerprinting of IR/Raman data can possibly give access to information regarding the presence of various ring structures in the amorphous network. The available experimental data is summarized in table 8.3.

First, we will present the structural properties of the models, that represent the *different* classes in section 8.3.1. In the second subsection (c.f. subsection 8.3.2), we will discuss in detail the dependence of the properties of the models of each class on the specific choice of the parameters used in the generation of the models in the class.

8.3.1 Comparison of classes

In this section we compare the structural properties of those models, that are typical for each class. We show the data for those models that were optimized using the local optimization procedure IV, in which we optimized the cell

First coordination sphere			
Pair	$\overline{d}$	CN	local geometry
B-N	1.43	2.95	trig. plan.
Si-N	1.72	3.82	tetrahedr.
N-B	1.43		trig. planar
N-Si	1.72		trig. planar
N-(Si/B)	n.a.	2.95	trig. planar

Second coordination sphere			
B-B	B-Si	Si-B	Si-Si
4-5	1.4	1.8	6

ρ_{exp}	1.9 g/cm^3

Table 8.3: Summary of available experimental data, taken from references [64] [114] [167] for a-$Si_3B_3N_7$. The mean distances $\overline{d}$ are given in Å and the mean coordination numbers of the first and the second coordination spheres are dimensionless. The density ρ_{exp} is given in g/cm^3, and the local geometries describe the geometries of the first coordination spheres.

parameters and the atomic positions simultaneously, and employed interaction potential B. The reverse Monte-Carlo (RMC) data were determined from the minima *after* the local optimizations were performed. First we discuss the pair correlation functions, next we focus on the first coordination spheres and finally discuss the second coordination spheres and the ring statistics.

Pair correlation functions

Figure 8.1 shows a comparison of the X-ray and neutron pair correlation function $D_{N/X}(R)$ of the models, representing the different classes, and the experimental data, after the energy minimization and after the final RMC-fine-tuning, respectively. We find that the models agree with the general shape of the experimental function, and can associate the various peaks with well-defined atom-atom distances within the first and second neighbor spheres: 1.43 Å with B-N bond distances, 1.72 Å with Si-N bond distances, 2.44 Å with B-N-B and N-B-N distances, 2.74 Å with N-Si-N and Si-N-B distances and the shoulder at about Å with Si-N-Si distances, respectively (see also figure 8.2). Note also, that there exist additional small peaks at ≈ 3.8 and 4.2 Å. The best quantitative agreement is found for the crystal fragment (class B) and the sol-gel model (class E). We also note the fact that even after the RMC-fine tuning there exist noticeable differences between the various models, which are greater than the internal spread (c.f. subsection 8.3.2).

In figure 8.2, we show the contributions of the partial pair correlation functions $D^{AB}_{N/X}(R)$ for neutron (N) and X-ray (X) scattering experiments determined from procedures one and five after RMC-refinement. As mentioned above, the first four peaks at 1.43 Å, 1.72 Å, 2.44 Å, 2.74 Å and the shoulder at 3.1 Å can be associated with B-N distances, Si-N distances, B-B and N-(B)-N distances, Si-B and N-(Si)-N distances and finally Si-Si distances. The shallow peaks between ≈ 3.8 and 4.2 Å in the experimental pair correlation function can be associated with 3^{rd} neighbor Si-N and B-N distances, whereas the oscillations at ≈ 4.5 to 5 Å come from 4^{th} neighbor N-N and Si-N distances. Note also that there exist small peaks in the B-B, Si-B, Si-B, Si-Si and N-N partial pair correlation functions at ≈ 2.05, 2.2 and 2.6 Å, which indicate the existence of edge sharing polyhedra in the structural models (see below for further discussion.). We have summarized the different peak assignments in table 8.4. The differences in the models of the different classes can be most easily seen in the intensities of the B-B, Si-B and the B-N partial pair correlation functions depicted in figure 8.2 for models belonging to classes A and B. The difference of the intensities of the peaks at 2.5 Å and 2.75 Å belonging to the B-B and Si-B partial pair correlation functions, shows the difference in the second coordination sphere of the models A and B. The models of class A (melt model, black curves) contain more Si-B next-nearest neighbor pairs than the models of class B. On the other hand, there exist more B-B and Si-Si next-nearest neighbor pairs in the models of class B (gray curves) than in class A. Note also, that in the models of class E more Si-Si/B-B next-nearest neighbor pairs exist than the models of found in class A.

Local coordinations and angular distribution functions

Table 8.5 shows the mean coordination numbers and the distribution of the coordination

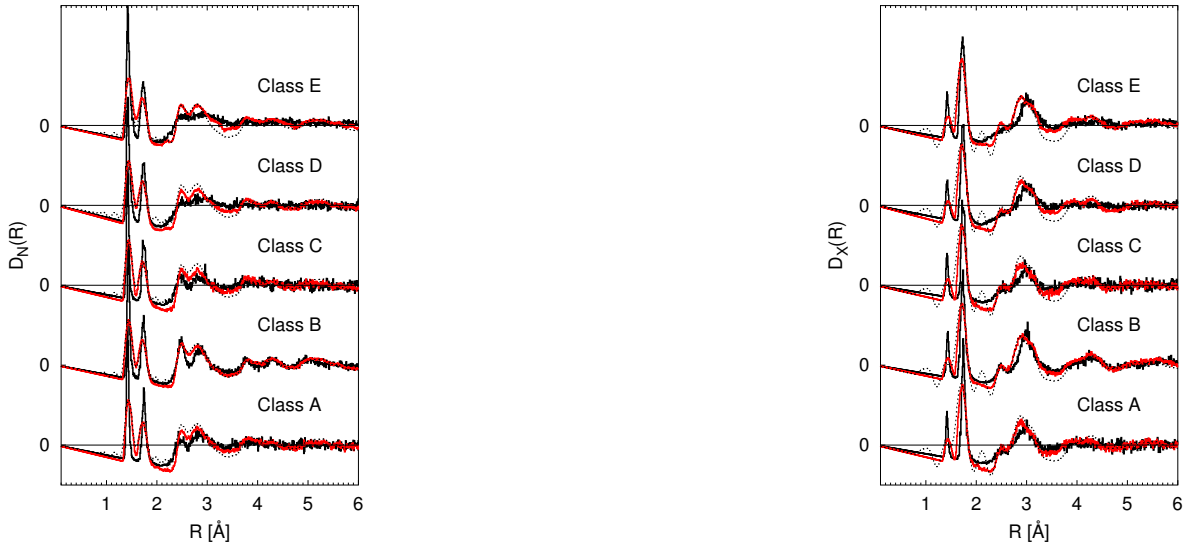

Figure 8.1: Neutron (left) and X-ray (right) diffraction pair correlation functions $D_{N/X}(R)$ for the models of the classes A-E, after thermal treatment and after local optimizations. The gray curves are the pair correlation functions after the RMC-refinement, the full black lines show the pair correlations functions after the local optimizations and the dashed curves are the experimental pair correlation functions. The distances R are given in Å. Note that the differences of intensities of the peaks are due to the the different scattering factors of the pairs of atom, that contribute to that peak.

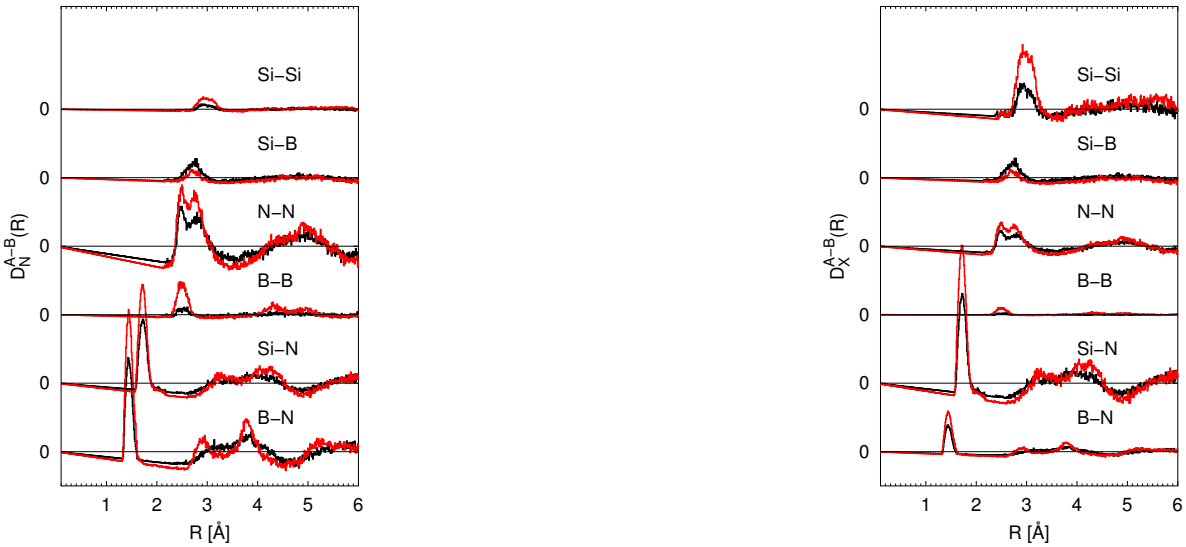

Figure 8.2: Contributions of the partial pair correlation functions $D_{N/X}^{AB}(R)$ (A, B=Si, B and N) to the pair correlation functions $D_{N/X}(R)$ for models of procedure 1, representing class A (black curves) and procedure 5, representing class B (grey curves). The partial pair correlation functions were calculated from the refined models, after slow cooling and local optimization. Left: pair correlation functions from neutron scattering, right: X-ray scattering. Note that the differences of intensities of the peaks are due to the the different scattering factors of the pairs of atom, that contribute to that peak.

Peak	Pairs/Distances
1.43	B-N(I) 1.43
1.72	Si-N(I) 1.72
2.50	N-N(I) 2.50,B-B(I) 2.50
2.77	N-N(II) 2.71,Si-B(I) 2.75
3.00	B-N(II) 2.90, Si-Si(I) 3.0
3.80	B-N(III) 3.80
4.20	Si-N(II) 4.20, B-B (IV) 4.25
5.20	N-N(III) 5.2, B-B(V) 5.0

Table 8.4: Peak positions in the experimental pair correlation functions of a-$Si_3B_3N_7$ and the corresponding atom-atom distances, that are determined in this work. All distances are given in Å. We have added roman numerals to those pairs that contribute to more than one peak in the experimental pair correlation function.

spheres of silicon, boron and nitrogen of the refined models. Clearly, silicon atoms are mainly fourfold coordinated, whereas boron atoms are surround by three nitrogen atoms, and nitrogen is surrounded mostly by three cations. Comparing the silicon and boron atoms, we find that boron atoms achieve their ideal coordination number of 3 more often than the silicon atoms, and that coordination defects will be more frequently found at silicon than at boron.[5] Differences between the models belonging to different classes can be found in the distribution of the nitrogen coordination spheres NSi_xB_{3-x}. For models derived from the classes A, C and D the distribution of NSi_xB_{3-x} shows a preference for NSi_2B_1- and NSi_1B_2 coordination spheres. Contrary to this observation, the models of classes B and E contain a higher percentage of NSi_3 and NB_3 coordination spheres.

Figures 8.3 show the angular distribution functions for the N-B-N, the N-Si-N and (B/Si)-N-(B/Si) angles. While all models clearly show that the dominant angles at Si, B, and N are those that correspond to a tetrahedral and trigonal coordination, respectively, we see that all models also exhibit a small peak at 90 degrees in the N-Si-N and N-B-N distributions. This indicates that a certain amount of edge connected SiN_4-tetrahedra and BN_3-triangles is present in all these models. The interatomic distances $d_{90}(\mathrm{X}-\mathrm{Y})$, with X,Y=Si or B, corresponding to these 90 degree angles can be calculated from $d^2_\phi(\mathrm{X}-\mathrm{Y}) = d^2(\mathrm{X}-\mathrm{N}) + d^2(\mathrm{Y}-\mathrm{N}) - 2\cdot d(\mathrm{Y}-\mathrm{N})\cdot d(\mathrm{X}-\mathrm{N})\cos(\phi)$, and this yields for a bonding angle $\phi(\mathrm{X}-\mathrm{N}-\mathrm{Y}) \approx 90°$, $d_{90}(\mathrm{B}-\mathrm{B}) \approx 2.02$ Å, $d_{90}(\mathrm{Si}-\mathrm{B}) \approx 2.23$ Å and $d_{90}(\mathrm{Si}-\mathrm{Si}) \approx 2.44$ Å. Since these values are close to other relevant interatomic distances, they will at most result in small shoulders of large peaks in the total pair correlation functions. Note however, that small peaks at these positions can be found in the partial pair correlation functions (see figure 8.2). The angular distribution function of boron atoms is sharper than the one for silicon and for nitrogen atoms. We also mention the good agreement between the angular distribution function of the models before and after the RMC refinement.

Second coordination spheres and ring statistics

One of the great advantages of a computer model of an amorphous material is the ability to exactly determine the local coordination of any atom beyond the first neighborhood and other characteristics such as the distribution of ring sizes. Table 8.6 shows the distributions of the second coordination spheres of the atoms for the five different model classes. We find, that even though all models yielded similar values for the first coordination sphere and similar results for the angular distribution functions, the second (cation-cation) coordination spheres demonstrate the differences between the model classes. As mentioned above, the models corresponding to classes B and E contain more Si-Si and in particular B-B next-nearest neighbor contacts than all other models, thus being in best agreement with experiment. The ring size distributions of the different models are listed in table 8.7. We note that there exist about 7-10 % of 4-rings in the models generated in classes A-C and about 12-14 % in classes D and E. The existence of these 4-rings was already suggested by the small peaks at $\approx 90°$ in the angular

[5] The models representing the classes D and E contain ≈ 10-15 % fourfold coordinated boron atoms. However this effect is a combination of an effect of the interaction potential and the insufficient equilibration in the generation of the raw models.

Class	Si	SiN_4	SiN_3	SiN_5	B	BN_3	BN_4	BN_2
A	3.96	0.94	0.05	0.01	3.03	0.97	0.03	0.00
B	3.78	0.76	0.23	0.01	3.06	0.91	0.07	0.02
C	3.94	0.92	0.07	0.01	3.02	0.97	0.02	0.01
D	3.83	0.81	0.17	0.01	3.14	0.85	0.14	0.01
E	3.63	0.62	0.37	0.01	3.17	0.81	0.18	0.01

(a) Si/B

Class	N-Si	N-B	NSi_3B_0	NSi_2B_1	NSi_1B_2	NSi_0B_3
A	1.70	1.30	0.10	0.48	0.31	0.02
B	1.62	1.31	0.33	0.13	0.13	0.26
C	1.69	1.29	0.16	0.39	0.30	0.07
D	1.64	1.34	0.16	0.33	0.28	0.08
E	1.56	1.36	0.14	0.28	0.24	0.12

(b) N

Table 8.5: Mean coordination numbers and distribution of coordination spheres for silicon and boron (top) and nitrogen (bottom) for the refined models. In the upper table, columns labelled Si/B contain the mean coordination number of silicon and boron, respectively. The data in the columns labelled $X\mathrm{N}_y$ are the fractions of $X\mathrm{N}_y$ (X=Si,B) building units. In the lower table, columns labelled N-Si/N-B contain the mean number of silicon and boron atoms surrounding a nitrogen atom. The columns labelled $\mathrm{NSi}_x\mathrm{B}_y$ contain the fraction of $\mathrm{NSi}_x\mathrm{B}_y$ building units found in the structures. Note that the distribution of $\mathrm{NSi}_x\mathrm{B}_y$ was calculated for all nitrogen atoms but only the data for threefold coordinated nitrogen is shown.

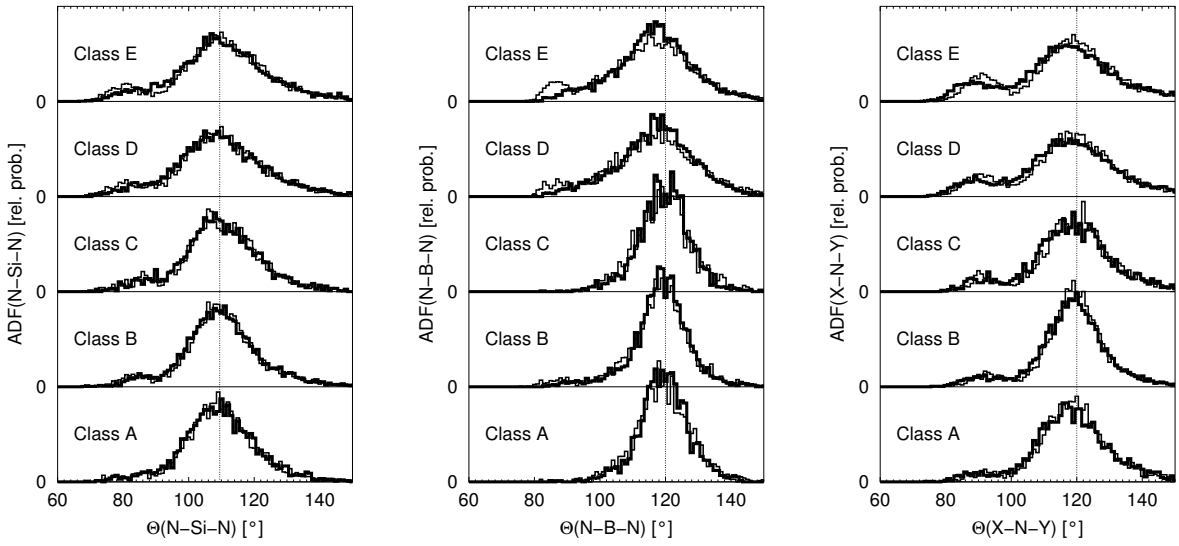

Figure 8.3: Angular distribution functions (ADF) of the first coordination spheres of silicon (left), boron (middle) and nitrogen (right) atoms for the models representing the classes A-E. The thick black curves are calculated from the RMC-refined models, whereas the thin black curves are from the locally optimized models, both calculated from 'cooled' models. The dotted vertical lines are at positions of bonding angles that correspond to tetrahedral (109.47°)(left) and trigonal planar (120°)(middle and right) coordination geometries.

Model	Si	B	N	f_{abc}
A	0	2	2	0.06
	1	1	2	0.61
	2	0	2	0.37
B	0	2	2	0.22
	1	1	2	0.28
	2	0	2	0.50
C	0	2	2	0.07
	1	1	2	0.48
	2	0	2	0.50
D	0	2	2	0.26
	1	1	2	0.58
	2	0	2	0.17
E	0	2	2	0.30
	1	1	2	0.57
	2	0	2	0.12

Model	Si	B	N	f_{abc}
A	0	2	2	0.05
	1	1	2	0.59
	2	0	2	0.38
B	0	2	2	0.19
	1	1	2	0.30
	2	0	2	0.50
C	0	2	2	0.03
	1	1	2	0.45
	2	0	2	0.55
D	0	2	2	0.21
	1	1	2	0.59
	2	0	2	0.20
E	0	2	2	0.24
	1	1	2	0.60
	2	0	2	0.16

Table 8.8: Average fraction f_{abc} of occurences of 4-rings with the specified compositions. Note, that the fractions do not sum up to one due the averaging. The numbers are the probabilities of selecting a ring with composition $Si_aB_bN_c$ from rings of size 4, given that a ring of size 4 has been found. The left table shows the data calculated from the optimized models and right data from the refined models.

Class	Si	B	N	%
A	0	3	3	0.01
	1	2	3	0.20
	2	1	3	0.58
	3	0	3	0.20
B	0	3	3	0.34
	1	2	3	0.13
	2	1	3	0.13
	3	0	3	0.40
C	0	3	3	0.01
	1	2	3	0.26
	2	1	3	0.44
	3	0	3	0.28
D	0	3	3	0.05
	1	2	3	0.27
	2	1	3	0.40
	3	0	3	0.27
E	0	3	3	0.10
	1	2	3	0.33
	2	1	3	0.34
	3	0	3	0.23

Model	Si	B	N	%
A	0	3	3	0.01
	1	2	3	0.21
	2	1	3	0.58
	3	0	3	0.20
B	0	3	3	0.35
	1	2	3	0.13
	2	1	3	0.14
	3	0	3	0.38
C	0	3	3	0.02
	1	2	3	0.27
	2	1	3	0.44
	3	0	3	0.27
D	0	3	3	0.06
	1	2	3	0.28
	2	1	3	0.40
	3	0	3	0.26
E	0	3	3	0.11
	1	2	3	0.34
	2	1	3	0.33
	3	0	3	0.23

Table 8.9: Average fraction f_{abc} of occurences of 6-rings. Note, that fractions f_{abc} do not sum up to one due to the averaging. The numbers are the probabilities of selecting a ring with composition $Si_aB_bN_c$ from rings of size 6, given that a ring of size 6 has been found. The left table shows the data calculated from the optimized models and right data from the refined models.

Class	Si-Si	Si-B	B-B	B-Si
A	3.81	3.99	1.96	3.99
B	5.66	1.39	4.64	1.39
C	4.24	3.32	2.54	3.32
D	4.17	3.18	2.84	3.18
E	3.79	2.76	3.29	2.76
Exp	6	1.8	4-5	1.4

Table 8.6: Mean coordination numbers of the second coordination spheres of silicon and boron atoms for the refined models representing classes A-E.

distribution functions and in the small prepeaks in the partial pair correlation functions. Note that no preference for edge-sharing between two SiN_4-tetrahedra over edge-sharing between an SiN_4 tetrahedron and a BN_3 triangles can be observed in the distribution of the compositions of four-membered rings (c.f. table 8.8). Furthermore, no rings exceeding a size of 16 atoms exist in the structures. The differences between model classes can again be detected in the higher fraction of six-membered rings found in the structures of class B (see below). These models were derived from the crystal fragment model and thus contained a considerable number of borazene rings (B_3N_3). These borazene rings are still present in the structures of class B. Table 8.9 shows the distribution of the compositions of six-membered rings. Quite remarkably the models of class B contain $\approx$ 40 % B_3N_3 and Si_3N_3 rings, clearly showing that a considerable part of the initial structure has remained intact. Finally, the models derived from class E contain fewer six-membered rings than model generated in class B, but the relative amount of borazene rings in class E models is considerably higher, than the corresponding fraction of borazene rings in the models of classes A, C and D.

8.3.2 Comparison of classes and procedures

In the previous subsections, we have presented and compared the results for typical models of each class for the optimized and the refined models. Now we are going to focus on each class separately, and analyze the different procedures involved. We have to address four different aspects: influence of specific modeling parameters if present, parameters of the global optimization if performed, effect of the two potentials used for the refinement and energy relaxation, and the effect of performing only a constant pressure local minimization or a combination of constant volume followed by constant pressure minimization. We present our results for the models determined from the local optimizations only, since the RMC-refinement procedure does not change the structural properties significantly.

Class	$n=4$	$n=6$	$n=8$	$n=10$	$n=12$
A	0.06	0.27	0.39	0.26	0.02
B	0.08	0.41	0.32	0.15	0.04
C	0.08	0.27	0.37	0.24	0.03
D	0.13	0.24	0.36	0.23	0.04
E	0.16	0.27	0.31	0.19	0.05

(a) Optimized

Class	$n=4$	$n=6$	$n=8$	$n=10$	$n=12$
A	0.05	0.28	0.39	0.27	0.02
B	0.06	0.41	0.32	0.16	0.04
C	0.07	0.27	0.37	0.25	0.04
D	0.10	0.24	0.36	0.25	0.05
E	0.12	0.27	0.31	0.21	0.06

(b) Refined

Table 8.7: Ring size distributions of rings of size n containing silicon, boron and nitrogen atoms. The numbers in the columns labelled n are the fractions of rings of size n for each class. The upper table contains the data for the optimized models and the lower table contains the data for the refined models.

We have found that the effect of the choice of potential for the final local optimizations is the same for all procedures, and does not correlate with the other choices of optimization parameters or influence the comparison between two procedures, except for those procedures, that employed very fast cooling. Thus, all the comparison data we show below are for calculations with the more complex potential B. We have performed these comparisons also with potential A, of course, and the various trends are the same as for potential B (see appendix B.1 for details of the topological properties of

the models for the different local optimizations and refinements.).

Regarding the question of performing only one constant pressure minimization or a combination of constant volume followed by constant pressure, we found that the effect is most pronounced for those procedures where neither a global optimization nor a slow cooling stage had been included. In these latter cases, we find that only performing constant pressure minimizations right away led to somewhat lower densities than first allowing the system to remove extreme tensions by constant volume minimizations.

For the RCP model, we are not going to present a specific analysis. The only parameters that can be varied are those in the specific modeling algorithm (no global optimization stage present). A detailed analysis of the influence of the various parameters for the RCP model has already been given (see [67] and chapters 5 and 7) for several example systems such as a-SiO_2, a-Si_3N_4, and amorphous Si/O/N. Similarly, for the sol-gel model, and a detailed analysis of the many model parameters and possible sub-models that can be constructed within the context of the sol-gel model would go beyond the purview of this chapter, and is presented in chapter 6.

Class A: Cooling-from-melt models

Figure 8.4 shows the pair correlation functions for the three procedures 1 (MD), 2 (MC), and 3 (GO), plus the outcome of the direct application of the conjugate gradient minimizations to the structures equilibrated at 2500 K. The comparison of the pair correlation functions of the MC and MD cooling using comparable cooling rates shows no difference between these methods. We again find the peaks at 1.43 Å and 1.72 Å resembling B-N and Si-N interatomic distances. Note that these peaks are slightly wider for faster cooling. Furthermore, within each procedure, slower cooling leads to more pronounced peaks at $\approx$ 2.4 and 2.74 Å. The pair correlation functions are rather featureless for distances longer than 3.5 Å. Finally, quenching the (at 2500 K) equilibrated models, leads to pair correlation functions that are similar to the one calculated for models that were rapidly cooled and locally optimized.

Each of the three procedures was performed for three different cooling rates, with the global optimization simulated annealing, in addition, starting from three very high initial temperatures. Fast cooling leads to stronger deviations from the ideal coordination numbers three and four for boron and silicon, respectively. Additionally, we find for the MC and MD cooling procedures, that higher cooling rates lead to the existence of a higher fraction of four-membered rings. Finally, no clear dependence of the mean coordination numbers of second coordination spheres on either T_0 or γ can be deduced from our data.

Class B: Crystal fragment models

In this section, we analyze the models derived from the crystal fragment model by procedures 4, 5 and 6. Within each procedure, we investigate both the dependence on the initial temperature T_0 at which the systems were equilibrated and on the cooling rates employed in the cooling process.

Figure 8.5 shows the pair correlation function for the three procedures 4, 5 and 6 for different initial temperatures and cooling rates, together with the direct minimization for each initial density. The models obtained from a slow cooling process that started after the system had been 'equilibrated' at a low temperature (T_0 = 2000 K and 1000 K), exhibit a well structured pair correlation function. These pair correlation functions contain all peaks up to $\approx$ 5 Å, that have already been discussed in section 8.3.1 and summarized in table 8.4. However, keeping the system at 2000 K or 3000 K prior to cooling leads to significant differences in the pair correlation functions of the models, obtained after cooling. For the NPT-simulations (middle part of figure 8.5), the pair correlation functions become featureless at distances $R > 3.5$ Å for the two slowest cooling rates, if the system was equilibrated at 2000 K, and for all cooling rates, if the system was kept at 3000 K prior to cooling. In the NVT-simulations, the lack of features at distances R > 3.5 Å can be found for the initial temperature T_0 = 3000 K. For the global optimizations, we find similar results. Note that the cooling rates employed in the global opti-

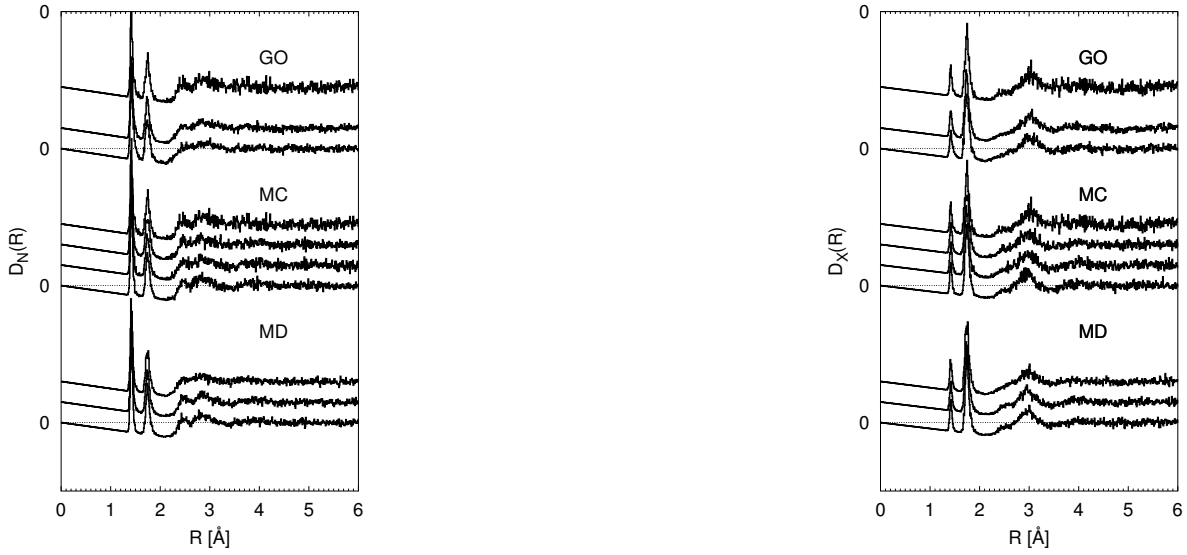

Figure 8.4: Pair correlation functions for neutron (left) and X-ray (right) scattering calculated from optimized models of class A. The pair correlation functions that are labelled with MD/MC are obtained from optimized models after MD/MC cooling with different cooling rates. Similarly GO refers to the global optimizations. For each procedure, we show from bottom to top, the data for lowest cooling rate, the medium cooling rate and the fastest cooling rates. The fourth curve within each section shows the pair correlation functions of those models that were obtained by locally optimizing the starting configurations of each procedure. For the MC and MD models the structures were equilibrated at T_0 = 2500 K and the GO section shows the data for a system heated to 7000K. Curves are shifted for clarity.

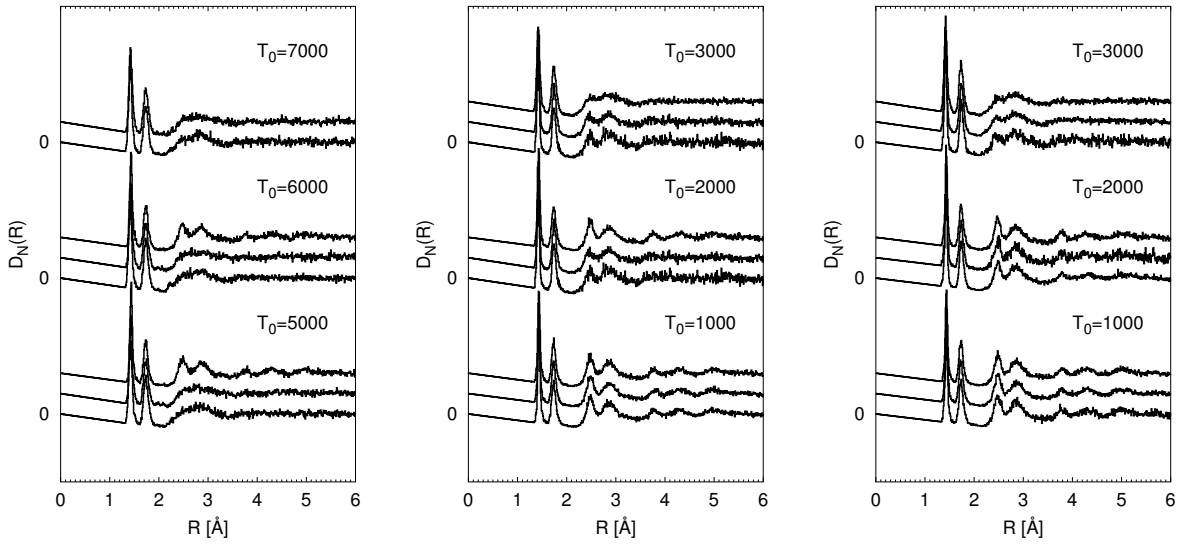

Figure 8.5: Neutron scattering pair correlation functions calculated from the models of class B (crystal fragments). Left: Global optimization, middle NPT-MC cooling and right NVT-MC cooling procedure. For each procedure, we show the data for the locally optimized models after the cooling. We distinguish, for each procedure, between the initial temperatures T_0 (given in K inside the figure), and the cooling rates γ, that were employed in the cooling procedures. For a given initial temperatures T_0, we show from bottom to top the data for the slowest, the medium and the fastest cooling rates. Curves are shifted for clarity.

P	T_0	γ	Si-N	B-N	N-Si	N-B	Si-Si	Si-B	B-B	B-Si
1	2500	0	3.95	3.08	1.69	1.32	3.82	3.85	2.14	3.85
1	2500	1	3.97	3.07	1.70	1.31	3.84	3.91	2.08	3.91
1	2500	2	3.96	3.06	1.70	1.31	3.79	3.98	2.06	3.98
1	2500	3	3.97	3.02	1.70	1.30	3.81	3.99	1.96	3.99
2	2500	0	3.85	3.15	1.65	1.35	3.74	3.90	2.31	3.90
2	2500	1	3.94	3.10	1.69	1.33	3.70	4.05	2.03	4.05
2	2500	2	3.95	3.07	1.69	1.32	3.67	4.02	2.03	4.02
2	2500	3	3.97	3.05	1.70	1.31	3.72	4.08	1.97	4.08
3	0	0	3.85	3.15	1.65	1.35	3.74	3.90	2.31	3.90
3	5000	1	3.87	3.12	1.66	1.34	3.79	3.90	2.27	3.90
3	5000	2	3.92	3.14	1.68	1.35	3.76	3.81	2.31	3.81
3	6000	1	3.85	3.17	1.65	1.35	3.75	3.89	2.36	3.89
3	6000	2	3.91	3.18	1.68	1.36	3.70	3.91	2.27	3.91
3	7000	1	3.86	3.15	1.66	1.35	3.72	3.83	2.33	3.83
3	7000	2	3.91	3.18	1.68	1.37	3.90	3.75	2.47	3.75

Table 8.10: Coordination numbers of the first and second coordination spheres of the models of class A. The columns labelled Si-N and B-N contain the mean coordination numbers of silicon and boron atoms. Similarly, columns labelled N-Si and N-B contain the average number of silicon and boron atoms surrounding a nitrogen atom in its first coordination sphere. The mean number of next-nearest silicon and boron atoms around a silicon atom are given in the columns labelled Si-Si and Si-B and the mean number of next-nearest silicon and boron atoms around a boron atom can be found in columns B-Si and B-B. P is the procedure used in the generation of these models. T_0 is the temperature (in K) at which the structures were thermalized. γ=0,1,2,3 refer to results of the local optimizations with no cooling, fast, medium and slow cooling, respectively.

P	T_0	γ	$n=4$	$n=6$	$n=8$	$n=10$	$n=12$
1	2500	0	0.09	0.23	0.41	0.24	0.03
1	2500	1	0.09	0.25	0.38	0.25	0.04
1	2500	2	0.07	0.27	0.38	0.26	0.02
1	2500	3	0.06	0.27	0.39	0.26	0.02
2	2500	0	0.04	0.24	0.43	0.27	0.02
2	2500	1	0.08	0.27	0.37	0.27	0.02
2	2500	2	0.07	0.27	0.38	0.25	0.03
2	2500	3	0.05	0.31	0.38	0.24	0.02
3	0	0	0.04	0.24	0.43	0.27	0.02
3	5000	1	0.04	0.24	0.43	0.26	0.02
3	5000	2	0.11	0.23	0.36	0.26	0.03
3	6000	1	0.05	0.23	0.43	0.27	0.02
3	6000	2	0.11	0.24	0.36	0.25	0.02
3	7000	1	0.08	0.24	0.41	0.25	0.03
3	7000	2	0.12	0.24	0.37	0.25	0.03

Table 8.11: Distribution of ring size n calculated from the models that were generated in class A. P is the procedure used in the generation of these models. T_0 is the temperature (in K) at which the structures were thermalized. γ=0,1,2,3 refer to results of the local optimizations with no cooling, fast, medium and slow cooling, respectively.

mizations were an order of magnitude larger than the ones employed in the NPT and NVT cooling schemes. Heating the system to 5000 K or 6000 K followed by rapid cooling results in still well structured pair correlation functions.

The data for the first coordination spheres of the models obtained via global optimizations and, to a lesser extent of those obtained via slow MC cooling, show similarities to the data derived from the models obtained by melt cooling.(Table 8.12) Slower cooling leads to smaller deviations of the coordination numbers of silicon and boron from their ideal values 3 and 4, respectively. We also mention that nitrogen atoms are always threefold coordinated as in the melt models, and that the nitrogen coordination does not show any preference for N-B coordination over N-Si coordination. However the second coordination spheres reveal differences among the models and shows the dependence of the structural properties on the thermal history. We find a decrease of the number of Si-Si and B-B next nearest neighbors with decreasing cooling rates γ for all models that were heated to temperatures $T \geq 3000$ K. For the slowest cooling rates (procedures 5 and 6), we also note that these coordination numbers of the second coordination spheres approach the values found for the models determined from melt processing. Noticably, this approach to the 'melt-values' is *not* found for the models, that were only heated to 1000 K initially or were cooled very fast from 2000K. In this context, we would also like to point out, that this mixing of Si and B cations in the overall structure is only visible for $T_0 = 3000$ K in the NVT cooling simulations in contrast to the NPT simulations, were this mixing sets in for models heated to 2000 K and cooled slowly. The analysis of the ring statistics (c.f. table 8.13), again shows the (dis)similarities to the models obtained from the melt procedure. Fast cooling leads to a higher fraction of four-membered rings in all models, regardless of their thermal treatment. The differences between the models become clearer, if we focus on the fraction of six-membered rings. The fraction of six-membered rings decreases from a high value of ≈ 40 % to the values of ≈ 25 %, once we heat the system to temperatures above 2000 K and keep it at that temperature for a sufficiently long time. Note that the breakdown of 'ring-ordering' is closely correlated with the increase in the number of Si-B next nearest neigbors. Finally we note that these effects are visible in the NVT-simulations only, if we heat the system to 3000 K.

Cluster models

Figure 8.6 shows the pair correlation function for the open cluster and the periodically repeated cluster interior, together with the corresponding quench results. Again, we find the same peaks in the pair correlation function as in the models derived from the melt-cooling procedures and the crystal fragment models. Note, however, that the first two peaks at 1.43 and 1.72 Å in the pair correlation function of the open cluster models, are substantially broader than the ones found for the periodically repeated interior of the cluster because of surface effects. Concerning the effects of choice of the initial temperatures, the second double peak in the pair correlation functions of the open cluster models are more blurred than the corresponding peaks in the periodically repeated interior of the cluster. For the latter models, the splitting of that second double peak is much more pronounced, for slower cooling rates. Returning to surface effects, we show in figure 8.7 the dependence of the density of the open cluster models on the distance from the center of gravity of the cluster. Note that the cluster radius is ≈ 12 Å for the equilibration at 1500 K and ≈ 11 Å at 2500 K, and the densities are around 2.75 g/cm^3.

The structural properties of the cluster based models depend on the process parameters that were employed in the generation of these models in a similar manner as do the structural properties of the crystal fragment models (Table 8.14). Silicon atoms are mainly tetrahedrally coordinated by nitrogen, boron and nitrogen atoms are mainly trigonally planar coordinated by nitrogen, and silicon or boron, respectively. Slower cooling leads to an increased coordination number of silicon and faster cooling leads to more BN_4 units. The second coordination spheres of the cluster-based models do not show a preference for a high number of Si-Si *and* B-B next nearest neighbors over Si-B and B-Si nearest neighbor,

P	T_0	γ	Si-N	B-N	N-Si	N-B	Si-Si	Si-B	B-B	B-Si
4	0	0	3.78	3.17	1.62	1.36	5.76	1.34	5.00	1.34
4	5000	1	3.76	3.12	1.61	1.34	5.71	1.27	4.90	1.27
4	5000	2	3.79	3.06	1.62	1.31	5.37	1.49	4.13	1.49
4	5000	3	3.83	2.98	1.64	1.28	4.15	2.70	2.64	2.70
4	6000	1	3.77	3.14	1.62	1.34	5.65	1.35	4.79	1.35
4	6000	2	3.79	3.04	1.63	1.30	5.12	1.66	3.88	1.66
4	6000	3	3.80	2.97	1.63	1.27	3.71	3.01	2.29	3.01
4	7000	1	3.74	3.11	1.61	1.33	5.47	1.29	4.69	1.29
4	7000	2	3.79	3.04	1.62	1.30	4.91	1.88	3.64	1.88
4	7000	3	3.76	2.99	1.61	1.28	3.52	3.17	2.13	3.17
5	1000	1	3.82	3.08	1.64	1.32	5.76	1.42	4.70	1.42
5	1000	2	3.83	3.06	1.64	1.31	5.77	1.44	4.60	1.44
5	1000	3	3.83	3.07	1.64	1.32	5.78	1.41	4.67	1.41
5	2000	1	3.85	3.03	1.65	1.30	5.64	1.52	4.39	1.52
5	2000	2	3.94	3.04	1.69	1.31	3.91	3.65	2.21	3.65
5	2000	3	3.97	3.03	1.70	1.30	3.92	3.83	2.11	3.83
5	3000	1	3.92	2.99	1.68	1.28	4.79	2.57	3.02	2.57
5	3000	2	3.94	3.04	1.69	1.31	3.91	3.65	2.21	3.65
5	3000	3	3.97	3.03	1.70	1.30	3.92	3.83	2.11	3.83
6	1000	1	3.79	3.07	1.62	1.31	5.69	1.34	4.68	1.34
6	1000	2	3.80	3.05	1.63	1.30	5.70	1.33	4.66	1.33
6	1000	3	3.83	3.00	1.65	1.29	5.71	1.40	4.46	1.40
6	2000	1	3.84	3.01	1.64	1.29	5.63	1.41	4.41	1.41
6	2000	2	3.90	2.97	1.68	1.27	5.25	2.04	3.67	2.04
6	2000	3	3.92	2.96	1.68	1.27	5.16	2.22	3.45	2.22
6	3000	1	3.88	2.99	1.66	1.28	4.57	2.57	2.89	2.57
6	3000	2	3.89	2.96	1.67	1.27	3.83	3.40	2.08	3.40
6	3000	3	3.91	3.01	1.68	1.29	3.61	3.73	1.98	3.73

Table 8.12: Coordination numbers of the first and second coordination spheres of the models of class B. The columns labelled Si-N and B-N contain the mean coordination numbers of silicon and boron atoms. Similarly, columns labelled N-Si and N-B contain the average number of silicon and boron atoms surrounding a nitrogen atom in its first coordination sphere. The mean number of next-nearest silicon and boron atoms around a silicon atom are given in the columns labelled Si-Si and Si-B and the mean number of next-nearest silicon and boron atoms around a boron atom can be found in columns B-Si and B-B. P is the procedure used in the generation of these models. T_0 is the temperature (in K) at which the structures were thermalized. γ=0,1,2,3 refer to results of the local optimizations with no cooling, fast, medium and slow cooling, respectively.

P	T_0	γ	$n=4$	$n=6$	$n=8$	$n=10$	$n=12$
4	0	0	0.09	0.42	0.34	0.13	0.03
4	5000	1	0.09	0.38	0.35	0.14	0.03
4	5000	2	0.16	0.26	0.30	0.19	0.07
4	5000	3	0.17	0.28	0.28	0.15	0.06
4	6000	1	0.10	0.35	0.35	0.15	0.04
4	6000	2	0.18	0.24	0.29	0.19	0.08
4	6000	3	0.18	0.25	0.26	0.20	0.07
4	7000	1	0.12	0.31	0.32	0.18	0.05
4	7000	2	0.16	0.23	0.29	0.20	0.09
4	7000	3	0.17	0.26	0.27	0.17	0.08
5	1000	1	0.08	0.42	0.32	0.14	0.03
5	1000	2	0.08	0.42	0.32	0.14	0.03
5	1000	3	0.08	0.41	0.32	0.15	0.04
5	2000	1	0.09	0.39	0.31	0.16	0.04
5	2000	2	0.10	0.28	0.35	0.23	0.04
5	2000	3	0.08	0.33	0.34	0.21	0.04
5	3000	1	0.12	0.28	0.33	0.19	0.06
5	3000	2	0.10	0.28	0.35	0.23	0.04
5	3000	3	0.08	0.33	0.34	0.21	0.04
6	1000	1	0.08	0.41	0.33	0.14	0.04
6	1000	2	0.09	0.42	0.32	0.14	0.03
6	1000	3	0.08	0.42	0.32	0.14	0.04
6	2000	1	0.10	0.40	0.30	0.15	0.04
6	2000	2	0.09	0.40	0.31	0.15	0.03
6	2000	3	0.09	0.41	0.31	0.14	0.03
6	3000	1	0.15	0.27	0.30	0.19	0.06
6	3000	2	0.12	0.29	0.32	0.19	0.06
6	3000	3	0.12	0.34	0.31	0.19	0.04

Table 8.13: Distribution of ring size n calculated from the models that were generated in class B. P is the procedure used in the generation of these models. T_0 is the temperature (in K) at which the structures were thermalized. γ=0,1,2,3 refer to results of the local optimizations with no cooling, fast, medium and slow cooling, respectively.

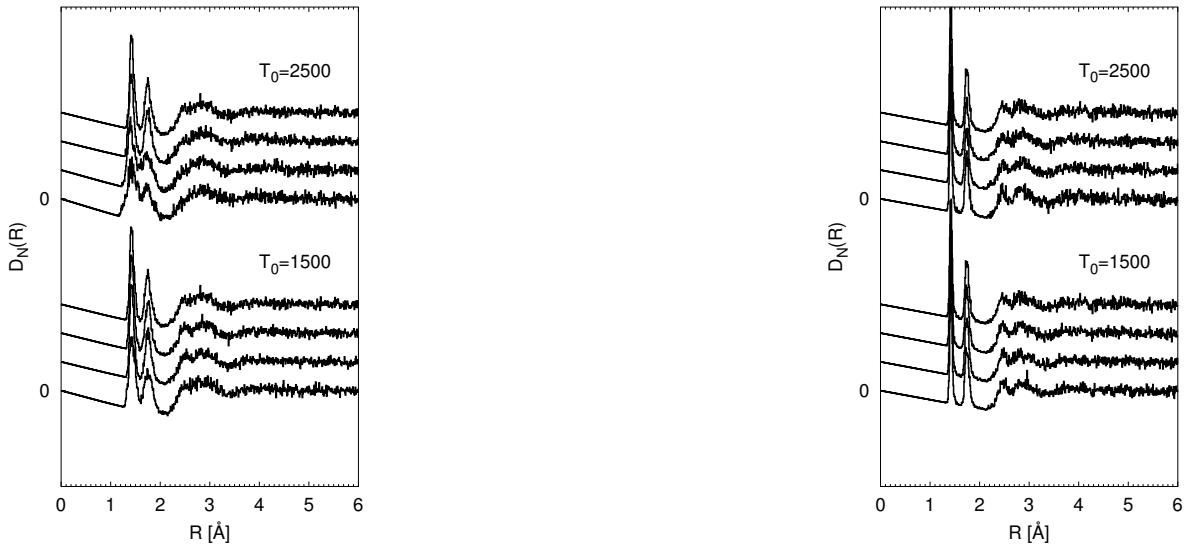

Figure 8.6: Neutron pair correlation functions calculated from the models of class C (cluster-derived models). Left: Open cluster model, right: periodically repeated interior of cluster. Each plot contains sets of pair correlation functions of those models that were equilibrated at the initial temperatures T_0 (given in K inside the figure) and cooled to 0 K using different cooling rates. Within each set we show from bottom to top the pair correlation functions of the models after slow, medium, fast cooling rate, and and no cooling had been performed prior to the local optimization.

but only show an increased number of Si-Si next nearest neighbors. This higher number of Si-Si next-nearest neighbor decreases however, if the system is equilibrated at 1500 K for open boundary conditions and at 2500 K followed by slow cooling for periodic boundary conditions. The analysis of the first and second coordination spheres of the open-cluster models were restricted to those atoms, that lay inside a cube of edge length $a = 2 \cdot d = 2 \cdot R_{cluster}/\sqrt{3} \approx 16.2$ Å, with the center of the cube at the center of gravity of the cluster. Here $R_{cluster}$ is the radius of the open cluster, calculated as the maximum distance any atom has from the center of gravity of the cluster. With this construction, the mean number of next nearest neighbors will already decrease due to surface effects. Searching for next nearest neighbors (at distances between 2.5 and 3.2 Å from an atom close the border of the cube ≈ 8 Å from the center of gravity of the open cluster, will lead to searches in regions of the cluster, that are $\approx 11-12$ Å away from the center of gravity of the cluster and thus in a region where possibly no atoms exist at all. Note that only 60 % of the atoms of the open cluster are included in the analysis when including this restriction. The ring statistics, especially for larger rings, will be even more prone to surface effects. Thus, we show only the data for the periodically repeated interior of the clusters in table 8.15. For these structures, we only find very small differences in the mean coordination numbers of the bulk and border region atoms. Here, we defined atoms to belong to the border region of the periodically repeated unit cell, if they had a maximum distance of 2.5 Å from the unit cell faces. Finally, we note that similar to the crystal fragment model, only those cluster based structures could be distinguished from the melt-based structures, which had been cooled rapidly or had only been relaxed at 1500 K.

Class E: Sol-Gel models

In figure 8.8 we show the X-ray and neutron scattering pair correlation functions of the models generated by procedure 1 of the sol-gel algorithms presented in chapter 6 for different choices of the local optimization strategy, together with the results of the RMC-refined models. We observe effects of the choice of the interaction potential in the intensity of the

P	T_0	γ	Si-N	B-N	N-Si	N-B	Si-Si	Si-B	B-B	B-Si
7	0	0	3.79	3.06	1.58	1.40	4.21	2.53	3.22	2.25
7	1500	0	3.84	3.03	1.72	1.31	3.72	2.96	2.36	3.19
7	1500	1	3.88	3.03	1.74	1.32	3.76	3.01	2.39	3.22
7	1500	2	3.86	3.02	1.72	1.32	3.77	2.99	2.37	3.17
7	1500	3	3.88	3.02	1.74	1.30	3.77	3.06	2.35	3.27
7	2500	0	3.70	2.90	1.70	1.23	3.33	3.08	1.65	3.46
7	2500	1	3.78	2.94	1.72	1.26	3.49	3.31	1.71	3.60
7	2500	2	3.81	2.93	1.73	1.25	3.52	3.27	1.75	3.57
7	2500	3	3.80	2.99	1.72	1.29	3.51	3.45	1.76	3.66
8	1500	0	3.98	3.05	1.70	1.31	4.29	3.38	2.57	3.38
8	1500	1	3.98	3.02	1.70	1.30	4.27	3.36	2.55	3.36
8	1500	2	3.98	3.04	1.70	1.30	4.26	3.40	2.57	3.40
8	1500	3	3.96	3.02	1.70	1.30	4.26	3.35	2.54	3.35
8	2500	0	3.91	3.08	1.68	1.32	3.77	3.72	2.15	3.72
8	2500	1	3.91	3.06	1.67	1.31	3.65	3.76	2.09	3.76
8	2500	2	3.92	3.07	1.68	1.31	3.68	3.83	2.09	3.83
8	2500	3	3.94	3.03	1.69	1.29	3.68	3.92	1.98	3.92

Table 8.14: Coordination numbers of the first and second coordination spheres of the models of class C. The columns labelled Si-N and B-N contain the mean coordination numbers of silicon and boron atoms. Similarly, columns labelled N-Si and N-B contain the average number of silicon and boron atoms surrounding a nitrogen atom in its first coordination sphere. The mean number of next-nearest silicon and boron atoms around a silicon atom are given in the columns labelled Si-Si and Si-B and the mean number of next-nearest silicon and boron atoms around a boron atom can be found in columns B-Si and B-B. P is the procedure used in the generation of these models. T_0 is the temperature (in K) at which the structures were thermalized. γ=0,1,2,3 refer to results of the local optimizations with no cooling, fast, medium and slow cooling, respectively.

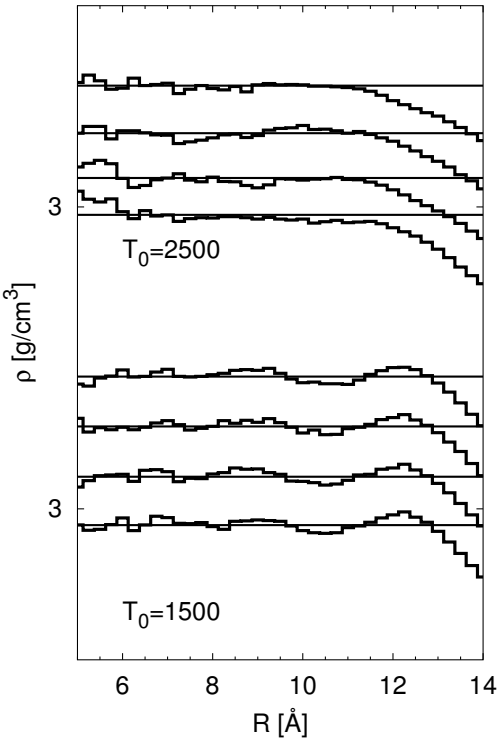

Figure 8.7: Dependence of the densities of the open cluster models on the distance from the center of gravity of the cluster. For each initial temperature T_0 (given in K inside the figure), we show the data for locally optimized models after slow, medium and fast cooling as well as without cooling (from bottom to top). Curves are shifted for clarity.

peak at ≈ 2.45 Å of the second double peak in the pair correlation functions. However the pair correlation functions of the RMC-refined models are barely distinguishable from each other and agree with the experimental data fairly well. Note also that the number of initial aggregation sites does not influence the pair correlation function.

These models show a significant percentage of SiN_3 and BN_4 building units, resulting in rather low silicon mean coordination numbers and rather high boron coordination numbers compared to the experimental data (Table 8.16). The second coordination sphere of these models show a high number of B-B and Si-Si next nearest neighbors , which is an effect of the kinetic factor $p^0_{(\mathrm{N-B})} = 0.99$, which induces a higher bonding probability of free nitrogen atoms to boron than to silicon atoms, as already mentioned in section 8.2.1. Note, that a high number of like cation next nearest neighbors remains visible, if we relax these sol-gel models via NPT-MC simulations at temperatures below 1000 K (see section 6.3.1 in chapter 6). Finally, we observe no preferred existence of six-membered rings in the sol-gel modelled structures (table 8.17).

P	T_0	γ	$n=4$	6	8	10	12
7	0	0	0.07	0.26	0.28	0.27	0.09
7	1500	0	0.08	0.27	0.28	0.24	0.10
7	1500	1	0.09	0.26	0.29	0.24	0.09
7	1500	2	0.08	0.27	0.31	0.24	0.08
7	1500	3	0.08	0.28	0.32	0.23	0.08
7	2500	0	0.13	0.22	0.27	0.25	0.09
7	2500	1	0.12	0.24	0.32	0.23	0.07
7	2500	2	0.12	0.26	0.29	0.22	0.09
7	2500	3	0.10	0.27	0.32	0.22	0.07
8	1500	0	0.09	0.27	0.37	0.24	0.03
8	1500	1	0.08	0.27	0.38	0.24	0.03
8	1500	2	0.08	0.28	0.36	0.25	0.03
8	1500	3	0.08	0.27	0.37	0.24	0.03
8	2500	0	0.13	0.28	0.33	0.22	0.04
8	2500	1	0.12	0.25	0.35	0.24	0.04
8	2500	2	0.10	0.27	0.34	0.24	0.04
8	2500	3	0.08	0.29	0.35	0.26	0.03

Table 8.15: Distribution of ring size n calculated from the models that were generated in class C. P is the procedure used in the generation of these models. T_0 is the temperature (in K) at which the structures were thermalized. γ=0,1,2,3 refer to results of the local optimizations with no cooling, fast, medium and slow cooling, respectively.

8.4 Bulk Properties

8.4.1 Density and energy

As is well known from models for other amorphous compounds forming covalent networks such as a-SiO_2, one of the most difficult quantities to model is the overall density.[169, 20] The reason for this can be found both in the intrinsic faults of the models regarding structure design and energy function employed, and in the hidden features of the experimental structure in the nearly "inaccessible" range of 1/2 - 2 nm, which could not be taken into account during the modeling process. On this

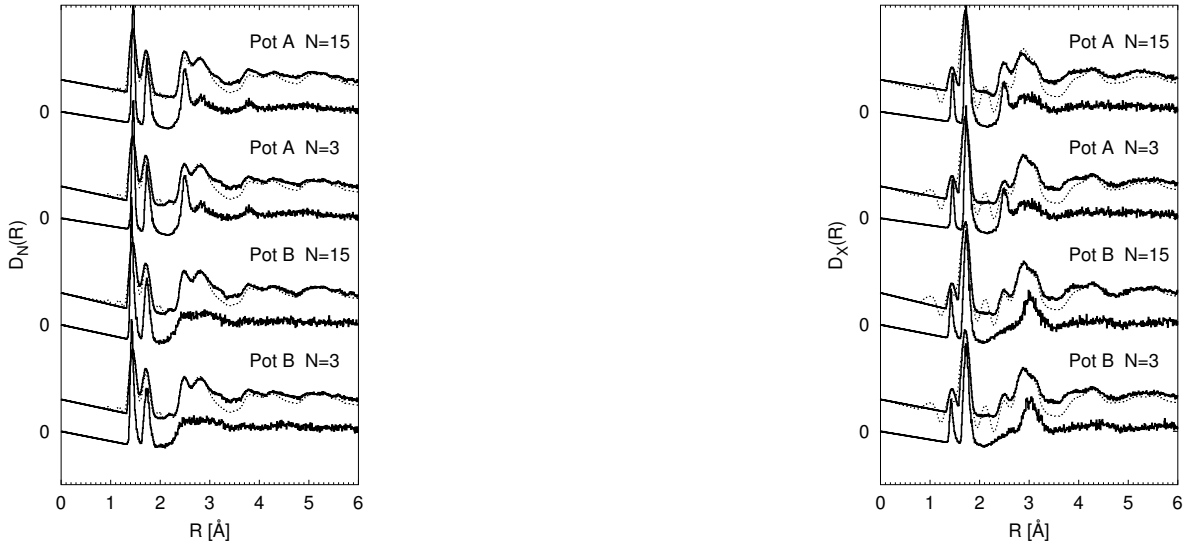

Figure 8.8: Neutron(left) and X-ray pair correlation functions (right) for the class E (sol-gel models) for the two interaction potentials A, B and the results after RMC refinement (upper curves). The dashed curves are the experimental data. The numbers in the figure are number of initial atoms placed on the lattice. Curves are shifted for clarity.

P	T_0	γ	Si-N	B-N	N-Si	N-B	Si-Si	Si-B	B-B	B-Si
10	95	1	3.63	3.21	1.56	1.38	3.89	2.62	3.48	2.62
10	95	2	3.68	3.21	1.58	1.38	3.67	3.04	2.98	3.04
10	99	1	3.62	3.22	1.55	1.38	4.33	2.08	4.09	2.08
10	99	2	3.66	3.24	1.57	1.39	3.84	2.79	3.39	2.79

Table 8.16: Coordination numbers of the first and second coordination spheres of the models of class E. The columns labelled Si-N and B-N contain the mean coordination numbers of silicon and boron atoms. Similarly, columns labelled N-Si and N-B contain the average number of silicon and boron atoms surrounding a nitrogen atom in its first coordination sphere. The mean number of next-nearest silicon and boron atoms around a silicon atom are given in the columns labelled Si-Si and Si-B and the mean number of next-nearest silicon and boron atoms around a boron atom can be found in columns B-Si and B-B. The column labelled N gives the number of initially placed atoms and the columns labelled p(N-B) give the probability of binding a boron atom to a nitrogen atom.

P	$p^0_{\mathrm{N-B}}$	γ	4	6	8	10	12
10	95	1	0.15	0.28	0.30	0.19	0.05
10	95	2	0.16	0.27	0.31	0.18	0.05
10	99	1	0.16	0.26	0.31	0.19	0.05
10	99	2	0.16	0.27	0.31	0.19	0.05

Table 8.17: Distribution of ring size n calculated from the models that were generated in class E. P is the procedure used in the generation of these models. The column labelled N gives the number of initially placed atoms and the columns labelled $p^0_{(\mathrm{N-B})}$ give the initial probability of binding a boron atom to a nitrogen atom.

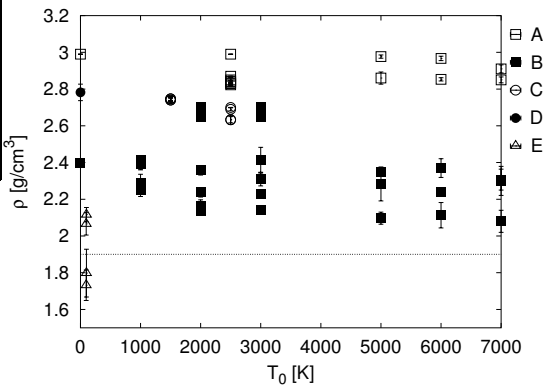

Figure 8.9: Dependence of the densities of the locally optimized models on the initial temperatures employed in their generation. We plot the data for the different classes, seperately. The data for classes D, E are independent of the initial temperature and are placed at arbitrary positions. The dotted horizontal line is the experimental density at 298 K.

length scale, we are usually not able to determine from the experimental measurements, whether a "dense" packing of the building units (tetrahedra, octahedra, etc.) is present, or whether small voids exist that are stable within the macroscopic real compound. Typically, these would not appear in the context of a high-temperature MD/MC simulation or any other modeling procedure that explicitly aims at generating the microscopic structure of the dense portion of the amorphous material.

Figure 8.9 shows the densities calculated for the various models. Again, we find that the closest agreement with experiment is found for the crystal fragment model (class B) and the sol-gel model (class E). However, in all cases, the void-free regions show a density of $\rho^{dense} \approx 2.5 - 2.8$ g/cm^3. This should be compared with the density of hypothetical crystalline ternary compounds ($\rho^{cryst} \approx 2.9$ g/cm^3), and the appropriate weighted average of the experimental densities of crystalline BN and Si_3N_4 ($\rho^{aver} \approx 2.75$ g/cm^3). This suggests that the reason for the surprisingly low density of a-$Si_3B_3N_7$ might be the existence of stable voids with diameters below 1 nm, which would be difficult to determine experimentally. Since the synthesis route via the sol-gel process would naively be expected to lead to many mismatches and the formation of cavities of all sizes, the fact that the final density of the sol-gel model agrees best with experiment appears to be self-consistent, and justifies faith in the model generating procedure. However, it is not clear, how significant this result truly is. Since we cannot follow the full synthesis route of the sol-gel process, we note that the good agreement with the result for the sol-gel model might be just fortuitous. Furthermore, the data depicted in figure 8.9 shows a wide spread even for a single model class, and thus we discuss the dependence of the densities of the models on the process parameter employed in their generation next, and later discuss the influence of voids.

Figure 8.10 shows the dependence of the densities of the melt based and crytal-fragment based models on the cooling rates γ^A_{NVT} and γ^A_{NPT} after constant pressure local optimizations. Note that under constant volume conditions in the cooling procedures the variations in the densities stem from the local optimization step. In that figure we have included the densities of the models after local optimization using interaction potentials A/B (open/closed) symbols. The densities of the melt based models are significantly higher than the densities of the crystal fragment based models. For both models we find a decrease of the final densities after slower cooling during the NVT-stage of the simulations. No difference between the melt based MD cooled models (A_1) and the melt based MC cooled models (A_2) is observable. Furthermore the densities of the crystal fragment based models are lower, if the final local op-

timization stage was performed using interaction potential A, compared to the densities of the models that were optimized using interaction potential B. Note also that a similar effect is visible for the very rapidly cooled melt based models. The NVT cooling simulation relieve the strain in the system, and the final constant pressure local optimizations bring the system to the closest minimum with respect to both atomic positions and cell parameters, thereby not changing the densities dramatically. Similarly, potential effects are most pronounced if the system was cooled rapidly, thus leaving the system in a highly strained state. Then the local optimizations 'can do' a lot and noticeable effects of the choice of the interaction potential can be identified.

The NPT cooling procedure shows, that slower cooling leads to higher densities of the final structural models after local optimization (c. f. figure 8.10(b)) for the crystal fragment-based models as well as the cluster-derived models. Note, however, that the densities of crystal-fragment models change by about 50 % and do not only depend on the choice of the cooling rates, but also on the choice of the initial temperature T_0, that were used in the NPT-cooling simulation. The densities of the models that were cooled very rapidly (γ = 0.1 K/MCC) are rather low ($\approx$ 2.3 g/cm^3, approximately equal to the densities of the NVT cooled models). But for slower cooling the densities of the crystal fragment based models reach the densities of the melt based models, provided that the system was heated to at least 2000 K. Note that it did not matter, whether we performed the local optimization in a two step manner (constant volume followed by constant pressure local optimizations) or directly under constant pressure conditions (open and closed symbols in figure 8.10). [6] The reason for the dramatic change in the density of crystal fragment models can be found in the structural freezing-in of the system at temperatures below 2000 K. Figure 8.11 depicting the dependence of the densities on the temperature for different cooling rates after the system had been prepared at 3000 K. Clearly, below 2000 K the changes in densities become very small, and for very low temperatures the densities hardly change. Note also, that the rapid cooling with 10^{-1} K/MCC leads to lower densities than slower cooling, since the time spent above 3000 K is too short.

The energies of the crystal fragment-based models are higher than the energies of the melt-based and the cluster-based models. Even though these energies fall into different ranges, we find for the NVT- and the NPT-cooling procedures, that slow cooling leads to lower energies (see figure 8.12) for both regimes. Furthermore, the energies of the NPT slowly cooled crystal fragment based models fall into the same regime as the melt based models. Note also that the energies of the sol-gel-based models are higher than the energies of the low-density crystal fragment models and that the energies of the RCP-based models are higher than energies of the melt-based models, but still below the energies of the crystal fragment-based models. The energies do not depend on the specific choice of the local optimization procedure. Even though the magnitudes of the energies are different for the two interaction potentials, the dependence of the energies on the model class and on the cooling rates are the same for both interaction potential.

In figure 8.13, we show a scatter plot of the density vs. the excess energy $\Delta E^{A/B} = E^{A/B}_{amorph} - E^{A/B}_{cryst}$, where $E^{A/B}_{cryst}$ are the potential energies of a hypothetical crystalline polymorph[144] for $Si_3B_3N_7$. The density is the higher, the lower the energy, thus showing that the higher density models are energetically more favorable.

8.4.2 Stability of voids

As mentioned above, a critical issue is the stability of the voids. Clearly, in the melt, these voids are not (or no longer) present, as we have seen in the heating of the crystal fragment beyond the melting temperature in subsection 8.3.2, where the density increased from 2.2 to 2.6 g/cm^3. Similarly, our simulations in subsection 8.3.2 indicate that no significant voids are created during the quenching from the melt. However, during the sol-gel synthesis route the system remains far below

[6] The effect of the choice of the interaction potential are similar to the ones of the NVT simulation discussed above and the dependence on the cooling rate is the same for either choice of potential.

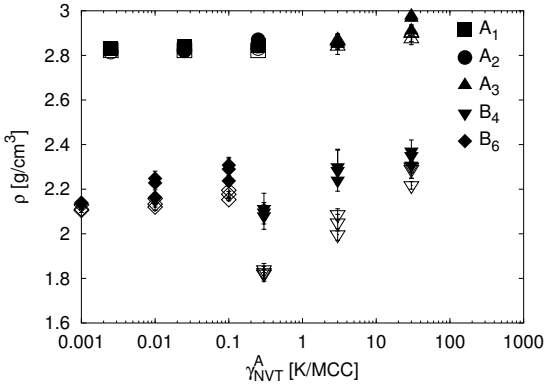

(a) NVT

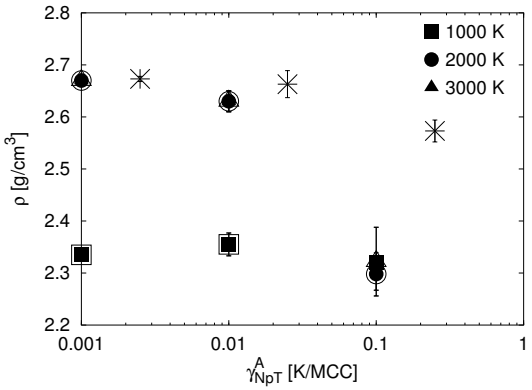

(b) NPT

Figure 8.10: Dependency of the densities ρ (in g/cm^3) of the different model classes on the cooling rate $\gamma^A_{NVT/NPT}$. The models A_i/B_i were generated by different procedures i from the melt-based models (A) and crystal fragment based models (B). The cooling simulations were run in the NVT ensemble and used interaction potential A. The local optimizations employed interaction potentials A (open symbols) and B (closed symbols) under constant pressure conditions. Note that the crystal fragment based models of procedure B_4/B_6 had different initial densities $\rho(B_4) = 1.54$ and $\rho(B_6) = 2.01$ g/cm^3, respectively. For one cooling rate, we depict the data for different initial temperatures T_0 by the same symbol.

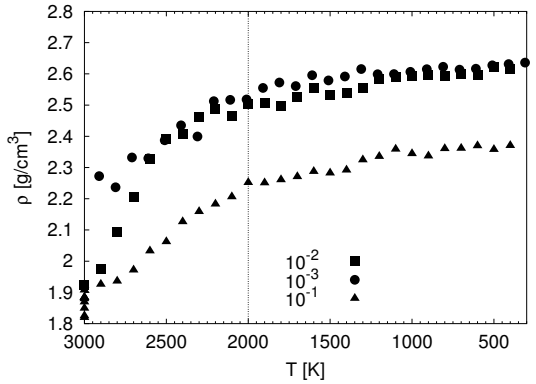

Figure 8.11: Dependence of the densities (in g/cm^3) of the crystal fragment based models on temperature $T(t)$ during cooling for three different cooling rates γ. The initial temperature T_0 was 3000 K. Interaction potential A was employed in the cooling procedures. The dotted vertical line is the temperature of the ergodic to non-ergodic transition.

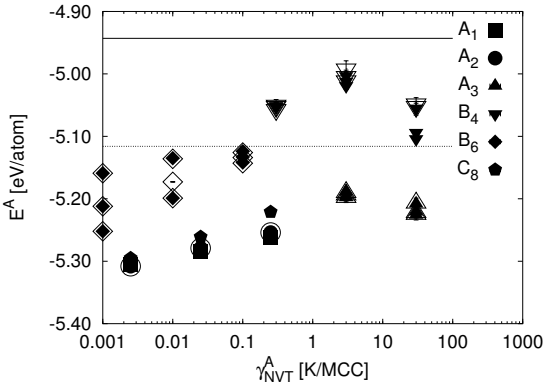

Figure 8.12: Dependence of the energies E (in eV/Atom) of the different models on the cooling rate γ^A_{NVT}. The models A_i/B_i were generated by different procedures i from the melt-based models (A) and crystal fragment based models (B). The cooling took place in the NVT ensemble. Interaction potential A was employed in the cooling procedures and in the final local optimizations. Filled/open symbols show the densities of the models that were locally optimized under constant pressure condition without/with a preceding constant volume local optimization. The dotted horizontal line is the average energy of the random close packing-based models and the full horizontal line is average energy of the sol-gel-based models.

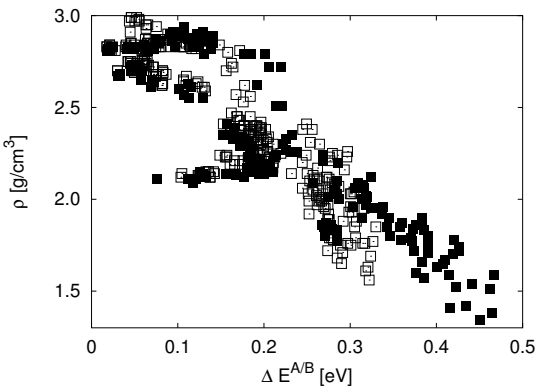

Figure 8.13: Dependence of the densities ρ (in g/cm^3) on the excess energies $\Delta E_{A/B}$ (in eV/Atom). The data calculated with potential A is shown as filled squares and the data for potential B as open squares. The excess energies $\Delta E_{A/B} = E^{amorph}_{A/B} - E^{cryst}_{A/B}$, were calculated with respect to a hypothetical crystalline polymorph of $Si_3B_3N_7$. See text for details.

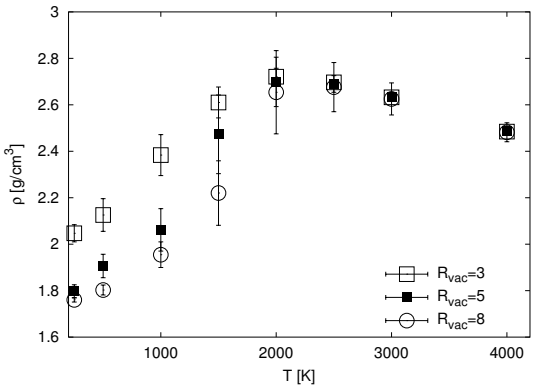

Figure 8.14: Temperature dependence of average densities for models that included voids of radii $R_{Vac} = 3$, 5 and 8 Å.

the melting temperature, and voids in bulk a-$Si_3B_3N_7$ might prove to be quite stable up to, say, 1500 K.

We note that in a real system, a slow coarsening process takes place, where larger pores grow at the expense of the smaller ones.[85] However, this only corresponds to a "reshuffling" of empty space within the material without a change in the overall density. The space occupied by voids in the system can only be eliminated from the system via migration of vacancies to the surface (the "infinite" pore). But once a crust near the surface has been depleted of vacancies, it acts as a barrier, and the removal of further voids from the real system will essentially come to a halt. In contrast, during constant pressure simulations with periodic boundary conditions, the "surface" is effectively only one cell constant ($\approx 20 - 40$ Å!) away, and voids will vanish tremendously more quickly than in real bulk systems.

Thus, we have investigated the stability of voids of various sizes ($R_{vac} = 3$ Å, 5 Å, and 8 Å for long simulation times (10^6 MCC) over a wide range of temperatures at zero external pressure (see section 9.3.4 for details). The model system consisted of 5200 randomly arranged atoms and we introduced a number of voids of sizes $R_{void} = 3$, 5 and 8 Å to prepare systems with initial densities of ≈ 1.8 g/cm^3 and calculated the averages densities from those configurations that are were generated in the last 20 % of the run time to reduce aging effects. Figure 8.14 depicting the temperature dependences of the average densities, clearly shows that larger voids are more stable than smaller voids, and that voids of radii > 5 Å are stable up to 1500 K. For all configurations we checked by visual inspection that the original voids are still present in the structure at the end of the simulations.

8.4.3 Phonon densities of states and bulk moduli

We used the GULP-program for the calculation of the phonon spectra $g_{vib}(\nu)$ and the bulk moduli B of the different models and calculated these properties for all models after employing the four local optimization strategies. First, we show the bulk moduli as a function of the excess energy $\Delta E_{A/B}$, for the two interaction potentials A and B, for all of the ≈ 500 local minima that occurred in the study of the different models. The excess energies $\Delta E_{A/B} = E^{amorph}_{A/B} - E^{cryst}_{A/B}$ were calculated with respect to a hypothetical high energy *crystalline* polymorph of the $Si_3B_3N_7$ system. We find a distinct correlation between the potential energy and the elastic strength of the material. The lower the energy of the amorphous structures the higher are the bulk moduli. Note also that the values of the bulk moduli of the investigated systems depend very little on the choice of the interaction potential. Only for the high lying minima differences be-

tween the two interaction potentials can be observed. Figure 8.16, depicting the dependence of the bulk moduli on the densities of the minima after the local optimizations employing either of the two interaction potentials, clearly shows a correlation between the bulk moduli and the densities. The more dense the system, the higher is its bulk modulus. Note also that the values of the bulk moduli do not depend significantly on the choice of the interaction potential.

Figure 8.17 shows the phonon spectra calculated as averages over all structures found for each class, employing interaction potentials A and B in the local optimization and the subsequent matrix diagonization. The overall shape of the spectra are the same, with only slight differences in the high-frequency regions, namely the peak at about 1500 cm^{-1} is less pronounced for the models of classes B and E. Comparison to the calculated phonon densities of states of crystalline β-Si_3N_4 and hexagonal boron nitride shows that the peak at 1500 cm^{-1} can be associated with vibrations of hexagonal boron nitride, while the peaks at $\approx$ 1000 cm^{-1} stems mostly from Si-N lattice vibrations.[7] Note that the choice of interaction potential does not change the phonon densities of states significantly. Only the intensities of the peaks in the phonon spectra of the crystal fragment models depend on the choice of the interaction potential.

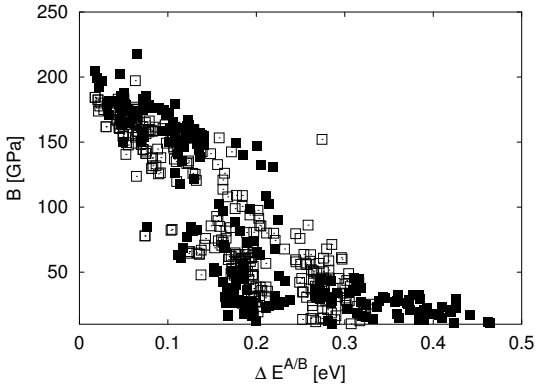

Figure 8.15: Dependence of the bulk moduli B (in GPa) on the excess energies $\Delta E_{A/B}$ (in eV/Atom). The data calculated with potential A is shown as filled squares and the data for potential B as open squares. The excess energies $\Delta E_{A/B} = E_{A/B}^{amorph} - E_{A/B}^{cryst}$, were calculated with respect to a high-energy hypothetical crystalline polymorph of $Si_3B_3N_7$. See text for details.

8.5 Discussion

First we discuss the structural properties of the different model classes and compare these properties to the experimental data, examine the dependence of the structural properties on the process parameters used in the generation of the models and compare these dependences to the results of computer simulations of different systems. Next we focus on the bulk properties of the models and discuss their dependence on the process parameters used in their generation of these models. Finally, we will discuss some method related aspects.

In all structural models boron and silicon atoms are mainly trigonally planar and tetra-

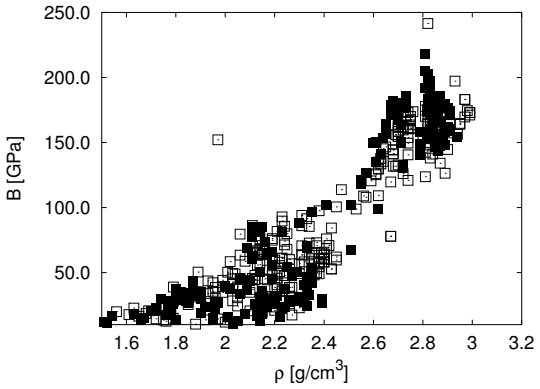

Figure 8.16: Dependence of the bulk moduli B (in GPa) on the densities ρ (in g/cm^3) of the minima. Filled symbols show the data for interaction potental A and open symbols the data for interaction potential B. See text for details.

[7] In section 11.3.3, we perform a detailed peak assignment based on the eigenvector analysis of a-$Si_3B_3N_7$.

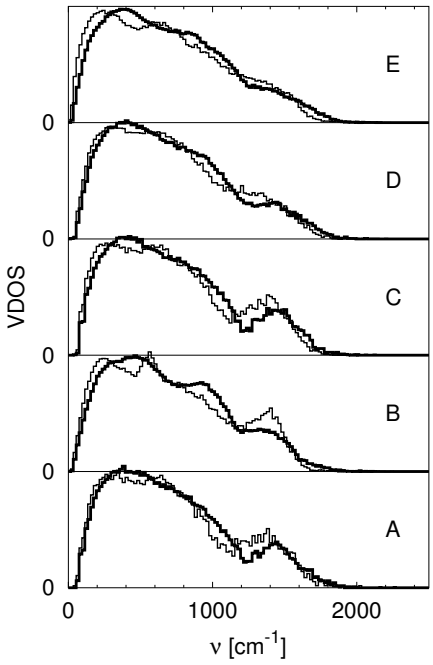

Figure 8.17: Phonon spectra of models representing the classes A-E. Thin lines are the phonon densities of states calculated after local optimizations using potential A and bold lines represent data after local optimizations using potential B.

hedrally surrounded by three and four nitrogen nearest neighbors, respectively, and nitrogen atoms are surrounded by three cations (silicon or boron atoms). These results agree well with the experimental investigations of a-$Si_3B_3N_7$. Independent of the model classes, we found that faster cooling leads to more coordination defects, i.e. deviations from the ideal coordination numbers four, three and three of silicon, boron and nitrogen atoms, respectively. The RCP-based models and the sol-gel based models were only quenched (viz. infinitely fast cooling) and showed a higher number of coordination defects, confirming the general observation that faster cooling leads to more coordination defects. Vollmayr et al. found similar cooling rate dependences in their study of the structural properties of a-SiO_2[169]. Note, however that in the a-$Si_3B_3N_7$ system two cationic atoms exist that show a different relative number of coordination defects. These defects are more pronounced for silicon than for boron atoms, clearly showing that nitrogen atoms are more tightly bound to boron than to silicon atoms.

Even though the first coordination spheres of the atoms were almost identical, significant differences were found in the second coordination spheres of the models. The melt-, cluster- and RCP-based models showed a rather homogenous distributions of the number of cations surrounding a given cation in the second coordination sphere, but the crystal-fragment- and sol-gel-based models showed a preference for boron atoms surrounding a boron atom in the second coordination sphere. Similarly in the latter models, silicon was mostly surrounded by silicon atoms in the second coordination sphere. The results for the crystal fragment based and the sol-gel based models are in good agreement with *all* experimental data, thus indicating that the microscopic structure of the real a-$Si_3B_3N_7$ material is close to these models. Furthermore for the crystal-fragment based models, the heterogeneous distributions of cations disappeared once the system was heated above 2000 K for a sufficiently long time, thus providing evidence that above $T_C \approx 2000$ K the memory of the type of amorphous structure in the solid state vanishes. Note that this occured for the simulations that were performed both in the NVT- and for those in the NPT- ensemble and that these results did not depend on the local optimization strategy employed. Note further that, NPT-MC-relaxations of the sol-gel based models at temperatures below and above T_C showed that the heterogenous distributions of cations remained unchanged at temperatures below T_C but disappeared at temperatures above T_C (see chapter 6).

The X-ray and neutron pair correlation functions of the crystal-fragment-based models and the sol-gel-based models showed good agreement with the experimental data as long as the system was kept below 2000 K. These pair correlation functions were clearly distinguishable from the ones of the other classes, which fit the experimental data (at 298 K) only moderately. Note also that the disappearance of the heterogenous distribution of cations at temperatures $T > T_C$ is closely followed by the disappearance of the clearly distinguishable features at distances $R > 3.5$ Å in the pair correlation functions of the different models. Furthermore this lack of features at distances

$R > 3.5$ Å is common to all models except for the low temperature crystal fragment-model and the sol-gel-model.

The ring distributions in a-$Si_3B_3N_7$ are quite difficult to characterize, due to the existence of many different compositions of rings of sizes n. However, the structures are all compact, since no large rings containing more than 16 atoms are found in all structures. We did not find significant cooling rate effects in the overall distribution of ring sizes, only an increase of four-membered rings in the models obtained after very fast cooling was detectable. These results on the ring statistics are similar the results of Vollmayr et. al. [170] on the a-SiO_2 system. Again focussing on the crystal fragment based model, we found a change of the ring distributions from a preference for six membered rings that were mostly Si_3N_3 and B_3N_3 rings to a distribution of ring sizes, that closely resembled the ring size distributions of the other models, once the system was heated above 2000 K.

The models belonging to the various classes are also characterized by different densities, ranging from 1.8 g/cm^3 to 2.9 g/cm^3. Clearly the 'low-temperature' crystal fragment based models and the sol-gel based models come closest to the experimental densities. The densities of the models belonging to the other classes are all greater than 2.6 g/cm^3, indicating that the synthesis route is important for the final density of the 'product'. Even though the magnitudes of the densities were specific for one model class, the cooling rate dependence of the densities followed a general scheme. For the NVT-simulations, we found that slow cooling led to *lower* densities of the locally optimized models, regardless of the strategy employed in the local optimizations. In the NVT-cooling schemes, we relieved the strain at constant (relatively large) volume. Thus the slower we cool, the smaller was the final strain, and the final constant pressure local optimization does not shrink the cell volume by a large amount, since this local optimization only leads the system to a close-by local minimum of the energy hypersurface. Contrary to the NVT-simulations, the NPT-simulations led to higher densities of the models after slow cooling and local optimization. For a-SiO_2, Vollmayr et al. found a decrease of the density with increasing cooling rate in a MD-NPT computer simulation study, but the authors pointed out that these results may be due to the density anomaly of a-SiO_2. In a study on binary Lennard-Jones glasses, the same authors[170] found that the density increases with decreasing cooling rates. Note that, experimentally, the density of borosilicate glasses increases upon slower cooling.[94, 69]

The crystal fragment-based models showed a 40 % change in the density once these models were heated to temperatures above 2000 K, clearly indicating a transition to a denser state at higher temperatures. Note that the structural changes of the second coordination spheres discussed in the preceding section accompany these changes of density. Furthermore, the study of NPT- relaxations of the sol-gel models showed a dependence of the densities and the distribution of next-nearest neighbors on the temperature, which was similar to the dependences of these quantities in the crystal fragment based models.

The energies of the models belonging to the different classes also allowed for a distinction of the different models. The denser models had lower energies than the lower density (crystal fragment based and sol-gel based) models, thus indicating that the denser models are energetically more stable than the low-density models. An exception were the dense RCP-based models, due to the large number of coordination defects in these structures. Furthermore, the dependences of the energies on the cooling rates was independent of the investigated model class and ensemble used in the simulation. Slower cooling led to lower energies, except for the highest cooling rates at which the system fell out of equilibrium very quickly. These cooling rates effect on the energies have also been found in computer simulations of spin glasses, a-SiO_2 and Lennard-Jones glasses, just to name a few of the investigated glassy systems.

The crystal fragment-based models are only metastable with respect to the melt-based models. However, at sufficiently low temperatures (i. e. below 2000 K), the time scale of our simulation procedures are not sufficient to bring the system to one of its low energy/high

density configurations.[8] which are structurally different from the low temperature structures the simulation were started from. One possible explanation for this metastability and thus the low density of the amorphous compounds observed experimentally is the stability of voids in the structure. Our simulations showed, that voids of radii of 8Å are stable up to 1500 K. This void-based explaination of the low-density of a-$Si_3B_3N_7$ is also supported by experimental results of Sauter et al.[132] of the vacancy sizes in amorphous B-C-N ceramics. One should note, that our simulations actually underestimate the stability of voids. In the experiments a dense crust will form at the surface of the material once all the voids near the surface have been expelled. Thus the densification of the ceramic is strongly inhibited. In contrast, voids can be rather easily removed in a simulation with periodic boundary conditions - the effective surface is only a few nanometers away.

Similar to the results of Omeltschenko et al.[120] on low densitiy amorphous Si_3N_4, the bulk moduli of the a-$Si_3B_3N_7$ models decreased with decreasing density of the models. Furthermore our results support Stillinger's view[172], that the bulk modulus of an amorphous material depends on the height of the minimum on the energy landscape, thus indicating that the low-lying minima have steeper walls than the high-lying minima.

In general our results did neither depend on the choice of interaction potential used in the local optimization nor on the way these local optimizations were performed. The choice of the interaction potential affected the properties of only those models, that were rapidly quenched, but the dependences on the cooling rates was not affected by either choice of the interaction potential.

8.6 Summary and conclusion

We showed that the properties of the amorphous ceramic a-$Si_3B_3N_7$ strongly depend on the way we 'synthesize' different models belonging to different classes on the computer. The models that contained a certain degree of heterogeneity in the second coordination sphere agreed well with the experimental pair correlation functions, the experimentally determined first and second coordination spheres and the experimental densities. The unusually low density of this compound is most probably due to existence of sub-nanometer sized voids. Our results also showed, that the amorphous ceramics produced by the sol-gel route are less dense, and probably energetically less stable, than those one might be able to synthesize in the future via e. g. the glass formation route. Nevertheless for application below $T_C \approx 2000$ K, the present ceramic should prove to be sufficiently stable for long-time applications.

The inclusion of a kinetic factor into the modelling approaches showed that aspects of the synthesis route should be included in future modelling strategies for these new types of amorphous compounds. Finally, we would like to point to the plethora of rather different and experimentally distinguishable amorphous structures that will be found when following different synthesis routes. Clearly, one expects a similar behaviour to occur in other complex amorphous systems such as multinary amorphous oxides.

[8] Of course, these low energy/high density models are only metastable at infinite simulations times.

Part IV

Thermodynamic Properties of $Si_3B_3N_7$, Glassiness and Aging

Chapter 9

Thermodynamic properties of $Si_3B_3N_7$

9.1 Introduction

In the previous chapters, we have shown that the main building units of a-$Si_3B_3N_7$are SiN_4 tetrahedra and BN_3 and $N(Si/B)_3$ triangles. Furthermore, at length scales $\leq$ 7 Å, heterogeneities in the cation-cation next-nearest neighbor distributions exist. We have provided evidence, that these heterogeneities are due to the special synthesis route employed in their generation. Furthermore the low-density (both experimentally and simulated) of the models could be traced back to the synthesis route resulting in the existence of voids on the sub-nanometer length scale. However, the low-density structures were compactified when heated above 2000 K and the heterogeneity was removed on doing such a thermal treatment.

In order to understand the thermodynamic behaviour more thoroughly, we will now investigate the (metastable) phase diagram of $Si_3B_3N_7$, with a particular focus on the high-temperature liquid-gas region of the ternary system. After a short description of the simulation method, we are going to analyze the computed pressure data and the cluster size distributions as function of temperature and volume, and construct the phase diagram of the ternary $Si_3B_3N_7$-fluid. Finally, we are going to address the issue of the surprisingly low density of the (metastable) amorphous ceramic and analyze the stability of nano-size cavities in the amorphous solid more thoroughly.

9.2 Method

9.2.1 Model

The model of $Si_3B_3N_7$ we employed for the thermodynamics computations consisted of 162 Si-atoms, 162 B-atoms and 378 N-atoms ($N_{atom} = 702$), respectively, in a periodically repeated cubic box and we used interaction potential A (see section 3.9). The simulations were performed at fixed temperature and volume, with a Monte-Carlo algorithm using the Metropolis acceptance criterion.[1] The move-class consisted of single atom moves. The temperatures investigated ranged from 250 K to 7000 K, and the volumes (of the periodically repeated simulation cell) ranged from 5000 Å^3 to $2.5 \cdot 10^6$ Å^3, corresponding to number densities ρ_N from 0.12 atoms/Å^3 to 10^{-5} atoms/Å^3. For each temperature and volume we performed runs of length 10^6 MCC, resulting in about 600 data points for each of the two procedures described below. Since it is known that the system exhibits aging effects,[2] we have only used the last $2 \cdot 10^5$ MCC (corresponding to a time window of about 100 ps) after a waiting time of $t_w = 8 \cdot 10^5$ MCC, for analysis purposes in order to allow the system to reach at least quasi-equilibrium.

It is well-known that, for low temperatures, the time scales of the simulations are much too short for the system to reach full equilibrium[92, 87]. Thus, we have performed two different sets of simulations that differed in the starting configuration, in order to be able to place the results into the proper context. In *procedure 1*, the starting configurations

[1] Note that the kinetic energy ($3/2 k_B T$ per atom) does not appear in MC-simulations.

[2] see [68] and chapter 12.

for the simulations were generated by equilibration of a ternary melt at $T = 2000$ K in a simulation cell of volume $19.1 \times 19.1 \times 19.1$ Å$^3 \approx 7000$ Å^3, followed by a re-scaling to the volume under consideration. Thus, the initial atom arrangement could be denoted as a "stretched melt" configuration. For very large volumes, the subsequent process can be visualized as a condensation from the gas phase. In *procedure 2* we generated the starting configuration by placing the relaxed melt configuration unchanged at the center of the simulation cell. We called this arrangement a "free block" configuration, and the time evolution corresponds to the evaporation from the condensed phase.

9.2.2 Analysis

In order to distinguish between solid, liquid and gaseous phases several criteria were used, which were based on one-time properties such as the (potential) energy, pressure and cluster distributions, as well as on two-point properties like the diffusion coefficient and the bond-survival probabilities. To analyze the one-time properties, we registered the potential energy E_{pot}, the pressure P, the distribution of connected clusters every 100^{th} MCC.

Clusters were identified using a topology-based criterion (see section 4.1.2) yielding the cluster size distribution at time t, $h(S_{cl};t)$ ($S_{cl} = 1,\ldots,N_{atom}$). From $h(S_{cl};t)$, we extracted the average cluster size at a given time $S_{mean}(t)$, the size of the largest cluster present $S_{max}(t)$, and the number of clusters at time t, $N_{cl}(t)$. Furthermore, the distributions were averaged over the observation time of $2 \cdot 10^5$ MCC (after a waiting time of $t_w = 8 \cdot 10^5$ MCC), yielding $\langle h(S_{cl})\rangle_t$, $\langle S_{mean}\rangle_t$, $\langle S_{max}\rangle_t$, and $\langle N_{cl}\rangle_t$. As discussed in section 4.1.2, from $\langle h(S_{cl})\rangle_t$, one can derive the likelihood $\langle L(S_{cl})\rangle_t$ of an atom to be found as part of a cluster of size S_{cl},

$$\langle L(S_{cl})\rangle_t = \frac{S_{cl}\cdot\langle h(S_{cl})\rangle_t}{N_{atom}}. \qquad (9.1)$$

For the two-time properties, we calculated the mean square displacement $MSD(t_{obs};T,V)$ and the bond survival probabilities $BSP^{(SiN)}(t_w,t_{obs};T,V)$ and $BSP^{(BN)}(t_w,t_{obs};T,V)$, i.e. the likelihood that a given Si-N or B-N bond, respectively, observed at time $t_w (= 5\cdot 10^5$ MCC) still exists after a time $t_{obs} (= 5\cdot 10^5$ MCC) has elapsed. From the mean squared displacement $MSD(t_{obs})$, we calculated the diffusion coefficients

$$D(T,V) = \lim_{t_{obs}\to\infty} \frac{MSD(t_{obs};T,V)}{6t_{obs}}. \qquad (9.2)$$

Note that in the non-equilibrium regime, equation 9.2 only gives an estimate for the diffusion coefficient, since in that regime the linear relationship between t_{obs} and the $MSD(t_{obs};V,T)$ does not hold in general. But for the present purpose this estimate suffices.

Two steps were required to assign a simulated system, for a given set of thermodynamic parameters (V,T), to the solid, liquid or gaseous state. First we needed to identify the condensed states (solid and liquid) and the gaseous states, and in a second step, we had to distinguish between solid and liquid states. In contrast to a system in the thermodynamic limit ($N_{atom}, V \to \infty$, with $\rho_N = N_{atom}/V =$ constant), the simulations can never realize a condensed phase of infinite size, and furthermore surface effects (i.e. interface between condensed and gas phase) need to be taken into account. Thus, in order to gain a quantitative handle that allows us to assign a label "condensed"/"gaseous" to a point (V,T) in the phase diagram, we have chosen $S^*_{cl} = 50$ as a delimiter, after careful inspection of the cluster size distributions we have obtained. If the likelihood to be part of a cluster with size $S_{cl} \le S^*_{cl}$,

$$\begin{aligned} f(S_{cl},S^*_{cl}) &= 1/N_{atom} \sum_{S_{cl}\le S^*_{cl}} S_{cl}\cdot\langle h(S_{cl})\rangle_t \\ &= \sum_{S_{cl}\le S^*_{cl}} \langle L(S_{cl})\rangle_t, \end{aligned} \qquad (9.3)$$

exceeds a predefined cutoff $f_{cut} (= 0.9)$, the system as a whole is considered to be in the gaseous phase, while for $f(S_{cl},S^*_{cl}) < (1 - f_{cut} = 0.1)$, the system as a whole is assigned to the condensed state. For intermediate values, the system was considered to be in the two-phase region, where a condensed and a

gaseous phase co-exist. Even though these assignments to a condensed or a gaseous state depend on the choices of S^* and f_{cut}, we found no significant effect on the final assignments for a wide range of these parameters (see figure 9.8).

In the second step, we have used the bond-survival probabilities as a criterion for distinguishing between the solid and the liquid state of $Si_3B_3N_7$. We note that the structure remains essentially unchanged, if most of the bonds are preserved for a given observation time t_{obs}. Thus, we called the condensed system liquid, if the BSPs for a condensed phase had dropped below a value $1/e$.[3] On the other hand, if the BSPs for the condensed phase were larger than 0.8, we identified the system as an (amorphous) solid. Note that the "BSP-criterion" alone could not be used to distinguish between the gaseous state and the solid state, since a system consisting of gas molecules only, will also show a high value of the bond-survival probabilities. Here, the diffusion coefficient could be used as a criterion, in principle.

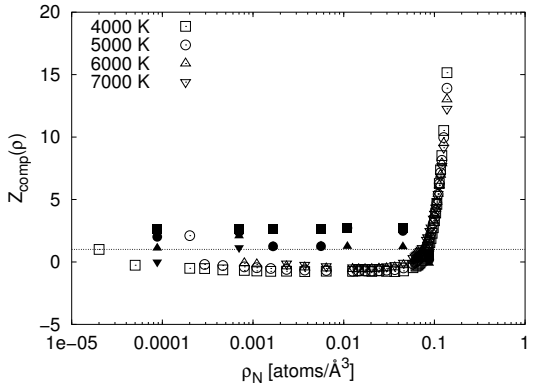

(a) Compression factors

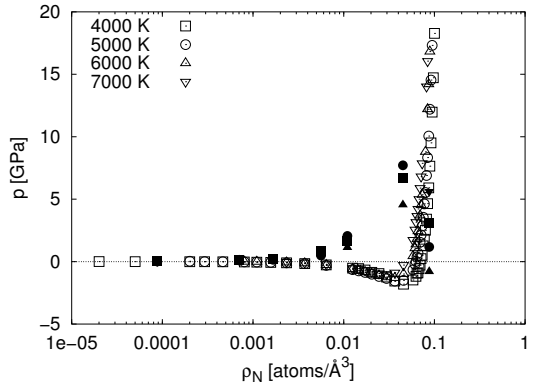

(b) Pressure

Figure 9.1: Dependence of the compression factor $Z(\rho_N) = \frac{p \cdot V}{N k_B T}$ and the pressure p on the number density ρ_N for procedures 1 (open symbols) and 2 (filled symbols) for selected isotherms.

9.3 Results

9.3.1 Ternary liquid-gas region

Using procedure 1 outlined in the previous section, we have calculated the pressure at each given volume and temperature. Fig. 9.1(a) shows the so-called compression coefficient[168] $Z = pV/N_{atom}k_BT$ as a function of number density $\rho_N = N_{atom}/V$, which would equal one for an ideal gas. For a given temperature, Z rapidly increases to high positive values for high densities, crosses zero near $\rho_N = 0.1$ atoms/Å^3 (close to the equilibrium value for the starting melt, corresponding for $Si_3B_3N_7$ to a mass density of $\rho_m = 2.7$ g/cm^3), exhibits a negative minimum value around $\rho_N = 0.08$ atoms/Å^3, and then slowly increases monotonically for $\rho_N \to 0$. Fig. 9.1(b) shows the pressure computed according to eq. 3.23 for high temperatures. The general shape resembles the one observed for e.g. a van der Waals gas, but we do find negative pressures for densities below $\rho_N = 0.08$ atoms/Å^3.

For the second procedure, we see from figure 9.1(b) that for the most part $p(V,T) > 0$, dropping below zero only for low temperatures at intermediate densities ($0.01 < \rho_N < 0.1$ atoms/Å^3). It appears that for the free block model the major contribution to the pressure stems from the few atoms that have evaporated from the condensed phase and behave nearly like an ideal gas. In contrast, in the first procedure the negative pressures are presumably due to the energy loss associated with the formation of the comparatively large numbers of clusters starting at intermediate densities.

[3] Note that for a system that relaxes according to a Debye-law, a value of the BSPs larger than $1/e$ would imply that the relaxation times τ exceeded the observation time t_{obs}.

9.3.2 Cluster size distribution in the fluid phase

One conclusion from the preceding subsection 9.3.1, would be that $Si_3B_3N_7$ does not necessarily behave like a simple fluid. Thus, within the range of our simulations, the mean-field picture is not appropriate for a quantitative description. This agrees with our work studying the glass transition (see chapters 10 and 12): Judging from the specific heat curves, there appears to occur a considerable release of configurational entropy far above the actual glass transition at $T = T_G \approx 2000 - 2500$ K that was computed based on the peak in the specific heat and the decrease of the diffusion constants.

The reason for this disparity lies in the fact that upon melting / softening of the crystalline / amorphous solid, we do not quickly reach a phase consisting of individual atoms or molecules, respectively. Instead, we observe a wide distribution of long-lived Si/B/N clusters in the fluid phase(s).

Fig. 9.2(a) and fig. 9.2(b) show the time-average of the average size of the observed clusters $\langle S_{mean} \rangle_t$, and the average number of clusters $\langle N_{cl} \rangle_t$ present, respectively, as a function of T and V, for both procedures. As expected, the mean cluster size decreases with increasing temperature and decreasing density, for both procedures, although we note the markedly higher values at low temperatures and low densities for procedure 2.

However, the mean cluster size is not necessarily a very significant measure of the cluster distribution. While at low densities and high temperatures we would expect that the cluster sizes cluster around the average value, this might not be true for the low density-low temperature region. Here, we might deal with a large piece of solid surrounded by a few atoms or very small clusters in the gas phase. Thus, we show in fig. 9.2(c) the time-averaged size of the largest cluster observed for each configuration, $\langle S_{max} \rangle_t$, as a function of density. For procedure 1, we see that for temperatures up to 2500 K the maximal cluster size $\langle S_{max} \rangle_t$ observed remains constant ≈ 700 atoms (as in the solid state) down to a density of 0.01 atoms/Å^3 which corresponds to about $1/10$ of the density in the solid

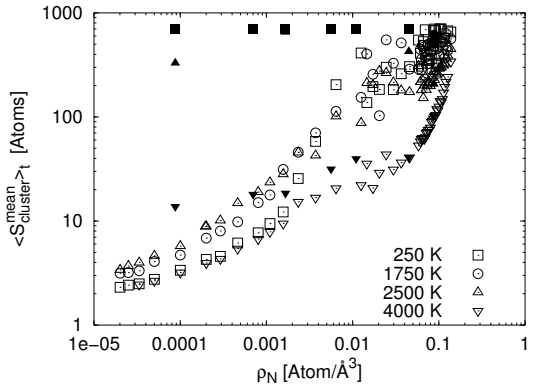

(a) Mean cluster size

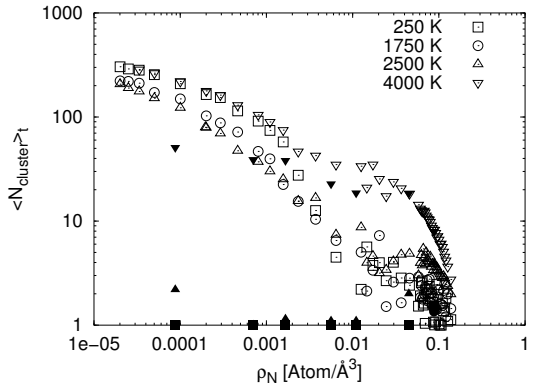

(b) Number of clusters

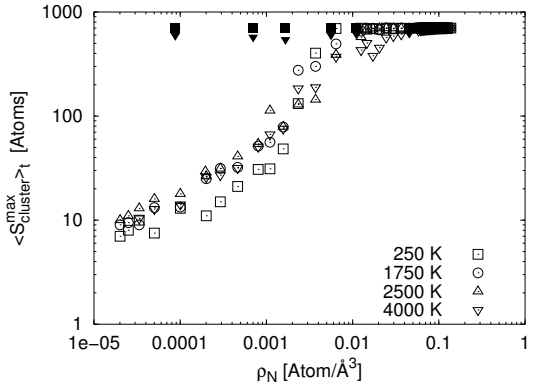

(c) Maximum cluster size

Figure 9.2: Dependence of the mean cluster size $\langle S^{mean}_{cluster} \rangle$, the number of clusters $N_{cluster}$ and the maximum cluster size $\langle S^{max}_{cluster} \rangle$ on the number density ρ_N for selected isotherms calculated from configurations generated by procedure 1 (open symbols) and procedure 2 (filled symbols)

.

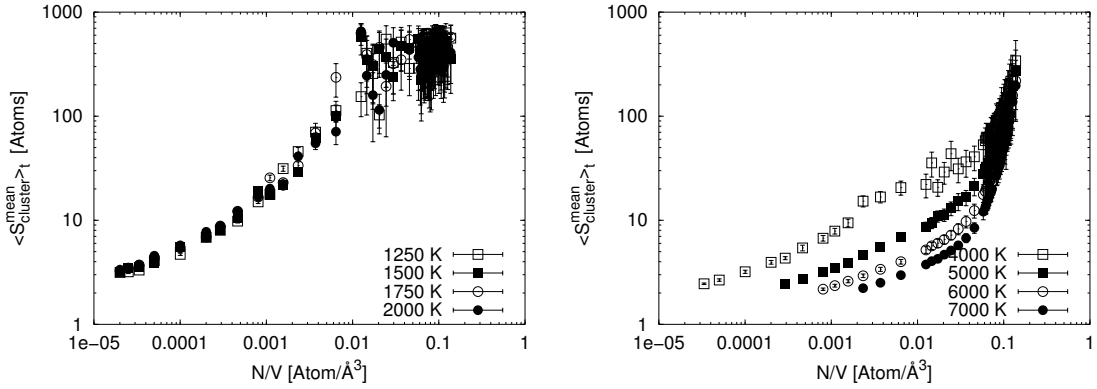

(a) Mean cluster size $\langle S_{mean} \rangle$

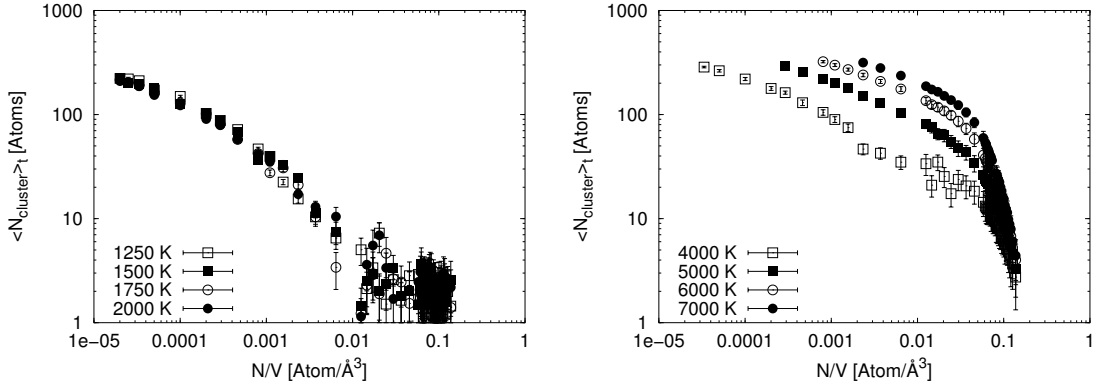

(b) Number of clusters $\langle N_{cl} \rangle$

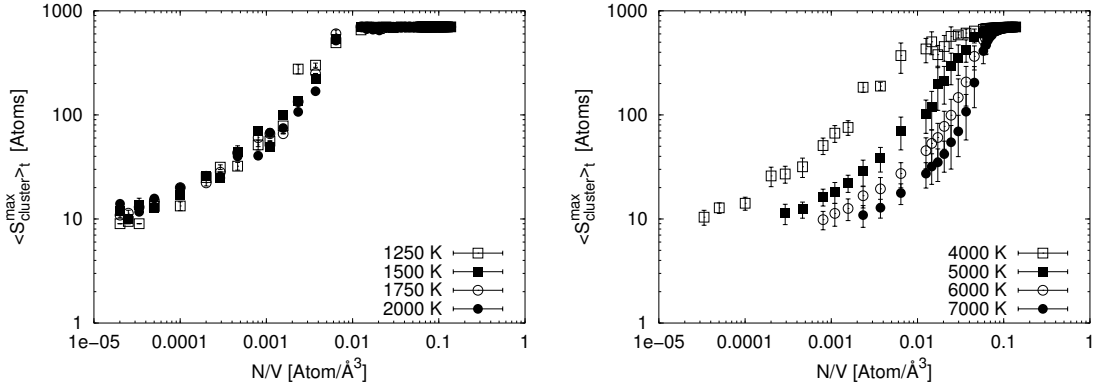

(c) Maximum cluster size $\langle S_{max} \rangle_t$

Figure 9.3: Dependence of time averaged cluster distribution properties on the number density $N/V = \rho_N$ for different temperatures given (in K) in the legends. The number densities ρ_N are given in atoms/Å^3. The properties were calculated from configurations generated by procedure 1.

state. For these volume-temperature combinations, the average cluster size $\langle S_{mean} \rangle_t$ already begins to decrease indicating the presence of "gas molecules" in addition to the solid/liquid phase. Procedure 2 leads to the same behavior but again with a larger stability of the large clusters (encompassing nearly all atoms in the simulation cell) for low densities.

One should note that the curves for $\langle S_{max} \rangle_t$ are nearly identical for $T \leq 4000$ K, although for low temperatures we are clearly dealing with a solid, while for temperatures exceeding 2000 K a melt is present (c.f. the analysis in subsection 9.3.3 and figure 9.3), for both procedures. Similarly, we see that the data points for $\langle N_{cl} \rangle_t$ for densities below 0.01 atoms/Å^3 also fall on the same curve for temperatures up to 3000 K for procedure 1. This suggests the interpretation that up to 4000 K we can easily distinguish between a condensed and a gaseous phase, which is probably no longer true above 4000 K.

An interesting but hard to quantify observation in the stretched melt model is the fact that in the low density range ($\rho_N < 0.01$ atoms/Å^3) we often find that the large clusters do not form compact objects. Instead, they appear to take on rather diffuse shapes, suggesting that we are either dealing with many smaller clusters or fragments that are more or less loosely connected to each other, or witness the slow compactification of a very large cluster from many small ones.

For temperatures exceeding 4000 K, we find, for both procedures, that clusters of the size of the whole system are only present at very high densities, while the mean cluster size decreases much more rapidly with volume than even for temperatures in the range $2000 - 3000$ K. Clearly, the range of volumes where equilibrium between a condensed phase and a gaseous phase exists is shrinking, and the fluid consists of small clusters that interconnect periodically.

More details are gained from the study of the actual cluster distribution. In figures 9.4 to 9.6, we show for all temperatures, the likelihood of an atom to be part of a cluster of size S_{cl}, $\langle L(S_{cl}) \rangle_t$ for both procedures. A binary distribution of $\langle L(S_{cl}) \rangle_t$ with peaks near $S_{cl} = 1$ and $S_{cl} = N_{atom}$, indicates a condensed phase in equilibrium with a gaseous phase, while a function with a single peak corresponds to an essentially homogeneous fluid phase. We see that for procedure 1, a multicluster phase is found for all temperatures for a density below 0.01 atoms/Å^3, with some small amount of "gas" phase present already at higher densities and low temperatures. In contrast, procedure 2 yields essentially no gas phase for temperatures up to 3000 K, and even at 4000 K some remnant of a condensed phase appears to be present for all densities.

Finally, an important aspect is the stability of the clusters and, for the large ones encompassing nearly the whole system, their viscosity. In order to estimate these quantities, we have computed the bond survival probabilities BSP between the atoms, and the diffusion coefficients D(V,T).

Figure 9.7 shows the dependence of the bond survival probabilities BSP ($t_w = 5 \cdot 10^5$ MCC, $t_{obs} = 5 \cdot 10^5$ MCC) for Si-N and B-N on the densities and the temperature, for both procedures. For fixed temperature, all curves for procedure 1 exhibit a very flat minimum in the density range 0.1 atoms/Å$^3 > \rho_N > 0.01$ atoms/Å^3, where both the depth of the minimum and its breadth increase with temperature. For procedure 2, this effect is much less visible: for fixed temperature, the BSPs are nearly constant as a function of density.

Qualitatively, this can be understood as follows: For all temperatures, the high-density region has a reduced atom mobility such that a sizeable fraction of the bonds is going to survive on the time scale measured (≈ 250 psec)[4]. Similarly, in the gaseous phase, the few bonds that still exist after a relaxation for a time $t_w = 5 \cdot 10^5$ MCC are likely to have survived for another time span of $t_{obs} = 5 \cdot 10^5$ MCC.[5] Inbetween, the condensed phase and the large clusters are going to exhibit the full malleability of the relaxed condensed state, which is essentially independent of volume for quite a range of densities.

By comparing the BSP with those of our

[4]For high enough pressures, we are dealing with a solid phase even at very high temperatures - there is no critical point in the solid/fluid transition.

[5]Keep in mind that the free energy barriers associated with bond switches in the liquid are much lower than those associated with the break-up of a small molecule or cluster.

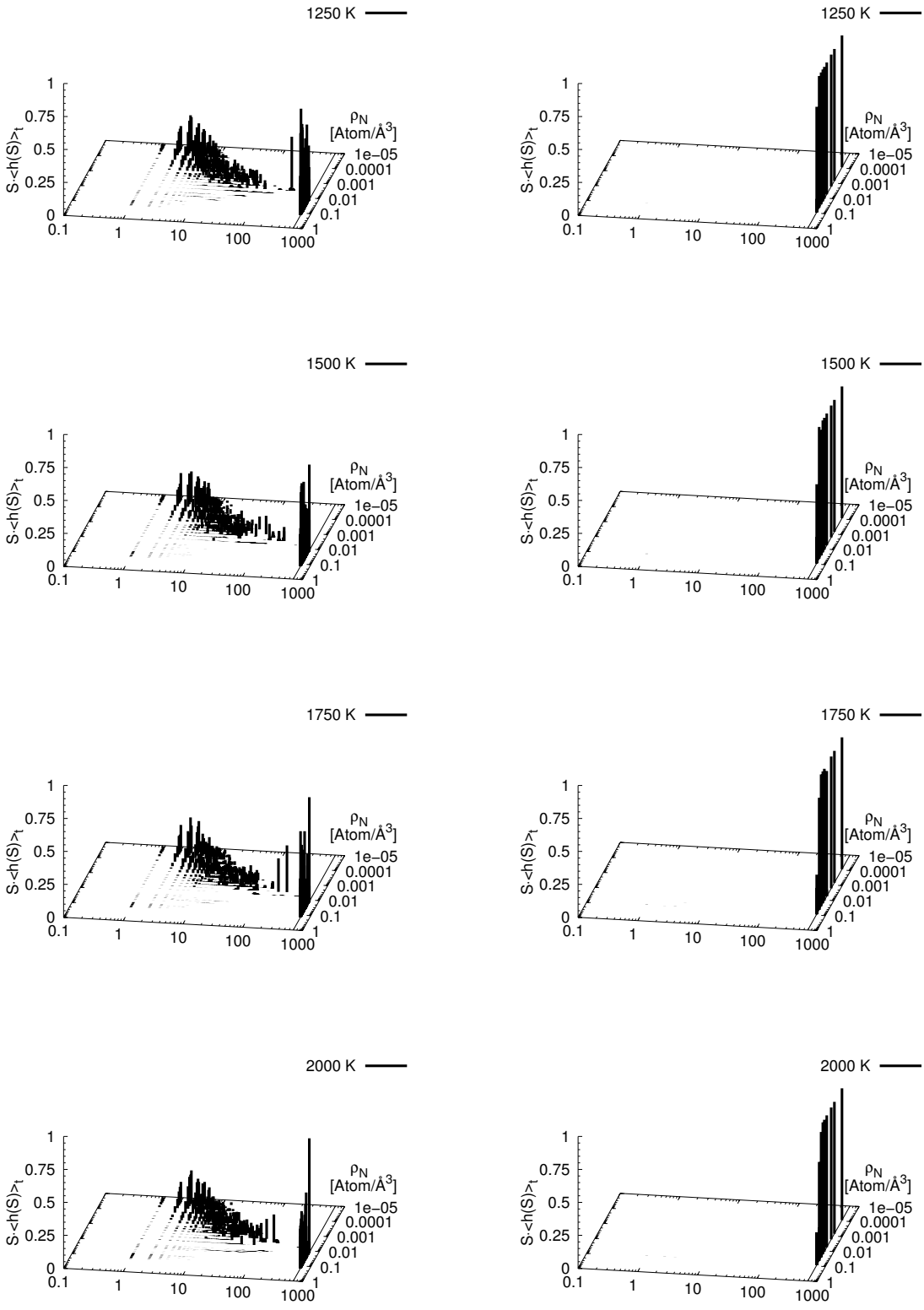

(a) Procedure 1

(b) Procedure 2

Figure 9.4: Dependence of the distribution of the mean number of atoms $S \cdot \langle h(S) \rangle$ inside a cluster of size $S_{cluster}$ on the number density $\rho_N = N/V$ for temperatures $T \leq 2000$ K.

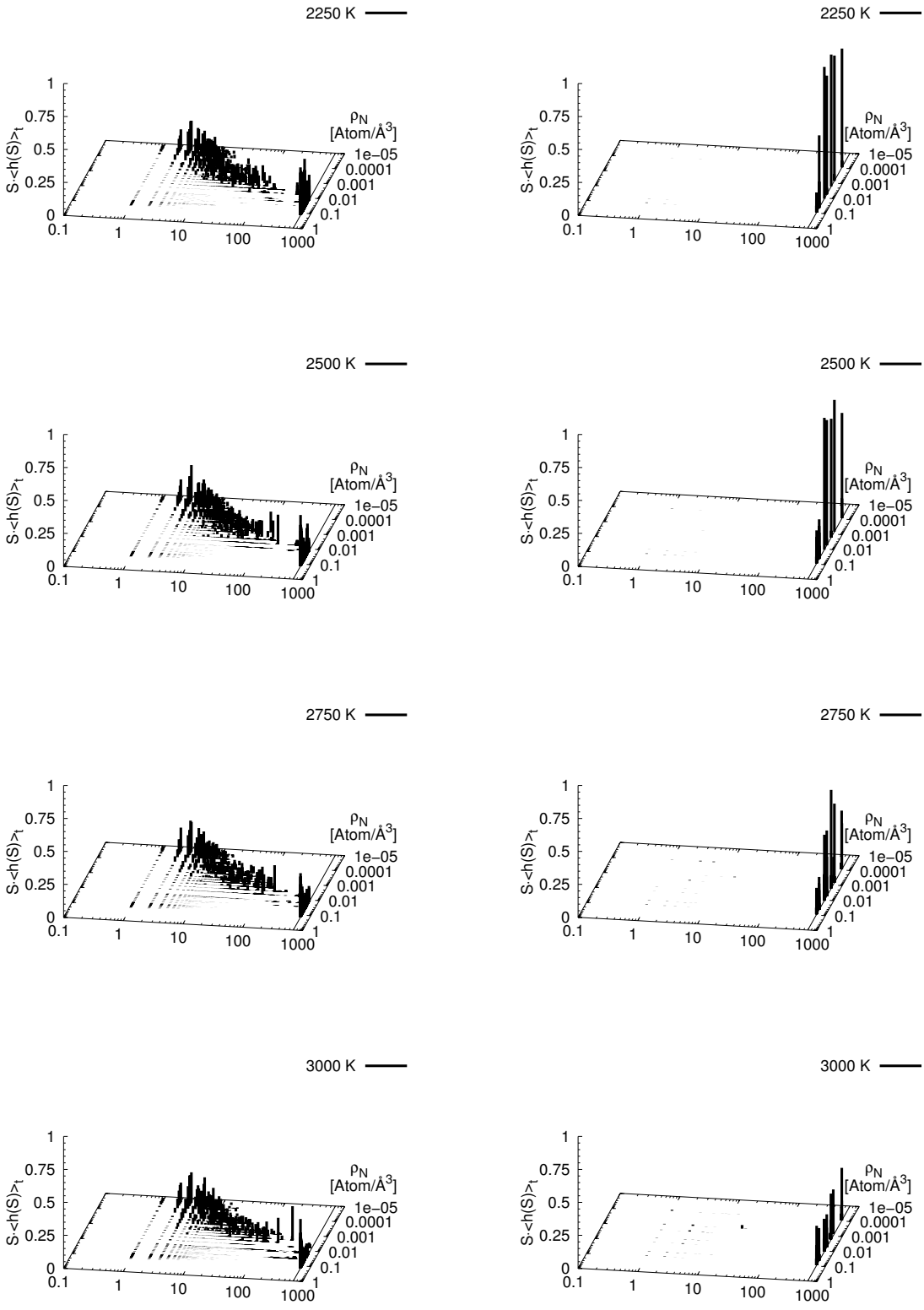

(a) Procedure 1

(b) Procedure 2

Figure 9.5: Dependence of the distribution of the mean number of atoms $S \cdot \langle h(S) \rangle$ inside a cluster of size $S_{cluster}$ on the number density $\rho_N = N/V$ for temperatures $2000 \leq T \leq 3000$ K.

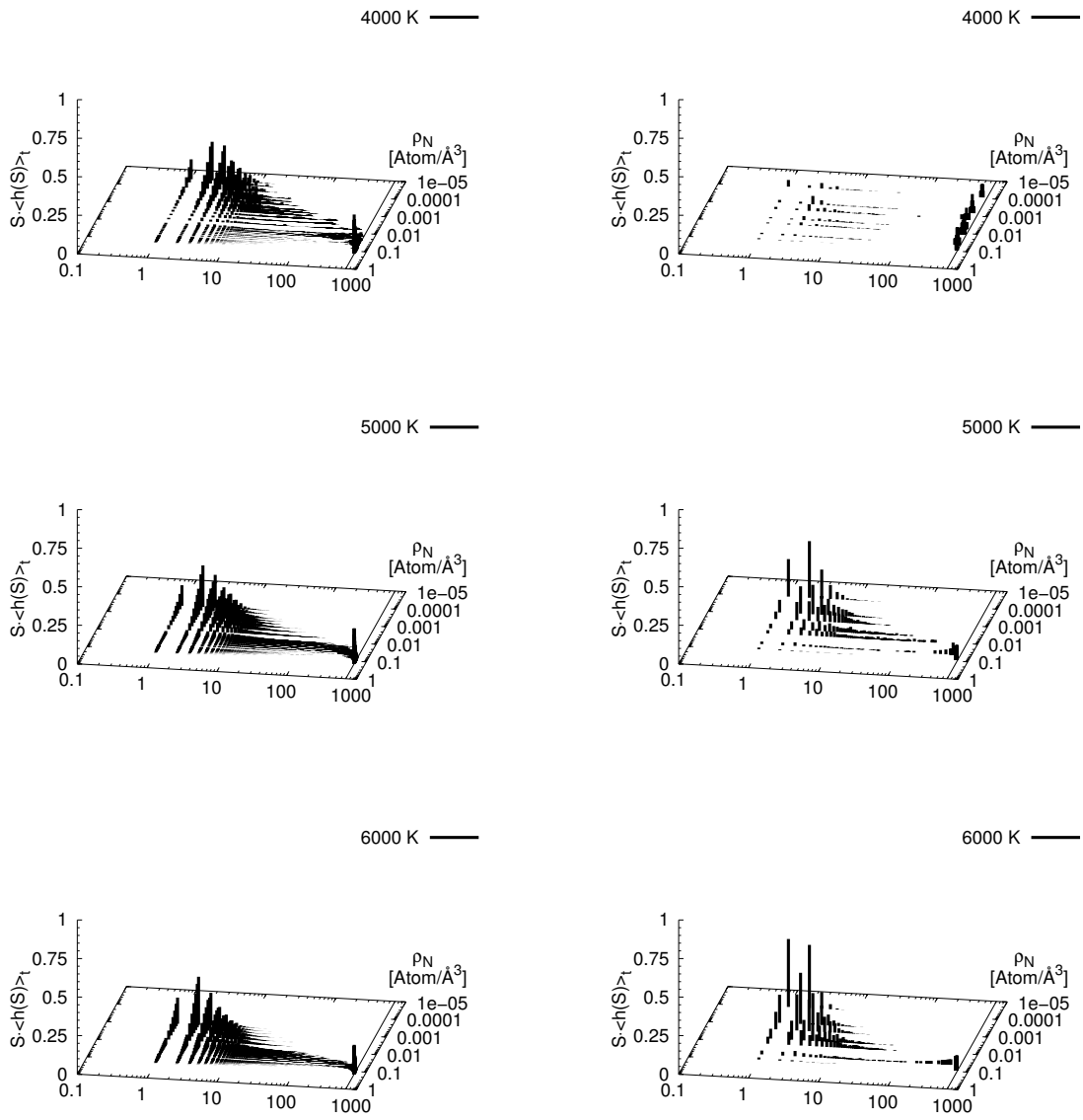

(a) Procedure 1

(b) Procedure 2

Figure 9.6: Dependence of the distribution of the mean number of atoms $S \cdot \langle h(S) \rangle$ inside a cluster of size $S_{cluster}$ on the number density $\rho_N = N/V$ for temperatures $T > 3000$ K.

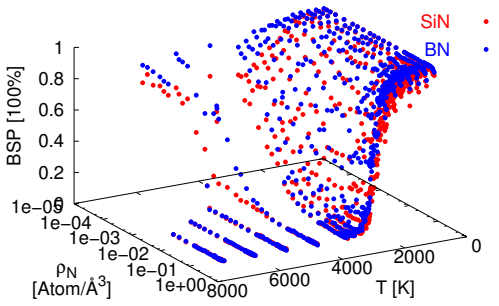

(a) Procedure 1

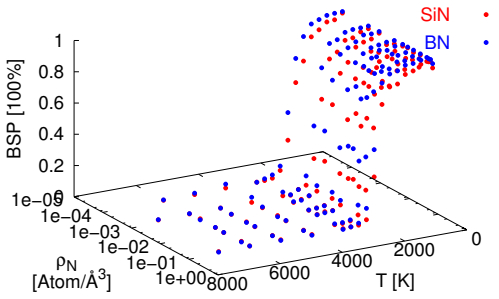

(b) Procedure 2

Figure 9.7: Temperature and density dependence of the time averaged bond survival probabilities BSP for silicon nitrogen (red) and boron nitrogen bonds (blue). The temperature is given in K and the densities are given in Atoms/Å^3. The time averages were calculated over the last $2 \cdot 10^4$ MCC observation time steps and the BSP were calculated with respect to a waiting $t_w = 5 \cdot 10^5$ MCC. The total observation time was $t_{obs} = 5 \cdot 10^5$ MCC.

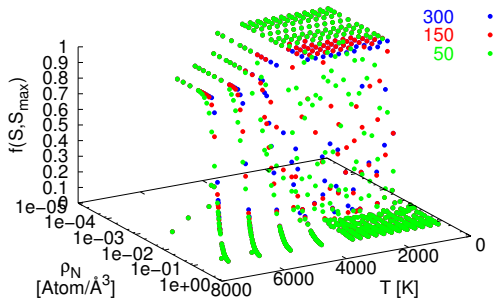

(a) Procedure 1

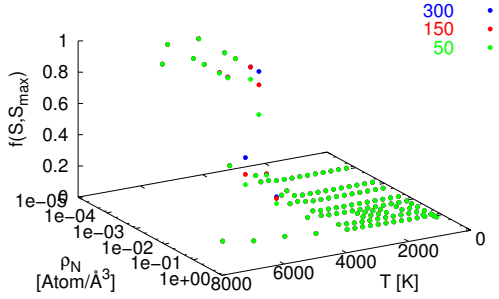

(b) Procedure 2

Figure 9.8: Dependence of fraction of atoms $f(S, S^*)$ defined by equation 9.3 on the number density ρ_N (given in Atoms/Å^3) and the temperature T (given in K) for three different choices for maximum cluster size S^* employed in the calculation of $f(S, S^*)$

studies of aging and the ergodic-non-ergodic transition (chapters 10 and 12), we select $1/e(\approx 0.3)$ and 0.8 as the critical values for the BSP: For $BSP < 1/e$, we are dealing with a liquid, and $BSP > 0.8$ indicates a solid.

Finally, we turn to the diffusion constants shown in figure 9.9. Similar to the distinction between a glass and a (supercooled) liquid, we called the system an (amorphous) solid[6], if the diffusion coefficients $D(V,T)$ were below 0.01 Å^2/MCC (corresponding to about $2{\cdot}10^{-3}$ cm^2/sec). Using this approach, we note that the condensed phase remains solid up to about 1750 K. Furthermore, we see a significant increase of $D(V,T)$ for all temperatures when lowering the density - here, the contribution of the gas phase to the average diffusion coefficient makes itself felt, of course.

9.3.3 Construction of the (metastable) phase diagram

From the results of the previous subsection 9.3.2, we can construct phase diagrams in the (V,T) plane, shown in fig. 9.10 Both procedures yield very similar results for densities above 0.01 atoms/Å^3, and also for temperatures above 4000 K. As expected, the differences are most visible in the low temperature-low density region. In order to decide, which of the two procedures produces the more accurate results in which region of the phase diagram, we have estimated the free energy for both procedures, using

$$F^{(1,2)} \approx \langle E \rangle_t^{(1,2)} - T\langle S \rangle_t^{(1,2)}, \qquad (9.4)$$

where $\langle E \rangle_t^{(1,2)} = \langle E_{kin} \rangle_t^{(1,2)} + \langle E_{pot} \rangle_t^{(1,2)} = \langle E_{pot} \rangle_t^{(1,2)} + 3/2 N k_B T$. For the entropic contribution $\langle S \rangle_t$, we employed a simple lattice gas approximation[7]

$$\langle S \rangle_t \approx \langle N_{cl} \rangle_t \ln(V/V_0), \qquad (9.5)$$

where we assume that the cell volume $V \gg V_0$ is much greater than the cluster, and the average number of clusters is much greater than 1.

[6]Recall that up to now, no crystalline ternary modification has been synthesized, and we have not seen any tendency to form crystalline phases in our simulations.

[7]See appendix A.1 for details.

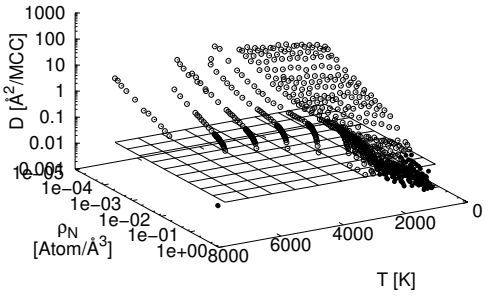

(a) Procedure 1

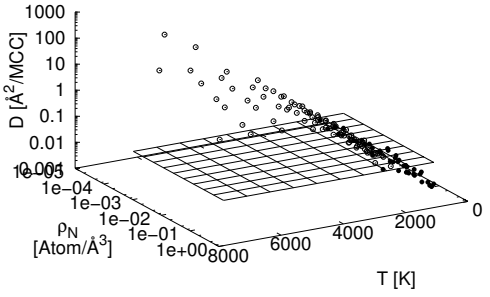

(b) Procedure 2

Figure 9.9: Temperature and density dependence of the diffusion coefficients D. The temperature is given in K and the densities are given in Atoms/Å^3.

Since we are only interested in the approximate difference between the two systems, we did not include the entropic contributions due to the vibrations of the atoms belonging to the various clusters in this simple estimate.

Using equation 9.4, we find that for $T \leq 3000$ K, $F^{(2)} \leq F^{(1)}$ (c.f. fig. 9.11). In particular, the low density region $\rho_N < 0.01$ atoms/Å^3 appears to be better described by procedure 2. Thus, for this volume and temperature range, the system is in the condensed phase, with only a minute amount of gas phase present. On the other hand, for $T \geq 4000$ K, $F^{(1)} \leq F^{(2)}$, indicating that here in the low density region a gas-like cluster fluid is present that is separated from the condensed (liquid) phase by a two-phase co-existence region.

Figure 9.12 shows the final (metastable) phase diagram. We see that up to about 2000 K, the system is a solid for all densities investigated. For $T \approx 1750 - 2000$ K, we find a "liquid-solid" co-existence region, based on the analysis of the BSPs and the diffusion coefficients. Apart from technical aspects of the simulations, such as finite simulation times and system sizes, the reason for the existence of such a region is the occurrence of a glass transition in this temperature range between the liquid melt and the amorphous solid. Up to about $3000 - 4000$ K, we find the liquid state, with a small admixture of gas phase molecules. For even higher temperatures, the gaseous state prevails. Here, we also find a certain volume range, where both liquid and gas phase are present in substantial amounts. Extrapolating from our data, we estimate that this co-existence region should continue up to about $8000-9000$ K, resulting in a critical point at about $\rho_{cr} \approx 0.03$ atoms/Å^3 and $T_{cr} \approx 8500$ K.

9.3.4 Cavities in the amorphous phase

As was noted in the introduction, the experimentally observed density of the (amorphous) solid phase is about 30 % less than the weighted average of the binary crystalline compounds Si_3N_4 and BN. Furthermore, slow cooling from the melt in simulations (see chapter 8) also leads to densities in the amorphous phase that are considerably higher ($\rho_m \approx 2.7$ g/cm^3) than the experimental value.

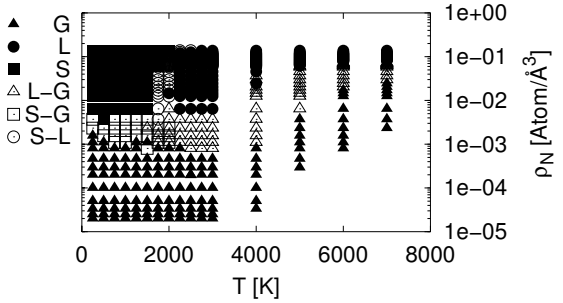

(a) Procedure 1

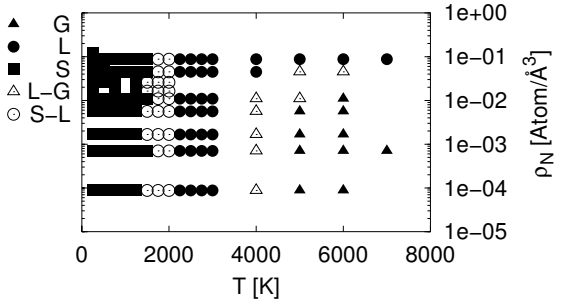

(b) Procedure 2

Figure 9.10: Estimates of phase diagrams of the $Si_3B_3N_7$ system using procedures 1 and 2. G: gas phase, L: liquid phase, S: solid phase, L-G: liquid-gas region, S-L: solid liquid coexistence S-G: solid-gas coexistence.

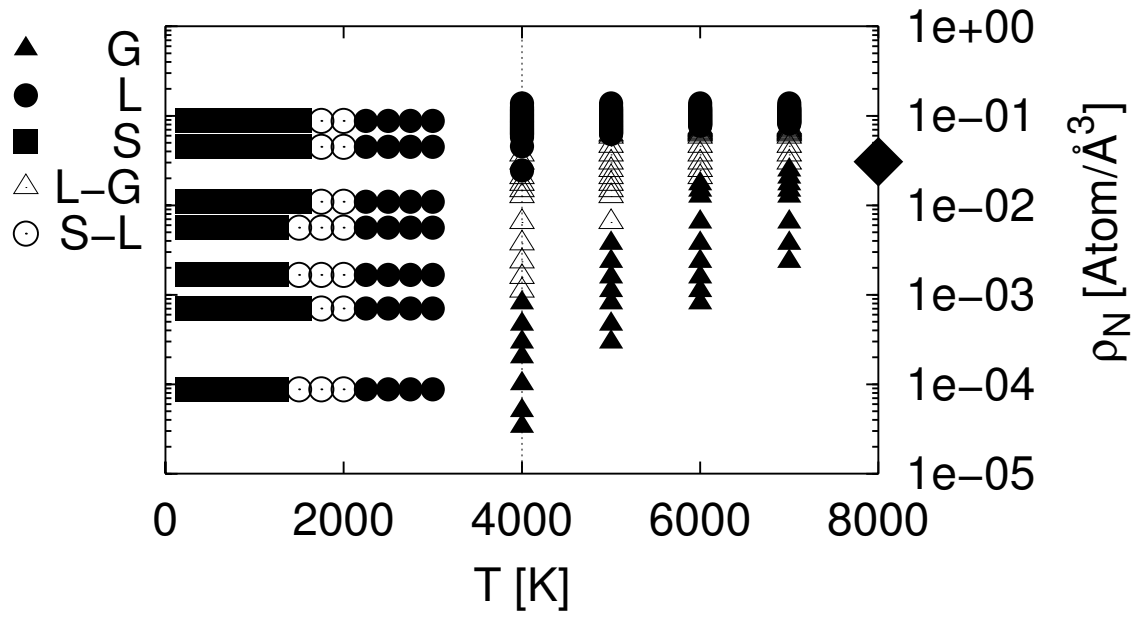

Figure 9.12: Phase diagram estimate for $Si_3B_3N_7$. G: gas phase, L: liquid phase, S: solid phase, L-G: liquid-gas region, S-L: solid liquid coexistence. The data below 4000 K (indicated by the dotted vertical line) was taken from procedure 2 and the data above 4000 K was taken from procedure 1. See figure 9.10 for comparison. The large filled diamond is the estimate of the critical point of the $Si_3B_3N_7$-system.

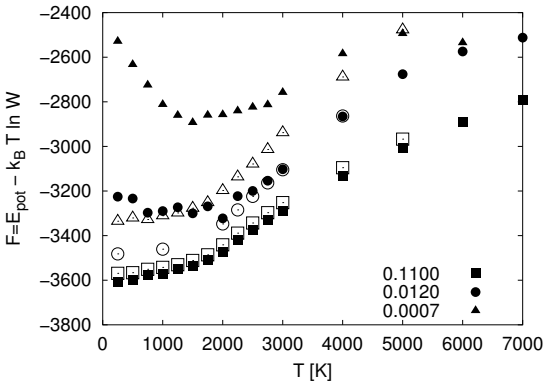

Figure 9.11: Temperature dependence of the free energy estimates $F^{1,2}(T;V)$ for procedures 1(open symbols) and 2 (filled symbols) for three typical isochores. The free energies are given in eV and the temperature is given in K. Number densities are given inside the figure.

One possible reason is the existence of small voids below the nanometer scale, which might escape detection in the experiment but nevertheless are stable enough to survive the high temperatures the compound faces during synthesis and later applications. Experimentally, this interpretation is supported by the fact that the available a-$Si_3B_3N_7$ samples have all been synthesized via the sol-gel process, which starts with the formation of oligomeric networks from single molecule precursors. These polymers are then pyrolized at about 1500 K to form the final ceramic. Simulations of this process (see chapter 6) suggest that during the polymerization and pyrolysis stages a substantial number of nano-size cavities might be formed and/or survive leading to a homogeneous (on length scales above 1 nm) ceramic containing about 30 % nano-voids.

From the thermodynamic point of view, two issues are of interest: the coarsening process in the system, and the stability of the cavities as function of size and external temperature. One should note in this context, that during real coarsening processes in the experiment, the coarsening by itself does not change the total volume of the material containing the voids - only the diffusion of voids/vacancies to the surface (the infinite pore!) can reduce the volume and raise the density. After the voids near the surface have been eliminated, a crust is formed, which prevents further changes in the density although the coarsening inside the material can continue. In contrast, during constant pressure simulations with periodic boundary conditions the size of the simulation cell can easily change. As a consequence, the vacancies can easily be removed from the system - in a way the "surface" is only about the length of the simulation cell (here: 40 Å!) away. Thus, the stability of voids we observe in such simulations will actually lie much below the one in real materials.

In the following, we are going to present two sets of simulations: Constant volume simulations at the experimental density ($\rho = 1.9$ g/cm^3) for a range of temperatures in the solid state (T $<$ 2000 K) and in the liquid state (T$>$ 2000 K), analogous to those presented in subsection 9.3.1, and constant pressure simulations at the same density but with voids of various sizes already present.

Turning to the first set of runs, we note that the process of creating starting configurations at high volume (low density) by re-scaling of equilibrated melt configurations results in starting configurations that contain an essentially homogeneously distribution of "sub-Ångstrom size cavities" due to an equal stretching of the bonds among the atoms ("stretched melt configurations"). For low temperatures, i.e. in the solid amorphous state, this should lead to the formation of larger voids via a coarsening process. Once these voids have reached a size sufficient for them to possess an intrinsic stability, i.e. beyond the critical nucleation size for voids, we can relax the constant volume requirement and study their stability using constant pressure simulations.

Fig. 9.13 shows the average void size as function of time in MCC. Since we were expressly interested in the non-equilibrium phenomenon of coarsening, we have started collecting the data after a short initialization phase of 5000 MCC. We are not able do detect any coarsening processes during the simulations. However averaging over these trajectories, we observe two different regimes in the temperature dependence of the average number of voids $N_{voids}(T)$ (see figure 9.14). For temperatures $T < 2000$ K, the number of voids decreases with increasing temperature, and for $T > 2000$ K, the number of voids increases

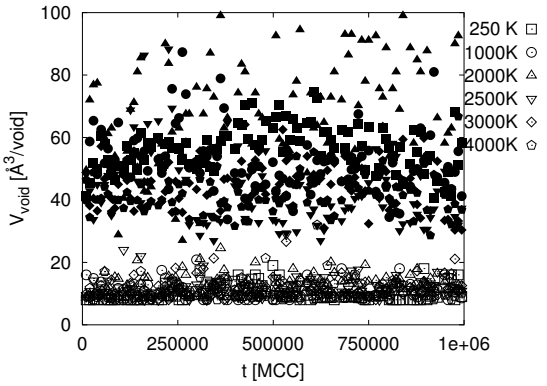

Figure 9.13: Time dependence of the mean void size in the 'stretched-melt' configurations. The configurations were calculated at fixed density 1.9 g/cm^3 and the temperatures given in figure. Open/filled symbols depict results for lattice spacings of 2.0/3.0 Å, that were employed in the void determination algorithm described in section 4.1.2, respectively.

with increasing temperature. Note that the number of voids is determined from a lattice with lattice spacing Δa, and the shape of the voids is not necessarily spherical, and thus the results depend on the lattice spacing. Figure 9.15, depicting the dependence of the number of determined voids on the lattice spacing Δa, shows that for the selected lattice spacing, we determined the maximum number of voids. For $\Delta a \leq 2.0$ Å, the algorithm would determine too few voids, since it is very likely to find a very large cluster of voids, that reaches through the whole simulation cell. On the other hand, using a very large lattice spacing, leads to a too coarsened picture of the void size distribution, since in that case it is very likely to find an atom in a cube, thus leading to an erroneous conclusion that the analyze cube of volume 5^3 Å^3 is occupied.

However, since the time scales we are able to cover in our simulations are not very large compared to the ones typically observed in coarsening experiments (see above), we have in addition studied systems containing larger predefined cavities (see also section 8.4.2). Here, we employed constant pressure simulations at temperatures up to 4000 K. In order to start from locally equilibrated configurations, we first placed spherical cavities of various sizes ($R_p = 3, 5, 8$ Å) inside simulation

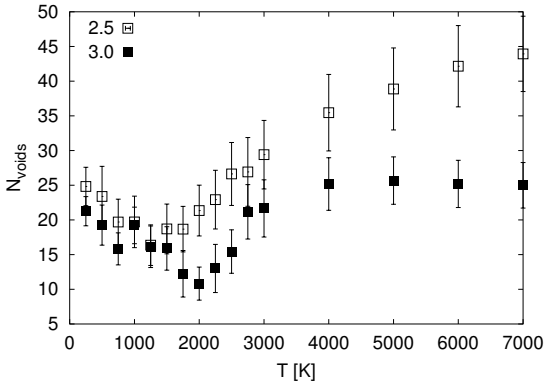

(a) Number of voids

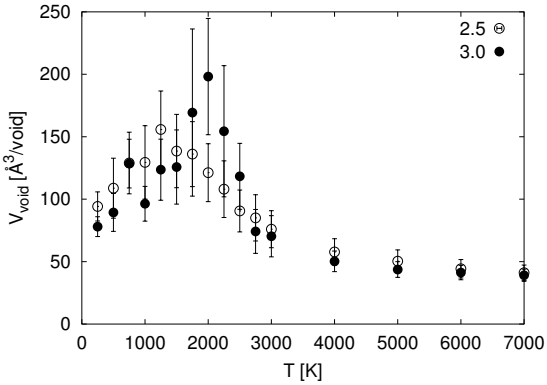

(b) Volume of voids

Figure 9.14: Temperature dependence of the mean number of voids and the mean void volume inside 'stretched melt' configurations, that have a density of 1.9 g/cm^3. Open/filled symbols depict results for lattice spacings of 2.5/3.0 Å, that were employed in the void determination algorithm described in section 4.1.2, respectively.

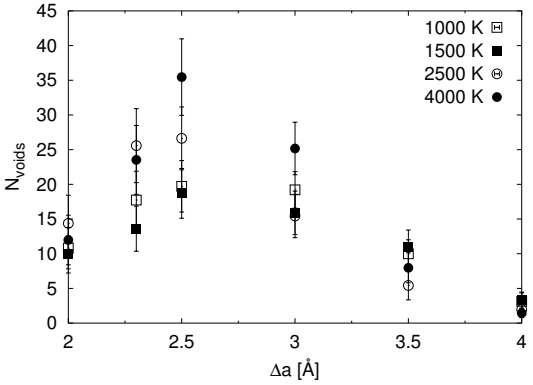

Figure 9.15: Dependence of the mean number of voids inside 'stretched melt' configurations, that have a density of 1.9 g/cm^3 on the lattice spacing Δa for different isotherms.

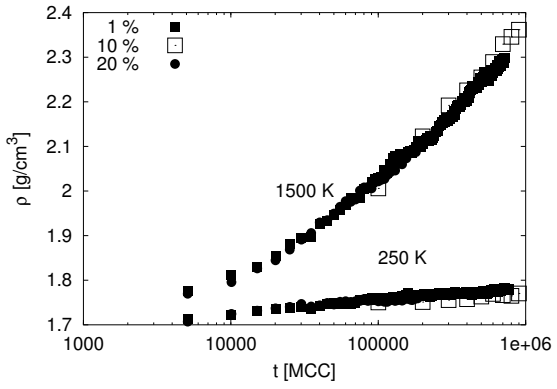

Figure 9.16: Time dependence of the mass density ρ (in g/cm^3) for different probabilities of performing a cell variation in the MC-NPT simulations. The system size was 5200 atoms and initially voids of radius $R_{vac} = 8$ Å, were introduced. See also figure 9.17.

cells filled with 5200 atoms at the experimental density of 1.9 g/cm^3. These configurations were equilibrated for $5 \cdot 10^4$ MCC with fixed cavities inside at temperature T and zero external pressure. The moveclass consisted of single atom displacements (99 %) and isotropic cell changes (1 %).[8] In order to avoid changes in the cavities already during this initialization phase, we replaced the cavity by an impenetrable hard sphere, for computational purposes:

$$V_{pore-atom}(d) = \begin{cases} +\infty & : \quad d \leq R_p \\ 0 & : \quad d > R_p \end{cases} , \quad (9.6)$$

where d equals the distance between the center of the pore and the atom.

Next, we removed these spheres and allowed the system to relax for 10^6 MCC. In this fashion, we could observe the stability of large cavities as function of temperature and time, and also compare the energies of these configurations with the ones we found during the equilibration of the stretched-melt configuration.[9]

[8] The relaxation calculations were repeated for different ratios of atom/cell moves and no significant variations were found (see figure 9.16).

[9] A further advantage of starting with large cavities from the outset is the fact that such cavities are expected to exist during the final pyrolysis stage of the sol-gel process as mentioned earlier (see chapter 6). Thus, we can consider these solids with predefined cavities as representatives of the outcome of the sol-gel process.

Not surprisingly, we find that large voids are more stable than small ones (c.f. figs. 9.18 and 9.17). But even cavities with diameter 3 Å remain stable after a first densification phase up to 1000 K, while voids with diameter 8 Å survive up to 1500 K. Keeping in mind the effective closeness of the "surface", this suggests that nano-voids can very well survive the high temperature treatment the amorphous ceramic is exposed to. This agrees well with the observation that the diffusities of the hard-spheres rapidly decreases when decreasing the temperature below 2000 K (see figure 9.19). Fig. 9.18 shows the densities of the relaxed material averaged over the final $2 \cdot 10^5$ time steps, where one again sees that for the largest vacancies the most rapid increase in density only occurs above 1500 K.

9.4 Discussion

In the preceding section, we have analyzed the cluster size distribution observed for the two simulation procedures. Next, we have used these distributions together with information about the bond survival probability and some simple estimates of the free energy to deduce a phase diagram for the ternary region of the system $Si_3B_3N_7$. Finally, we have investigated the stability of voids inside the amorphous solid a-$Si_3B_3N_7$, in order to understand the surprisingly low density of this ceramic.

By extrapolation from the phase diagram, we estimated that the system should possess a critical point in the liquid-gas region at about $T_{cr} \approx 8500$ K and $\rho_{cr} \approx 0.03$ atoms/Å^3. Another way to gain an estimate for the location of this critical point is to attempt to fit the $p(V,T)$ curves in the high-temperature regime to an empirical equation of state. As we noted in subsection 9.3.3, procedure 1 appears to lead to somewhat more realistic values for this region ($T \geq 4000$ K). Thus, we have performed a fit of the simulated data of procedure 1 to a van der Waals equation,

$$(p + p_0(V,T))(V - b(V,T)) = N_{atom} k_B T, \quad (9.7)$$

where p_0 is commonly assumed to depend on volume via $p_0 = a/V^2$, and b is identified with the atomic volume $b = N_{atom} V_{atom} = V_0$.

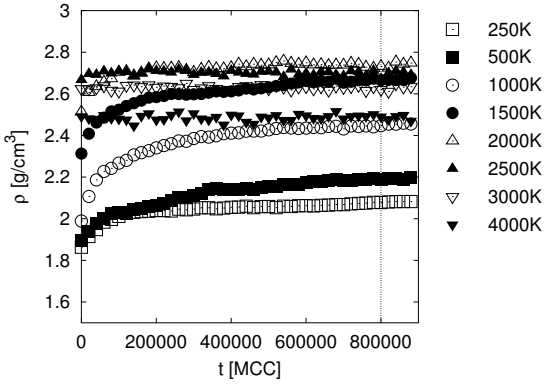

(a) R_{vac}=3 Å

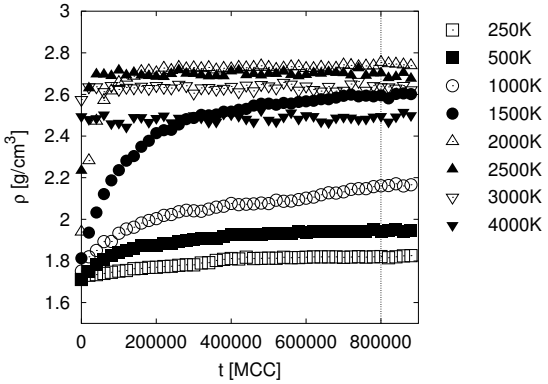

(b) R_{vac}=5 Å

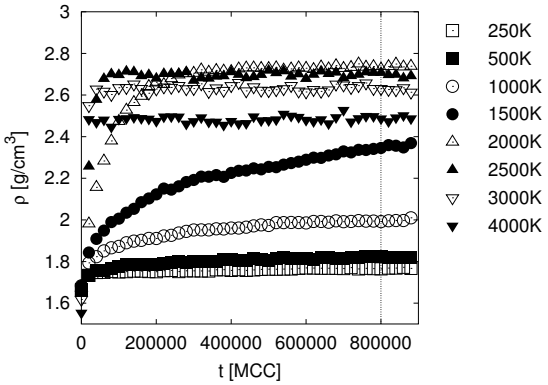

(c) R_{vac}=8 Å

Figure 9.17: Dependence of the mass density ρ (given in g/cm^3) on the simulation time t (in MCC) for vacancies of radii $R_{vac} = 3, 5$ and 8 Å at various temperatures both below and above the glass transition temperature $T_c \approx$ 2000 K. The dotted vertical lines in the figure indicated the time t_w after the time averaging has been performed.

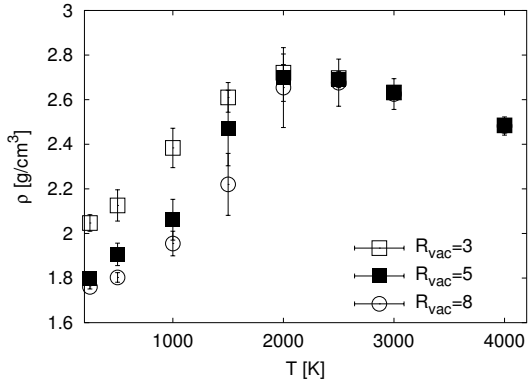

Figure 9.18: Temperature dependence of the time averaged mass densities ρ (in g/cm^3) for the amorphous $Si_3B_3N_7$ system that contained voids of radii $R_{vac} = 3, 5$ and 8 Å initially.

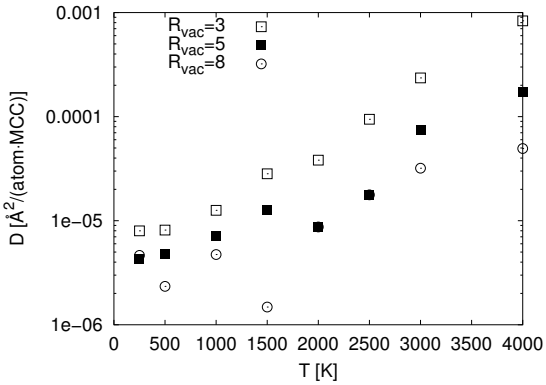

Figure 9.19: Temperature dependence of the diffusion coefficients of the vacancies, modelled as hard-spheres for different sizes of vacancies.

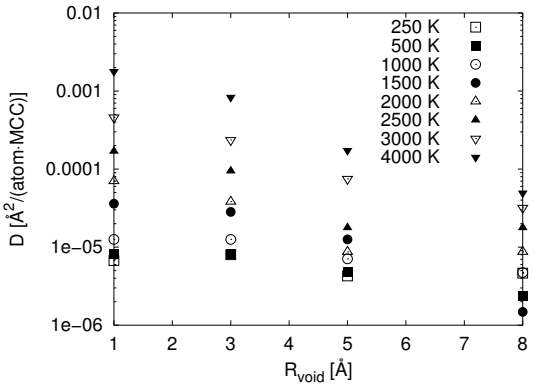

Figure 9.20: Dependence of the diffusion coefficients of the vacancies on their size for different temperatures. The vacancies were modelled as hard-spheres with radii R_{vac}. The vacancy size of 1 Å corresponds to the diffusion of the atoms.

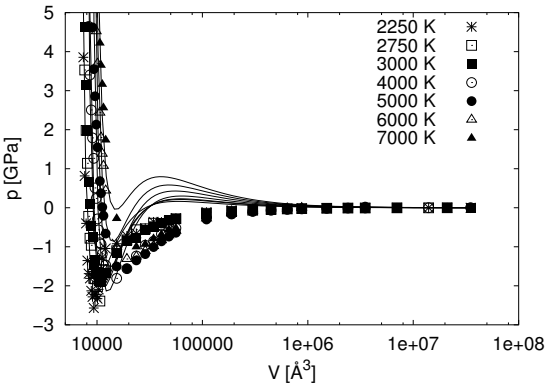

Figure 9.21: Volume dependence of the pressure and fits to the van der Waals equation 9.7 for isotherms above 2250 K calculated from procedure 1.

As we see from figure 9.21, the fit works best for high and low densities, while the negative pressures in the intermediate density region are not well described. From the fit parameters, we can now calculate the critical values for pressure, temperature and density, $p_{cr} \approx 1.3$ GPa, $T_{cr} \approx 8000$ K and $\rho_{cr} \approx 0.032$ atoms/Å^3, respectively. This is in satisfactory agreement with our rough estimate from the phase diagram.

Of course, we cannot expect the system to completely obey the equation of state of a van der Waals fluid. The reason is that the mean field picture that justifies eq. 9.7 by assuming essentially identical monoatomic featureless fluid particles interacting with the mean field created by the other particles in the system, qualitatively fails for $Si_3B_3N_7$. As we saw in subsection 9.3.2, even at very high temperatures and large volumes, we still observe nonneglible atom-atom interactions that result in the presence of small clusters of atoms in the fluid phase. Of course, these will contribute to the free energy of the system, and, in the context of the van der Waals picture, result in terms in p_0 that are only very weakly dependent on volume, $p_0 \approx a_1/V^\alpha + a_2/V^2$, with $0 < \alpha < 2$.

On the other hand, the mean field picture is moderately realistic for the state of the fluid at high densities, where most atoms are part of larger clusters, and thus all atoms experience the same "average" interaction over the observation time. We note that, on this level of sophistication, this also includes the solid state of the system. As we have seen, distinguishing between the liquid and the solid state is more subtle at this level, of course, and requires the introduction of time-dependent quantities such as the bond survival probability, or the mean square displacement.

Another issue we should mention is the fact that quite a number of data points are in a region, where in the van der Waals picture we would expect the system to be thermodynamically unstable. In our simulations, this makes itself felt as a phase separation into e.g. a liquid-plus-gas or a solid-plus-gas mixture. One possible way to improve on the van der Waals fit is to use a virial expansion of Z as function of powers of the density. This has been done, and it does improve the fit, but does not lead to much further insight.

We have repeatedly indicated that the phase diagram we present is an intrinsically metastable one, and strictly only applies for the ternary region of the space of Si/B/N compounds. The reason for this caveat is threefold:

For one, the time scales of the simulations we are able to perform[10] are several orders of magnitude below those needed for the system to reach full thermodynamic equilibrium. One consequence of this is that we never observe a crystalline variant of $Si_3B_3N_7$ nor the formation of crystalline binary phases such as Si_3N_4 or BN. Furthermore, except at high temperatures, we did not reach convergence of the two simulation procedures to the same equilibrium state[11]. While we were able to perform some simple (free energy based) estimates, which procedure was more appropriate for which region of the phase diagram, we were not assured to have reached equilibrium in either one. In the solid state at low temperatures, all configurations observed were amorphous structures. For comparison, we also computed the energy of several hypothetical crystalline structure candidates, and also the energies of the binary crystalline compounds β-Si_3N_4 and h-BN. We find that the energetically lowest state corresponds to a weighted mixture of β-Si_3N_4 and h-BN, fol-

[10] The simulations presented took the equivalent of about 10 years on an AMD+1800 processor.

[11] Many other criteria did appear to indicate equilibrium at temperatures above 2000 K, however, such as the potential energy.

lowed by the ternary crystalline modifications of $Si_3B_3N_7$ (see table 3.1). Thus, the ternary phase diagram derived can only be termed "metastable".

We do know that the ternary crystalline state does melt at about 2500 K (see chapter 10). Thus, including the crystalline state does not have much of an influence on the shape of the phase diagram, except at very high densities. Regarding the BN and Si_3N_4 phase separation, we do have to note that this would (in the context of the simulations using a finite simulation cell) correspond to an unpleasant interface, at least in the solid state, which might prevent us from seeing it compared to e.g. the ternary crystalline state. Even though it would be highly interesting, to put bulk BN and Si_3N_4 into a simulation cell and just heat the two solid phases and investigate the phase behaviour of these mixtures, the current computational power and difficult algorithmic questions prohibit these kind of investigations at the moment.

A second complication is the finite size of the system. While simulations of e.g. Lennard-Jones and soft-sphere systems have been performed in the past[12], $Si_3B_3N_7$ is considerably more involved, and thus we were limited in the system size we could treat. As is well-known, finite size effects, in particular the existence of non-negligible surfaces of the condensed phase and the formation of interfaces between condensed and gaseous phases, bedevil the computer experimentalist[42]. Clearly, this is a reason behind the appearance of negative pressures at intermediate densities. In order to gain some insight into the effects of finite size, we have repeated the calculations for a system of half the size ($N_{atom} = 351$), for both procedures. In order to save some computation time, we have performed these calculations on a wider grid of volume values, but for the full temperature range. We find no qualitative change from the results in the larger system, as can be seen from figure 9.22, in which we plot the temperature dependence of the average potential energies of configurations generated by procedure 2 for system sizes 702 and 351 atoms.

[12]See chapters 8-10 of Frenkel's book [42].

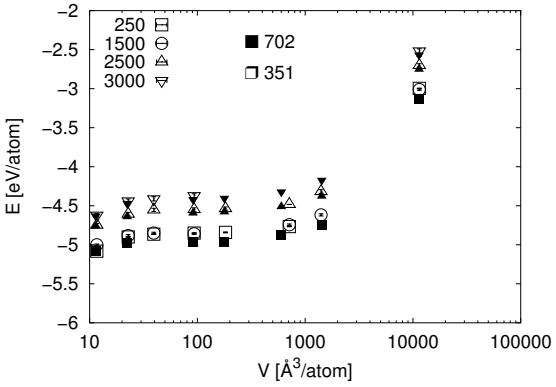

Figure 9.22: Volume dependence of the potential energy for selected isotherms for two system sizes generated by procedure 2.

Finally, there is the question of the potential we have employed to model the interactions among the atoms. While it is well-suited to represent hetero-atom interactions between different types of atoms, it does not properly apply to the elements themselves, i.e. for neither elementary Si or B nor N_2 molecules can one compute the correct bond energies that would allow a comparison with the bond energies among those different types of atoms. In particular, our results must exclude the formation of Si, B or N_2 vapor. Especially the latter is sorely missed, since it might most easily form at high temperatures and low pressures, opening a possibly important route to decomposition of the ternary compound. From the point of view of the experimentalist, mapping the phase diagram outlined in this work should therefore presumably take place in a nitrogen saturated atmosphere.

A very rough estimate of the pressure needed to suppress the evolution of N_2 from the condensed phase at relatively low temperatures can be derived from comparing the free energies,[13]

$$F(Si_3B_3N_7) \approx E(Si_3B_3N_7) \approx E(Si_3N_4)+E(BN) \tag{9.8}$$

and

$$F(Si, B, N_2) \approx E(Si, B)+E(N_2)-k_BT \ln g(N_2), \tag{9.9}$$

where $g(N_2)$ is the number of ways N_2 molecules can be placed in a cubical box of volume V.

[13]For details of the approximations, see appendix A.2

This yields

$$p_{limit}(T) \approx \rho_{limit} k_B T, \tag{9.10}$$

with

$$\rho_{limit} \approx 0.1 \cdot \exp[(E(\mathrm{Si_3N_4}) + E(\mathrm{BN}) - E(\mathrm{Si,B}) - E(\mathrm{N_2}))/(N(\mathrm{N_2})k_B)T] \tag{9.11}$$

in units of atoms/Å^3. Taking these data from experiment, we find $p_{limit} \approx 0.16\ k_B T$. In particular, p_{limit}(2000 K) $\approx$ 0.01 eV/atom $\approx$ 4 GPa.

A similar cluster-size analysis has been performed in the past[139] for the derivation of the phase diagrams of many elementary compounds, such as elemental sodium. There, an analytical mean-field expression of interacting clusters was investigated and the corresponding Gibbs free energy was minimized with respect to the average cluster size and the overall density. For metals, it was found that the typical cluster sizes were very small ($N_{cl} = 1-3$)[14], while for group 4 elements that exhibit a stronger tendency towards network formation, the melt contained clusters of size up to ten close to the freezing temperature.

Much of the more recent work has focused on the liquid-gas region and to a lesser extent on the solid-gas region, where large computer simulations have been performed. In particular, Lennard-Jones[79, 73, 14] type and hard and soft sphere systems[2] have been investigated. However, these systems are not well suited to model network forming systems that can exhibit a wide variety of clusters in the liquid-gas region of the phase diagram. This also extends to the Gibbs ensemble simulations of phase-equilibration[121], since the exchange of atoms between the liquid (not to mention the solid[15]) and gaseous phases is far from trivial in a system like $Si_3B_3N_7$.

Turning to the question of nano-voids in the amorphous solid a-$Si_3B_3N_7$, we note that the larger voids are more stable than smaller voids below 1500 K, and that only above 1500 K the density of the void-prepared a-$Si_3B_3N_7$ increased significantly in the variable cell MC-simulations.

The vacancy analysis of the NVT simulations at $\rho_M = 1.9$ g/cm^3, has shown, that above the glass transition temperature of $T_G \approx 2250$K, the average void volume decreases with increasing temperature, whereas below T_G, the average void volume increases with increasing temperature; most probably, the surrounding Si/B/N matrix compactifies. Furthermore, the diffusion coefficients of the voids, modelled as hard spheres, follow approximately a $D(R_{void}, T) \propto R_{void}^{\alpha(T)}$ law (see figure 9.20), with a temperature dependent exponent $\alpha(T) = 2-3$. Unfortunately, it is impossible to study the dynamics of the voids once the hard sphere constraints are removed due to algorithmic difficulties in the identification of the voids, together with a subsequent analysis of the void's motion. Nevertheless, one should note that due to the isotropic amorphous nature of the material, no fast diffusive pathways (e.g. via grain boundaries[140]) are available that allow the exchange of material among the pores and thus speed up the coarsening process. Thus once a certain size of cavities has been reached such that no contact via shape modulation is possible anymore[16], we expect further coarsening processes to follow the Lifshitz-Slyozov $t^{1/3}$ law[93]. As a consequence, we are unlikely to observe many pores larger than 1 nm in real materials, unless these have been formed already during the sol-gel process. Finally, these voids have not yet been observed experimentally for a-$Si_3B_3N_7$ due to measurement difficulties, but recent work by Sauter et al. [132] has shown that in amorphous Si-B-C ceramics, voids with a diameter of about 6-8 Å are present.

[14] In the super-cooled state, the cluster size could increase considerably.

[15] An interesting extension to Gibbs ensemble simulations to cover solid-vapor phase equilibria has recently been proposed [27]

[16] Once two cavities get into contact, the surface tension in the neck leads to a rapid merger [90, 141].

Chapter 10

Glassiness of a-$Si_3B_3N_7$

10.1 Introduction

In chapter 9, we determined the metastable phase diagram of the $Si_3B_3N_7$-system for a wide range of densities and temperatures. In this and the forthcoming chapters, we focus on the density regime (ρ_N= 0.07 - 0.11 $Å^{-3}$), in which we observed a solid-to-liquid transition of the $Si_3B_3N_7$system. We will show that a-$Si_3B_3N_7$ indeed shows a glass transition by determining the temperature T_C at which an ergodic to non-ergodic transition occurs. Furthermore we show that close to T_C the self-diffusion coefficient D decreases by orders of magnitude. Additionally we show that the topology of the amorphous covalent network is effectively frozen in below T_C. The total of these observations allows us to predict a glass transition for a-$Si_3B_3N_7$.

10.2 Models and Techniques

In sections 6.3 and 8.4.2, we saw that the low-densities models of a-$Si_3B_3N_7$, compactify at elevated temperatures to give low-energy models with higher density. Therefore, we focus on the low-energy/high-density models we expect to have the highest statistical weight in (quasi-) equilibrium.

We consider a system of N = 702 atoms, which was originally generated by melting the hypothetical crystalline polymorph β_2-$Si_3B_3N_7$[89] at 2500-3000 K using MD-simulations[66]. The atoms were confined to a cubic simulation cell of side length 19.1 Å (ρ_N = 0.11 $Å^{-3}$), and we performed NVT-MC-relaxations at temperatures between 250 and 7000 K for $2 \cdot 10^5$ MCC.[1] Note that the mass density was kept constant at $\rho_{Liquid} \approx 2.75$ g/cm^3. In the MC-simulations, the moveclass consisted of the usual single atom displacements and the maximum atomic displacement d_{max} was adjusted at each temperature to reach an acceptance ratio of 50 % (see section 3.3 for simulation details).

In order to compare the melting point T_M with the glass transition temperature T_G (typically $T_G \approx \frac{2}{3}T_M$[62]), we determined the melting point T_M of the $Si_3B_3N_7$-system. We heated a recently predicted crystalline polymorph of the $Si_3B_3N_7$-system [144] using NVT-MC simulations at different temperatures between 250 and 6000 K. Note that the density of the crystalline modification is $\rho_{Crystal}$ = 2.78 g/cm^3. We denote this procedure 'crystal heating', in contrast to the 'liquid-cooling' scheme described in the previous paragraph.

We determined the ergodic-to-non ergodic transition temperature $T_C \approx T_G$ for the a-$Si_3B_3N_7$-system as that temperature at which the fluctuation-dissipation theorem (FDT) for the potential energy is violated for the first time, upon cooling the system. The FDT for the potential energy holds, if

$$\frac{\Delta\langle E\rangle_{t_w\leq t\leq t_w+t_{obs}}(T)}{\Delta T} \approx \frac{\sigma^2(E)_{t_w\leq t\leq t_w+t_{obs}}(T)}{k_B T^2}, \tag{10.1}$$

where $\langle E\rangle_{t_w\leq t\leq t_w+t_{obs}}$ is the average potential energy of the configurations generated at temperature T and averaged over time after a waiting time t_w. $\Delta\langle E\rangle$ is the change in the average potential energy accompanying a

[1] At each temperature, we generated nine MC-trajectories below 2000 K and 3 MC-trajectories above 2000 K, respectively.

change in change in temperature ΔT. Similarly $\sigma^2(E)_{t_w \leq t \leq t_w + t_{obs}}(T)$ are the fluctuations in the potential energy of the configurations generated at temperature T after a waiting time t_w has elapsed.

As usual the diffusion coefficients were determined from the Einstein-Smoluchwski equation 3.26, after first checking the validity of that equation. The topological stabitity of the networks were characterized by the time dependence of the bond survival propabibalities at a given temperature, and fitting the bond survival probabilities to a Kohlrausch-Williams-Watts law:

$$BSP^{BN/SiN}(t) = \exp[-(t/\tau_{BSP})^{\beta}] \quad (10.2)$$

yielded the relaxation times τ_{BSP} for the B-N and the Si-N bonds in the network, respectively.[2] Fitting the temperature dependence of the diffusion coefficient D and the relaxation times τ_{BSP} to an Arrhenius law,

$$\begin{aligned} D &= A\exp(-\Delta E_D/k_BT), \\ &\text{and} \\ \tau_{BSP} &= A\exp((\Delta E)_{BSP}/k_BT), \end{aligned} \quad (10.3)$$

gave the formal activation energies of diffusion ΔE_D and for bond breaking ΔE_{BSP}. Furthermore, from the diffusion coefficients, one can estimate the critical temperature T_C^{MCT} suggested by the mode-coupling theory (MCT) and the exponent γ of the power-law divergence

$$D \propto (T - T_c^{MCT})^{\gamma}. \quad (10.4)$$

10.2.1 Results

First, we will discuss the temperature dependence of various properties derived from the 'liquid-cooling' procedure, and then turn to the determination of the melting point of the hypothetical crystalline polymorph.

Cooling the liquid

Peaks in the specific heat C_V commonly are associated with phase transitions and, as mentioned, the ergodic to non-ergodic transition of a system is indicated by the violation of the fluctuation-dissipation theorem. Figure 10.1, depicting the temperature dependence of the specific heats C_V calculated according to the l.h.s and the r.h.s of equation 10.1, respectively, clearly shows that in the temperature range 2000-2500 K a phase transition occurs, and furthermore that below 2000 K, the fluctuation-dissipation theorem is violated and ergodicity is broken, hence allowing us to identify $T_C = 2250$ K with the temperature, at which the glass transition occurs. We already note at this stage that the specific heats show some aspects related to aging phenomena, since the specific heat calculated from the fluctuations depends both on the time t_{obs} over which the fluctuations are measured and on the waiting time $t_w = 10^5$ MCC. (see inset of figure 10.1).[3]

Our suggestion of a glass transition occuring at 2250 K is further supported by the significant decrease of the diffusion coefficients $D_{\mathrm{Si/B/N}}(T)$ as T_C is approached from above. Note, that above 2000 K, we are in a regime, where the mean squared displacement MSD depends linearly on time and does not depend on the waiting time t_w, at which the reference configuration for the calculation of the mean squared displacements was chosen. (see fig. 10.2). Furthermore the relaxation times τ_{BSP}, derived from fitting the time dependence of the bond-survival probabilities (fig. 10.4) of the B-N and Si-N bonds, to a Kohlrausch-Williams-Watts law (eq. 10.2), shows that at approximately 2000 K the relaxation times exceed the time scales of our computer experiment. Thus, below 2250 K the network topology is essentially frozen and the system behaves like a solid.

Furthermore, we observe that B-N bonds are more stable than the Si-N bonds, since the corresponding relaxation times are longer for the B-N bonds. Both the diffusion coefficients and the relaxation times τ_{BSP} could be fitted to an Arrhenius law in the temperature range from 2000 to 4000 K, yielding the formal activation energies ΔE_D and ΔE_{BSP} summarized in table 10.1(a).[4] Surprisingly, the activation

[2] The relaxation times τ_{BSP} are independent of the exponent β.

[3] Aging phenomena are more thoroughly discussed in chapter 12.

[4] Fitting the total diffusion coefficient D_{total} to a power law (eq. 10.4) over the whole temperature range, yields a critical temperature $T_c^{MCT} \approx 1965K$.

energies for Si-N bond-breaking are slightly higher than the activation energies for B-N bond breaking. Note also that the activation energies for silicon diffusion and boron diffusion in the liquid state are similar, whereas the activation energies for nitrogen diffusion are slightly higher than their cationic counterparts. This agrees with the experimental observations in the solid state (table 10.1(b)), where it is found that nitrogen diffusion requires a slightly higher activation energy than silicon diffusion. We cannot rigourosly compare the diffusion coefficients to experimental data, since the unit of time of the Monte-Carlo simulations is not known.

A rough estimate is feasible, however, by comparing the mean squared displacements calculated from NVT-MD simulations at 2500 K to the MC results at the temperatures. This results in an estimate of 1 MCC $\approx$ 0.2 fs. Thus a diffusion coefficient of 0.01 Å^2/(MCC) corresponds to a diffusion coefficient of $2 \cdot 10^{-4}$ cm^2/s, which is of the same order of magnitude as the values (D_{Si}(4000 K) $\approx$ 10^{-4} cm^2/s)) one obtains for simulations in amorphous silica above the ergodic to non-ergodic transition temperature.[75] In that context, we note that our activation energies ΔE_D for silicon are about a factor of three smaller than the values obtained from the simulations of amorphous silica.

Below the ergodic to nonergodic transition temperature T_c, the data analysis is severely hampered by insufficient statistics. What can be said however is that the system does not crystallize (see figure 10.8) and the solid amorphous network becomes stiffer as time passes, since more bonds survive the longer the amorphous system has been allowed to relax (see figure 10.6). Note, that it would be also interesting to compare the waiting time and temperature dependence of relaxation times τ_{BSP} in that temperature regime, but the run lengths possible for our simulations do not allow such a comparison.

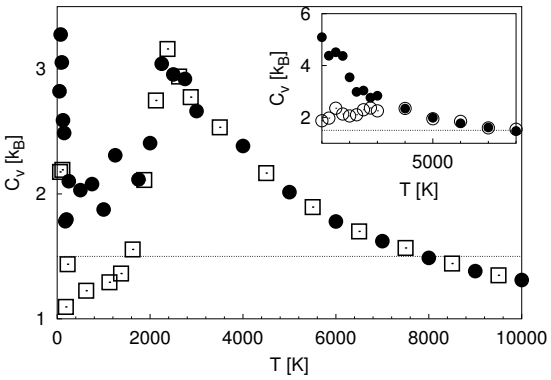

Figure 10.1: Temperature dependence of the specific heat C_V. Open symbols are the specific heats calculated from numerical differentation (l.h.s of equation 10.1) and filled symbols represent the specific heats calculated from the fluctuations (r.h.s of equation 10.1. The inset shows the specific heat calculated from the fluctuations for observation times $t_{obs} = 10^4$ shorter (open circles) than the waiting time $t_w = 10^4$ MCC and an order of magnitude larger observation times $t_{obs} = 10^5$ MCC (filled circles) than the waiting time $t_w = 10^4$ MCC.

Heating of a crystalline polymorph

In the previous subsection, we discussed the temperature dependence of various one-time and two-time properties, once we cool a liquid below the ergodic to non-ergodic transition temperature T_C, which we tentatively identified with the glass transition temperature T_G below which the structural properties changes only very little. It would be of interest to compare the glass transition temperature with the melting temperature T_M of the system. Thus in this section, we analyze the melting of a crystalline polymorph of $Si_3B_3N_7$ in order to determine the melting point.[5] Furthermore, we compare the temperature dependences of the specific heats, the diffusion coefficients and the relaxation times obtained from melting the crystalline polymorphs to the data obtained when cooling from the liquid state.

The specific heat C_V of the heated crystalline polymorph shows a sharp peak at approximately $2500K$ (see figure 10.7), close to the critical temperature observed when cooling the liquid. Furthermore, the data is clearly equilibrium data in the whole temperature range on the time scale of our simulations,

[5] It seems that the melting point of none of the crystalline polymorphs of crystalline silica has been determined in the context of computer simulations and compared to the results of the glassy state of amorphous silica.

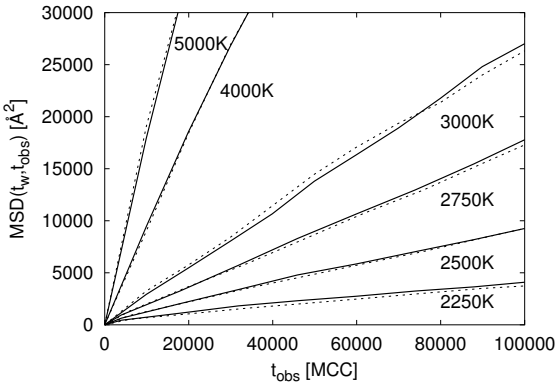

Figure 10.2: Time dependence of the mean square displacements MSD in Å^2 for different temperatures T > T_c. Full lines are the data for a waiting time $t_w = 10^5$ MCC and dotted lines are for waiting times $t_w = 10^4$ MCC.

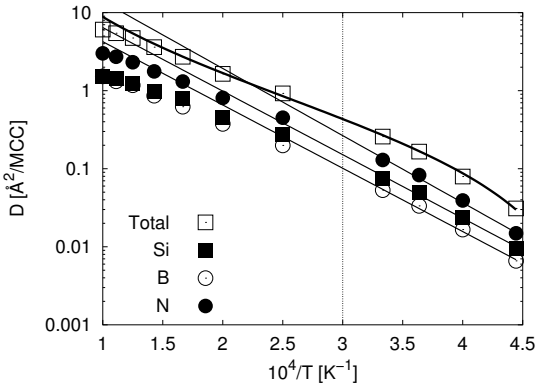

Figure 10.3: Arrhenius plot of the temperature dependence of the diffusion coefficients $D_{Si/B}$ calculated from the mean squared displacements (MSD) depicted in figure 10.2. Full lines are fits to an Arrhenius law (equation 10.3). The very bold line is a fit to a power law (eq. 10.4) yielding a critical temperature $T_c^{MCT} = 1965K$ and an exponent $\gamma = 1.7$.

since both prescriptions yield the same results. Furthermore, we note that the specific heat below 1800 K, is close to $\frac{3}{2}k_B$, the value one expects as the contribution from the potential energy in the harmonic approximation.

The heated crystals remain quasi-crystalline up to about 2250 K, as can be seen from figure 10.8, in which we show the average pair correlation functions g(R) of the heated crystals for different temperatures. In addition, we show in figure 10.9 snapshots of the configurations sampled at different temperatures. Clearly the system remains crystalline below $T_C = 2250$, and in figure 10.10, we show the integrated peak intensities

$$I(R_0) = \frac{1}{N_p} \sum_{R_i \geq R_{min}}^{R_i \leq R_{max}} g(R_i), \qquad (10.5)$$

calculated from the pair distribution functions g(R) depicted in figure 10.8 for two peaks located at $R_0 = 4.1$ and $R_0 = 5.2$ Å, respectively, where these peaks indicate long-range order in the system. Above 2750 K, the peak intensity becomes rather small, whereas below 2000 K the peak intensity is considerably higher, thus showing that also from a structural point of view, the system undergoes a transition to a disordered liquid state.

Comparing the structural properties of the heated crystal and the cooled liquid, we observe a change of various structural properties at about 2250 K. (see figure 10.11). Below 2000 K, the average number of nearest neighbors (Si-N and B-N) does not change much, except that some silicon atoms with coordination numbers > 4 are removed from the structures and a significant number of Si-N bonds contained in SiN_4 tetrahedra is broken above 1500 K. Furthermore the average number of nearest neighbors of silicon coincide above 1500 K for both procedures. Note, that the average number of nearest neighbors of boron atoms remains essentially constant over all temperatures. For the average number of next nearest B-B, Si-B and Si-Si neighbors, we also find that these numbers are independent of the chosen procedure at temperatures T > 2250 K. Note that below 2250 K, we always observe the structural properties corresponding to the frozen liquid or the heated crystal, respectively.

Next, we compare the specific heats of the heated crystal and the cooled liquid in figure 10.12. The specific heats C_V were calculated by numerical differentiation according to the l.h.s of equation 10.1. In the liquid phase above 2500 K, the specific heats are identical, and both curves show a peak at ≈ 2500 K. As already mentioned, at temperatures below 2000 K, the cooled melt has clearly fallen out of equilibrium and a comparison between the two procedures is useless. Note however that between 2000 and 2500 K, the specific heats are almost identical, showing that we have

	Diffusion ΔE	BSP ΔE
Si	1.615±0.09	1.64±0.02
B	1.611±0.06	1.60±0.02
N	1.707±0.08	n.a.

(a) Simulations in the liquid state

El.	System	ΔE	Ref.
N	α-Si_3N_4	2.4	[83]
N	β-Si_3N_4	8.1	[83]
N	a-$Si_3BC_{4.3}N_2$	7.0	[136]
Si	α-Si_3N_4	2.1	[82]
Si	a-$Si_{2.6}N_{3.3}C_{4.1}$	5.5	[137]
Si	a-$Si_3BC_{4.3}N_2$	5.7	[137]

(b) Experimental data for solids

Table 10.1: Comparison of the activation energies for diffusion of silicon, boron, and nitrogen and bond breaking of Si-N and B-N bonds obtained from fitting the diffusion coefficients $D_{Si/B/N}$ and the relaxation times τ_{BSP} of B-N and Si-N bonds to an Arrhenius law (Table 10.1(a)). Table 10.1(b) lists the experimental activation energies in the solid. All activation energies are given in eV/atom.

.

obtained equilibrium-like data in the supercooled temperature regime between 2000 and 2500 K.

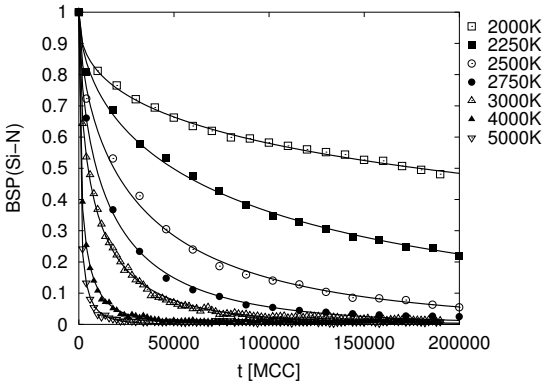

(a) Si-N

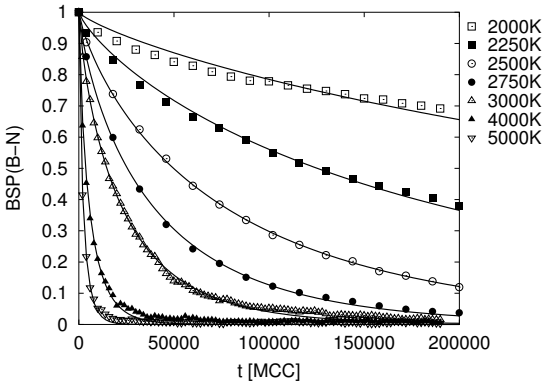

(b) B-N

Figure 10.4: Time dependence of the bond surivival probabilities BSP's for Si-N and B-N bonds for temperatures T > T_c. Full lines are fits to the Kohlrausch-Williams-Watts law (equation 10.2). The exponents β were approximately 0.4 for Si-N bonds and 0.6 for the B-N bonds, respectively.

Since the heated crystal melts to form a liquid at ≈ 2500 K at a pressure of 2 GPa (see figure 10.13) it is worth to compare the dynamical properties of the cooled liquid and the heated crystals, since one would assume that these properties are similar. We show the temperature dependence of the diffusion coefficients $D(T)$, and, complementing this, the relaxation times $\tau_{BSP}(T)$ of the B-N bonds for the cooled liquid and the heated crystal in figures 10.15 and 10.14, respectively. Clearly diffusion in the heated crystal requires a higher activation energy. Furthermore, the network of heated crystal is stiffer than the network of the cooled liquid at the same temperature, since a higher activation energy is required to break a B-N bond. [6]

10.3 Summary

By locating a peak in the equilibrium specific heat C_V, we showed that crystalline $Si_3B_3N_7$ melts at about $T_M \approx 2500$ K forming a complex liquid. The melting is accompanied by a dramatic increase in the diffusion coefficients and a dramatic decrease of the relaxation times τ_{BSP}. Furthermore, structural re-

[6] The fit to a power law of the diffusion coefficients of the heated crystal, was not satisfactory, thus we cannot determine the critical temperature accurately.

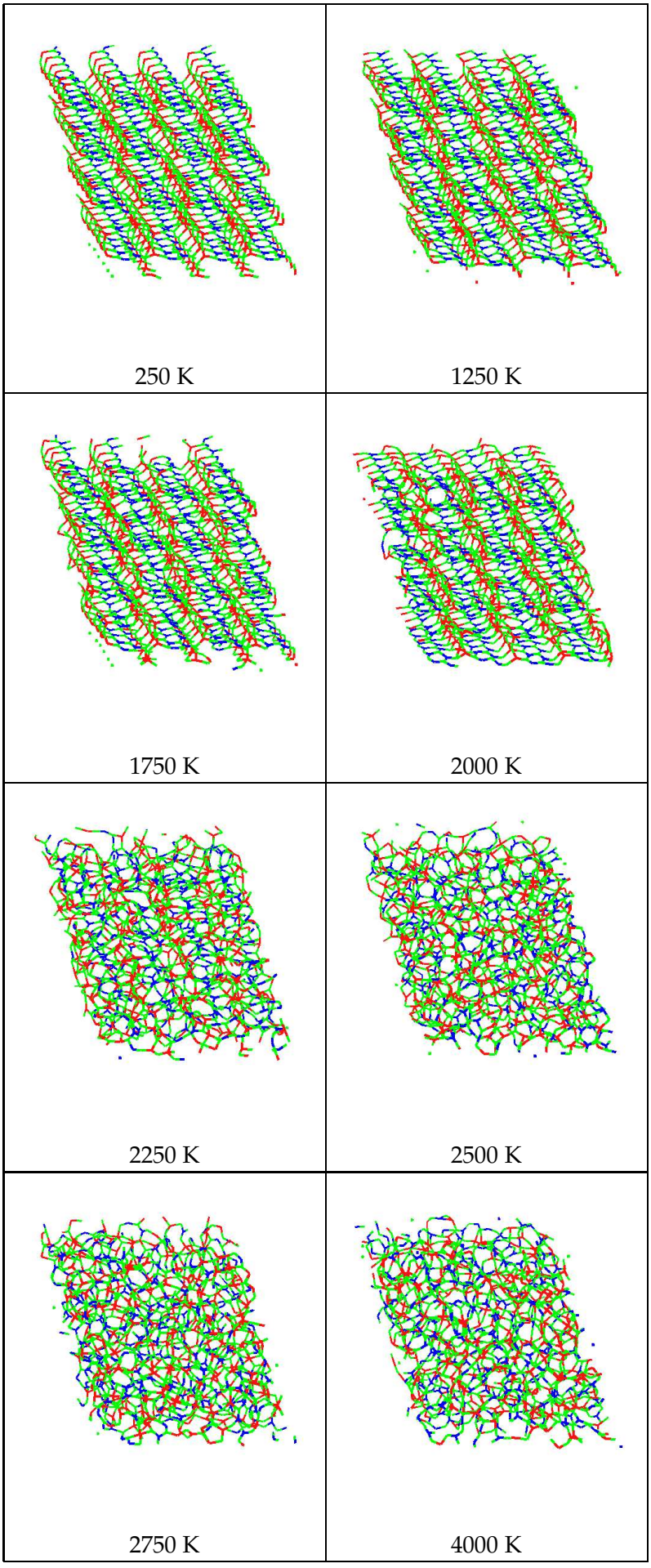

Figure 10.9: Snapshots of typical configuration of the melted crystal at the specified temperatures.

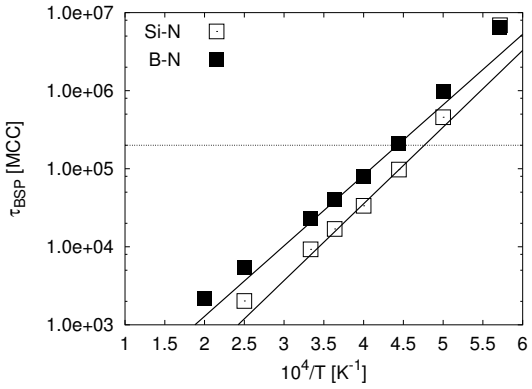

Figure 10.5: Temperature dependence of the relaxation times τ_{BSP} of the bond survival propabilities determined from the fit to the KWW-law (equation 10.2). Full lines are fits to an Arrhenius law in the temperature regime 2250-4000 K yielding the activation energies given in table 10.1(a). The dotted horizontal line show the length of computer simulations.

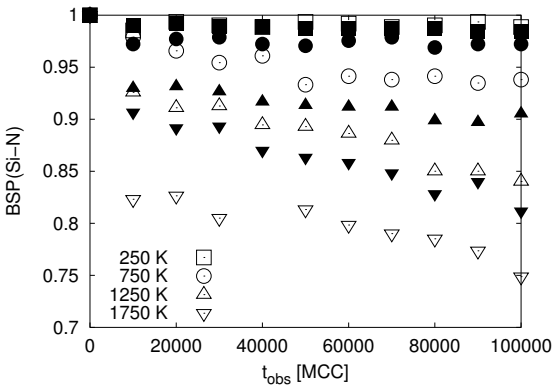

(a) Si-N

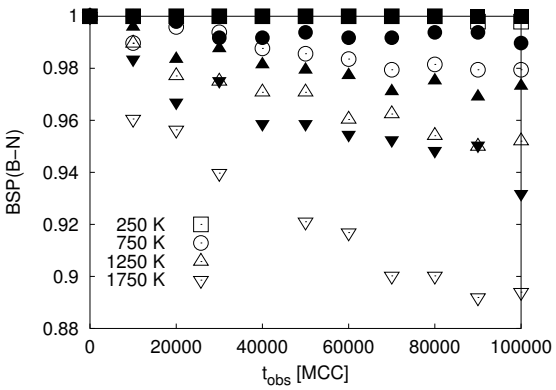

(b) B-N

Figure 10.6: Waiting and observation time dependence of the bond survival probability of Si-N and B-N bonds for waiting time $t_w = 10^4$ MCC (open symbols) and $t_w = 10^5$ (filled symbols) MCC.

arrangements in the first and the second coordination sphere occured at the melting temperature T_M. Comparing the results of the melting procedure to the (cooling from the liquid) procedure, shows that the liquid begins to solidify slightly below to the melting temperature T_M and forms an amorphous solid thereby undergoing a glass transition.[7] Furthermore, even below 2000 K, the supercooled liquid continues to stiffen, while the heated crystal has already reached a dynamical regime dominated by harmonic motion about the crystalline structure.

The analysis of the temperature dependence of the diffusion coefficients D, calculated upon cooling, showed that close to the melting point T_M the diffusion coefficients and the relaxation times τ_{BSP} followed an Arrhenius law. The activation energies of the heated crystal were higher than the activation energies of the cooled liquid. This demonstrates that the heated crystal is stiffer than the cooled liquid at the same temperature. Furthermore we showed, that below the melting point T_M, one can calculate the diffusion coefficients according to the Einstein-Smoluchowski equation. These diffusion coefficients show an equilibrium like behaviour even below the melting point. Furthermore, it seems that the specific heats C_V of the cooled liquid are equilibrium-like below T_M, thus indicating that below T_M = 2500 K, the system is super-cooled.

[7] The glass transition temperature $T_G \approx 2250$ K, is an upper estimate for the experimentally observable glass transition temperature, of course.

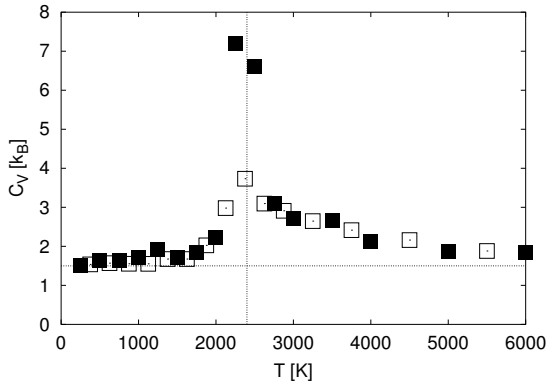

Figure 10.7: Temperature dependence of the specific heats C_V for the heated crystalline polymorph. Open symbols depict data calculated according to the l.h.s of equation 10.1 and full symbols represent the data calculated according to the r.h.s of equation 10.1. Note that the enhanced peak in specific heat calculated from the fluctuations (filled symbols) is due to an aging effect.

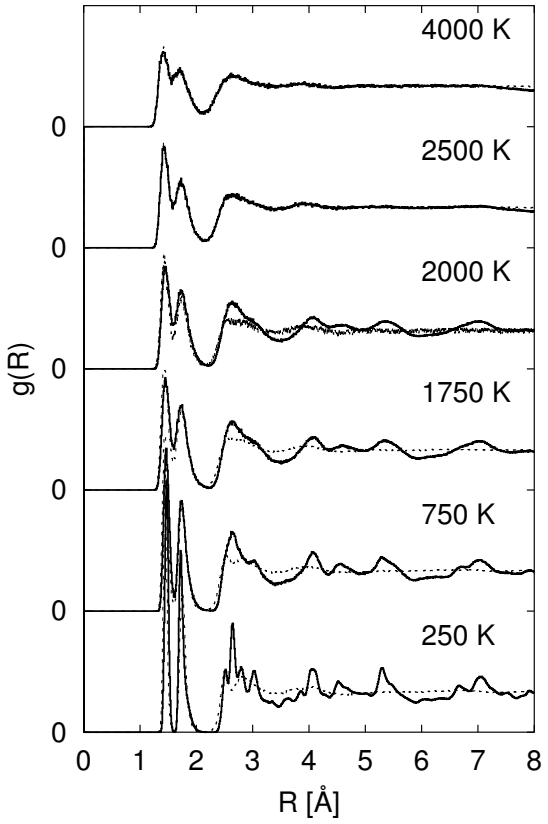

Figure 10.8: Average pair distribution functions g(R) of the heated crystal (full lines) and the cooled liquid at (dotted lines) for temperatures given inside the figure.

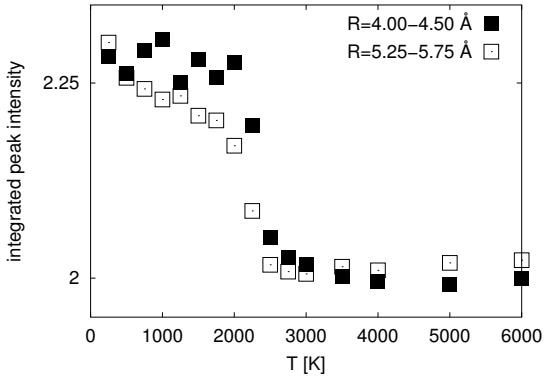

Figure 10.10: Temperature dependence of the integrated peak intensities of peaks between 4 and 6 Å in the pair distribution function g(R) depicted in figure 10.8. The selected peaks indicate long range order in the heated crystal. The integration intervals are given inside the figure.

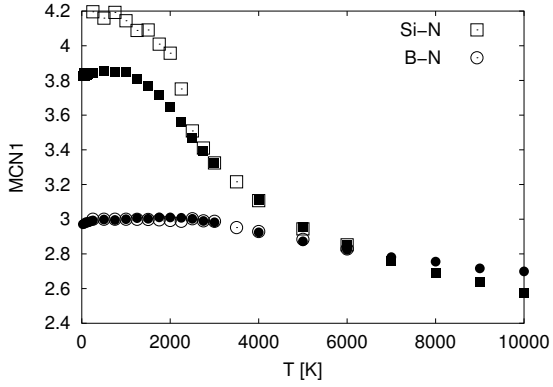

(a) First coordination sphere

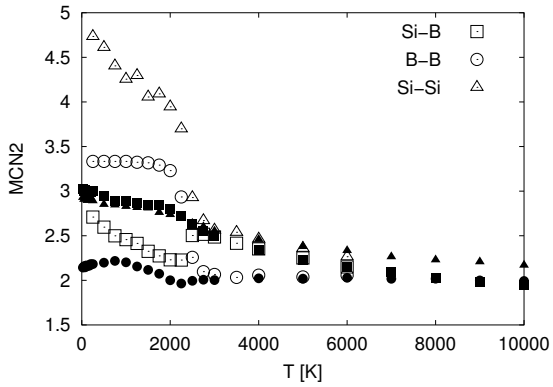

(b) Second coordination sphere

Figure 10.11: Temperature dependence of the mean coordination numbers of the first and second coordination sphere of silicon and boron atoms. Open symbols are the data for the heated crystals and filled symbols are the data for the cooled liquid.

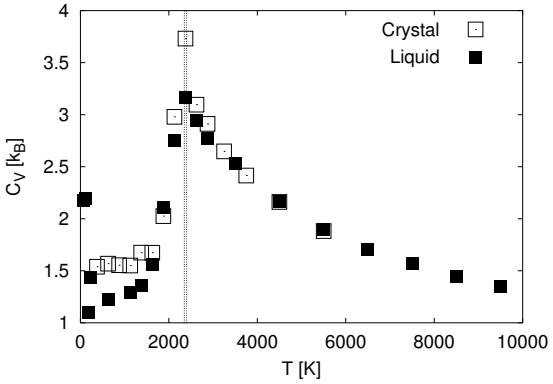

Figure 10.12: Temperature dependence of the specific heats of the heated crystal and the cooled liquid. The dotted vertical line is the peak position at $\approx$ 2450 K.

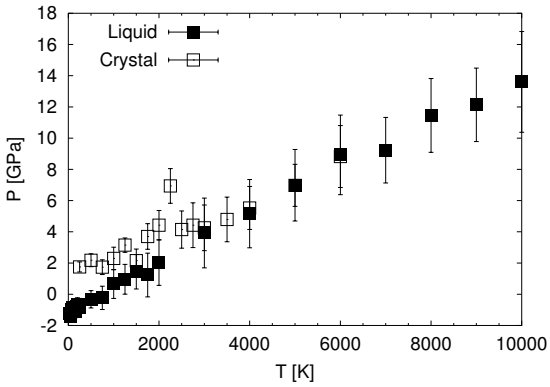

Figure 10.13: Temperature dependence of the pressure P, calculated by equation 3.23, for the heating the crystal (symbols) and the cooling the liquid procedures(symbols).

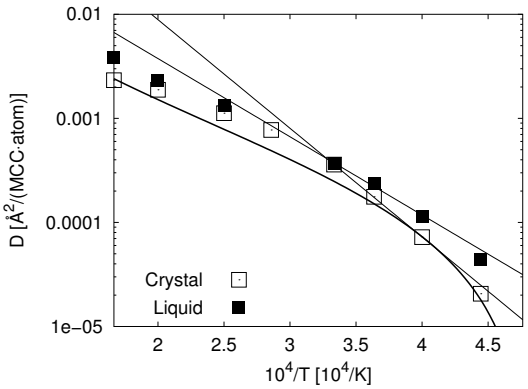

Figure 10.14: Temperature dependence of the diffusion coefficients of the cooled liquid and the heated crystals. Straight lines are fits to an Arrhenius law for temperatures between 2000 and 4000 K, yielding activation energies $\Delta E_D(Crystal) = 2.07 \pm 0.04$ eV/atom and $\Delta E_D(Liquid) = 1.49 \pm 0.11$ eV/atom

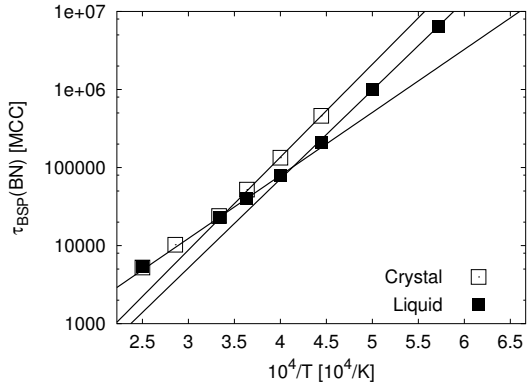

Figure 10.15: Temperature dependence of the relaxation times $\tau_{BSP}(\mathrm{B-N})$ calculated from the KWW equation for the liquid and the heated crystals. Straight lines are fits to an Arrhenius law for temperatures between 2000 and 4000 K, yielding activation energies $\Delta E_{BSP}(\mathrm{B-N;Crystal}) = 2.36 \pm 0.03$ eV/atom and $\Delta E_{BSP}(\mathrm{B-N;liquid}) = 1.79 \pm 0.04$. The dotted line is a fit to an Arrhenius law for temperatures between 2500 and 1500 K of the relaxation times of the bond survival probabilities of cooled liquid. In that regime the activation energy is 2.26 ± 0.02 eV/atom

Chapter 11

Properties of the energy landscape of a-$Si_3B_3N_7$

11.1 Introduction

In the previous chapters, we have discussed the 'metastable' phase diagram of the $Si_3B_3N_7$-system and subsequently shown that a-$Si_3B_3N_7$ undergoes a glass transition at $T_G =$ 2250 K. In this chapter, we will discuss the properties of the energy landscape and the vibrational properties of a-$Si_3B_3N_7$, using a combination of MC-techniques and gradient optimizations for the melt and the crystal fragment model introduced in section 8.2.1. First, we briefly recall the two structural models used and the energy function employed, together with the exploration techniques we have used. Next, the results will be presented in detail, and finally we will deduce some general features of this energy landscape and discuss the consequences for the static and dynamical properties of the system, and possible connections to the energy landscapes of various other glass-forming model systems.

11.2 Models and Techniques

11.2.1 Monte-Carlo simulations and local optimizations

We investigated the energy landscape(s) of two different models (I, II) of a-$Si_3B_3N_7$ in a temperature range from 25 K to 7000 K, using a combination of NVT Monte Carlo (MC) simulations and local optimization techniques. We employed the two-body interaction potential A. We generated model I by 'melting' the hypothetical crystalline phase β_2-$Si_3B_3N_7$,[89] via NVT MD-simulations. Model II was a hand-built model containing small fragments ($\oslash \approx 1/2$ nm) of the crystalline binary phases β-Si_3N_4 and hexagonal BN.[66] The two models were chosen from among a larger number of possible ones, because the discussion of the structural properties in section 8.3 had shown them to be limiting cases with respect to the local cation distribution: Model I exhibited a completely homogeneous distribution, while the nanocrystallite-based model II was, by construction, very heterogeneous.

The models consisted of 702 (I) and 1144 (II) atoms, respectively, and we fixed the densities at $\rho(I) \approx 2.75$ g/cm^3, $\rho(II) \approx 1.5$ g/cm^3. We generated three different trajectories with run lengths of $2 \cdot 10^5$ to $2 \cdot 10^6$ Monte-Carlo cycles (MCC) for each model by NVT-MC simulations. Here, one MCC consisted of N_{atom} of the usual random atomic displacements.

We used two different procedures (a and b), summarized in figure 11.2.1, for the local optimizations. In procedure a, we collected sets of logarithmically spaced halting points $\mathbf{H}^A(T) = \{h^A(t,T)\}$ ($t = 1, 2, 5, 8, 9 \times 10^x$ MCC, $x = 2, 3, 4$) from the trajectories and determined the set of minima $\mathbf{A}_{min}(T) \equiv \{a_{min}(t,T)\}$ from these holding points using the conjugate-gradient optimization technique. Procedure b consisted of two steps. We selected sets of holding points $\mathbf{H}^B(T) \equiv \{h^B(t;T)\}$ at evenly spaced time intervals (Δt=40000 MCC) along a trajectory and performed ten quench runs ($T = 0$ K Monte Carlo simulations) from each holding point.[1] In the second step of procedure B, we optimized the end configurations of the quench

[1] The halting criterion of the quench runs was the net atomic displacement per MCC dropping below 0.001 Å/atom.

runs $\mathbf{Q}(t;T) \equiv \{q_j(t;T) \equiv q_j[h^B(T,t)]\}$ by the conjugate gradient method, yielding the set of minima $\mathbf{B}_{min}(T) \equiv \{b_{min,j}(t;T)\}$.

11.2.2 Data analysis

We characterized the energy landscape of a-$Si_3B_3N_7$ by the single-point properties of the configurations $\vec{X}(t;T)$ [2] and by two-point properties that relate two configurations, e.g. a minimum with a quench point or a holding point at time t. Note, that the data was collected for temperatures both in the equilibrium and in the non-equilibrium regime above and below $T_C = 2250$ K, respectively.

The analysis of the single point properties focused on the energies and the vibrational properties of the minima, the holding points and the quench points, respectively. We analyzed the atomic contributions to the vibrational modes and the localizations of these modes. Additionally, we were interested in properties of the imaginary modes found at a given temperature and energy. This connected to the analysis of two point properties, where connections between the vibrational modes and relaxational modes can be found. These can yield insight into possible hierarchical aspects of the energy landscape and the system's dynamics, and indicate relationships between experimentally accessible properties and features of the energy landscape.

Single point properties

We chose the energy $E(\vec{X}(t;T))$ of the configurations and the properties derived from the eigenvalues $\lambda_i = \omega_i^2$ and the eigenvectors $\vec{e}(\omega_i)$ of the dynamical matrix $D_{ij}^{\alpha\beta}(\vec{X}(t;T))$ as single-point properties to be investigated. Additionally, we characterized the average local curvatures at points of the energy landscape, by the arithmetic mean of the real and imaginary frequencies,

$$\langle \omega_{real} \rangle = \frac{1}{N_{real}} \sum_i^{N_{real}} \omega_i \quad \text{and} \quad \langle \omega_{imag} \rangle = \frac{1}{N_{imag}} \sum_i^{N_{imag}} \omega_i \tag{11.1}$$

The maximum number of 'diffusive' directions is given by the fraction of imaginary modes

$$f_{imag} = \frac{N_{imag}}{3N-6}. \tag{11.2}$$

Of course, f_{imag} differs from 0 only for the quench and the holding points.

The participation ratio $\rho_R(\vec{X})$ of a configuration $\vec{X}$ was used to identify the degree of localization of the mode i with frequency ω_i. The joint contribution of elements of type α (α = B, N, Si) to a vibrational mode i of frequency ω_i was characterized by the projected density of states $PDOS_\alpha(\omega_i)$, whereas the contributions of buildings units β were analyzed by the $CDOS_\beta(\omega_i)$. For details see section 4.3.1.

Two-point properties

An important question when analyzing the properties of systems with complex energy landscapes is the connection between the energy landscape the system explores at a given temperature T, and the "underlying" set of minima, saddle points and barriers that are present in that region of the landscape. In particular, it is of interest to know, to what extent the dynamics of the system can be understood in terms of the properties of the local minima and their (low energy) connecting saddle points.

Thus, we have investigated the differences of the potential energies of the holding points and the quench points, the quench points and the minima, and the holding points and the minima. Additionally we calculated reference energies $E_{ref}(t;T) = E(h^A(t;T)) - 3/2Nk_BT$ by subtracting the average potential energy associated with the vibrational motion in the harmonic approximation from the energy of the halting point, for each holding point $h^A(t;T)$ in procedure A. This reference energy $E_{ref}(h^A(t;T))$ should equal the

[2] Recall that we describe the configuration of the N atoms by the $3N$-dimensional vector $\vec{X}$, whose components are the Cartesian coordinates of the atoms.

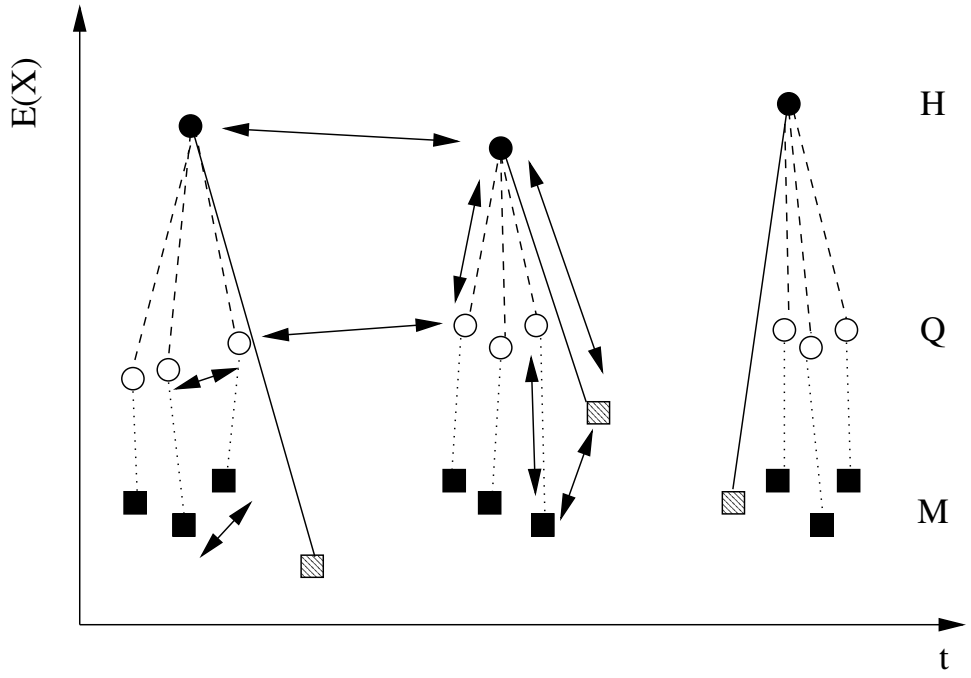

Figure 11.1: Schematic description of the local optimization procedures A and B. Filled circles represent the holding points H selected along a trajectory at temperature T. From each holding point, conjugate gradients optimizations (solid lines) are performed in procedure A to give the minima set $\mathbf{A}_{min}(T)$ (hatched squares). In procedure B quench runs (dashed lines) are performed from each holding point H and the end points (open circles) of the quench runs are further optimized by the conjugate gradient method (dotted lines) resulting in the minima set $\mathbf{B}_{min}(T)$ (filled squares). The double arrows ($\leftrightarrow$) indicate the two-point properties calculated for the characterization of the energy landscape (see section 11.2.2 for details).

energy $E(a_{min}(t;T))$ of the underlying minima a_{min} in the harmonic approximation, if the major portion of the trajectories consisted in harmonic motion around local minima (plus e.g. minima hopping). Thus, the excess energy $\Delta E_{ref} = E_{ref}(h^A(t;T)) - E(a_{min}(t;T))$ between the holding points and the minima indicates deviations from the harmonic approximation as well as deviations from a description of the dynamics on the energy landscape in terms of the minima.

Another important aspect is the structural relationship between e.g. holding points and their associated quench points and minima, or between holding points at different times along the trajectory. To address this issue, we have analyzed the topography of the energy landscape by the mean squared displacement (MSD) between two configurations $\vec{X}(1)$ and $\vec{X}(2)$, which we denote by

$$d^2(\vec{X}(1),\vec{X}(2)) = \sum_{j=1}^{N} (\Delta x_j)^2 \qquad (11.3)$$

in this section. (see equation 3.25)

Here $(\Delta x_j)^n = |\vec{x}_j(2) - \vec{x}_j(1)|^n$, is the nth power of the absolute value of the (3-dimensional) difference vector of the position vectors $\vec{x}_j(1/2)$ of atom j in configuration 1 and 2, respectively. Additionally, we determined the number of common chemical bonds that existed in two configurations (yielding the bond survival probability BSP), and the number of identical coordination spheres that existed in two distinct configurations. We defined a chemical bond between two atoms i, j, if the interatomic distance r_{ij} lay in the interval $r_{min} \leq r_{ij} \leq r_{max}$, and the set of bonds emanating from atom j defined the coordination sphere $cs(j)$ of the atom j.

Possible correlations between the eigenvectors $\vec{e}_i(M)$ of the vibrational modes of the minima and the eigenvectors corresponding to the imaginary modes of the holding/quench points $\vec{e}_j^{\,imag}(H)$ can be detected by expanding the eigenvectors $\vec{e}_i(M)$ of the real modes at the minima in terms of the orthonormal set of the eigenvectors of the dynamical matrix at the holding/quench points:

$$\vec{e}_i(M) = \sum_{j=1}^{N_{imag}} a_{ji}\vec{e}_j^{\,imag}(H) \qquad (11.4)$$

$$+ \sum_{k=1}^{N_{real}} b_{ki}\vec{e}_k^{\,real}(H) \qquad (11.5)$$

with the expansion coefficient a_{ji} and b_{ki} for the imaginary(j) and the real modes (k) modes of the holding/quench points defined by:

$$a_{ji} = \vec{e}_i(M)\cdot\vec{e}_j^{\,imag}(H) \qquad (11.6)$$

$$b_{ki} = \vec{e}_i(M)\cdot\vec{e}_k^{\,real}(H). \qquad (11.7)$$

Note, that the sum in equation 11.4 is restricted to the imaginary modes and the sum in equation 11.5 to the real modes of the holding/quench point configurations. Since the eigenvectors of the holding/quench points are an orthonormal set, the squared eigenvector $|\vec{e}_i(M)|^2$ reads:

$$|\vec{e}_i(M)|^2 = \sum_{j=1}^{N_{imag}} a_{ji}^2 + \sum_{k=1}^{N_{real}} a_{ki}^2. \qquad (11.8)$$

Thus a real mode $\vec{e}_i(M)$ becomes a 'reactive' mode r with eigenvector $\vec{e}_r$, i.e. a linear combination of the imaginary modes $\vec{e}_j(H)$ of the holding point, if the frequency dependent coefficient

$$\zeta(\omega_i) = \sum_{j=1}^{N_{imag}} a_{ji}^2 \approx 1. \qquad (11.9)$$

Complementary to this projection of the real modes onto the imaginary modes, we expanded the imaginary modes of the holding/quench points into the set of vibrational modes of the minima.

$$\vec{e}_i(H)^{\,+} = \sum_{k}^{N_{real}} c_{ki}\vec{e}_k(M) \qquad (11.10)$$

$$\vec{e}_i(H)^{\,-} = \sum_{k}^{N_{real}} d_{ki}\vec{e}_k(M),$$

where the superscripts $^+$ and $^-$ indicate real and imaginary modes, respectively. The expansion coefficients c_{ki} and d_{ki} were given by

$$c_{ki} = \vec{e}_i(M)\cdot\vec{e}_k^{\,+}(H) \qquad (11.11)$$

$$d_{ki} = \vec{e}_i(M)\cdot\vec{e}_k^{\,-}(H).$$

Averaging procedures

We averaged all single-point properties both over time and over the sets of data points collected at the temperatures at which the trajectories were generated. Note, that we calculated time averages in the non-equilibrium regime for observation times t greater than a typical waiting time t_w of 10^4 MCC, to reduce aging effects. Additionally, we mention that, all results for the end points of the quench run were first averaged for each holding point from which the quench runs were started, then over time and finally over the ensemble of trajectories at temperature T.

For each trajectory, we calculated the averages of the two point properties, which depend on the initial time t_1 and the time difference $\Delta t = t_2 - t_1$ for different initial times t_1. Subsequently, we calculated the average over the different trajectories for each temperature and selected initial times t_1.

The averaging procedure for the data of the quench runs (procedure B) requires some further comment. For each holding point, h(t;T), we calculated the average values of the two-point properties that related pairs of quench configurations and pairs of minima. The two-point properties TPP(a,b) that relate sets of quench configurations/minima that were generated from successive holding points $h(T, t; s_i)$, $h(T, t + \Delta t; s_i)$ from the *same* trajectory s_i at temperature T, were calculated as follows. For each pair a/b of quench/minima configurations $\vec{X}_{Q,M}(t; H(T; s_i)), \vec{X}_{Q,M}(t + \Delta t; H(T; s_i))$, we calculated the TPP(a,b) for each of the $10 \cdot 10 = 100$ pairs, then averaged over the holding point times t and subsequently over the sets of trajectories.

Due to aging phenomena, the temperature dependence of various properties is not completely straightforward and/or meaningful in the non-equilibrium regime. Therefore, we also analyzed our data as a function of the potential energy of the configurations, and in terms of the energies of the minima and the differences between the energies of the holding/quench points and the associated minima.

11.3 Results

This section is divided into three subsections. In subsections 11.3.1 and 11.3.2, we describe the properties of the energy landscape of models I and II determined by procedures A and B, respectively. In subsection 11.3.3, we discuss the vibrational properties of a-$Si_3B_3N_7$.

11.3.1 Procedure A

One-point properties

The average equilibrium energies of the holding points and minima for a trajectory at a temperature T are the first step in the characterization of the energy landscape. However establishing equilibrium at all temperatures T is quite a difficult task and aging effects become important. To study these aging effects (see also chapter 12), we analyzed the time and temperature dependence of the average energies of the minima (figures 11.2(a) and 11.2(b)) for temperatures T below and above the ergodic to non-ergodic transition temperature $T_C \approx 2250K$. We observed a logarithmic time dependence $E_M(t;T) = e_0(T) - b(T)log(t)$, after an initial time $t_{init} \approx 1000$ MCC, for all temperatures $T < T_C$.[3] For this temperature regime, we found the overall lowest energies of the minima at temperatures T just below the transition temperature T_C. Additionally, the logarithmic decay rate $b(T)$ was the highest just below the transition temperature and decreased almost linearly as the temperature decreased below T_C (see figure 11.2(c) and 11.2(b)). Note, that even though the decay rate for the crystal fragment model (model II) is higher than the decay rate of the melt based model, the maximum decay rate is still found just below the critical temperature T_C = 2250 K.

The temperature dependence of the time and trajectory averaged energies of the minima showed two different regimes (see Fig. 11.3), which did not depend on the model investigated. For temperatures in the interval $3000K > T \geq T_C \approx 2250$ K, the average energy of the minima rapidly increased with increasing temperature, and for $T \geq 3000$ K the

[3] For temperatures $T > T_C$, no drift occurs, and the energies fluctuate around their equilibrium values.

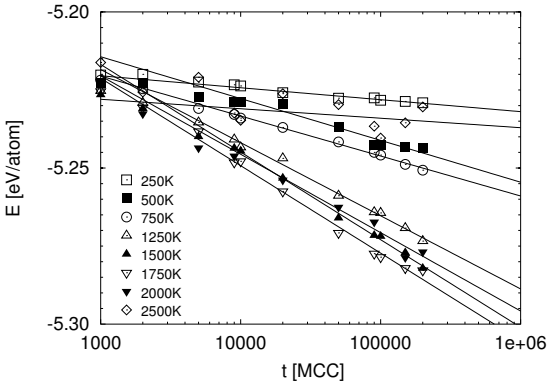

(a) Model I

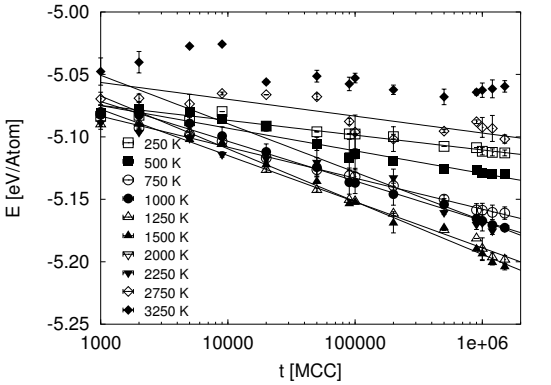

(b) Model II

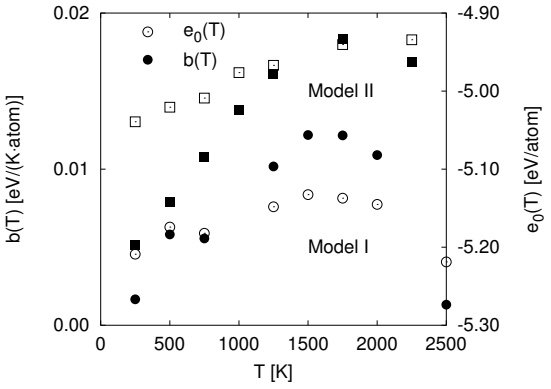

(c) Temperature dependence of fitting parameters $e_0(T)$ (empty symbols) and $b(T)$ (filled symbols) for model I (circles) and model II (squares).

Figure 11.2: Time dependences of the energy of the minima found during the MC-simulations at temperatures T $\leq$ 3500 K for models I and II using procedure a. Note the logarithmic time scales in the subfigures 11.2(a) and 11.2(b).

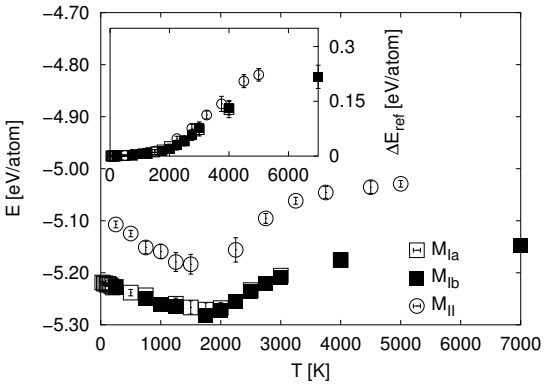

Figure 11.3: Temperature dependence of the time averaged energies of the minima. The inset shows the temperature dependence of the time averaged reference energies ΔE_{ref}. In the averaging procedure, we omitted the first 10^4 MCC to reduce aging effects visible in figures 11.2(a) 11.2(b). $M_{Ia/b}$ represent the data of the minima of model I, generated by procedures a and b, described above and M_{II} is the data for the minima of the crystal fragment model II.

rate of increase of the average energy of the minima was considerably smaller. For temperatures $T < 2000$K, the average energy of the minima increased with decreasing temperature, in contrast to what would be expected for equilibrium-like behaviour.

For temperatures $T < 1000K$, the average reference energies $E_{ref}(T)$ were identical with the average minimum energies, and the difference ΔE_{ref} began to increase slightly with T up to $T \approx 2000K$. At this temperature, the increase of $\Delta E_{ref}(T)$ became more pronounced (see inset of figure 11.3). Turning to the landscape observed using model II (crystal fragment model) for a-$Si_3B_3N_7$, we first note the high degree of similarity to the results found for model I. The two curves $E_{min}(T)$ (and $\Delta E_{ref}(T)$ in the inset) are very similar, with the energies of the melt-based configurations (model I) lower than the crystal fragment ones.[4] Again, we leave the harmonic (minimum hopping) region when increasing the temperature above 2000 K.

Next we turn to the average vibrational

[4]This relates to the fact that the crystal fragment models are less dens than the melt-based models. Recall fig. 8.13 in section 8.4.1, where the energies were correlated to the densities of the models.

properties of the minima and the holding points of models I and II. For both models the mean vibrational frequency of the real modes of vibrations of the minima again showed two regimes. In the (high-temperature) equilibrium regime, the mean vibrational frequencies of the minima increased with decreasing temperature, and in the (low-temperature) non-equilibrium regime (figure 11.4), the mean vibrational frequencies decreased. Comparing figures 11.4(a) and 11.3, we see that the energetically deeper minima exhibit higher mean frequencies, indicating somewhat steeper walls of the deep minima (see also fig. 8.15 of section 8.4.1). The average vibrational properties did not depend on the procedure employed but only on the model investigated, and on average, the minimum configurations of the crystal-fragment model are somewhat softer and they 'see' less steeper walls surrounding them. Surprisingly the average frequencies of the imaginary modes of the holding points (fig. 11.4(b)) only depended on the temperature but not on the models investigated. However, the mean frequency of the imaginary modes does not show the two regime behaviour, that was observed for the mean energies of the minima, the reference energies and the mean vibrational frequencies. This two-regime behaviour is only found in the temperature dependence of the fraction of imaginary modes f_{imag}. The fraction of imaginary modes depended on the temperature T, similar to the dependence of the reference energies ΔE_{ref}. For $T < 1000$ K, they were close zero, thus the system spends most of its time at close to the minima, whereas between 1000 and 2000 K the harmonic approximation breaks down. Above 2000 K, we find a steep increase of the fraction of imaginary modes of the holding points, but note that the only 20 % the total number of vibrational modes are imaginary modes even at 7000 K. This agrees nicely with the formation of clusters in the liquid phase even at high temperatures (see chapter 9).

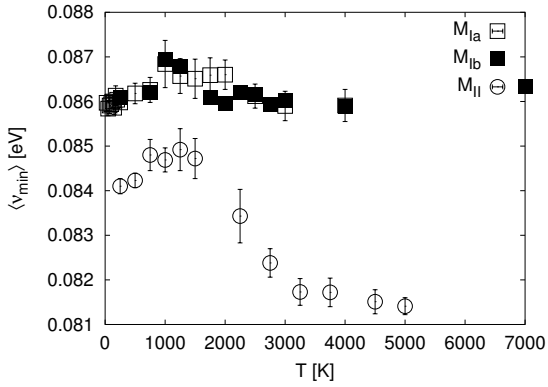

(a) Mean vibrational frequency of minima $\langle \nu_{min} \rangle$

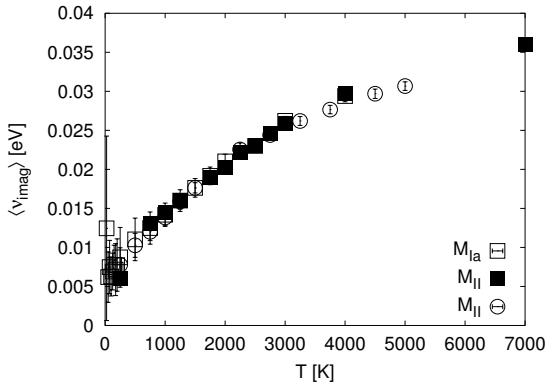

(b) Mean frequencies $\langle \nu_{imag} \rangle$ of imaginary modes of holding point configurations

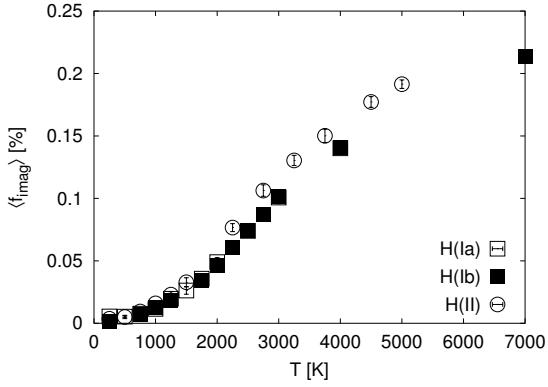

(c) Average fraction f_{imag} of imaginary modes of holding point configurations

Figure 11.4: Temperature dependence of average vibrational properties of the minima and the holding points generated by procedure Ia,Ib and II.

Two point properties

The average distances between the holding points and the minima reached from these holding points, increased with temperature

(figure 11.5) and this increase became more pronounced at about 2000K. Note again, that the procedure employed did not influence these results, only the distances between the holding points and the minima of the crystal fragment model are a slightly larger. The distances between successive minima are an order of magnitude larger than the distances between the holding points and the minima over the whole temperature range, the effect being more pronounced above 2000 K. In this context, we note that the minima and the holding points were topologically similar for temperatures $T \leq 2000$ K, since the bond survival probabilities (the fraction of the number of bonds common to both structures) were close to one (figure 11.6). This showed that in the low temperature regime, the holding points and the minima were related by small atom rearrangements that do not change the topology. On the other hand, for temperatures $T > 2000$ K, the BSP decreased with increasing temperature. Here the B-N bonds were stronger than the Si-N bonds.

The diffusion coefficients calculated from the mean squared distance between subsequent minima and subsequent holding points are indistinguishable[5](see figure 11.7). Again no dependence on the procedure employed in the generation of the minima from the holding points can be detected. Furthermore the coefficients of diffusion are slightly higher for the crystal fragment model, which has a lower density.[6] Note also that the diffusion coefficient in the equilibrium regime could be fitted by a power-law $D(T) = A \cdot (T - T_X)^\gamma$, with a critical temperature $T_X \approx 2000$K, close to the critical temperature T_C, that we determined earlier in the analysis of the energies, the mean vibrational frequencies and fraction of imaginary modes. Note that a fit to the Arrhenius equation $D \propto \exp(-\Delta E/k_B T)$ (dotted lines in figure 11.7) was also satisfactory in the range between 2000 and 3000 K.

Another way to view this result is that the distance between consecutive holding points along a trajectory is essentially equal to the distance between the two associated local minima. Thus, the trajectory does not perform a random walk "on the surface" of a single attractor or in the transition region between two widely separated large attractors. Instead, there appears to be some degree of homogeneity of the landscape on a global level, with a high similarity of the landscape below the various holding points.

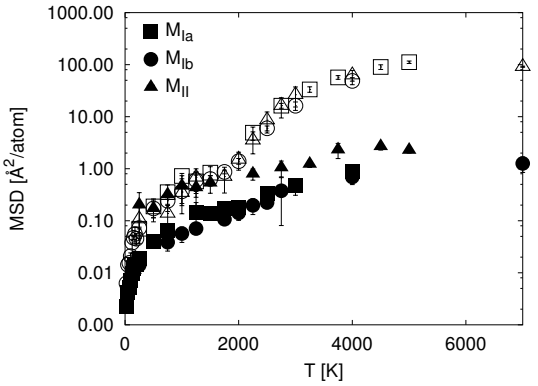

Figure 11.5: Temperature dependence of the distance between holding points and minima (filled symbols) and distances between successive minima (open symbols), $\Delta t \approx 40000$ MCC time steps apart.

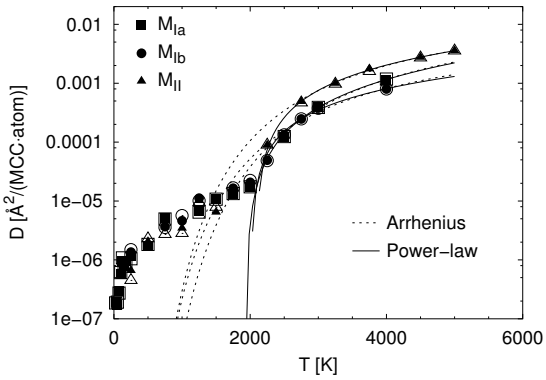

Figure 11.7: Temperature dependence of the diffusion coefficients D for models I and II calculated from the mean squared displacements $MSD(\Delta t)$ of minima (filled symbols) and holding points (open symbols) that were generated at times $t_1 + \Delta t$.

11.3.2 Procedure B

One-point and two-point properties

The general observation when surveying the results from procedure b is that qualitatively,

[5]Recall that for temperatures $T \leq T_C$, equation 3.26 is a rough approximation, only.

[6]In chapter 9.3.1, we showed that the diffusion coefficients indeed increase with decreasing density in the temperature regime of interest.

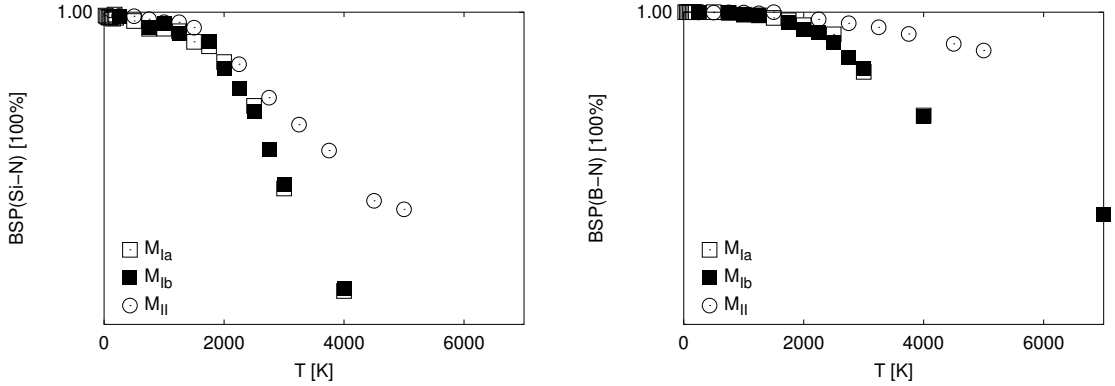

(a) BSP(Si-N) (b) BSP(B-N)

Figure 11.6: Temperature dependence of the bond survival probabilities between holding points and minima for procedures Ia,Ib and II.

and to a large extent quantitatively, the observations agree with those for procedure A. In particular, the average minimum energies again exhibit a logarithmic decrease with time for fixed temperature, and steeper slopes $b(T)$ for higher temperatures $T \leq T_C$, $E_{min}(t,T) = E_0(T) - b(T)\ln(t)$. On average, the energies of the minima for procedure b are equal to the minima found by procedure a (see figure 11.3) and the logarithmic decay laws are indistinguishable. (see figure 11.8). Regarding the other properties of the minima, they show e.g. the same vibrational spectra, and the eigenmodes are indistinguishable, too. Similarly, the topological and geometrical two-point properties for the holding points and the associated minima are quite analogous to those for procedure A.

The mean square distance between consecutive holding points, and the distances between minima associated with consecutive holding points are again the same, just as for procedure A (see figure 11.5). But this already points to an important aspect: The use of a quench swarm along the trajectory producing ten local minima per holding point does not result in widely disparate local minima. Instead, the minima appear to cluster rather closely around each other, with the centers of consecutive swarms exhibiting a similar separation as the holding points themselves.[7]

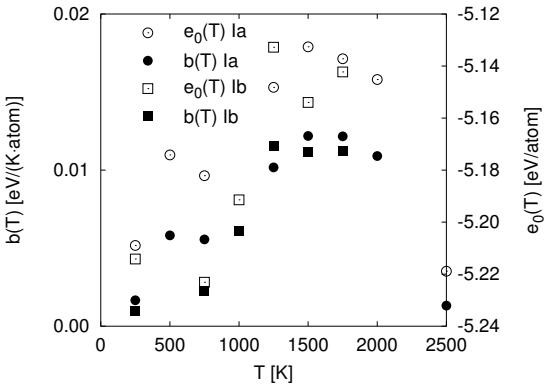

Figure 11.8: Temperature dependence of the fit parameters $e_0(T)$ and $b(T)$ of the logarithmic decay of the potential energies of configuration of model I generated by procedures A and B.

Fig. 11.9(a) shows the average energy of the endpoints of the quench runs, the holding points, and the final minima as function of temperature. Complementing this, figure 11.9(b) depicts the excess energies

$$\Delta^{Q_1} E_{ref} = \langle E(h^B(T))\rangle - \left(\langle E(q(T))\rangle + \frac{3}{2}Nk_BT\right) \tag{11.12}$$

[7] It is exactly such aspects of the landscape that can be investigated using swarms of quench runs along long trajectories. This method has been used to identify characteristic regions on crystalline landscapes[148], showing that the regions that can be largely associated with minima are much larger than those associated with transition regions, even at energies much above the saddle points. Procedure b implements this method.

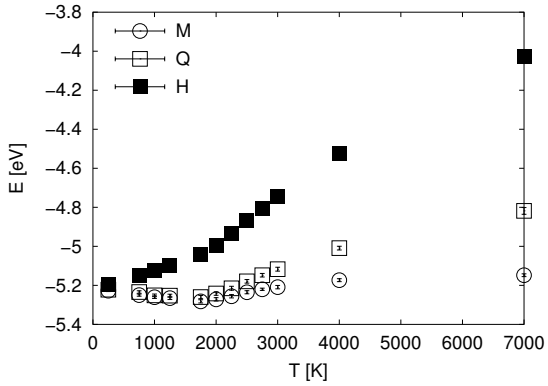

(a) Potential energies

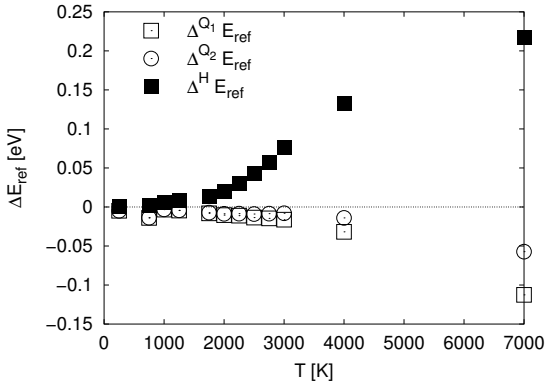

(b) Reference energies

Figure 11.9: Dependences of the potential energies $E_H(T), E_Q(T), E_M(T)$ and the reference energies $\Delta^{H,Q_1,Q_2}E_{ref}$ on the temperatures.

and

$$\Delta^{Q_2}E_{ref} = E(h^B(t;T)) - \left(\langle E(q(T))\rangle + \frac{1}{2}\langle N_{vib}(q(T))\rangle k_B T\right) \quad (11.13)$$

where $\langle E(h^B(T))\rangle \equiv E_H(T)$ and $\langle E(q(T))\rangle \equiv E_Q(T)$ are the mean potential energies of the holding and the quench points, respectively. The second bracketed terms on the r.h.s of equations 11.12 and 11.13 are the potential energies of the quench points plus the average vibrational energies of quench points. In equation 11.13 $\langle N_{vib}(q(T))\rangle = 3 \cdot N \cdot (1 - f_{imag})$ is the mean number of real vibrational degrees of freedom of the quench points. As expected the potential energies of the holding points are always higher than the energies of the quench points, whose energies are higher than the energies of the minima. As already seen in figure 11.3, the reference energies of the holding points, $\Delta^H E_{ref}$ begins to increase from zero at about 1000 K, and a significant increase of $\Delta^H E_{ref}$ is visible at approximately 2000 K. The reference energies of the quench points $\Delta^{Q_{1,2}}E_{ref}$ are effectively zero up to 2000 K and then *decrease* to negative values, thus indicating that the quench points determined by our procedure contain too many imaginary modes for these reference energies to be zero. Strikingly however, the decrease of the reference energies begins at a temperature of about 2000 K, which is just the temperature, where the ergodic to non ergodic transition occurs.

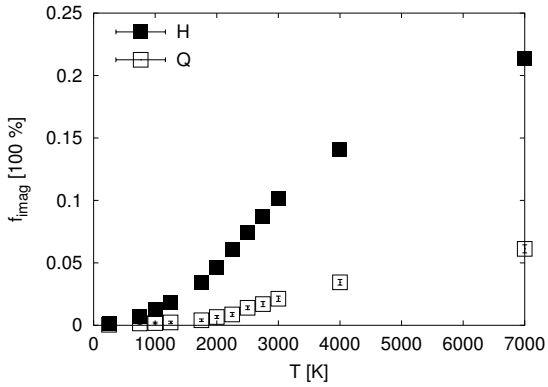

Figure 11.10: Dependence of the fraction of imaginary modes of the holding points (H) and the quench point (Q) on the temperature.

Similar to the reference energies, the fraction of imaginary modes $f_{imag}(H,Q)$ of the holding and the quench points increase substantially right at 1000 and 2000 K (figure 11.10). Recently, a similar behaviour of the fraction of imaginary modes of quasi saddles has been observed in simple Lennard-Jones systems, and the fraction of imaginary modes and diffusion coefficients have been related to the geometric properties of the potential energy landscape.[8] In that study, the potential energy as well as the difference of the potential energies of the saddle points and the underlying minima depended linearly on the fraction of imaginary modes. Figures 11.11(a) and 11.11(b), depicting the dependence of the potential energies and difference of the potential energies on the fraction of imaginary modes, show that a-$Si_3B_3N_7$ exhibits a similar

kind of behaviour. Furthermore, the energy landscape of a-$Si_3B_3N_7$ contains saddles, whose potential energy increase linearly with increasing the saddle order. Note that according to Cavagna[26] one could use the slopes m to calculate the effective potential energy barrier ΔE^{Cav} at a the critical temperature temperature T_C^{Cav}, if one assumes, that the saddles, which we approximate by the quench points, are the important parts of the energy landscape for the dynamics. However, the diffusion coefficients do not suffice to distinguish between a dynamics that is ruled by minimum hopping or by saddle hopping or by a simple flow across holding points, as one can infer from figure 11.12, where we summarized the temperature dependence of the diffusion coefficients $D_H(T)$, $D_Q(T)$ and $D_M(T)$ calculated from linear fits of the mean squared displacements $MSD(h^B(t_w), h^B(t_w + \Delta t); T)$ $MSD(q(t_w), q(t_w + \Delta t); T)$ and $MSD(m^B(t_w), m^B(t_w + \Delta t); T)$ of subsequent holding points, quench points and minima, respectively. These diffusion coefficients are almost identical, and thus they do not allow a distinction between the different scenarios proposed for energy landscape exploration in glassy materials. In the same context, we note that even though the diffusion coefficients divided by T depended linearly on the fraction of imaginary modes (fig. 11.13), as it has been observed in computer simulation studies of amorphous silica modelled by the BKS-potential[91], the significance of these observations is unclear and thus a further investigation of the energy landscape is necessary.

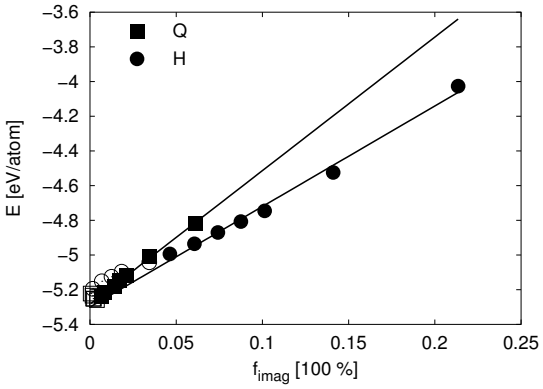

(a) Potential energy E

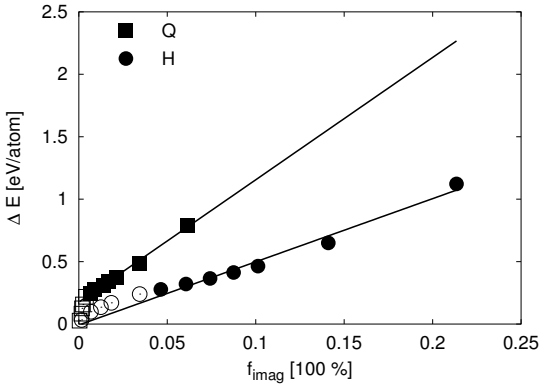

(b) Differences of potential energies $\Delta E_{H/Q}$

Figure 11.11: Dependence of the potential energies and the differences of the potential energies on the fraction of imaginary modes. Open symbols depict data collected at T $< T_C$ and filled symbols depict data for T $\geq T_C$. Straight lines are fits to a linear dependence of the energies/difference of energies on the fraction of imaginary modes. **??**.

Next, we study the temperature dependence of the average distances among the quench points $q_i(t;T) \leftrightarrow q_j(t;T)$ and among the minima $m_i(t;T) \leftrightarrow m_j(t;T)$ reachable from the same holding point $h^B(t)$ and the distances between the quench points and their associated minima $q_i(t;T) \leftrightarrow m_i(t;T)$ as well as the distances between a quench point and the minima found from the other quench points $q_i(t;T) \leftrightarrow m_j(t;T)$. Fig. 11.14 shows these average distances. We see that all distances grow with temperature, with the quench-quench and the quench-minima ones exhibiting exponential growth as function of temperature. For $T < T_C$, the separations among the minima and among the quench points are very similar, while for $T > T_C$, the separation among the minima increases more strongly and begins to approach the distances between quenches and minima. Considering the distances between quench points and minima, we note that they are an order of magnitude larger than the distance among quench points themselves. For $T < T_C$, this implies that the conjugate gradient part of the minimization does not lead to a dispersal of the quench swarm. For $T > T_C$, there is a larger dispersal at this stage.

In this context one should note that if the movement from holding point to quench point

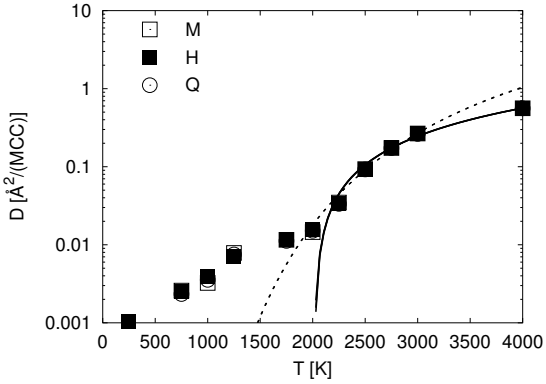

Figure 11.12: Dependence of the coefficients of diffusion $D^M(T)$, $D^Q(T)$ and $D^H(T)$ on temperature for minimum hopping (M), quench point hopping (Q) and holding point 'hopping' (H) scenarios.

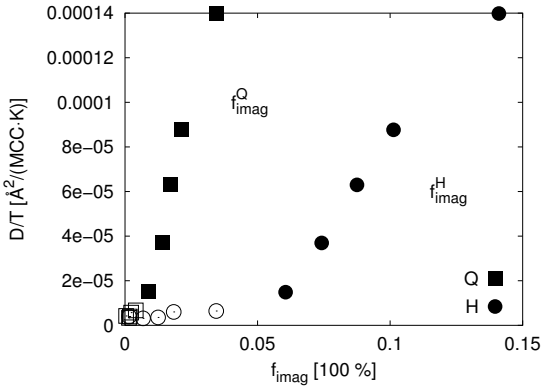

Figure 11.13: Dependence of the diffusion coefficients D^H, D^Q and D^M divided by T on the fraction of imaginary modes f^H_{imag} and f^Q_{imag}.

were to correspond to an unfocused random walk, the distance among the quench points would be of the same order of magnitude as the distance between holding point and quench point, and similarly for the quench-minimum gradient stage. Thus, the fact that there is an order of magnitude difference between these distances is quite remarkable. For comparison we show in figure 11.15 the temperature dependence of the average distances between holding points and the minima $h(t;T) \leftrightarrow m(t;T)$, which is the largest distance depicted in figure 11.14, and the distances between holding points/minima that are 40000 MCC apart. Clearly the distances between subsequent holding points are another order of magnitude larger than the distances explored during the quench swarm procedure

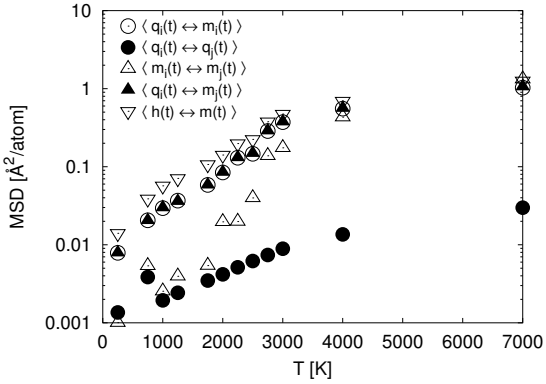

Figure 11.14: Temperature dependence of the average distances between different points on the energy landscape as explained in the text.

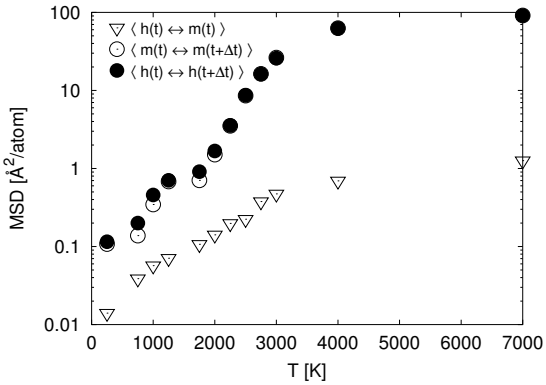

Figure 11.15: Temperature dependence of the average distances between different points on the energy landscape as explained in the text.

B.

Finally, we considered the eigenmodes of the imaginary frequencies of the quench points, and performed a projection onto the eigenmodes of the associated minima (see figure 11.16). We find that the imaginary modes project onto soft (low frequency) modes of the associated local minima (see figure 11.16). This is reasonable, since the quench algorithm is more likely to stop in saddle regions, where only flat downhill regions, with low curvature i.e. low frequency, exist.

Putting these results together, we see that during the quench stage from holding point to quench point, the swarm does not spread much, although quite a large distance (see fig. 11.15 for average holding point to quench point distances) has been covered. Quite generally, the spread in minimum points is quite small compared to the distance from the relevant holding point, and most of this spread oc-

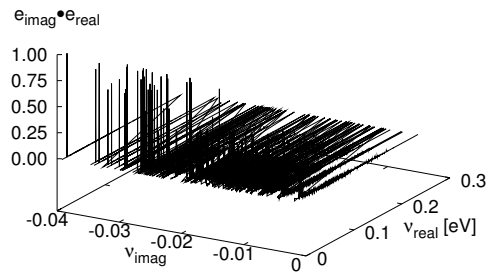

Figure 11.16: Projections of the imaginary eigenvectors of quench points collected at 1750 K onto the eigenvectors of the corresponding minima. Frequencies are given in eV.

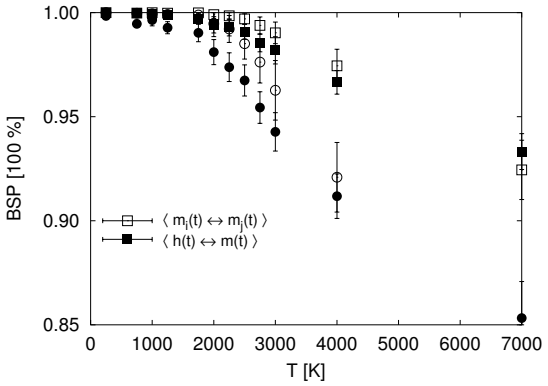

Figure 11.17: Temperature dependence of the bond survival probabilities among minima of the swarm $m_i(t) \leftrightarrow m_j(t)$ and between holding points and the minima $h(t) \leftrightarrow m(t)$. Circles: BSP(Si-N), squares: BSP(B-N).

curs in the gradient minimization stage. Taking into account that the quenches stop at critical points with few downhill directions, we note that the stochastic downhill dynamics on the landscape leads in essentially the same direction, quite similar to the behavior observed in the crystalline system, where the quench swarms mostly ended in the same minimum region.

These observations correlate with the behavior of the bond survival probabilities, where the topological similarity among the minima of a swarm was greater than the similarity between the minima and the associated holding point. Again, as function of temperature, the BSP decreased for temperatures exceeding the critical temperature. Furthermore, the B-N part of the network again proved to be more stable than the Si-N part, as had already been noted for procedure A. (see figure 11.17)

11.3.3 Vibrational properties

First, we focus on the detailed vibrational properties of the minima, the holding and quench points of the energy landscapes of a-$Si_3B_3N_7$ for the two models I and II. For the vibrational properties of the minima, we also perform a qualitative comparison to experimental data.

Minima

We observe two main peaks centered at 0.05 eV and 0.17 eV in the vibrational density of states (VDOS) for both models and for the two temperatures depicted in figure 11.18. Additionally, small peaks are visible at approximately 0.23 eV in the crystal fragment-based models both at 250 K and 2500 K. The second main peak at 0.17 eV becomes less intense in the VDOS of the high temperature minima of the crystal fragment-based model, whereas for the melt model this peak is somewhat broadened at higher temperatures. Difference between the VDOS of the two models are only noticeable in the slight shift to higher energies of the high energy vibrations of the peak at 0.17 eV for the low temperatures of vibrational spectra. Furthermore at higher temperatures, the low energy peak centered at 0.05 eV splits into two peaks at $\approx$ 0.03 and 0.08 eV and the spectra for the two models are distinguishable. Note also that the peak at 0.08 eV is already visible in the 'low-temperature' minima.

To study the nature of the aforementioned peaks, we follow Taraskin et. al. [126] and study the localization of the vibrational modes and the assignment of these modes to atomic and building unit contributions with the help of the participation ratio ρ_R, the atom and building unit projected densities of states $PDOS$ and the $CDOS$, respectively. Clearly, the vibrational modes in the main peak at 0.05 eV are all non-localized since the participation ratios $\rho_R(\nu)$ depicted in figures 11.19 and 11.20 are around 0.4, and the localization of modes is usually indicated by values on order of $1/N \approx 0.01$ of the participation ratio. By the

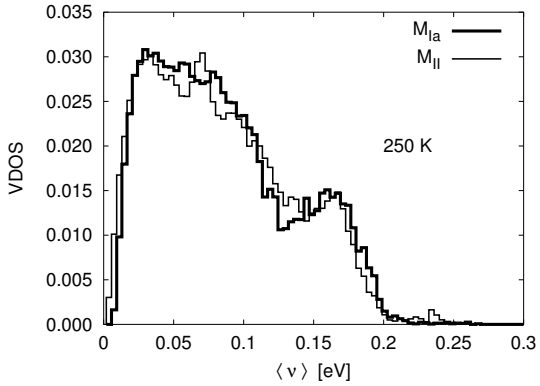

(a) 250 K

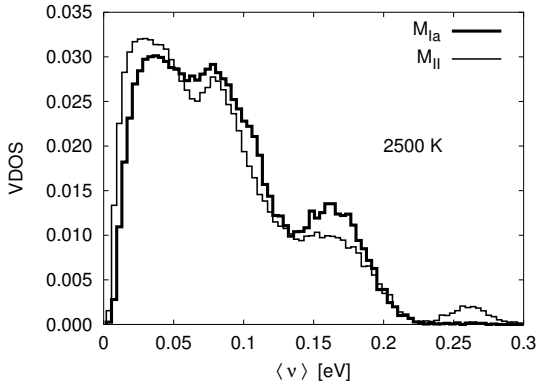

(b) 2500 K

Figure 11.18: Average phonon densities of states $VDOS(\nu)$ for minima collected at temperatures T = 250 K and T = 2500 K for models I and II.

same criterion, the vibrational modes with energy greater than 0.1 eV are localized and only very few atoms ($\approx$ 3-7 atoms) are involved in the vibrational modes. The localization of these modes is further supported by a size scaling analysis (inset of figure 11.21) of the participation ratios of random arrangements of 1300 and 2600 silicon, boron and nitrogen atoms. These configurations were optimized using interaction potential A. The value of the participation ratios of the system containing 2600 atoms are about half of the values of the 1300 atom system, as expected for a correct size scaling of the localized modes. In the low frequency range, no clear scaling is observed. Thus, we cannot decide whether these modes modes should be classified as localized as has been found in soft-sphere glasses[138]. In the atomic participation ratios (also shown in figures 11.19 and 11.20), the values of the atomic contributions to the participation ratio is proportional to the composition $Si_3B_3N_7$. Furthermore, the participation ratios of the configurations do not show any significant dependence on the investigated model or on the temperature at which these models were generated.

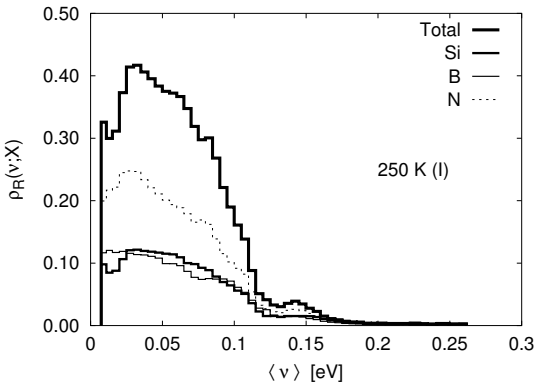

(a) 250 K

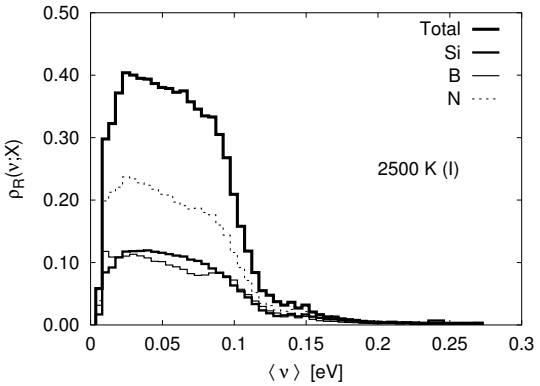

(b) 2500 K

Figure 11.19: Average participation ratios $\rho_R(\nu)$ for typical minima collected at temperatures T = 250 K and T = 2500 K for model I.

The building unit projections ($CDOS(\nu)$) of the vibrational eigenmodes reveal some differences between the two models (see figure 11.23). First, we first analyze the atomic contributions to the vibrational modes. Figure 11.22, depicting the atomic contributions to the eigenvectors of the vibrational modes, shows that the density of states at low energies is dominated by vibrations of silicon and nitrogen atoms, whereas the vibrations above 0.15

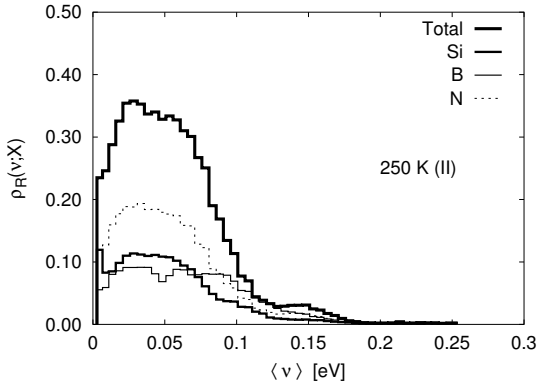

(a) T = 250 K

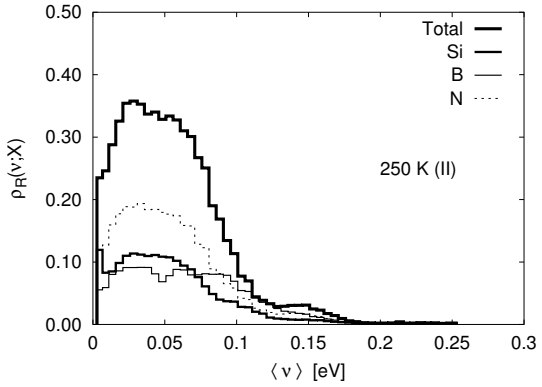

(b) T = 2500 K

Figure 11.20: Average participation ratios $\rho_R(\nu)$ for typical minima collected at temperatures T = 250 K and T = 2500 K for model II.

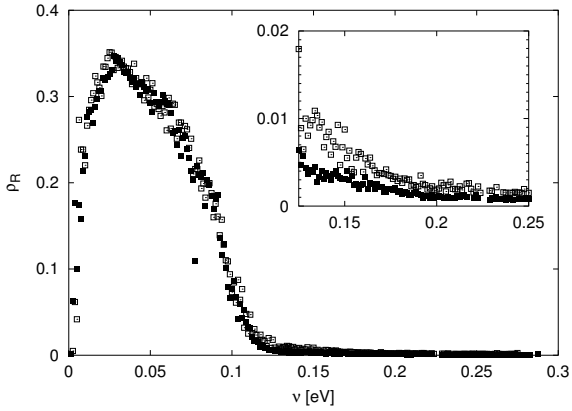

Figure 11.21: Participation ratios $\rho_R(\nu)$ of models of system sizes 1300 (open squares) and 2600 (filled squares). The two models are minima of an initially random arrangement of silicon, boron and nitrogen atoms. The inset shows an enlargement of the high frequency regime.

eV are clearly dominated by boron and nitrogen atoms and no contributions from the silicon atoms are discernible.[8]

Turning to the contributions of different possible building units of silicon, boron and nitrogen, the vibrations of silicon and boron atoms are dominated by vibrations of SiN_4 and BN_3 units, respectively. (figures 11.23(a) and 11.23(b)) In the low energy modes we also observe contributions from SiN_3 and BN_2 building units. In the high frequency region, the peaks at 0.25 eV are clearly due to BN_2 building units. The contributions from different nitrogen building units $NSi_{3-x}B_x$ (x=0,3) allows to distinguish among the models due to different probabilities of occurrences these building units (figure 11.23(c)). The main peak in the nitrogen contribution to the vibrational densities of states is dominated either by NSi_2B_1 units (melt-based model) or by NSi_3 building units. Note that the peak at 0.22 eV present for model I is due to undercoordinated nitrogen atoms, similar to the contributions of BN_2 units in the boron contributions to the vibrational densities of states. These assignments agree well with analysis of the participation ratios, were we had found that only 3-7 atoms contributed to these high frequency vibrational modes.

Based on the above analysis of the vibrational densities of states and the different contributions to it, we conclude that an experimental measurement of the vibrational densities of states will most probably not allow a distinction between the two models. However, the above analysis has shown that the different peaks in the vibrational densities of states can be attributed to different building unit vibrations, that are only localized in the high frequency ranges. Furthermore we mention, that the above assignments are in qualitative agreement with the experimental IR-spectra, which show broad peaks at 0.11 eV ($\approx$ 934 cm^{-1}) and 0.166 eV ($\approx$ 1339 cm^{-1})[171], which were assigned to Si-N vibrations and B-N vibrations, respectively. The vibrations above 0.2 eV ($\approx$ 1620 cm^{-1}), that we observed in our models are not found in the experimen-

[8]The atomic projections are model independent

tal IR-spectra. This is not surprising, since these were clearly due to coordination defects in the models, which are expected to be less common in well-annealed experimental a-$Si_3B_3N_7$.

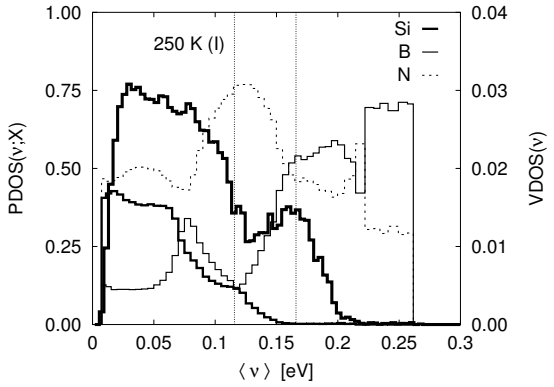

(a) Melt

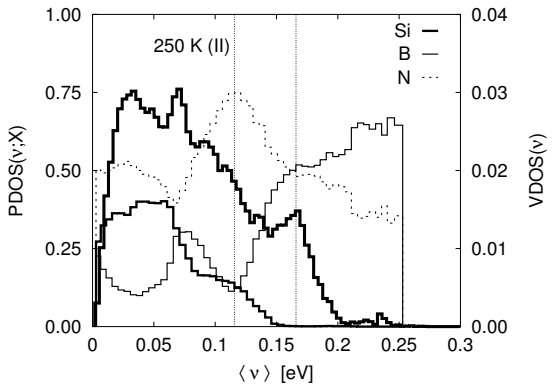

(b) Crystal fragment

Figure 11.22: Atomic contributions of silicon, boron and nitrogen atoms to the total vibrational densities of states (very bold line) for melt (top) and crystal fragment-based model (bottom) generated at 250 K. Dotted vertical lines indicate peak positions in the experimental IR-spectrum of a-$Si_3B_3N_7$ assigned to Si-N (0.11 eV) and B-N vibrations (0.16 eV).[171]

Holding and quench points

After analyzing the vibrational densities of states of the minima, we now turn to the discussion of the vibrational densities of states of the holding and quench points. As already mentioned, in these vibrational densities of states imaginary frequencies are observed, which will be denoted by negative frequencies.

The vibrational densities of states of the holding points of the two models, depicted in figure 11.24, differ from the phonon densities of states of the corresponding minima only in the high-frequency range ($\nu > 0.11$). On increasing the temperature, the intensity of the high frequency decreases, eventually turning into a shoulder, similar to the results for simple Lennard-Jones-systems[17, 149] and amorphous silica[18]. The maxima of the imaginary mode spectra shifted toward lower frequencies with increasing temperature and the maxima were more intense, independent of the model investigated. Concerning the participation ratios of the real and the imaginary modes of the holding points, we see that the high-frequency vibrations of the holding points show the same degree of localization as the high-frequency modes of the minima. Furthermore, we see from figure 11.25 that the imaginary modes at low imaginary frequencies, are localized modes (based on a participation ratio cutoff ρ_R^{cut} of 0.05). Sine the general features of the real and the imaginary modes are independent of the investigated model, we now focus on the properties of the real and imaginary modes derived from model I for a detailed analysis.

In figure 11.26, we show the participation ratios $\rho_R(\nu)$ of the holding points of model I for a wider range of temperatures. For temperatures $T < T_C$, the low frequency imaginary modes $\nu < -0.025$ have very low participation ratio indicating a higher degree of localization of these modes. Furthermore, in the frequency range $-0.01 < \nu < 0$, the participation ratios increase upon increasing the temperature but level off for temperatures above $T > 2000$ K (see the inset of figure 11.26, in which we plot the temperature dependence of the frequency averaged participation ratios of the imaginary frequencies). Thus, the character of the imaginary modes changes from a localized vibration to an extended type of motion at temperature T > 2000 K, which coincides with the critical temperature determined in the previous sections. As already mentioned, localized modes involve only very few atoms and these modes do not contribute significantly to the collective motion of the atoms. Thus these modes can

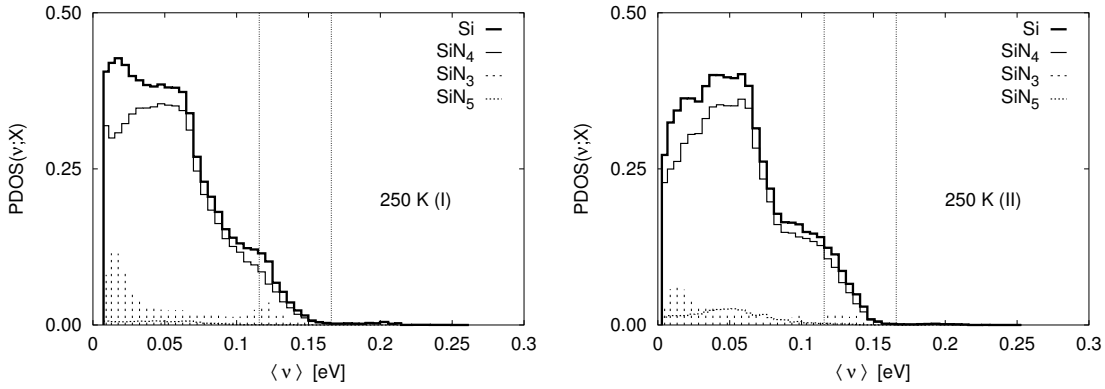

(a) Silicon

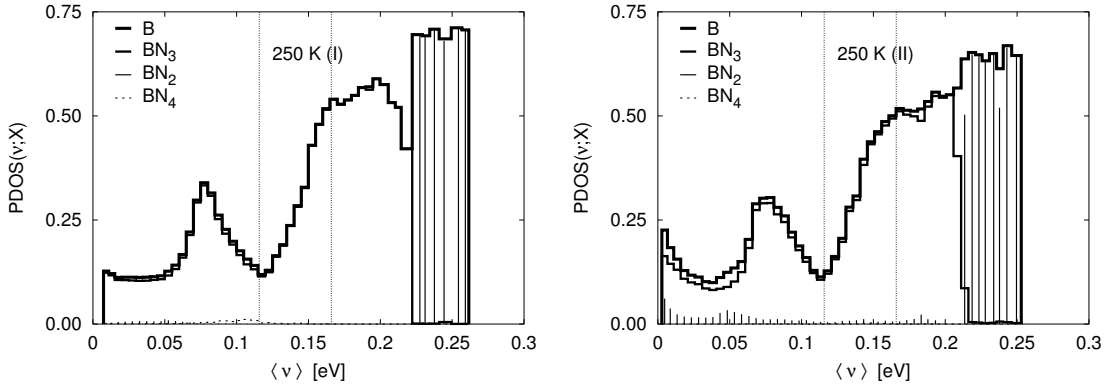

(b) Boron

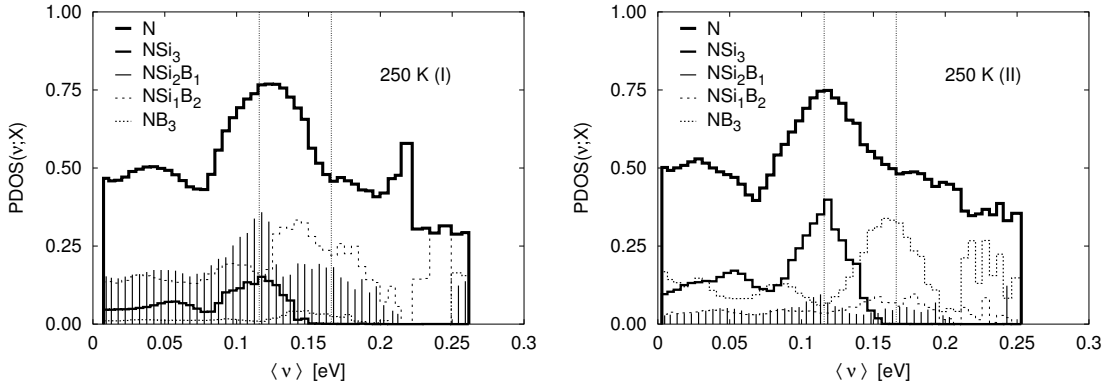

(c) Nitrogen

Figure 11.23: Building unit projections $CDOS(\nu)$ on the atom contributions to the vibrational densities of states of melt-based models (left) and crystal fragment based models (right) generated at 250 K.. Dotted vertical lines indicate peak positions in the experimental IR-spectrum of a-$Si_3B_3N_7$ assigned to Si-N (0.11 eV) and B-N vibrations (0.16 eV).[171]

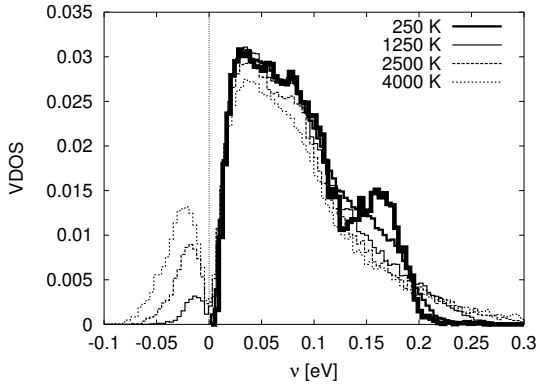

(a) Melt

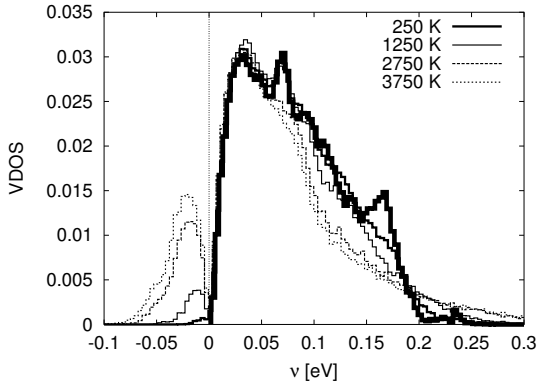

(b) Crystal fragment

Figure 11.24: Average vibrational densities of states VDOS of the holding points generated along trajectories at the temperatures given in the figure for the melt-based and the crystal fragment based models. In each figure, the bold line is the average phonon spectrum of the minima generated at 250 K.

be subtracted[9] from the total number of imaginary modes yielding the corrected number of imaginary modes f_{imag}^{corr}, depicted in figure 11.27. Even though the choice of ρ_R^{cut} to distinguish between localized and non-localized modes is somewhat arbitrary, a conservative estimate based on the finite size analysis of the real modes of vibrations of the minima, suggested ρ_R^{cut}=0.05(see figure 11.21). For that choice, the corrected fraction of imaginary of modes begins to increase just at 1750 K. Note that effectively all imaginary modes for temperatures T < 2000 K are labeled 'localized' and approximately 30-50 % of the imaginary modes at higher temperatures are also localized.

[9]The aforementioned anharmonic contributions to the imaginary mode spectrum cannot be removed by this technique.

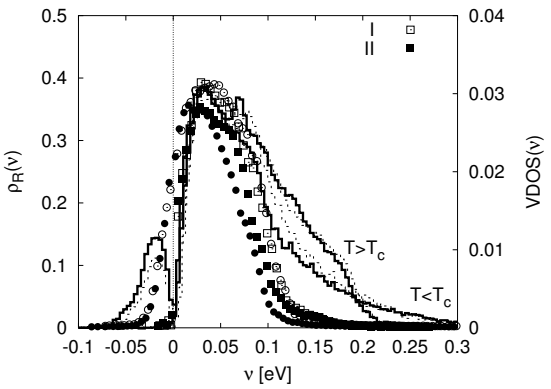

Figure 11.25: Average participation ratio of holding point configurations of the melt based model (I) and the crystal fragment model (II) from trajectories generated at 2500 K (circles) and 250 K (squares). The full lines are the vibrational densities of states of the holding points of model II, whereas dashed lines are the average VDOSs of the holding points of model I.

In the previous subsections, we argued that rearrangement processes a-$Si_3B_3N_7$ are due to Si-N bond-breakings. Figure 11.28, depicting the contributions of silicon, boron and nitrogen atoms to the eigenvectors of the imaginary modes of the holding points at two temperatures above and below the critical temperature, clearly shows that the important contributions to the eigenvectors of the imaginary modes at the maxima of the imaginary mode spectrum are located at silicon and nitrogen atoms. This provides us with additional evidence that the Si-N bonds are the weaker part of the amorphous network and responsible for the rearrangement processes that occur in a-$Si_3B_3N_7$. [10] Note that the eigenvectors of the imaginary modes with frequencies below the maximum of the density of states of the imaginary modes are dominated by boron and nitrogen atoms. [11]

[10]One could extend this type of analysis of the precise nature of the building units by analyzing projections onto the eigenmodes of elementary building units (e.g. SiN_4 tetrahedra) as performed by Taraskin[126] and Oligschleger[116] for amorphous SiO_2.

[11]A further analysis showed, that the eigenvectors of these modes are mostly located at boron atoms, that are

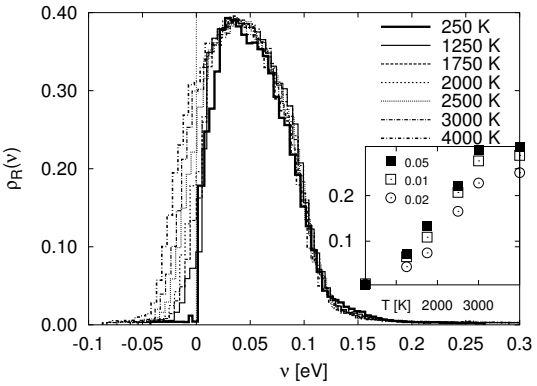

Figure 11.26: Average participation ratio and vibrational density of states of holding point configurations of the melt based model (I) from trajectories generated at the temperatures given in the legend. The inset shows the temperature dependence of the average participation ratios of the imaginary frequencies greater than -0.02, -0.01 and -0.005 eV.

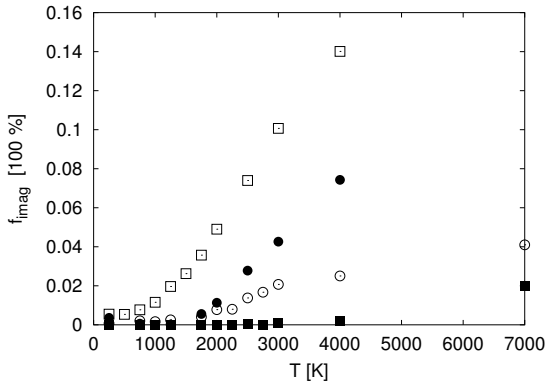

Figure 11.27: Temperature dependence of the corrected fraction of imaginary modes $f_{imag}^{corr}(T)$ for the holding point configurations (squares) and quench points (circles). Open symbols represent the uncorrected data. The participation ratio cutoff was $\rho_R^{cut}(\nu) = 0.05$.

Finally we compare the vibrational properties of the quench points sampled at temperature T_1 to the vibrational properties of the holding points sampled at temperature $T_2 < T_1$. (see figure 11.30). Apart from the less pronounced peak in the high-frequency regime in the vibrational densities of states of the holding points, the spectra of the holding points and the quench points are indistinguishable. Note also that the degree of localizations of the modes are also identical. Comparing the energies the holding and of the quench points (see figure 11.9), we note that these are fall into the same energy range.

11.4 Discussion

Collecting the various results presented, the following picture of the energy landscape of a-$Si_3B_3N_7$ emerges: A multitude of local minima is connected via low-lying saddles. For $T < 1000$ K, the dynamics consists in minima-hopping, i.e. the walker is found most of the time within the harmonic part of the local minima. However, this does not mean that the walker is below all saddles: in most directions, the walls around the minima increase nearly parabolically, while in a few other directions, the transition to neighboring minima is possible - very similar to the shape observed for minima in a-Se.[117]

The saddles are rather flat, and the deeper the minima, the steeper the walls on average. But, in general, all the minima are very similar in their vibrational properties. From the point of view of the minima, we see no great difference between the two very distinct amorphous structures (models I and II), whose landscapes have been investigated in this chapter. Above the low-lying saddles and their associated minima, we find higher-lying states (holding points) that show certain topological differences to the minima - in contrast, the low lying saddles associated with the quench points are topologically nearly identical with the minima.

An important observation is that starting at $T = 1000$ K, the trajectories lie at energies that are higher than one would expect from adding the average potential energy of a set of harmonic oscillators ($3/2N_{atom}k_BT$) to the energies of the minima. Since for the minima in material systems we would expect a net-softening of the minimum region instead, this is a rather surprising result. Cavagna has suggested that the cause for similar observations in Lennard-Jones systems[26, 25] might be that the walkers no longer "oscillate" about the minima but now have the saddles as their reference points, and thus a higher reference energy than the energies of the minima. This might be a possible explanation for the tem-

surrounded by three nitrogen atoms.

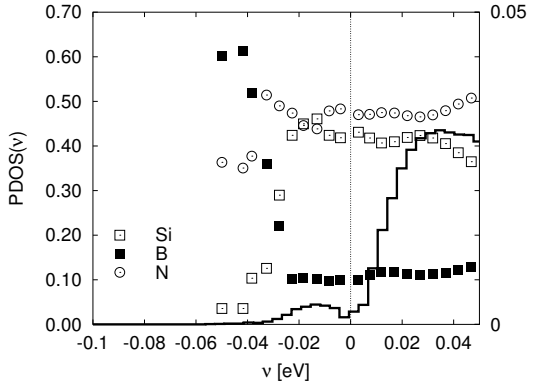

(a) 1250 K

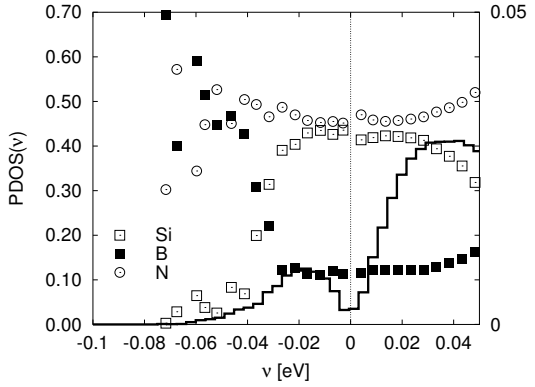

(b) 2500 K

Figure 11.28: Average contributions of silicon, boron and nitrogen atoms to the imaginary modes of the holding points configurations of model I generated at 1250 and 2500 K. In each figure, the full line is the vibrational densities of states.

peratures up to the ergodic-non-ergodic transition $T_C \approx 2000$ K. Furthermore, for $T \geq T_C$, the energy difference between the holding points and the quench points, which are usually close to the relevant saddle points[12] is close to the vibrational energy of the quench points.[13]

Thus the description of Cavagna of the dynamics on the energy landscape seems to produce a correct description. What is missing however a reason for the success of the description in terms of the saddle hopping sce-

[12]The statistical weight of the higher saddles is too small; else the quenches would have stopped earlier.

[13]The negative reference energies $\Delta^{Q_2}E_{ref}$ are most probably due to approximating the true saddles with the quench points.

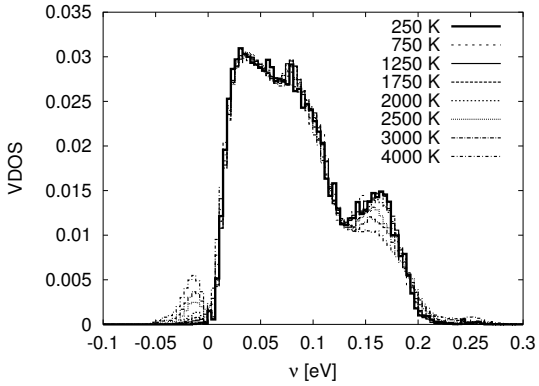

(a) VDOS

Figure 11.29: Average vibrational densities of states $VDOS(\nu)$ of quench points generated from trajectories at temperatures given in the figure.

nario. One possibility is that, analogous to the behavior observed in lattice network models of glasses,[145, 147] trapping occurs, i.e., the local accessible density of states grows approximately exponentially, and the walker cannot enter the region where this fast growth is present for $T > T_{trap}$. In contrast, for $T < T_{trap}$, the walker drops to the bottom of this region, now facing very high barriers that need to be crossed.

The dynamical effect is profound: due to the very high reference energy (at the top of the exponentially growing region), the walker floats above all low-lying energy barriers and is highly mobile, while after dropping into the rugged valley, the mobility becomes very restricted. Since this effect takes place over a very small range of temperatures, it has been suggested as a possible explanation for the occurrence of the glass transition with $T_{trap} \approx T_{glass}$.[143] Obviously, the presence of a trapping transition around $T \approx 2000$ K (i.e. $T_{trap} \approx T_C$) would agree well with the rapid increase in the atomic mobility around T_C. Note, that above T_C, all atoms are involved in the atomic motions, whereas below T_C, the only fewer atoms seem to involved in the atomic motion, as has already been proposed by Goldstein.

The logarithmic decrease of the average energy, both of holding points and minima, as function of time along the trajectories for $T < T_C$ nicely correlates with the aging that has

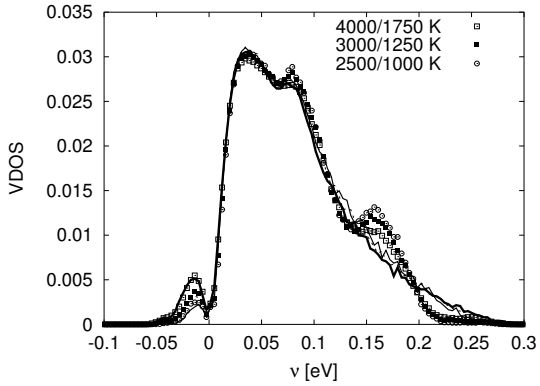

(a) $VDOS(\nu)$

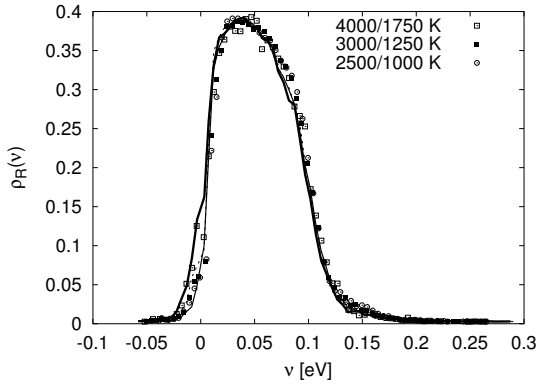

(b) $\rho_R(\nu)$

Figure 11.30: Comparison of the vibrational densities of states and the participation ratios of the quench points generated from trajectories at temperature T_1 (symbols) to the data of the holding points at temperature T_2 (lines). Labels inside figure indicate temperatures T_1/T_2.

been observed in the system (see chapter 12). General explanations of aging behavior[152] have suggested that the landscape should possess some kind of hierarchical structure. Direct evidence for or against a real hierarchy is difficult to obtain for continuous landscapes such as this one (in contrast to discrete landscapes such as lattice networks[146] or polymers[142]). Nevertheless, the fact that the typical distance from a holding point to the associated quench points is an order of magnitude larger than the distances among the quench points, suggests that each of the holding points is associated with only one particular basin containing many small local minima and saddles.[14]

Finally, we need to understand the fact that at high temperatures the minima found lie considerably higher that those observed for $T < T_C$. This might appear trivial, based on "experience", but it is not. These higher-lying minima are less steep indicating they might be somewhat larger than the low-lying ones, but else they are very similar. Furthermore, there must be enough high-lying minima and saddle points available to prevent the walker from reaching deep-lying minima on the downhill path from the holding points. One might be tempted to speak of a "different" part of the energy landscape for the "liquid" state.

Together with the ergodic-non-ergodic transition and the aging phenomena, this suggests that we have a rugged landscape with a "basin"-based hierarchy, but where for each basin both the local density of states and the local density of minima grow very rapidly, possibly exponentially for the accessible density of states. In addition, the energy difference of the saddle points to 'their' associated minima also shows a steady increase with the energy of the minima, but probably not as fast as the density of states itself.

Finally, the increase in the number of imaginary modes of the quench points indicates that the associated flat transition regions (probably harboring several saddle points at higher energies) slowly change in complexity with energy. But the fact that even the holding points with the highest energies still exhibit frequency spectra with over 80 % real frequencies, shows that even in this energy range most of the movement is not diffusive but some kind of oscillatory motion. In this context one should note that for temperatures up to 4000 K, the system is still in the condensed (liquid) phase. Only for $T > 4000$ K are we dealing with a cluster fluid, where the average cluster size lies below 50 atoms. For that region of configurations space, the landscape one explores will exhibit rather different properties, of course[15]. But the investigation we have

[14] Similar observations have been made in simulations on Lennard-Jones systems[33, 7].

[15] Neither have we considered the region of the landscape associated with the crystalline modifications of $Si_3B_3N_7$, or with mixtures of large Si_3N_4 and BN crystallites. Nevertheless, the results for model II show that for

performed here has focussed on the ternary system for temperatures below the gaseous phase, and yields a satisfactory description of the landscape of amorphous $Si_3B_3N_7$.

mixtures of crystallites with a diameter below 1 nm, the features of the landscape do not differ substantially from those of the region containing the melt-derived structures.

Chapter 12

Aging behaviour of a-$Si_3B_3N_7$

12.1 Introduction

Determining whether a possibly non-ergodic system has "for all practical purposes" reached thermal (quasi-)equilibrium is not straightforward and possibly constitutes an ill-posed question. Physical properties of amorphous systems are known to drift with the time t_w, or age, elapsed since the quench into the glassy phase. For short observation times $t_{obs} \ll t_w$, the drift is undetectable and a state of quasi-equilibrium is revealed by the approximate validity of the fluctuation-dissipation theorem. Concomitant to the violations of the fluctuation-dissipation theorem for $t_{obs} > t_w$, the correlation and response functions acquire an additional dependence on t_w. This breaking of time translational invariance has been observed e.g. in the magnetic susceptibility of spin glasses, both in experiments[115] and model simulations[74, 24], in measurements of C_p for a-Se[156], and also in simulations of the dynamical structure factor of e.g. a-SiO_2 above the glass transition temperature[86].

To detect ergodicity breaking we use 1) the specific heat C_V, which we calculate in three different ways, all agreeing in equilibrium but markedly differing if ergodicity is broken, and 2) the two-time energy-energy average $\phi(t_w, t_{obs}; T)$, and the related two-time autocorrelation function $C_E(t_w, t_{obs}; T)$. In quasi-equilibrium, the former equals one and the latter equals a generalized standard equilibrium specific heat $k_B T^2 C_V(t_w, t_{obs}; T)$. The age dependent C_V has been studied experimentally, e.g. for charge-density-wave systems[19], but does not appear to have been theoretically explored outside of two-level systems at very low temperatures[123].

Since aging is linked to the complexity of the energy landscape of the system, we repeat some aspects of the latter (see chapter 11) and compare them to the aging behaviour, emphasizing their relation to the non-equilibrium dynamics. Furthermore, we show by analyzing the waiting time dependences of two-time properties like the mean-squared displacement or the bond-survival-probabilities that these aging phenomena can also be observed in quantities related to structural properties.

12.2 Model and Techniques

The model of a-$Si_3B_3N_7$ consisted of 162 Si-atoms, 162 B-atoms and 378 N-atoms, respectively, in a $19.1 \times 19.1 \times 19.1$ Å^3 cubic box at density $\rho_M = 2.75$ g/cm^3. As an interaction potential, we employed the two-body potential A. The simulations were performed at fixed temperature and volume, with a Monte-Carlo algorithm using the Metropolis acceptance criterion and the usual atomic displacements serving as the moveclass. Note that the kinetic energy ($3/2 k_B T$ per atom) does not appear in MC-simulations, and that all quantities studied relate to the configurational energy.

The temperatures investigated ranged from 25 to 7000 K. For each temperature up to 3000 K and above 3000 K, 9 and 3 runs, respectively, of length $t_{total} = 2 \times 10^5$ MCC were performed. In addition, for a pair of selected temperatures (1250 K and 4000 K), ensembles of 100 runs of length $t_{total} = 10^6$ MCC were studied. The energy as function of time was registered every 10 MCC. Along the individual trajectories for $T = 250, ..., 7000$ K, halting points x_H were chosen, from which both con-

jugate gradient minimizations ($x_H \rightarrow x_{min}^{(1)}$) and a set of 10 stochastic quenches ($T = 0$ K MC-runs) followed by conjugate gradient minimizations ($x_H \rightarrow x_Q \rightarrow x_{min}^{(2)}$) were performed.[1] In the following, $t_{init} \approx 1000$ MCC is the initialization time of the MC-simulations needed for the system to reach equilibrium in the ergodic regime (i.e. at high temperatures), while $t_w \geq t_{init}$ is the waiting time before the observations begin.

12.3 Ergodicity from specific heats

To investigate ergodicity versus temperature, we studied the specific heat C_V and the two-time energy-energy average

$$\phi(t_w, t_{obs}; T) = \frac{\langle E(t_w)E(t_w + t_{obs})\rangle_{ens}}{\langle E(t_w)E(t_w)\rangle_{ens}}(T), \tag{12.1}$$

where the subscript "ens" always denotes an average over all trajectories. C_V was calculated using three different computational prescriptions. First

$$C_V^a(T) = \frac{\partial\langle\langle E\rangle_{t\in[t_w,t_{total}]}\rangle_{ens}(T)}{\partial T}, \tag{12.2}$$

where time averaging extends from t_w to the end of the simulation t_{total} and the temperature derivative is performed after the averaging. Secondly

$$C_V^b(T) = \frac{\langle E(T+\Delta T; t_w)\rangle_{t\in[t_w,t_w+t_{obs}];t_{obs}\ll t_w}}{2\Delta T} - \frac{\langle E(T-\Delta T; t_w)\rangle_{t\in[t_w,t_w+t_{obs}];t_{obs}\ll t_w}}{2\Delta T}. \tag{12.3}$$

This emulates a step experiment where the system ages at temperature T. The time averages over the observation time $t_{obs} \ll t_w$ are performed at temperatures $T \pm \Delta T$, where $\Delta T \approx 0.1T$. Finally we gauge the energy fluctuations in $[t_w, t_w + t_{obs}]$ by calculating

$$C_V^c(T) = \frac{\langle\langle E^2\rangle_{t\in[t_w,t_w+t_{obs}]} - \langle E\rangle^2_{t\in[t_w,t_w+t_{obs}]}\rangle_{ens}(T)}{k_B T^2}, \tag{12.4}$$

for a range of observation times t_{obs} which straddles t_w.

The experimental setups are depicted in figure 12.1 . Rapidly bringing a system from its initial temperature T_i to its final temperature T_f leads to two different scenarios. For temperatures $T_f > T_G$, the system equilibrates very quickly, and the average energies and the fluctuations in e.g. the potential energy neither depend on the choice of t_w nor on the choice of t_{obs} and the system is in thermodynamic equilibrium. The situation changes, if the temperatures T_f are smaller than the glass transition temperature T_G. In that case the calculated mean energies depend both on the waiting time t_w and the observation times t_{obs}, and the fluctuations $\sigma^2(E)$, depend even more very strongly on the choice of the waiting times t_w and the chosen observation time t_{obs}. For practical purposes, the prescription for the calculation of C_V^a has only a very weak t_{obs} dependence. By way of contrast, when increasing t_{obs} past t_w the observed dynamics in C_V^c changes dramatically from quasi-equilibrium to off-equilibrium (cf. inset in fig.12.4). C_V^b, which mimics an experiment performed after some relatively long equilibration time t_w, (see figures 12.2 and 12.3) likely yields the most "realistic" value for the specific heat for all temperatures.

As shown in fig. 12.4 the above prescriptions yield, as expected, almost identical results in the high-T ergodic dynamical regime, but differ at low T. This indicates that below $T_C \approx 2000 - 3000$ K ergodicity is broken. Further evidence stems from the observation that for $T < T_C$, the motion is sub-diffusive (see figure 12.6), while for $T > T_C$ standard diffusion is observed: For $T > T_C \approx 2100$ K, the diffusion coefficients for B, Si and N, follow a power law $D \propto (T - T_C)^\gamma$ with $\gamma = 1.7$, showing structural freezing-in. Similarly, the relaxation times associated with the bond survival probabilities of B-N and Si-N bonds display a rapid increase below T_C (see chapter 10 for details).

[1] See chapter 11 for details.

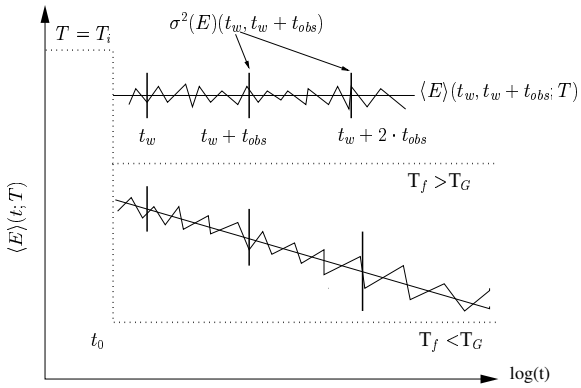

Figure 12.1: Experimental setup and typical time dependences of measured one-time and two-time properties of an equilibrium and non-equilibrium (aging) system. The dotted lines depict the temperature schedule used to cool a system from an initial temperature T_i to it final temperatures $T_f > T_G$ (upper part) and $T_f < T_G$ (lower part) at time t_0. t_w is the waiting time before measurements of the one or the two time quantities begins, and t_{obs} are the observation times for which a property has been measured. Full lines depict the potential energy of the system. $\sigma^2(E)(t_w, t_w + t_{obs}; T_f)$ are the fluctuations in energy. For temperatures $T > T_G$ the system is in equilibrium, and for $T < T_G$ the system is aging.

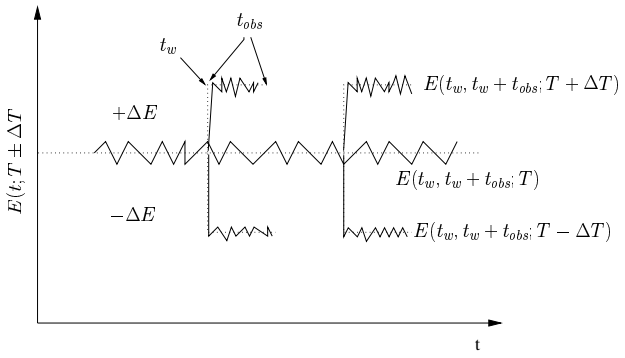

Figure 12.2: Sketch of the step experiment for the determination of the specific heat $C_V^b(T)$. At various times t_w, the temperature is raised/lowered by $\pm\Delta T$, and the changes in potential energy $\pm\Delta E$ due to the temperature changes are recorded for times $t_{obs} \ll t_w$. See also figure 12.3.

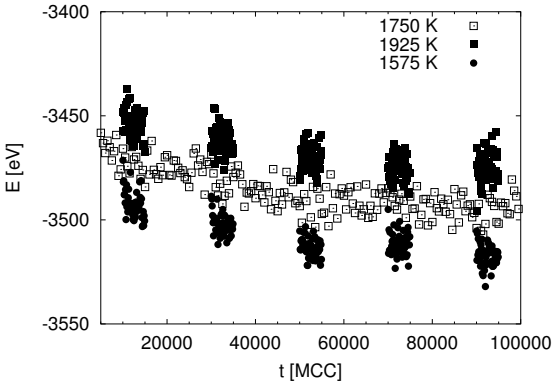

Figure 12.3: Results for the step experiment at initial temperature $T_i = 1750$ K described in the text.

For $T > T_C$, the two-point correlation function always remains very close to the equilibrium value 1. The aging behavior in the glassy phase is shown in fig. 12.5 for $T = 1250$ K, and for three different waiting times $t_w = 3 \cdot 10^3, 10^4, 10^5$. In the non-equilibrium regime $t_{obs} \geq t_w$, ϕ is seen to deviate strongly from its equilibrium value $\phi_{eq} \equiv 1$. The closely related autocorrelation function $C_E(t_w, t_{obs}; T) \equiv \langle E(t_w) \cdot E(t_w + t_{obs}) \rangle_{ens} - \langle E(t_w) \rangle_{ens} \cdot \langle E(t_w + t_{obs}) \rangle_{ens}$ also exhibits the expected aging behavior, i.e. a marked decrease to zero from an almost constant value ($\propto C_V(t_w)$) once t_{obs} exceeds t_w. This monotonic dependence on t_w of the time range $t_{obs} \in [0, t_w]$ during which (quasi-)equilibrium behavior is still observed, correlates with the stiffening of the response of the system characteristic for aging processes: The longer the system is allowed to equilibrate, the longer is the subsequent time range during which equilibrium-like behavior is observed. This effect concurs with our observation that for $T \leq T_C$ we can fit $E(t; T)$ (and also $\langle E(t; T) \rangle_{ens}$) over the interval $[t_{init}, t_{total}]$ as a logarithmically decreasing function, $E(t; T) = E_0(T) - A(T) \ln\left(\frac{t}{t_0(T)}\right)$ (see also chapter 11). Neglecting the fluctuations compared to the drift, one has $\phi(t_w, t_{obs}; T) \approx \frac{E(t_w + t_{obs}) E(t_w)}{E(t_w) E(t_w)}$. Expanding ϕ for $t_{obs} \ll t_w$ then yields

$$\phi(t_w . t_{obs}; T) \approx 1 + \frac{A}{|E(t_w)|} \frac{t_{obs}}{t_w}. \qquad (12.5)$$

Thus, $\phi(t_w, t_{obs}; T)$ substantially deviates from 1 for $t_{obs} > t_w$, as observed in the simulations. The inset shows $C_E(t_w, t_{obs}; T)$ plotted as function of the scaled variable t_{obs}/t_w. As t_{obs} increases, the data appears to collapse on a single curve, indicating that t_{obs}/t_w scaling can be expected to hold asymptotically.

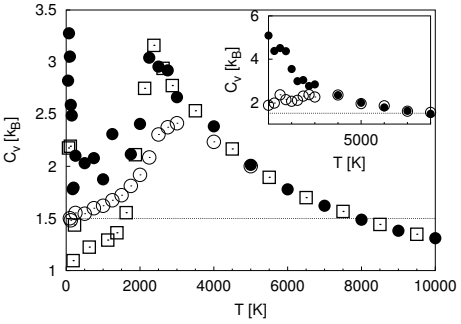

Figure 12.4: Temperature dependence of the specific heats $C_V^{a,b,c}$. The waiting t_w and the observation times t_{obs} were 10^5 MCC for C_V^a $(Box)$and C_V^c •, and $t_w \geq 10^5$, $t_{obs} = 5 \cdot 10^3$ for C_V^b (∘). Inset (note the different y-scale): C_V^c for $t_w = 10^4$, $t_{obs} = 10^4$ (∘),10^5 (•). Note that $C_V^c \approx C_V^b$ for $t_{obs} \leq t_w$, while for $t_{obs} > t_w$ the two quantities differ.

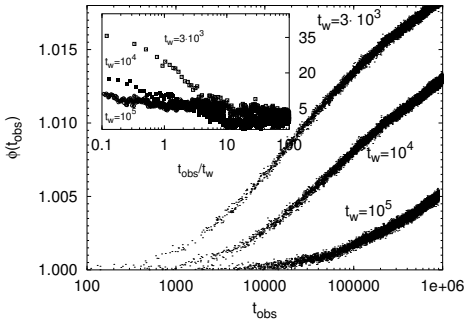

Figure 12.5: Observation and waiting time dependences of the two-time energy-energy average $\phi(t_w, t_{obs}; T)$ for 1250 K, for an ensemble size of 100 runs (raw data). The inset shows the two-time autocorrelation function $C_E(t_w, t_{obs}; T = 1250K)$. Since, even for 100 runs (corresponding to ca. one year of CPU time on an AMD 1800+ MP processor), the scatter in C_E is relatively large, the data in the inset are averaged over ten time steps.

Up to now, we have analyzed the properties of the energies along the trajectories and shown that the responses (measured with respect to the energies) become weaker as the system ages for a time t_w. The stiffening of the response characteristic of aging systems, is also reflected in the mean squared displacements and the bond-survival-probabilities. Figure 12.6, depicting the mean squared displacements of all atoms and the bond-survival probabilities for logarithmically spaced waiting times t_w, shows that the system becomes stiffer as the waiting time is increased. The distances traveled for the same observation times t_{obs} become smaller. Furthermore, the time dependence of the $MSD(t_w, t_{obs})$ can be divided into two regimes I and II. For short times, the $MSD(t_w, t_{obs}) \propto t^{\alpha}$ follows a power law with an exponent $\alpha_I = 0.5$, independent of t_w, and at longer times $\alpha_{II} \approx 0.78$. Note that our data does not allow to tell whether aging phenomena are present in the MSD.

The waiting time and observation time dependence of the bond-survival probabilities also reflects the aging behaviour of the system. The longer the system has aged, the longer it takes to break a bond on average. Very roughly, the observation time t_{obs} needed to break a bond is proportional to the age (t_w) of the system.

12.4 Energy landscape

Finally, we would like to link the non-equilibrium behavior to the properties of the energy landscape of a-$Si_3B_3N_7$, discussed in chapter 11. Figure 12.7 shows the average energy $\langle E(t; T, x_{min}^{(1)})\rangle_{ens}$ of local minima $x_{min}^{(1)}$ found by applying a conjugate gradient algorithm for logarithmically spaced halting points along several trajectories as a function of time for different temperatures.

We note that $\langle E(t; T, x_{min}^{(1)})\rangle_{ens}$ decreases logarithmically with time for $T < T_C$ analogously to $\langle E(t; T)\rangle_{ens}$ [7]. A fit of the logarithmic slope yields $A(T) = 76.29 \cdot T - 134.56 \cdot T^2$, which qualitatively agrees with the low temperature expansion of $\langle E(t; T)\rangle_{ens}$ for the so-called LS-tree models[151], suggesting that the landscape of a-$Si_3B_3N_7$ might possess some hierarchical aspects in that energy range relevant for $T < T_C$.

For fixed simulation time, the deepest local minima are reached for $T = 1750$ K, which lies right below T_C. We find a similar behavior for the average energy $\langle E(T; x_{min}^{(2)})\rangle$ of the local minima $x_{min}^{(2)}$ found after quenching plus gradient minimization starting from the holding points x_h, shown as a function of temperature in fig. 12.8. We clearly recognize a minimum in this curve at $T \approx 1750$ K, and

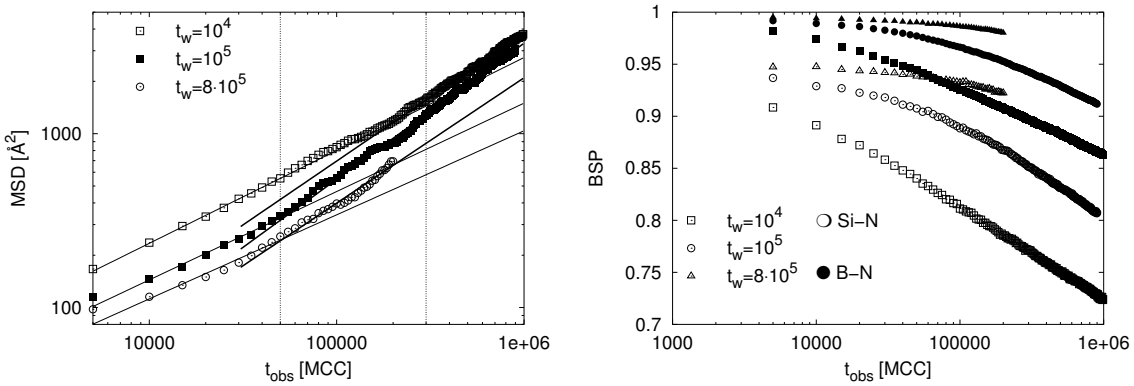

(a) MSD (b) BSP

Figure 12.6: Waiting time and observation time dependence of the mean squared displacement (MSD) and the bond survival probabilities (BSPs) of Si-N and B-N bonds after instantenuous temperature changes from 4000 to 1250 K. In the double-log plot of the mean squared displacements, the dotted vertical lines indicate two different regimes, I and II, for the power law increase of the MSD with increasing observation time $MSD(t_{obs}) \propto a \cdot t^{\alpha}$ yielding $\alpha_I \approx 0.50$ and $\alpha_{II} = 0.78$.

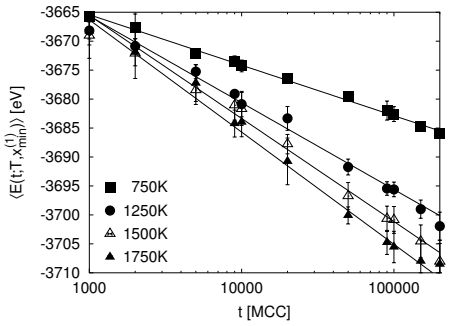

Figure 12.7: Time dependence of the average energies $\langle E(t;T,x_{min}^{(1)})\rangle_{ens}$ of the minima $x_{min}^{(1)}$ for selected temperatures $T = 750$ K, 1250 K, 1500 K, 1750 K.

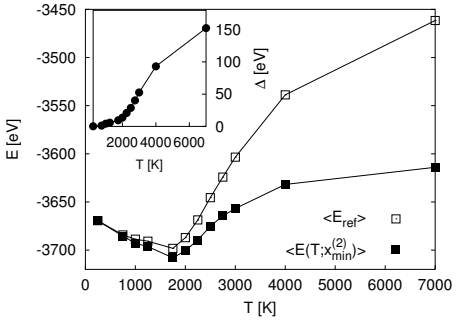

Figure 12.8: Temperature dependence of the average energies $\langle\langle E(T;x_{min}^{(2)})\rangle_{t_{obs}}\rangle_{ens}$ of the minima $x_{min}^{(2)}$ (Full squares). The open squares are values of reference energies $E_{ref}(T)$ (see text). The inset shows the temperature dependence of the excess energy Δ (see text).

the largest increase occurs at $T \approx T_C$. Analogous observations are well-known from e.g. global optimization studies of complex systems, where it has been found that reaching the deepest local minima using Monte-Carlo-type search algorithms is achieved by spending most of the search time in the temperature interval slightly below the glass transition temperature[84]. Thus this result serves as another confirmation that ergodicity breaking is taking place at $T \approx T_C$.

12.5 Discussion

The computational analysis of a-$Si_3B_3N_7$ using $C_V^{a,b,c}$ and $\phi(t_w, t_{obs}; T)$ shows that this amorphous material can be expected to exhibit a glass transition with a concurrent break in the ergodicity at about $T_C \approx 2250$ K if pressures high enough to prevent decomposition are applied. Regarding its structural dynamics and aging properties for $T < T_C$, a-$Si_3B_3N_7$ exhibits a general behavior similar to standard test systems (Lennard-Jones, a-SiO_2) and CDW systems, insofar as we observe a freezing-in of the structure, and a waiting-time dependence of the two-time correlation function and the specific heat.

This aging phenomenon is related to the slow non-exponential relaxation dynamics on the energy landscape for $T < T_C$, resulting in a logarithmic drift towards lower energies. This applies both to the actual trajectories and the time-sequence of observed local minima. Furthermore, the dynamics on the energy landscape is accompanied by a stiffening of the amorphous network as reflected in the decreasing distances traveled through the energy landscape and the higher probability of bonds to survive. Independent of these aspect of the dynamics, we find that starting around T_C the average potential energy greatly exceeds the value associated with harmonic vibrations at T_C. 'Thermodynamically', this makes itself felt as a peak in the specific heat, which is often associated with the so-called 'configurational entropy' due to an increased availability of additional amorphous configurations.

Part V

Summary and Outlook

Chapter 13

Summary and Outlook

13.1 Summary

In the first part of this thesis, two new approaches for the structural modelling of amorphous ceramics have been developed, that overcome the time scale problems one encounters when using computer simulation methods for the modelling of complex materials like the amorphous nitridic ceramics.

The first one, the *random close packing* approach,[67] has been successfully applied to different chemical systems like a-SiO_2, a-B_2O_3, a-Si_3N_4 and the $SiO_{2-z}N_{2z/3}$-system. For the latter, it has been shown, that the structural properties of these SiONs are best described by a network of corner-sharing $SiO_{4-x}N_x$-tetrahedra. These tetrahedra are linked via trigonally planar coordinated nitrogen atoms and non-linear two-fold coordinated oxygen atoms. Furthermore, the $SiO_{4-x}N_x$-tetrahedra are most probably randomly distributed inside the structure, since no phase separation was observed. The good agreement between the distribution of tetrahedra and the mean-field model developed to describe the distribution of the tetrahedra provided additional evidence for the randomness of the distribution of the $SiO_{4-x}N_x$-tetrahedra.

The second new method is a separation of time scales approach for the modelling of the sol-gel synthesis of a-$Si_3B_3N_7$. This method, which can be rather easily modified to apply to other sol-gel processes had to be developed for essentially two reasons: the time scales of computer simulations of about 10 ns are much shorter than the time scales of real experiments (about 10^{14} ns). Thus a full simulation of the synthesis of these substances using classical interaction potentials will not be feasible within the next decades. Furthermore, conventional algorithms for generating amorphous structures, tend to produce low-energy configurations. However, in case of the amorphous nitridic ceramics, the experimentally observed structures are most likely metastable ones corresponding to high energy configurations.

Within the separation of time scales approach, we showed that the formation of boron-rich island and silicon-rich islands in the structural models can be traced back to different speeds of N-B and N-Si bond formation. Furthermore, this modelling approach has cast some doubt on the stability of the TADB precursor molecules during the formation of these islands, since keeping Si-N-B linkages in TADB-molecules unchanged during the modelling procedure hindered the growth of silicon rich and boron rich islands in the resulting oligomers. The separation of time scales approach has also shown, that due to the synthesis route, vacancies or voids are formed, that remain stable up to 1500 K. This explains the unusually low density of the a-$Si_3B_3N_7$-material.

The main part of the thesis has dealt with a-$Si_3B_3N_7$. The structural properties of this compound have been investigated experimentally (by others) in parallel to the theoretical research performed in this thesis. The surprising experimental results on the structural and the bulk properties of these materials, i. e. the formation of silicon containing and boron enriched islands as well as the material's unusual low density, required the investigation of a high number of different modelling procedures, and the development of the two new approaches mentioned above.

The comparison of the structural and the bulk properties of the models generated by

distinct modelling techniques showed that the structural properties of these materials strongly depend on the synthesis routes. It is especially noteworthy, that the low-energy structures are the denser ones, and that the conventional synthesis route for glasses via melting and cooling should result in structures with a density of about 2.7 g/cm^3, compared to the experimentally observed density of 1.9 g/cm^3. Our results suggest that around 2000 K and at a pressure of 2-4 GPa, the material will most probably compactify. During such a process, small voids of radius $R_{void} < 3$ Å will first be removed, while larger voids are expected to be stable up to temperatures of 1500 K. Furthermore, above 2000 K, the observed silicon-rich and boron-rich islands will disappear, accompanied by a densification, and the formation of a network of homogeneously distributed SiN_4-tetrahedra and BN_3-triangles. We also note that the bulk moduli of the densified structures ($B^{high-dens} \approx$ 150-200 GPa) will be significantly higher than the bulk moduli of the low density structures ($B^{low-dens} \approx 60 - 100$ GPa). Furthermore, the vibrational properties of the models were in satisfactory agreement with experimental data. Our investigations also provide evidence, that a material produced by sintering of BN and Si_3N_4 nano-particles will exhibit structural properties similar to the properties of the sol-gel synthesized materials.

To understand the equilibrium properties of the $Si_3B_3N_7$-system, we have calculated the 'metastable' phase diagram of the system, by two different approaches, starting from a dilute liquid and a solid + gas initial configuration, respectively. We showed, that the $Si_3B_3N_7$-system is solid below 2000 K, and transforms into a liquid containing small cluster-like atom aggregates, in a narrow temperature range. Furthermore, we determined the liquid-gas critical point of the system to lie at about T_{crit}= 8000 K and critical densities of about 0.03 atom/Å^3. Focusing on the liquid-solid region, we have shown that a-$Si_3B_3N_7$ will undergo a glass transition at about 2250 K and a pressure of about 2 GPa, slightly below the melting temperature of a hypothetical crystalline polymorph, as indicated by the rapid decrease of the diffusion coefficients.

In the context of the glass transition, we have analyzed the energy landscape of a-$Si_3B_3N_7$, and showed that the dynamics on the energy landscape can be divided into two regimes. Far below the glass transition temperature T_G, the dynamics is clearly dominated by hops between different, but adjacent minima. Furthermore, these minima are related to each other by localized rearrangements comprising only few atoms. At higher temperatures, but still below T_G, the re-arrangements involve an increasing number of atoms. Finally, above T_G, these rearrangements comprise all atoms of the configurations. Our analysis of the quench points, which we could identify with low-lying saddle points, has shown that, above T_G, the dynamics on the energy landscape can most likely be described by a saddle hopping scenario.

We have investigated the aging behavior of a-$Si_3B_3N_7$.[68] The aging behaviour is characterized by logarithmic time dependences, and the two-time properties strongly depended on the waiting time t_w that elapsed before a measurement began. Furthermore, the fluctuation dissipation theorem is violated in a very peculiar way, and our data provided evidence, that for long times, the properties depend only on the ratio t_{obs}/t_w (instead of t_w and t_{obs} separately). The crossover from equilibrium to non-equilibrium behaviour is only observed for observation times t_{obs} greater or equal to the waiting time t_w. The aging behavior of a-$Si_3B_3N_7$ manifests itself not only in properties of the energy landscape, but also in various properties related to structural aspects such as the bond survival probabilities or the mean squared displacements. After very long waiting times, the amorphous network becomes stiffer, and the distances covered while exploring configuration space become shorter. Thus, through the aging process, it became harder for the system to reach different regions of configuration space, since the barriers for escape effectively increased.

13.2 Outlook

A thorough understanding of amorphous nitridic ceramics requires a detailed understanding of the microscopic structural and dy-

namical properties, which -in principle- may be gained from computer simulations. As mentioned above, computer simulations are severely hampered by time scale problems, e.g. the available computational resources are too small to study time dependent properties on experimental time scales.

Lattice-based approximations or approximations involving elementary building units could serve as useful tools towards a microscopic understanding of the dynamic properties of the amorphous nitridic ceramics. Within these modelling approaches one should use some information about the reaction rates of the elementary steps involved in the genesis of these materials. In that context, we note that an application of the methods developed in this thesis to the commercially interesting carbon-containing Si/B/N/C-ceramics would be very interesting. But in order to study these ceramics at elevated temperatures and for large system sizes, effective pair potentials have to be developed first.

Experimentally, it would be highly interesting to investigate the temperature and pressure dependence of the structural and the bulk properties of a-$Si_3B_3N_7$ in the temperature range of the predicted glass transition, and to compare these with the results of our simulations. Note, that it may also be possible to crystallize $Si_3B_3N_7$, after thermal treatment above 2000 K and pressures of several GPa.

The interpretation of the glass transition in the framework of the energy landscape picture - a field of current research - is quite difficult. As the example of a-$Si_3B_3N_7$ has shown, conclusive evidence about the important properties of the energy landscape that lead to the slow dynamics in glassy materials is difficult to obtain. A full theoretical description of the glass transition, requires the understanding of the energy landscape of glass forming systems in great detail. In particular, there is a pressing need for a more detailed analysis of the density of states of the minima, saddles and holding points. Furthermore, from a theoretical point of view, it must become clearer how the dynamics between many saddles can be modelled, how to distinguish between the two different scenarios (minimum vs. saddle hopping), and what are the true reason(s) for the successful description of the dynamics in terms of the saddles ruled scenario or the tree-graph models. And last but not least, while these theoretically important questions are being clarified, an equally crucial effort should be devoted to connecting these theoretical results to experimental data.

Appendix A

Free energy estimates for the $Si_3B_3N_7$-system

A.1 Free energy estimate for cluster distributions

To calculate the average entropic contribution $\langle S \rangle_t$ to the free energy $F = E_{pot} + 3/2 N k_B T - T \cdot \langle S \rangle_t$ arising from the different clusters occuring inside a volume V of the unit cell,[1] we assume that on average $\langle N_{cl} \rangle$ clusters of mean size $\langle S_{mean} \rangle = \frac{N_{atom}}{\langle N_{cl} \rangle}$ and volume $V_{cl} = \langle S_{mean} \rangle \cdot V_{atom}$ ($V_0 = N_{atom} \cdot V_{atom}$ is the volume occupied by the atoms in the system) exist. To proceed, we mentally divide the volume V into

$$N_{latt} = \frac{V}{\langle S_{mean} \rangle \cdot V_{atom}} = \frac{V \cdot \langle N_{cl} \rangle}{N_{atom} \cdot V_{atom}} = \frac{V}{V_0} \langle N_{cl} \rangle \tag{A.1}$$

cubes, and calculate the number of ways

$$W = \frac{N_{latt}!}{\langle N_{cl} \rangle_t ! (N_{latt} - \langle N_{cl} \rangle_t)!}, \tag{A.2}$$

one can arrange $\langle N_{cl} \rangle$ clusters on a lattice of N_{latt} sites. Using Stirling's approximation ($z! = z \ln z - z$) and noticing $S = k_B \ln W$ one finds for the entropic contribution

$$S/k_B = \ln W = \ln \frac{x!}{y! \cdot (y-x)!} \tag{A.3}$$

$$S/k_B = y \cdot \ln \left(\frac{x}{y} - 1 \right) - x \cdot \ln \left(1 - \frac{y}{x} \right) \tag{A.4}$$

with $x = N_{latt}$ and $y = \langle N_{cl} \rangle$. Returning to N_{latt} and $\langle N_{cl} \rangle$ variables yields:

$$S/k_B = \langle N_{cl} \rangle \ln \left(\frac{V}{V_0} - 1 \right) - \frac{V}{V_0} \langle N_{cl} \rangle \ln \left(1 - \frac{V_0}{V} \right) \tag{A.5}$$

If $V \gg V_0$, $\frac{V_0}{V} \ll 1$, and the second term in the last equation can be expanded into a power series,[2] yielding

$$S/k_B \approx \langle N_{cl} \rangle \ln \left(\frac{V}{V_0} - 1 \right) - \frac{V}{V_0} \langle N_{cl} \rangle \left(-\frac{V_0}{V} \right) \tag{A.6}$$

$$S/k_B \approx \langle N_{cl} \rangle \ln \left(\frac{V}{V_0} - 1 \right) + \langle N_{cl} \rangle \tag{A.7}$$

$$S/k_B \approx \langle N_{cl} \rangle \left(\ln \left(\frac{V}{V_0} - 1 \right) + 1 \right) \tag{A.8}$$

[1] We neglect the vibrational contributions to the entropy, S_{vib}^{intra} that is due to interatomic vibrations inside a cluster.

[2] $\ln(1-x) \approx -x$, for $x \ll 1$.

Now, since $\frac{V}{V_0} \gg 1$, $\ln\left(\frac{V}{V_0} - 1\right) \approx \ln\left(\frac{V}{V_0}\right) \gg 1$, equation A.8 becomes

$$S \approx k_B \langle N_{cl} \rangle \ln\left(\frac{V}{V_0}\right) \tag{A.9}$$

A.2 Free energy estimate for the decomposition of a-$Si_3B_3N_7$

Since the interaction potentials used in this thesis do not allow us to include the formation of nitrogen, we estimate the free energy change associated with a possible decomposition of a-$Si_3B_3N_7$ into silicon, boron and nitrogen N_2

$$\mathrm{Si_3B_3N_7}(s) \rightarrow \mathrm{Si_3N_4}(s) + 3\text{h-BN(s)} \rightarrow 3\mathrm{Si}(s) + 3\mathrm{B}(s) + \frac{7}{2}\mathrm{N_2}(g). \tag{A.10}$$

We calculate the free energy change of the decomposition reaction. Denoting the l.h.s. of A.10 by A and the r.h.s of A.10 B, the free energies read:

$$\begin{aligned} F_A &= E(\text{a-}\mathrm{Si_3B_3N_7}) - T \cdot S_{vib}(\text{a-}\mathrm{Si_3B_3N_7}) \\ &\approx E(\mathrm{Si_3N_4}) + 3E(\mathrm{BN}) - T \cdot (S_{vib}(\mathrm{Si_3N_4}) + S_{vib}(\text{h-BN})) \end{aligned} \tag{A.11}$$

and the free energy of the decomposition products in system B is

$$F_B = 3E(\mathrm{Si}) + 3E(\mathrm{B}) + \frac{7}{2}E(\mathrm{N_2}) - T \cdot (S_{vib}(\mathrm{Si}) + S_{vib}(\mathrm{B})) - T \cdot S(\mathrm{N_2}), \tag{A.12}$$

where $E(X)$ are the potential energies of the compounds/element X. Equating the above equations and assuming that vibrational contributions to the entropy $S_{vib}(\mathrm{Si_3N_4})$, S_{vib}(h-BN) and $S_{vib}(\mathrm{Si})$, $S_{vib}(\mathrm{B})$ of the different compounds/elements are approximately equal, yields the entropic contribution of the nitrogen molecules to the free energy,

$$T \cdot S(\mathrm{N_2}) = + \left(3E(\mathrm{Si}) + 3E(\mathrm{B}) + \frac{7}{2}E(\mathrm{N_2}) - (E(\mathrm{Si_3N_4}) + 3E(\mathrm{BN}))\right) \equiv \Delta E \tag{A.13}$$

To calculate the entropic contribution $S(\mathrm{N_2})$, we again assume that the volume V is subdivided into small sub volumes $V(\mathrm{N_2}) \approx r^3_{\mathrm{N_2}}$, and calculate the number of different ways, one can place $N(\mathrm{N_2})$ molecules of volume $V(\mathrm{N_2})$ onto the resulting lattice containing

$$N_{latt} = \frac{V}{V(\mathrm{N_2})} \tag{A.14}$$

lattice sites. If $V \gg V(\mathrm{N_2})$, we can use formula A.9, to calculate

$$S(\mathrm{N_2}) = k_B N(\mathrm{N_2}) \ln\left(\frac{V}{N(\mathrm{N_2})) \cdot V(\mathrm{N_2})}\right) = k_B N(\mathrm{N_2}) \ln\left(\frac{\rho_N^{-1}}{V(\mathrm{N_2})}\right) \tag{A.15}$$

Plugging this into equation A.13, yields

$$\rho_N = \frac{1}{V(\mathrm{N_2})} \cdot \exp\left(\frac{-\Delta E}{N(\mathrm{N_2}) k_B T}\right) \tag{A.16}$$

We approximate the potential energy differences ΔE, by the weighted sums of the heats of formation ΔH of the binary phases $\mathrm{Si_3N_4}$ and h-BN:

$$\mathrm{Si_3N_4}(s) \rightarrow 3\mathrm{Si}(s) + 2\mathrm{N_2}, \qquad \Delta H = +7.23\mathrm{eV/atom}\ [179] \tag{A.17}$$

$$3\text{h-BN}(s) \rightarrow 3\mathrm{B}(s)q + \frac{3}{2}\mathrm{N_2}, \qquad \Delta H = +7.56\mathrm{eV/atom}\ [135], \tag{A.18}$$

and the average size of a nitrogen molecule $r(\mathrm{N}_2)$ is about 2.1 Å,[3] yielding for the volume $V(\mathrm{N}_2) \approx 10\ \text{Å}^3$/molecule, and we finally obtain

$$\rho_N(N(\mathrm{N}_2)) \approx 0.1 \exp\left(+\frac{14.79\text{eV/atom}}{N(\mathrm{N}_2)k_BT}\right) \text{molecules/Å}^3. \tag{A.19}$$

Treating the N_2 molecules as an ideal gas yields a pressure

$$P(N(\mathrm{N}_2), T) = \rho_N(\mathrm{N}_2)k_BT, \tag{A.20}$$

in particular $P(N((\mathrm{N}_2 = 189), 2000\text{K}) \approx 4\,\text{GPa}$.

[3]The bond length of an N_2 molecule is 1.1 Å plus twice the atomic radius of about 0.5 Å.

Appendix B

Structural properties of a-$Si_3B_3N_7$

B.1 Dependence on the choice of interaction potentials

In section 8.3 of chapter 8 we reported on the structural and the topological properties of the structures belonging to classes A-E, representing different physical or chemical synthesis routes. The results presented there were calculated using the local optimization procedure IV, which employed interaction potential B and both atom positions and cell parameters were optimized simultaneously. For completeness, we summarize the topological properties of the structures generated by the local optimization procedures I-IV,[1] in which we employed interaction potentials A and B. In addition we include the results of the RMC-refinements performed after the local optimizations.

[1] In class C, we show only the data for optimization procedures II and IV.

Param			I		II		III		IV	
1	2500	1	3.98	3.93	4.07	4.00	3.94	3.91	3.97	3.91
1	2500	2	3.96	3.92	4.04	4.00	3.95	3.91	3.96	3.93
1	2500	3	3.97	3.96	4.06	4.00	3.97	3.96	3.97	3.96
2	2500	1	4.08	3.99	4.08	3.98	3.93	3.87	3.94	3.91
2	2500	2	4.06	4.02	4.06	4.02	3.97	3.91	3.95	3.93
2	2500	3	4.03	3.99	4.03	3.98	3.96	3.94	3.97	3.95
3	5000	1	3.93	3.87	3.95	3.87	3.82	3.82	3.87	3.83
3	5000	2	4.08	3.95	4.07	3.96	3.90	3.86	3.92	3.86
3	6000	1	3.96	3.90	3.97	3.89	3.85	3.83	3.85	3.83
3	6000	2	4.08	3.96	4.11	3.97	3.90	3.86	3.91	3.88
3	7000	1	3.99	3.92	4.03	3.93	3.86	3.84	3.86	3.83
3	7000	2	4.11	3.97	4.12	3.97	3.91	3.89	3.91	3.89

(a) Si-N

Param			I		II		III		IV	
1	2500	1	3.07	3.05	2.99	2.99	3.06	3.05	3.07	3.06
1	2500	2	3.06	3.06	3.00	3.00	3.04	3.06	3.06	3.05
1	2500	3	3.02	3.01	3.01	3.01	3.02	3.01	3.02	3.03
2	2500	1	3.01	3.01	3.01	3.01	3.10	3.08	3.10	3.08
2	2500	2	3.00	3.00	3.00	3.00	3.07	3.06	3.07	3.06
2	2500	3	3.00	3.00	3.00	3.00	3.05	3.05	3.05	3.04
3	5000	1	3.00	3.00	3.01	3.01	3.09	3.08	3.12	3.10
3	5000	2	3.00	3.00	3.01	3.01	3.14	3.12	3.14	3.13
3	6000	1	3.00	3.00	3.01	3.01	3.14	3.12	3.17	3.13
3	6000	2	3.02	3.02	3.02	3.02	3.14	3.12	3.18	3.16
3	7000	1	3.00	3.00	3.01	3.01	3.11	3.10	3.15	3.12
3	7000	2	3.01	3.01	3.03	3.02	3.14	3.11	3.18	3.15

(b) B-N

Table B.1: Class A: Topological properties (Si/B)-N. The first column indicates the cooling procedure used in the generation of the structures, the second column is the initial temperature of the cooling, and the third column is the cooling rate, where 0 corresponds to a local optimization and higher numbers refer to slower cooling. The roman numerals indicate the optimization procedure employed. For each optimization procedure the left column is the data before and right column is the data after RMC-refinement, respectively.

Param			I		II		III		IV	
1	2500	1	1.71	1.68	1.75	1.72	1.69	1.67	1.70	1.68
1	2500	2	1.70	1.68	1.73	1.71	1.70	1.67	1.70	1.69
1	2500	3	1.70	1.69	1.74	1.71	1.71	1.69	1.70	1.70
2	2500	1	1.75	1.71	1.75	1.71	1.69	1.66	1.69	1.68
2	2500	2	1.74	1.72	1.74	1.72	1.70	1.68	1.69	1.68
2	2500	3	1.73	1.71	1.73	1.71	1.70	1.69	1.70	1.69
3	5000	1	1.69	1.66	1.69	1.66	1.64	1.64	1.66	1.64
3	5000	2	1.75	1.69	1.74	1.70	1.67	1.66	1.68	1.66
3	6000	1	1.70	1.67	1.70	1.67	1.65	1.64	1.65	1.64
3	6000	2	1.75	1.69	1.76	1.70	1.67	1.66	1.68	1.66
3	7000	1	1.71	1.68	1.73	1.69	1.66	1.65	1.66	1.64
3	7000	2	1.76	1.70	1.77	1.71	1.68	1.66	1.68	1.67

(a) N-Si

Param			I		II		III		IV	
1	2500	1	1.31	1.31	1.28	1.28	1.31	1.31	1.31	1.31
1	2500	2	1.31	1.31	1.29	1.29	1.30	1.31	1.31	1.31
1	2500	3	1.30	1.29	1.29	1.29	1.30	1.29	1.30	1.30
2	2500	1	1.29	1.29	1.29	1.29	1.33	1.32	1.33	1.32
2	2500	2	1.29	1.29	1.29	1.29	1.32	1.31	1.32	1.31
2	2500	3	1.29	1.29	1.29	1.29	1.31	1.30	1.31	1.31
3	5000	1	1.29	1.29	1.29	1.29	1.33	1.32	1.34	1.33
3	5000	2	1.29	1.29	1.29	1.29	1.35	1.34	1.35	1.34
3	6000	1	1.29	1.29	1.29	1.29	1.35	1.34	1.35	1.34
3	6000	2	1.30	1.29	1.29	1.29	1.35	1.34	1.36	1.35
3	7000	1	1.29	1.29	1.29	1.29	1.33	1.33	1.35	1.34
3	7000	2	1.29	1.29	1.30	1.30	1.35	1.33	1.37	1.35

(b) N-B

Table B.2: Class A: Topological properties N-(Si/B). See table B.1 for explanation of the different columns headed Param and I-IV.

Param			I		II		III		IV	
1	2500	1	3.85	3.73	3.99	3.88	3.80	3.74	3.84	3.70
1	2500	2	3.79	3.75	3.92	3.88	3.77	3.72	3.79	3.73
1	2500	3	3.81	3.76	3.95	3.86	3.81	3.83	3.81	3.81
2	2500	1	3.93	3.79	3.94	3.75	3.67	3.59	3.70	3.66
2	2500	2	3.87	3.80	3.87	3.81	3.69	3.59	3.67	3.64
2	2500	3	3.83	3.78	3.83	3.77	3.67	3.67	3.72	3.71
3	5000	1	3.93	3.80	3.98	3.84	3.66	3.67	3.79	3.71
3	5000	2	4.14	3.94	4.10	3.92	3.75	3.68	3.76	3.69
3	6000	1	3.94	3.81	3.95	3.81	3.72	3.67	3.75	3.70
3	6000	2	4.06	3.87	4.12	3.88	3.71	3.65	3.70	3.63
3	7000	1	3.95	3.83	4.04	3.87	3.72	3.67	3.72	3.66
3	7000	2	4.22	3.97	4.27	4.06	3.90	3.86	3.90	3.84

(a) Si-Si

Param			I		II		III		IV	
1	2500	1	3.92	3.90	3.97	3.92	3.88	3.86	3.91	3.88
1	2500	2	3.97	3.95	4.04	4.00	3.95	3.94	3.98	3.95
1	2500	3	3.99	3.97	4.09	4.04	3.99	3.98	3.99	3.99
2	2500	1	4.14	4.06	4.14	4.05	4.03	3.98	4.05	4.01
2	2500	2	4.09	4.05	4.09	4.05	4.03	4.00	4.02	4.00
2	2500	3	4.14	4.11	4.14	4.11	4.07	4.06	4.08	4.07
3	5000	1	3.83	3.77	3.86	3.79	3.79	3.77	3.90	3.86
3	5000	2	3.84	3.74	3.86	3.76	3.77	3.75	3.81	3.75
3	6000	1	3.83	3.77	3.86	3.80	3.85	3.81	3.89	3.84
3	6000	2	3.94	3.83	3.97	3.88	3.86	3.82	3.91	3.89
3	7000	1	3.82	3.79	3.88	3.81	3.80	3.77	3.83	3.79
3	7000	2	3.84	3.74	3.85	3.74	3.71	3.69	3.75	3.72

(b) Si-B

Table B.3: Class A: Topological properties Si-(Si/B). See table B.1 for explanation of the different columns headed Param and I-IV.

Param			I		II		III		IV	
1	2500	1	3.92	3.90	3.97	3.92	3.88	3.86	3.91	3.88
1	2500	2	3.97	3.95	4.04	4.00	3.95	3.94	3.98	3.95
1	2500	3	3.99	3.97	4.09	4.04	3.99	3.98	3.99	3.99
2	2500	1	4.14	4.06	4.14	4.05	4.03	3.98	4.05	4.01
2	2500	2	4.09	4.05	4.09	4.05	4.03	4.00	4.02	4.00
2	2500	3	4.14	4.11	4.14	4.11	4.07	4.06	4.08	4.07
3	5000	1	3.83	3.77	3.86	3.79	3.79	3.77	3.90	3.86
3	5000	2	3.84	3.74	3.86	3.76	3.77	3.75	3.81	3.75
3	6000	1	3.83	3.77	3.86	3.80	3.85	3.81	3.89	3.84
3	6000	2	3.94	3.83	3.97	3.88	3.86	3.82	3.91	3.89
3	7000	1	3.82	3.79	3.88	3.81	3.80	3.77	3.83	3.79
3	7000	2	3.84	3.74	3.85	3.74	3.71	3.69	3.75	3.72

(a) B-Si

Param			I		II		III		IV	
1	2500	1	2.08	2.05	2.00	2.00	2.06	2.04	2.08	2.08
1	2500	2	2.06	2.07	1.96	1.96	2.02	2.09	2.06	2.06
1	2500	3	1.96	1.96	1.92	1.92	1.93	1.92	1.96	1.96
2	2500	1	1.91	1.91	1.90	1.90	2.01	2.00	2.03	2.02
2	2500	2	1.91	1.91	1.91	1.91	2.03	2.01	2.03	2.01
2	2500	3	1.89	1.89	1.89	1.89	1.97	1.97	1.97	1.97
3	5000	1	2.19	2.19	2.20	2.20	2.27	2.26	2.27	2.25
3	5000	2	2.12	2.12	2.15	2.15	2.31	2.29	2.31	2.30
3	6000	1	2.18	2.18	2.18	2.18	2.34	2.32	2.36	2.33
3	6000	2	2.08	2.08	2.09	2.09	2.21	2.19	2.27	2.24
3	7000	1	2.13	2.13	2.17	2.17	2.26	2.26	2.33	2.31
3	7000	2	2.22	2.22	2.25	2.24	2.39	2.36	2.47	2.43

(b) B-B

Table B.4: Class A: Topological properties B-(Si/B). See table B.1 for explanation of the different columns headed Param and I-IV.

Param			I		II		III		IV	
4	5000	1	4.00	3.91	4.03	3.92	3.69	3.67	3.76	3.73
4	5000	2	4.03	3.91	4.04	3.92	3.70	3.67	3.79	3.75
4	5000	3	3.92	3.84	3.92	3.84	3.79	3.75	3.83	3.78
4	6000	1	4.03	3.93	4.04	3.92	3.71	3.68	3.77	3.75
4	6000	2	4.00	3.88	4.00	3.89	3.75	3.71	3.79	3.75
4	6000	3	3.88	3.80	3.88	3.79	3.77	3.72	3.80	3.76
4	7000	2	3.93	3.85	3.99	3.88	3.76	3.72	3.79	3.74
4	7000	3	3.88	3.80	3.86	3.78	3.76	3.71	3.76	3.73
5	1000	1	4.02	3.93	4.02	3.93	3.80	3.78	3.82	3.78
5	1000	2	4.01	3.94	4.01	3.93	3.83	3.80	3.83	3.80
5	1000	3	4.02	3.94	4.02	3.94	3.81	3.78	3.83	3.78
5	2000	1	4.01	3.92	4.01	3.93	3.83	3.79	3.85	3.80
5	2000	2	4.04	3.96	4.04	3.97	3.93	3.90	3.94	3.90
5	2000	3	4.03	3.99	4.03	3.98	3.97	3.96	3.97	3.94
5	3000	1	4.04	3.96	4.04	3.95	3.91	3.86	3.92	3.87
5	3000	2	4.04	3.96	4.04	3.97	3.93	3.90	3.94	3.90
5	3000	3	4.03	3.99	4.03	3.98	3.97	3.96	3.97	3.94
6	1000	1	3.99	3.91	3.99	3.90	3.77	3.75	3.79	3.77
6	1000	2	3.97	3.91	3.97	3.92	3.79	3.76	3.80	3.78
6	1000	3	3.99	3.93	3.99	3.92	3.82	3.78	3.83	3.80
6	2000	1	3.99	3.92	3.99	3.92	3.82	3.78	3.84	3.80
6	2000	2	4.00	3.92	3.99	3.93	3.86	3.83	3.90	3.85
6	2000	3	4.00	3.95	4.00	3.94	3.92	3.88	3.92	3.90
6	3000	1	3.99	3.91	3.99	3.91	3.85	3.80	3.88	3.83
6	3000	2	3.97	3.90	3.97	3.91	3.89	0.00	3.89	3.85
6	3000	3	3.99	3.94	4.00	3.95	3.90	0.00	3.91	3.89

Table B.5: Class B: Topological properties Si-N. See B.1 for explanation of the different columns headed Param and I-IV.

Param			I		II		III		IV	
4	5000	1	2.83	2.83	2.92	2.92	3.06	3.03	3.12	3.08
4	5000	2	2.62	2.62	2.66	2.66	3.02	2.96	3.06	3.01
4	5000	3	2.63	2.63	2.64	2.64	2.94	2.92	2.98	2.95
4	6000	1	2.79	2.79	2.91	2.91	3.04	3.01	3.14	3.10
4	6000	2	2.63	2.63	2.62	2.62	2.99	2.94	3.04	2.99
4	6000	3	2.67	2.67	2.66	2.66	2.95	2.94	2.97	2.96
4	7000	2	2.55	2.55	2.63	2.63	3.01	2.96	3.04	2.99
4	7000	3	2.67	2.67	2.67	2.67	3.00	2.96	2.99	2.96
5	1000	1	2.96	2.96	2.96	2.96	3.09	3.07	3.08	3.06
5	1000	2	2.97	2.97	2.97	2.97	3.06	3.05	3.06	3.05
5	1000	3	2.96	2.96	2.96	2.96	3.07	3.05	3.07	3.06
5	2000	1	2.92	2.92	2.92	2.92	3.03	3.02	3.03	3.02
5	2000	2	2.99	2.99	2.99	2.99	3.05	3.04	3.04	3.03
5	2000	3	3.00	3.00	3.00	3.00	3.03	3.03	3.03	3.03
5	3000	1	2.84	2.84	2.84	2.84	2.99	2.98	2.99	2.98
5	3000	2	2.99	2.99	2.99	2.99	3.05	3.04	3.04	3.03
5	3000	3	3.00	3.00	3.00	3.00	3.03	3.03	3.03	3.03
6	1000	1	2.92	2.92	2.92	2.92	3.07	3.05	3.07	3.05
6	1000	2	2.93	2.93	2.93	2.93	3.05	3.03	3.05	3.04
6	1000	3	2.93	2.93	2.93	2.93	3.01	3.00	3.00	3.00
6	2000	1	2.90	2.90	2.89	2.89	3.02	3.01	3.01	3.00
6	2000	2	2.90	2.90	2.91	2.90	2.98	2.98	2.97	2.97
6	2000	3	2.92	2.92	2.92	2.92	2.97	2.97	2.96	2.96
6	3000	1	2.78	2.78	2.78	2.78	2.98	2.96	2.99	2.97
6	3000	2	2.87	2.87	2.87	2.87	2.95	0.00	2.96	2.95
6	3000	3	2.96	2.96	2.96	2.96	3.01	0.00	3.01	2.99

Table B.6: Class B: Topological properties B-N. See B.1 for explanation of the different columns headed Param and I-IV.

Param			I		II		III		IV	
4	5000	1	1.71	1.68	1.73	1.68	1.58	1.57	1.61	1.60
4	5000	2	1.73	1.68	1.73	1.68	1.59	1.57	1.62	1.61
4	5000	3	1.68	1.64	1.68	1.64	1.63	1.61	1.64	1.62
4	6000	1	1.73	1.68	1.73	1.68	1.59	1.57	1.62	1.61
4	6000	2	1.72	1.66	1.71	1.67	1.60	1.59	1.63	1.61
4	6000	3	1.66	1.63	1.66	1.62	1.61	1.59	1.63	1.61
4	7000	2	1.68	1.65	1.71	1.66	1.61	1.60	1.62	1.60
4	7000	3	1.67	1.62	1.65	1.62	1.62	1.59	1.61	1.60
5	1000	1	1.72	1.69	1.72	1.69	1.63	1.62	1.64	1.62
5	1000	2	1.72	1.69	1.72	1.69	1.64	1.63	1.64	1.63
5	1000	3	1.73	1.69	1.73	1.69	1.63	1.62	1.64	1.62
5	2000	1	1.72	1.68	1.72	1.69	1.64	1.62	1.65	1.62
5	2000	2	1.73	1.69	1.73	1.70	1.69	1.67	1.69	1.67
5	2000	3	1.73	1.71	1.73	1.71	1.70	1.70	1.70	1.69
5	3000	1	1.73	1.69	1.73	1.69	1.67	1.65	1.68	1.66
5	3000	2	1.73	1.69	1.73	1.70	1.69	1.67	1.69	1.67
5	3000	3	1.73	1.71	1.73	1.71	1.70	1.70	1.70	1.69
6	1000	1	1.71	1.67	1.71	1.67	1.62	1.61	1.62	1.62
6	1000	2	1.70	1.67	1.70	1.68	1.62	1.61	1.63	1.62
6	1000	3	1.71	1.68	1.71	1.68	1.64	1.62	1.65	1.63
6	2000	1	1.71	1.68	1.71	1.68	1.64	1.62	1.64	1.63
6	2000	2	1.71	1.68	1.71	1.68	1.65	1.64	1.68	1.65
6	2000	3	1.71	1.69	1.71	1.69	1.68	1.67	1.68	1.67
6	3000	1	1.71	1.67	1.71	1.68	1.65	1.63	1.66	1.64
6	3000	2	1.70	1.67	1.70	1.67	1.66	0.00	1.67	1.65
6	3000	3	1.71	1.69	1.71	1.69	1.67	0.00	1.68	1.67

Table B.7: Class B: Topological properties N-Si. See B.1 for explanation of the different columns headed Param and I-IV.

Param			I		II		III		IV	
4	5000	1	1.22	1.22	1.25	1.25	1.31	1.30	1.34	1.32
4	5000	2	1.12	1.12	1.14	1.14	1.29	1.26	1.31	1.29
4	5000	3	1.13	1.13	1.13	1.13	1.26	1.25	1.28	1.27
4	6000	1	1.19	1.19	1.25	1.25	1.30	1.29	1.34	1.33
4	6000	2	1.13	1.13	1.12	1.12	1.28	1.26	1.30	1.28
4	6000	3	1.14	1.14	1.14	1.14	1.27	1.26	1.27	1.27
4	7000	2	1.10	1.10	1.13	1.13	1.29	1.27	1.30	1.28
4	7000	3	1.14	1.14	1.15	1.15	1.29	1.27	1.28	1.27
5	1000	1	1.27	1.27	1.27	1.27	1.33	1.32	1.32	1.31
5	1000	2	1.27	1.27	1.27	1.27	1.31	1.31	1.31	1.31
5	1000	3	1.27	1.27	1.27	1.27	1.32	1.31	1.32	1.31
5	2000	1	1.25	1.25	1.25	1.25	1.30	1.29	1.30	1.29
5	2000	2	1.29	1.28	1.29	1.28	1.31	1.31	1.31	1.29
5	2000	3	1.29	1.28	1.29	1.28	1.30	1.30	1.30	1.30
5	3000	1	1.22	1.22	1.22	1.22	1.28	1.28	1.28	1.28
5	3000	2	1.29	1.28	1.29	1.28	1.31	1.31	1.31	1.29
5	3000	3	1.29	1.28	1.29	1.28	1.30	1.30	1.30	1.30
6	1000	1	1.25	1.25	1.25	1.25	1.32	1.31	1.31	1.31
6	1000	2	1.25	1.25	1.25	1.25	1.30	1.30	1.30	1.31
6	1000	3	1.26	1.26	1.26	1.26	1.29	1.29	1.29	1.29
6	2000	1	1.24	1.24	1.24	1.24	1.29	1.29	1.29	1.29
6	2000	2	1.24	1.24	1.25	1.24	1.28	1.28	1.27	1.27
6	2000	3	1.25	1.25	1.25	1.25	1.27	1.27	1.27	1.27
6	3000	1	1.19	1.19	1.19	1.19	1.28	1.27	1.28	1.27
6	3000	2	1.23	1.23	1.23	1.23	1.26	0.00	1.27	1.26
6	3000	3	1.27	1.27	1.27	1.27	1.29	0.00	1.29	1.28

Table B.8: Class B: Topological properties N-B. See B.1 for explanation of the different columns headed Param and I-IV.

Param			I		II		III		IV	
4	5000	1	6.41	6.22	6.47	6.25	5.54	5.49	5.71	5.63
4	5000	2	6.01	5.79	5.97	5.77	5.27	5.21	5.37	5.30
4	5000	3	4.31	4.20	4.31	4.19	4.09	4.04	4.15	4.12
4	6000	1	6.49	6.25	6.52	6.25	5.51	5.46	5.65	5.59
4	6000	2	5.56	5.38	5.53	5.34	4.99	4.94	5.12	5.06
4	6000	3	3.76	3.66	3.77	3.64	3.65	3.61	3.71	3.66
4	7000	2	5.02	4.90	5.18	4.97	4.85	4.81	4.91	4.81
4	7000	3	3.53	3.46	3.51	3.40	3.45	3.40	3.52	3.47
5	1000	1	6.44	6.26	6.45	6.26	5.72	5.62	5.76	5.65
5	1000	2	6.36	6.21	6.36	6.21	5.77	5.70	5.77	5.71
5	1000	3	6.43	6.26	6.43	6.27	5.74	5.68	5.78	5.66
5	2000	1	6.15	5.94	6.16	5.97	5.61	5.51	5.64	5.53
5	2000	2	4.09	3.99	4.09	3.99	3.89	3.83	3.91	3.84
5	2000	3	4.05	3.98	4.05	3.96	3.92	3.89	3.92	3.88
5	3000	1	5.14	4.98	5.14	4.97	4.79	4.71	4.79	4.70
5	3000	2	4.09	3.99	4.09	3.99	3.89	3.83	3.91	3.84
5	3000	3	4.05	3.98	4.05	3.96	3.92	3.89	3.92	3.88
6	1000	1	6.32	6.15	6.32	6.14	5.66	5.62	5.69	5.64
6	1000	2	6.22	6.11	6.22	6.12	5.65	5.59	5.70	5.66
6	1000	3	6.13	6.00	6.13	6.00	5.66	5.57	5.71	5.67
6	2000	1	6.06	5.94	6.06	5.93	5.58	5.51	5.63	5.53
6	2000	2	5.82	5.64	5.48	5.66	5.45	5.41	5.25	5.41
6	2000	3	5.37	5.29	5.37	5.27	5.14	5.09	5.16	5.10
6	3000	1	4.91	4.77	4.90	4.74	4.48	4.41	4.57	4.51
6	3000	2	3.98	3.86	3.97	3.88	3.81	0.00	3.83	3.77
6	3000	3	3.75	3.70	3.76	3.69	3.57	0.00	3.61	3.57

Table B.9: Class B: Topological properties Si-Si. See table B.1 for explanation of the different columns headed Param and I-IV.

Param			I		II		III		IV	
4	5000	1	1.04	1.03	1.21	1.18	1.08	1.06	1.27	1.25
4	5000	2	1.26	1.24	1.31	1.28	1.30	1.27	1.49	1.47
4	5000	3	2.49	2.46	2.51	2.47	2.63	2.60	2.70	2.67
4	6000	1	1.05	1.03	1.22	1.19	1.13	1.12	1.35	1.34
4	6000	2	1.47	1.43	1.49	1.45	1.59	1.58	1.66	1.63
4	6000	3	2.82	2.79	2.82	2.79	2.97	2.94	3.01	2.99
4	7000	2	1.68	1.66	1.76	1.74	1.85	1.81	1.88	1.86
4	7000	3	3.00	2.98	2.97	2.96	3.17	3.14	3.17	3.15
5	1000	1	1.28	1.25	1.28	1.25	1.41	1.44	1.42	1.40
5	1000	2	1.37	1.33	1.37	1.33	1.44	1.42	1.44	1.43
5	1000	3	1.32	1.29	1.32	1.29	1.39	1.37	1.41	1.39
5	2000	1	1.44	1.42	1.44	1.42	1.50	1.48	1.52	1.50
5	2000	2	3.71	3.66	3.71	3.67	3.65	3.63	3.65	3.62
5	2000	3	3.85	3.83	3.85	3.83	3.85	3.84	3.83	3.81
5	3000	1	2.55	2.51	2.55	2.51	2.56	2.52	2.57	2.54
5	3000	2	3.71	3.66	3.71	3.67	3.65	3.63	3.65	3.62
5	3000	3	3.85	3.83	3.85	3.83	3.85	3.84	3.83	3.81
6	1000	1	1.22	1.20	1.21	1.19	1.32	1.32	1.34	1.33
6	1000	2	1.25	1.24	1.25	1.23	1.32	1.31	1.33	1.32
6	1000	3	1.39	1.38	1.39	1.37	1.40	1.39	1.40	1.38
6	2000	1	1.37	1.36	1.37	1.36	1.40	1.39	1.41	1.41
6	2000	2	1.66	1.65	2.06	1.64	1.66	1.65	2.04	1.67
6	2000	3	2.24	2.22	2.24	2.22	2.21	2.21	2.22	2.21
6	3000	1	2.48	2.45	2.48	2.46	2.55	2.53	2.57	2.54
6	3000	2	3.40	3.35	3.40	3.36	3.39	0.00	3.40	3.38
6	3000	3	3.77	3.74	3.77	3.75	3.71	0.00	3.73	3.72

Table B.10: Class B: Topological properties Si-B. See table B.1 for explanation of the different columns headed Param and I-IV.

Param			I		II		III		IV	
4	5000	1	1.04	1.03	1.21	1.18	1.08	1.06	1.27	1.25
4	5000	2	1.26	1.24	1.31	1.28	1.30	1.27	1.49	1.47
4	5000	3	2.49	2.46	2.51	2.47	2.63	2.60	2.70	2.67
4	6000	1	1.05	1.03	1.22	1.19	1.13	1.12	1.35	1.34
4	6000	2	1.47	1.43	1.49	1.45	1.59	1.58	1.66	1.63
4	6000	3	2.82	2.79	2.82	2.79	2.97	2.94	3.01	2.99
4	7000	2	1.68	1.66	1.76	1.74	1.85	1.81	1.88	1.86
4	7000	3	3.00	2.98	2.97	2.96	3.17	3.14	3.17	3.15
5	1000	1	1.28	1.25	1.28	1.25	1.41	1.44	1.42	1.40
5	1000	2	1.37	1.33	1.37	1.33	1.44	1.42	1.44	1.43
5	1000	3	1.32	1.29	1.32	1.29	1.39	1.37	1.41	1.39
5	2000	1	1.44	1.42	1.44	1.42	1.50	1.48	1.52	1.50
5	2000	2	3.71	3.66	3.71	3.67	3.65	3.63	3.65	3.62
5	2000	3	3.85	3.83	3.85	3.83	3.85	3.84	3.83	3.81
5	3000	1	2.55	2.51	2.55	2.51	2.56	2.52	2.57	2.54
5	3000	2	3.71	3.66	3.71	3.67	3.65	3.63	3.65	3.62
5	3000	3	3.85	3.83	3.85	3.83	3.85	3.84	3.83	3.81
6	1000	1	1.22	1.20	1.21	1.19	1.32	1.32	1.34	1.33
6	1000	2	1.25	1.24	1.25	1.23	1.32	1.31	1.33	1.32
6	1000	3	1.39	1.38	1.39	1.37	1.40	1.39	1.40	1.38
6	2000	1	1.37	1.36	1.37	1.36	1.40	1.39	1.41	1.41
6	2000	2	1.66	1.65	2.06	1.64	1.66	1.65	2.04	1.67
6	2000	3	2.24	2.22	2.24	2.22	2.21	2.21	2.22	2.21
6	3000	1	2.48	2.45	2.48	2.46	2.55	2.53	2.57	2.54
6	3000	2	3.40	3.35	3.40	3.36	3.39	0.00	3.40	3.38
6	3000	3	3.77	3.74	3.77	3.75	3.71	0.00	3.73	3.72

Table B.11: Class B: Topological properties B-Si. See table B.1 for explanation of the different columns headed Param and I-IV.

Param			I		II		III		IV	
4	5000	1	4.30	4.30	4.52	4.52	4.75	4.70	4.90	4.83
4	5000	2	3.20	3.20	3.31	3.31	4.10	4.04	4.13	4.07
4	5000	3	1.97	1.97	1.99	1.99	2.54	2.53	2.64	2.61
4	6000	1	4.10	4.10	4.42	4.41	4.59	4.54	4.79	4.73
4	6000	2	3.07	3.07	3.04	3.04	3.69	3.65	3.88	3.82
4	6000	3	1.79	1.79	1.77	1.77	2.22	2.21	2.29	2.29
4	7000	2	2.64	2.64	2.84	2.84	3.50	3.44	3.64	3.59
4	7000	3	1.65	1.65	1.65	1.65	2.12	2.11	2.13	2.10
5	1000	1	4.53	4.53	4.53	4.53	4.71	4.69	4.70	4.66
5	1000	2	4.50	4.50	4.50	4.50	4.60	4.59	4.60	4.57
5	1000	3	4.51	4.51	4.51	4.51	4.69	4.67	4.67	4.64
5	2000	1	4.23	4.23	4.23	4.23	4.40	4.38	4.39	4.37
5	2000	2	2.17	2.17	2.17	2.17	2.23	2.23	2.21	2.21
5	2000	3	2.07	2.07	2.07	2.07	2.10	2.10	2.11	2.11
5	3000	1	2.71	2.71	2.71	2.71	3.03	3.02	3.02	3.02
5	3000	2	2.17	2.17	2.17	2.17	2.23	2.23	2.21	2.21
5	3000	3	2.07	2.07	2.07	2.07	2.10	2.10	2.11	2.11
6	1000	1	4.48	4.48	4.46	4.46	4.67	4.63	4.68	4.66
6	1000	2	4.45	4.45	4.44	4.44	4.64	4.62	4.66	4.64
6	1000	3	4.31	4.31	4.31	4.31	4.45	4.43	4.46	4.46
6	2000	1	4.14	4.14	4.14	4.14	4.41	4.40	4.41	4.39
6	2000	2	3.92	3.92	3.56	3.92	4.08	4.08	3.67	4.07
6	2000	3	3.33	3.33	3.33	3.33	3.45	3.44	3.45	3.44
6	3000	1	2.47	2.47	2.47	2.47	2.82	2.81	2.89	2.87
6	3000	2	1.93	1.93	1.93	1.93	2.05	0.00	2.08	2.08
6	3000	3	1.94	1.94	1.94	1.94	1.98	0.00	1.98	1.96

Table B.12: Class B: Topological properties B-B. See table B.1 for explanation of the different columns headed Param and I-IV.

Param			II		IV	
7	0	0	3.96	0.00	3.79	0.00
7	1500	0	4.01	0.00	3.84	0.00
7	1500	1	4.00	3.84	3.88	3.62
7	1500	2	4.01	3.86	3.86	3.61
7	1500	3	4.02	3.82	3.88	3.56
7	2500	0	3.89	0.00	3.70	0.00
7	2500	1	3.94	3.77	3.78	3.57
7	2500	2	3.97	3.74	3.81	3.53
7	2500	3	3.98	3.68	3.80	3.44
8	1500	0	4.05	0.00	3.98	0.00
8	1500	1	4.05	4.00	3.98	3.94
8	1500	2	4.04	4.02	3.98	3.95
8	1500	3	4.03	3.99	3.96	3.94
8	2500	0	4.04	0.00	3.91	0.00
8	2500	1	4.02	3.92	3.91	3.86
8	2500	2	4.03	3.97	3.92	3.89
8	2500	3	4.03	0.00	3.94	0.00

(a) Si-N

Param			II		IV	
7	0	0	2.97	0.00	3.06	0.00
7	1500	0	2.95	0.00	3.03	0.00
7	1500	1	2.95	2.87	3.03	2.92
7	1500	2	2.97	2.87	3.02	2.91
7	1500	3	2.98	2.89	3.02	2.92
7	2500	0	2.76	0.00	2.90	0.00
7	2500	1	2.81	2.69	2.94	2.75
7	2500	2	2.88	2.77	2.93	2.79
7	2500	3	2.95	2.83	2.99	2.83
8	1500	0	2.99	0.00	3.05	0.00
8	1500	1	2.99	2.99	3.02	3.01
8	1500	2	2.99	2.99	3.04	3.04
8	1500	3	2.99	2.99	3.02	3.02
8	2500	0	2.96	0.00	3.08	0.00
8	2500	1	2.96	2.96	3.06	3.05
8	2500	2	2.99	2.99	3.07	3.06
8	2500	3	2.99	0.00	3.03	0.00

(b) B-N

Table B.13: CLASS C: Topological properties (Si/B)-N. See table B.1 for explanation of the different columns headed Param and I-IV.

Param			II		IV	
7	0	0	1.69	0.00	1.58	0.00
7	1500	0	1.93	0.00	1.72	0.00
7	1500	1	1.92	1.73	1.74	1.63
7	1500	2	1.94	1.74	1.72	1.62
7	1500	3	1.94	1.72	1.74	1.60
7	2500	0	1.86	0.00	1.70	0.00
7	2500	1	1.88	1.70	1.72	1.60
7	2500	2	1.91	1.69	1.73	1.59
7	2500	3	1.91	1.66	1.72	1.55
8	1500	0	1.74	0.00	1.70	0.00
8	1500	1	1.73	1.71	1.70	1.69
8	1500	2	1.73	1.72	1.70	1.69
8	1500	3	1.73	1.71	1.70	1.69
8	2500	0	1.73	0.00	1.68	0.00
8	2500	1	1.72	1.68	1.67	1.66
8	2500	2	1.73	1.70	1.68	1.67
8	2500	3	1.72	0.00	1.69	0.00

(a) N-Si

Param			II		IV	
7	0	0	1.36	0.00	1.40	0.00
7	1500	0	1.29	0.00	1.31	0.00
7	1500	1	1.29	1.31	1.32	1.34
7	1500	2	1.29	1.31	1.32	1.33
7	1500	3	1.29	1.32	1.30	1.33
7	2500	0	1.19	0.00	1.23	0.00
7	2500	1	1.23	1.23	1.26	1.26
7	2500	2	1.24	1.27	1.25	1.28
7	2500	3	1.27	1.29	1.29	1.29
8	1500	0	1.28	0.00	1.31	0.00
8	1500	1	1.28	1.28	1.30	1.29
8	1500	2	1.28	1.28	1.30	1.30
8	1500	3	1.28	1.28	1.30	1.29
8	2500	0	1.27	0.00	1.32	0.00
8	2500	1	1.27	1.27	1.31	1.31
8	2500	2	1.28	1.28	1.31	1.31
8	2500	3	1.28	0.00	1.29	0.00

(b) N-B

Table B.14: CLASS C: Topological properties N-(Si/B). See table B.1 for explanation of the different columns headed Param and I-IV.

Param			II		IV	
7	0	0	4.52	0.00	4.21	0.00
7	1500	0	4.43	0.00	3.72	0.00
7	1500	1	4.34	4.42	3.76	3.88
7	1500	2	4.37	4.46	3.77	3.87
7	1500	3	4.35	4.36	3.77	3.72
7	2500	0	3.90	0.00	3.33	0.00
7	2500	1	4.01	3.76	3.49	3.27
7	2500	2	4.08	3.73	3.52	3.30
7	2500	3	4.08	3.67	3.51	3.05
8	1500	0	4.44	0.00	4.29	0.00
8	1500	1	4.43	4.36	4.27	4.24
8	1500	2	4.41	4.38	4.26	4.23
8	1500	3	4.40	4.33	4.26	4.24
8	2500	0	3.94	0.00	3.77	0.00
8	2500	1	3.87	3.74	3.65	3.59
8	2500	2	3.92	3.82	3.68	3.64
8	2500	3	3.79	0.00	3.68	0.00

(a) Si-Si

Param			II		IV	
7	0	0	2.31	0.00	2.53	0.00
7	1500	0	3.04	0.00	2.96	0.00
7	1500	1	3.03	3.22	3.01	3.04
7	1500	2	3.09	3.25	2.99	3.01
7	1500	3	3.13	3.27	3.06	3.03
7	2500	0	3.22	0.00	3.08	0.00
7	2500	1	3.41	3.44	3.31	3.29
7	2500	2	3.45	3.53	3.27	3.29
7	2500	3	3.63	3.63	3.45	3.36
8	1500	0	3.39	0.00	3.38	0.00
8	1500	1	3.39	3.37	3.36	3.32
8	1500	2	3.40	3.38	3.40	3.39
8	1500	3	3.38	3.36	3.35	3.35
8	2500	0	3.76	0.00	3.72	0.00
8	2500	1	3.79	3.74	3.76	3.73
8	2500	2	3.90	3.85	3.83	3.81
8	2500	3	3.97	0.00	3.92	0.00

(b) Si-B

Table B.15: CLASS C: Topological properties Si-(Si/B). See table B.1 for explanation of the different columns headed Param and I-IV.

Param			II		IV	
7	0	0	2.34	0.00	2.25	0.00
7	1500	0	3.57	0.00	3.19	0.00
7	1500	1	3.55	3.17	3.22	2.99
7	1500	2	3.55	3.20	3.17	2.98
7	1500	3	3.61	3.23	3.27	3.00
7	2500	0	3.64	0.00	3.46	0.00
7	2500	1	3.76	3.39	3.60	3.24
7	2500	2	3.88	3.48	3.57	3.23
7	2500	3	4.09	3.59	3.66	3.30
8	1500	0	3.39	0.00	3.38	0.00
8	1500	1	3.39	3.37	3.36	3.32
8	1500	2	3.40	3.38	3.40	3.39
8	1500	3	3.38	3.36	3.35	3.35
8	2500	0	3.76	0.00	3.72	0.00
8	2500	1	3.79	3.74	3.76	3.73
8	2500	2	3.90	3.85	3.83	3.81
8	2500	3	3.97	0.00	3.92	0.00

(a) B-Si

Param			II		IV	
7	0	0	3.00	0.00	3.22	0.00
7	1500	0	2.32	0.00	2.36	0.00
7	1500	1	2.30	2.54	2.39	2.61
7	1500	2	2.31	2.56	2.37	2.61
7	1500	3	2.31	2.57	2.35	2.58
7	2500	0	1.54	0.00	1.65	0.00
7	2500	1	1.59	1.61	1.71	1.71
7	2500	2	1.71	1.82	1.75	1.81
7	2500	3	1.70	1.83	1.76	1.82
8	1500	0	2.50	0.00	2.57	0.00
8	1500	1	2.50	2.50	2.55	2.54
8	1500	2	2.49	2.49	2.57	2.57
8	1500	3	2.52	2.52	2.54	2.54
8	2500	0	2.01	0.00	2.15	0.00
8	2500	1	1.99	1.99	2.09	2.08
8	2500	2	2.00	2.00	2.09	2.09
8	2500	3	1.95	0.00	1.98	0.00

(b) B-B

Table B.16: CLASS C: Topological properties B-(Si/B). See table B.1 for explanation of the different columns headed Param and I-IV.

Param			I		II		III		IV	
10	95	1	3.77	3.71	3.67	3.57	3.64	0.00	3.63	3.60
10	95	2	3.77	3.59	3.76	3.64	3.66	3.60	3.68	3.63
10	99	1	3.77	3.65	3.69	3.58	3.62	0.00	3.62	3.58
10	99	2	3.74	3.63	3.72	3.61	3.61	3.61	3.66	3.63

(a) Si-N

Param			I		II		III		IV	
10	95	1	2.97	2.96	2.96	2.96	3.16	0.00	3.21	3.12
10	95	2	2.95	2.93	2.95	2.95	3.17	3.12	3.21	3.13
10	99	1	2.98	2.99	2.97	2.97	3.18	0.00	3.22	3.13
10	99	2	2.97	2.96	2.96	2.96	3.19	3.10	3.24	3.17

(b) B-N

Table B.17: CLASS E: Topological properties (Si/B)-N. See table B.1 for explanation of the different columns headed Param and I-IV.

Param			I		II		III		IV	
10	95	1	1.61	1.59	1.57	1.53	1.56	0.00	1.56	1.54
10	95	2	1.62	1.54	1.61	1.56	1.57	1.54	1.58	1.56
10	99	1	1.61	1.56	1.58	1.54	1.55	0.00	1.55	1.54
10	99	2	1.60	1.56	1.60	1.55	1.55	1.55	1.57	1.56

(a) N-Si

Param			I		II		III		IV	
10	95	1	1.27	1.27	1.27	1.27	1.35	0.00	1.38	1.34
10	95	2	1.27	1.26	1.27	1.27	1.36	1.34	1.38	1.34
10	99	1	1.28	1.28	1.27	1.27	1.36	0.00	1.38	1.34
10	99	2	1.27	1.27	1.27	1.27	1.37	1.33	1.39	1.36

(b) N-B

Table B.18: CLASS E: Topological properties N-(Si/B). See table B.1 for explanation of the different columns headed Param and I-IV.

Param			I		II		III		IV	
10	95	1	4.34	4.29	4.08	3.94	3.88	0.00	3.89	3.84
10	95	2	3.90	3.61	3.90	3.72	3.61	3.50	3.67	3.62
10	99	1	4.78	4.63	4.58	4.39	4.29	0.00	4.33	4.27
10	99	2	3.89	3.67	3.84	3.69	3.68	3.55	3.84	3.79

(a) Si-Si

Param			I		II		III		IV	
10	95	1	2.50	2.45	2.39	2.33	2.63	0.00	2.62	2.57
10	95	2	2.88	2.76	2.84	2.77	2.94	2.90	3.04	2.97
10	99	1	2.03	1.97	1.97	1.92	2.06	0.00	2.08	2.02
10	99	2	2.69	2.69	2.68	2.60	2.68	2.80	2.79	2.76

(b) Si-B

Table B.19: CLASS E: Topological properties Si-(Si/B). See table B.1 for explanation of the different columns headed Param and I-IV.

Param			I		II		III		IV	
10	95	1	2.50	2.45	2.39	2.33	2.63	0.00	2.62	2.57
10	95	2	2.88	2.76	2.84	2.77	2.94	2.90	3.04	2.97
10	99	1	2.03	1.97	1.97	1.92	2.06	0.00	2.08	2.02
10	99	2	2.69	2.69	2.68	2.60	2.68	2.80	2.79	2.76

(a) B-Si

Param			I		II		III		IV	
10	95	1	3.29	3.36	3.30	3.30	3.34	0.00	3.48	3.38
10	95	2	2.87	2.77	2.90	2.90	2.93	2.89	2.98	2.90
10	99	1	3.99	3.96	3.97	3.97	4.05	0.00	4.09	3.98
10	99	2	3.30	3.21	3.28	3.27	3.28	3.00	3.39	3.29

(b) B-B

Table B.20: CLASS E: Topological properties B-(Si/B). See table B.1 for explanation of the different columns headed Param and I-IV.

Bibliography

[1] G. Adam and J.H. Gibbs. On the Temperature Dependence of Cooperative Relaxation Properties in Glass-forming Liquids. *Journal of Chemical Physics*, pages 139–146, 1965.

[2] R. Agrawal and D. Kofke. Thermodynamic and Structural Properties of Model Systems at Solid-Fluid Coexistence II. Melting and Sublimation of the Lennard-Jones Systems. *Molecular Physics*, 85(1):43–59, 1995.

[3] T. Aiyama, T. Fukunaga, K. Niihara, T. Hirai, and K. Suzuki. An X-ray Diffraction Study of the Amorphous Structure of Chemically Vapor-deposited Silicon Nitride. *Journal of Non-Crystalline Solids*, 33:131, 1979.

[4] M. Allen and D. Tildesley. *Computer Simulations of Liquids*. Clarendon Press Oxford, 1987.

[5] P. W. Anderson, B. I. Halperin, and C. M. Varma. Low-Temperature Thermal Properties of Glasses and Spin Glasses. *Philosophical Magazine*, 25:1–9, 1972.

[6] J. Andersson, J. Mattson, and P. Svendlindh. Monte-Carlo Studies of Ising Spin-glass systems: Aging Behaviour and Crossover between Equilibrium and Non-equilibrium Dynamics. *Physical Review B*, 46:8297–8304, 1992.

[7] L. Angelani, R. Di Leonardo, G. Parisi, and G. Ruocco. Topological Description of the Aging Dynamics in Simple Glasses. *Physical Review Letters*, 87:5502–5506, 2001.

[8] L. Angelani, R. Di Leonardo, G. Ruocco, A. Scala, and F. Sciortino. Quasisaddles as Relevant Points on the Potential Energy Surface in the Dynamics of Supercooled Liquids. *Journal of Chemical Physics*, 116(23):10297–10306, 2002.

[9] C. Angell, K. Ngai, G. McKenna, P. McMillan, and S. Martin. Relaxation in Glassforming Liquids and Amorphous Solids. *Journal of Applied Physics*, 88(6):3113–3157, 2000.

[10] F. Babalievsky. Cluster counting: The Hoshen-Kopelman Algorithm versus Spanning Tree Approaches. *International Journal of Modern Physics C*, 9(1):43–60, 1998.

[11] P. Baldus, M. Jansen, and D. Sporn. Ceramic Fibers for Matrix Composites in High-Temperature Engine Applications. *Science*, 285:699–703, 1999.

[12] R. Bansil, H. Herrmann, and D. Stauffer. Computer Simulation of Kinetics of Gelation by Addition Polymerization in a Solvent. *Macromolecules*, 17:998–1004, 1984.

[13] R. Bansil, M. Willings, and H. Herrmann. Spatial Correlation in Kinetic Gelation. *Journal of Physics A: Mathematical and General*, 19:L1209–L1213, 1986.

[14] M. Barroso and A.L. Ferreira. Solid-Fluid Coexistence of the Lennard-Jones System from Absolute Free Energy Calculations. *Journal of Chemical Physics*, 116(16):7145–7150, 2002.

[15] B. Beest, G. Kramer, and R. van Santen. Force Fields for Silicas and Aluminophosphate Based on Ab-initio Calculations. *Physical Review Letters*, 64:1955–1958, 1990.

[16] R. Bell and P. Dean. Structure of Vitreous Silica - Validity of Random Net-

work Theory. *Philosophical Magazine*, 25(6):1381, 1972.

[17] S. Bembenek and B. Laird. The Role of Localization in Glasses and Supercooled Liquids. *Journal of Chemical Physics*, 104(13):5199–5208, 1996.

[18] S. Bembenek and B. Laird. Instantenous Normal Modes Analyis of Amorphous and Supercooled Silica. *Journal of Chemical Physics*, 114(5):2340–2344, 2001.

[19] K. Biljakovic, J. Lasjaunias, P. Monceau, and F. Levy. Toward Equilibrium Ground State in Charge-Density-Wave Systems. *Physical Review Letters*, 67(14):1902–1905, 1991.

[20] K. Binder. Understanding the Glass Transition and the Amorphous State of Matter: can Computer Simulations Solve the Challenge? *Computer Physics Communications*, 122:168–175, 1999.

[21] K. Binder, J. Baschnagel, W. Kob, and W. Paul. Simulation of Models for the Glass Transition: Is there Progress ? cond-mat/0202337, 2002.

[22] K. Binder, J. Baschnagel, and W. Paul. Glass Transition of Polymer Melts: Test of Theoretical Concepts by Computer Simulation. *Progress in Polymer Science*, 28:115–172, 2003.

[23] L. Bonilla, F.G. Padilla, and F. Ritort. Aging in the Linear Harmonic Oscilattor. *Physica A*, 250:315–326, 1998.

[24] J. P. Bouchaud, L. Cugliandolo, J. Kurchan, and M. Mezard. *Spin Glasses and Random Fields*, chapter 7, pages 161–224. World Scientific, Singapore, 1997.

[25] K. Broderix, K.K. Bhattacharya, A. Cavagna, A. Zippelius, and I. Giardana. Energy Landscape of a Lennard-Jones Liquid: Statistics of Stationary Points. *Physical Review Letters*, 85(25):5360–5363, 2000.

[26] A. Cavagna. Fragile vs. Strong Liquids: A Saddle-Ruled Scenario. *Europhysics Letters*, 53:490–496, 2001.

[27] B. Chen, J. Siepmann, and M. Klein. Direct Gibbs Ensemble Monte Carlo Simulations for Solid-Vapor Phase Equilibria: Applications to Lennard-Jonessium and Carbon Dioxide. *Journal of Physical Chemistry B*, 105:9840–9848, 2001.

[28] A. Clarke and J. Wiley. Numerical Simulation of the Dense Random Packing of a Binary mixture of Hard spheres: Amorphous Metals. *Physical Review B*, 35(14):3570–3577, 1987.

[29] T. Cormen, C. Leiserson, and R. Rivest. *Introduction to Algorithms*. MIT Press Boston McGraw Hill New York, 1990.

[30] D. Heinemann, W. Assenmacher, W. Mader, M. Kroschel, and M. Jansen. Structural Characterization of Amorphous Ceramics in the System Si-B-N-(C) by Means of Transmission Electron Microscopy Methods. *Journal of Materials Research*, 14(9):3746–3753, 1999.

[31] P. de Gennes. On a relation between percolation theory and the elasticity of gels. *Journal de Physique Lettres*, 37:L1–L2, 1976.

[32] P. Debenedetti and F. Stillinger. Supercooled Liquids and the Glass Transition. *Nature*, 410:259–267, 2001.

[33] R. Di Leonardo, L. Angelani, G.Parisi, G. Ruocco, A. Scala, and F. Sciortino. Off-equilibrium Dynamics in the Energy Landscape of a Simple Glass Former. *Philosophical Magazine B*, 82:163–169, 2002.

[34] A. Einstein. Über eine neue Methode zur Bestimmung der Moleküldimension. *Annalen der Physik*, 1905.

[35] S. R. Elliott. *Physics of Amorphous Materials*. Longman Scientific & Technical, Essex, 1990.

[36] D. Engelhardt and D. Michel. *High-resolution Soli-State NMR of Silicates and Zeolites*, page 195. J. Wiley and Sons, New York, 1987.

[37] S. S. et. al. . Xfig 3.2, 1988.

[38] J. L. Finney. Random Packings and the Structure of Simple Liquids I. the Geometry of Random Close Packing. *Proc. Roy. Soc. London A*, 319:479–493, 1970.

[39] P. J. Flory. Molecular Size Distributions in Three Dimensional Polymers. I. Gelation. *Journal of the American Chemical Society*, 63(11):3083–3090, 1941.

[40] P. J. Flory. Molecular Size Distributions in Three Dimensional Polymers. II. Trifunctional Branching Units. *Journal of the American Chemical Society*, 63(11):3090–3096, 1941.

[41] P. J. Flory. Molecular Size Distributions in Three Dimensional Polymers. III. Tetrafunctional Branching Units. *Journal of the American Chemical Society*, 63(11):3096–3100, 1941.

[42] D. Frenkel and B. Smit. *Understanding Molecular Simulation From Algorithms to Applications*. Academic Press, San Diego, 2^{nd} edition, 2002.

[43] R. Frost, J. Schön, and P. Salamon. Simulation of Random Close Packed Discs and Spheres. *Computational Materials Science*, 1:343–350, 1993.

[44] J. D. Gale. GULP: A Computer Program for the Symmetry-adapted Simulation of Solids. *Journal of the Chemical Society Faraday Transactions*, 93:629–637, 1997.

[45] Y. M. Galperin, V. L. Gurevich, and D. A. Parshin. Theory of Low-temperature Thermal expansion of Glasses. *Physical Review B*, 32:6873–6883, 1985.

[46] M. Gastreich, 2001. Private Communication.

[47] M. Gastreich. *Werkzeuge zur Modellierung von Siliciumbornitrid-Keramiken*. PhD thesis, Universität Bonn, 2001.

[48] M. Gastreich and C. Marian. *Empirical potential for Polyborosilazane Ceramics*, pages 237–242. Physics of Glasses: Structure and Dynamics. American Institute of Physics, New Vork, 1999.

[49] M. Gastreich and C. Marian. A Systematic Theoretical Study of Molecular Si/N, B/N, Si/N/B Compounds and Parametrization of a Force-field. *Journal of Molecular Structure (THEOCHEM)*, 506:107–129, 2000.

[50] M. Gastreich, C. Marian, and J. Gale. An Empirical Two-Body Potential for Solid Silicon-Nitride, Boron-Nitride and Borosilazane Modifications. *Physical Review B*, 62:3117–3123, 2000.

[51] S. Geman and D. Geman. Stochastic relaxation, Gibbs-distribtion and the Bayesian Restoration of Images. *IEEE T. Pattern Anal*, 6(6):721–741, 1984.

[52] J. Gezelter, E. Rabani, and B. Berne. Can Imaginary Instantenous Normal Mode Frequencies Predict Barriers to Self-Diffusion. *Journal of Chemical Physics*, 107(12):4618–4627, 1997.

[53] J. Gibbs. *Elementary Principles in Statistical Mechanics. Developed with Special Reference to the Rational Foundations of Statistical Mechanics*. Dover Publications, New York, 2 edition, 1902. Uncorrected Version of the 1^{st} edition of Yale University Press 1902.

[54] J. Gibbs and E. DiMarzio. Nature of the Glass Transition and the Glassy State. *Journal of Chemical Physics*, 28(3):373–383, 1958.

[55] L. Gladden. Medium-range order in v-SiO_2. *Journal of Non-Crystalline Solids*, 119:318–330, 1990.

[56] S. Glasstone, K. Laidler, and H. Eyring. *The Theory of Rate Processes*. McGraw-Hill, New York, 1941.

[57] M. Goldstein. Viscous Liquids and the Glass Transition: A Potential Energy Barrier Picture. *Journal of Chemical Physics*, 51:3728–3739, 1969.

[58] W. Götze. The Essentials of the Mode-Coupling Theory for Glassy Dynamics. *Condensed Matter Physics*, 1(4):873–904, 1998.

[59] W. Götze. Recent Tests of the Mode-Coupling Theory for Glassy Dynamics. *Journal of Physics: Condensed Matter*, 11:A1–A45, 1999.

[60] T. S. Grigera, A. Cavagna, I.Giardinia, and G. Parisi. Geometric Approach to the Dynamic Glass Transition. *Physical Review Letters*, 88(5):0555021–055502–4, 2002.

[61] V. Gurevich, D. Parshin, and H. Schober. Anharmonicity, Vibrational Instability, and the Boson Peak in Glasses. *Physical Review B*, 67(9):094203–1–094203–10, 2003.

[62] I. Gutzow and J. Schmelzer. *The Vitreous State*. Springer, Berlin, 1995.

[63] R. Hagenmayer. Röntgen und Neutronenbeugung an nicht-translationssymmetrischen Festkörpern. Technical report, SFB408 Institut für Anorganische Chemie Universität Bonn, Gerhard-Domagk-Str. 1 53121 Bonn, July 2000.

[64] R. Hagenmayer, Utz Müller, Chris J. Benmore, Jörg Neuefeind, and Martin Jansen. Structural Studies on Amorphous Silicon Boron Nitride: Neutron Contrast Technique and High-energy X-ray Diffraction. *Journal of Materials Chemistry*, 9:2865, 1999.

[65] S. Hampshire. *Materials Science and Technology A Comprehensive Treatment*, volume 11, chapter 3, pages 121–168. VCH, Weinheim, 1993.

[66] A. Hannemann, J. Schön, C.Oligschleger, and M. Jansen. Modelling of Si-B-N-ceramics. In B. Müller, editor, *Proceedings XX. DGK Workshop on amorphous solids*, pages 1–11. DGK, U. Jena, 1999. also cond-mat/000319.

[67] A. Hannemann, J. Schön, and M. Jansen. A Random Close Packing Based Algorithm for the Generation of Continous Random Networks. *Computer Physics Communications*, 144:284–296, 2002.

[68] A. Hannemann, J. Schön, M. Jansen, and P. Sibani. Non-equilibrium Dynamics in Amorphous $Si_3B_3N_7$. cond-mat/0212245, 2002.

[69] H.E. Hagy and H.N. Ritland. Effect of Thermal History on Glass Expansion Characteristics. *Journal of the American Ceramic Society*, 40(12):436–442, 1957.

[70] H. Herrmann, D. Stauffer, and D. Landau. Computer Simulations of a Model for Irreversible Gelation. *Journal of Physics A: Mathematical and General*, 16:1221–1239, 1983.

[71] H. Herrmmann. Geometrical Cluster Growth Models and Kinetic Gelation. *Physics Report*, 136(3):153–227, 1986.

[72] B. Himmel, J. Claudius, T. Gerber, and C. Reinhold. Analysis of DC-sputtered Si_3N_4 Films using X-ray Diffraction and Computer Simulation. *Journal of Non-crystalline solids*, 162:136–143, 1993.

[73] M. Hitchcock and C.K. Hall. Solid-Liquid Equilibrium for Binary Lennard Jones Mixtures. *Journal of Chemical Physics*, 110(23):11433–11444, 1999.

[74] K. H. Hoffmann and P. Sibani. Diffusion in Hierarchies. *Physical Review A*, 38:4261–4270, 1988.

[75] J. Horbach and W. Kob. Static and dynamic properties of silica melt. *Physical Review B*, 60(5):3169–3181, 1999.

[76] M. Jansen and P. Baldus. High-Performance Ceramics - Amorphous Inorganic Networks from Molecluar Precursors. *Angewandte Chemie Int. Ed. Engl.*, pages 338–354, 1997.

[77] M. Jansen, B. Jäschke, and T. Jäschke. *Amorphous Multinary Ceramics in the Si-B-N-C System*, volume 101 of *Structure & Bonding*, pages 138–191. Springer-Verlag, Berlin, 2002.

[78] T. Jäschke. *Hochtemperaturstabile Si/B/N/C-Keramiken aus neuen Einkomponentenvorläufern*. PhD thesis, Universität Bonn, Shaker Verlag Aachen, 2002.

[79] J. Johnson, J. Zollweg, and K. Gubbins. The Lennard-Jones Equation of State Revisited. *Molecular Physics*, 78(3):591–618, 1993.

[80] R. Kaplow, T. A. Rowe, and B. L. Averbach. Atomic Arrangements in Vitreous Selenium. *Physical Review*, 168:1068–1079, 1968.

[81] T. Keyes. Unstable Modes in Supercooled and Normal Liquids: Density of States, Energy Barriers, and Self-Diffusion. *Journal of Chemical Physics*, 101(6):5081–5091, 1994.

[82] K.F. Kunz, V.K. Sarin, R.F. Davis, and S.R. Bryan. Self-Diffusion of Silicon-30 and Nitrogen-15 in α Phase Silicon Nitride. *Materials Science and Engeneering*, A105/A106:47–54, 1988.

[83] K. Kijima and S. Shirasaki. Nitrogen Self-Diffusion in Silicon Nitride. *Journal of Chemical Physics*, 65(7):2668–2671, 1976.

[84] S. Kirkpatrick, C. D. Gelatt Jr., and M. P. Vecchi. Optimization by Simulated Annealing. *Science*, 220:671–680, 1983.

[85] L. Kjeldgaard and J. C. Schön. Distinguishing different paths for rearrangements on surfaces. *J. Phys.: Cond. Mat.*, 6:1–18, 1994.

[86] W. Kob. Computer simulations of supercooled liquids and glasses. *J. Phys.: Cond. Matter*, 11:R85–R115, 1999.

[87] W. Kob. Supercooled Liquids, the Glass Transition, and Computer Simulations. In J. Barrat, M. Feigelmann, and J. Kurchan, editors, *Slow Relaxation and Nonequilibrium Dynamics in Condensed Matter*, volume Session LXVII of *Les Houches 2002 Summer School* . Les Houches Summer School, World Scientific Singapore, 2002. see also cond-mat/0212344.

[88] S. Kohn and M. Jansen. Evidence for the formation of Si-O-N-glasses. *Journal of Non-crystalline solids*, 44:111, 1998.

[89] P. Kroll and R. Hoffmann. Silicon Boron Nitrides: Hypothetical Polymmorphs of $Si_3B_3N_7$. *Angew. Chem. Int. Ed.*, 37:2527–2530, 1998.

[90] L. Kjeeldgaard and J.C Schön. Distinguishing Different Paths for Rearrangements on Surfaces. *Journal of Physics: Condensed Matter*, 6(36):7269–7286, 1994.

[91] E. La Nava, H. Stanley, and F. Sciortino. Configuration Space Connectivity across the Fragile-to-Strong Transition in Silica. *Physical Review Letters*, 88:035501–1–035501–3, 2002.

[92] D. Landau and K. Binder. *A Guide to Monte Carlo Simulations in Statistical Physics*. Cambridge University Press, Cambridge, 1 edition, 2000.

[93] I. M. Lifshitz and V. V. Slyozow. The Kinetics of Precipation from Supersaturated Solid Solutions. *Journal of Physical Chemistry of Solids*, 19(1/2):35–50, 1961.

[94] H. Lillie and H. Ritland. Fine Annealing of Optical Glass. *Journal of the American Ceramic Society*, 37(466-473):466–474, 1956.

[95] M. Lines. Hard-sphere Random-packing Model for an Ionic glass: Yttrium Iron Garnet. *Physical Review B*, 20(9):3729–3738, 1979.

[96] Y. Liu and R. Pandey. Kinetics of Gelation Growth in a Sol-Gel Transition by a Computer-Simulation Model. *Journal de Physique II*, 4:865–872, 1994.

[97] Y. Liu and R. Pandey. Inhomogeneity in gelation and nonuniversality of Sol-to-Gel Transitions Studied by a Computer Simulation Model. *Physical Review E*, 54(6):6609–6617, 1996.

[98] Y. Liu and R. Pandey. Sol-Gel Phase Transitions in Thermoreversible Gels: Onset of Gelation and Melting. *Journal of Chemical Physics*, 105(2):825–836, 1996.

[99] Y. Liu and R. Pandey. Computer-simulation Studies of Kinetic Gelation. *Physical Review B*, 55(13):8257–8266, 1997.

[100] B. Lubachesvky, F. Stillinger, and E. N. Pinson. Disks vs. Spheres: Contrasting Properties of Random Packings. *Journal of Statistical Physics*, 64(3/4):501–525, 1990.

[101] B. Lubachevsky and F. Stillinger. Geometric Properties of Random Disk Packings. *Journal of Statistical Physics*, 60(5/6):561–583, 1990.

[102] P. Lunkenheimer and A. Loidl. Dynamic Processes of the Glass Transition. *Advances in Solid State Physics*, 41:405–417, 2001.

[103] P. Lunkenheimer and A. Loidl. Dieletric Spectroscopy of Glass-forming Materials: α-Relaxation and Excess Wing. *Chemical Physics*, 284:205–219, 2002.

[104] P. Macedo, W. Capps, and T. Litowitz. Two-state Model for the Free Volume of Vitreous B_2O_3. *Journal of Chemical Physics*, 44:3357, 1966.

[105] B. Madan, T. Keyes, and G. Seeley. Diffusion in Supercooled Liquids via Normal Mode Analysis. *Journal of Chemical Physics*, 92(12):7565–7569, 1990.

[106] P. Manneville and L. de Seze. *Numerical Methods in the study of critical phemonema*. Springer, Berlin, 1981.

[107] R. L. McGreevy. Reverse Monte Carlo Methods for Structural Modelling. In C. R. A. Catlow, editor, *Computer Modelling in Inorganic Crystallography*, pages 151–184. Acad. Press, San Diego, 1997.

[108] K. Mehlhorn, S. Näher, M. Seel, and C. Uhrig. The LEDA User Manual. Technical report, MPI für Informatik, 66123 Saarbrücken, 1999.

[109] N. Metropolis, A. W. Rosenbluth, M. N. Rosenbluth, A. H. Teller, and E. Teller. Equation of State Calculations by Fast Computing Machines. *Journal of Chemical Physics*, 21:1087–1092, 1953.

[110] C. Monthus and J.P. Bouchaud. Models of Traps and Glass Phenomenology. *Journal of Physics A: Mathematical and General*, 29:3847–3869, 1996.

[111] B. Müller. In B. Müller, editor, *Proceedings of the DGK Workshop on Amorphous and Non-crystalline Solids*, pages 1–2. DGK, Jena University.

[112] U. Müller. *Anorganische Strukturchemie*. Teubner, Stuttgart, 1992.

[113] U. Müller, W. Hoffbauer, and M. Jansen. Poster at the DKG-Workshop "High-performance-ceramics" Stuttgart, 1999.

[114] U. Müller, W. Hoffbaur, and M. Jansen. Short-Range Ordering in Amorphous $Si_3B_3N_7$ as Determined by Multinuclear NMR-Spectroscopy. *Chemistry of Materials*, 12(8):2341–2346, 2000.

[115] P. Nordblad and P. Svendlidh. *Spin Glasses and Random Fields*, chapter 1, pages 1–28. World Scientific, Singapore, 1997.

[116] C. Oligschleger. Dynamics of SiO_2 glass. *Physical Review B*, 60(5):3182–3193, 1999.

[117] C. Oligschleger and J.C. Schön. Calculation of Vibrational Properties of Selenium. *Journal of Physics: Condensed Matter*, 9:1049–1066, 1997.

[118] C. Oligschleger, R. O. Jones, S. M. Reimann, and H. R. Schober. Model interatomic potential for simulations of selenium. *Physical Review B*, 53:6165–6173, 1996.

[119] C. Oligschleger and H. Schober. Collective Jumps in a Soft-Sphere Glass. *Physical Review B*, 59(2):811–821, 1999.

[120] A. Omeltschenko, A. Nakano, R. Kalia, and P. Vashishta. Structure, Mechanical Properties, and Thermal Transport in Microporous Silicon Nitride - Molecular Dynamics Simulations on a Parallel Machine. 33(9):667–672, 1996.

[121] A. Z. Panagiotopolus, N. Quirke, M. Stapleton, and D. Tildesley. Phase equilibria by Simulations in the Gibbs ensemble: Alternative Derivation, Generalization and Applications to Mixtures and Membrane Equilibria. *Molecular Physics*, 63:527–543, 1987.

[122] R. Pandey and Y. Liu. Simulations of Sol-Gel Modelling: Effects of Mobility, Reversibility and Quality of Solvent. *Journal of Sol-Gel Science and Technology*, 15:147–159, 1999.

[123] D. Parshin and S. Sahling. Heat releases in glasses at low temperatures. *Physical Review B*, 47(10):5677–5688, 1993.

[124] H. Putz. *RMC*. SCAI Gesellschaft für Mathematik und Datenverarbeitung (GMD), Schloss Birlinghoven, 1.0 edition, 12 2000.

[125] M. Rintoul and S. Torquato. Computer Simulations of Dense Hard-sphere Systems. *Journal of Chemical Physics*, 105(20):9258–9265, 1996.

[126] S. N. Taraskin and S.R. Elliott. Nature of Vibrational Excitations in Vitreous Silica. *Physical Review B*, 56:8605–8622, 1997.

[127] S. Reinhardt S and C.M. Marian and I. Frank. The Influence of Excess Ammonia on the Mechanism of the Reaction of Boron Trichloride with Ammonia - An Ab-Initio Molecular Dynamics Study. *Angewandte Chemie International Edition*, 40(19):3683, 2001.

[128] M. Sampoli, P. Benassi, R. Eramo, L. Angelani, and G. Ruocco. Potential Energy Landscape in Lennard-Jones Binary Mixture Model. cond-mat/0302005, 01 2003.

[129] S. Sastry. Evaluation of the Configurational Entropy of a Model Liquid from Computer Simulations. *Journal of Physics: Condensed Matter*, 12:6515–6523, 2000.

[130] S. Sastry, P. Debenedetti, and F. Stillinger. Signatures of Distinct Dynamical Regimes in the Energy landscape of a Glass-Forming Liquid. *Nature*, 393:554–557, 1998.

[131] S. Sastry, P. G. Debenedetti, F. H. Stillinger, T. B. Schroder, J. C. Dyre, and S. C. Glotzer. Potential Energy Landscape Signatures of Slow Dynamics in Glass forming Liquids. *Physica A*, 270:301–308, 1999.

[132] D. Sauter, M. Weinmann, F. Berger, P. Lamparter, K. Müller, and F. Aldinger. X-ray and Neutron Scattering and Solid State NMR Investigations on Precursor-Derived B-C-N Ceramics Using Isotopic Substituition. *Chemistry of Materials*, 14:2859–2870, 2002.

[133] A. Scala, C. Valeriani, F. Sciortino, and P. Tartaglia. Fluctuation-dissipation Relations and Energy Landscape in an Out-of-Equilibrium Strong Glass Former. *Physical Review Letters*, 90(11):115503–1–115503–4, 2003.

[134] G. Schaftenaar and J. Noordik. Molden: a Pre- and Post-Processing Program for Molecular and Electronic Structures. *Journal of Computer-Aided Molecular Design*, 14:123–134, 2000.

[135] P. Schissel and W. Williams. *Bulletin of the American Physical Society*, 4(2):139, 1959.

[136] H. Schmidt, G. Borchardt, S. Weber, H. Scherrer, H. Baumann, A. Müller, and J. Bill. Self-diffusion Studies of ^{15}N in amorphous $Si_3BC_{4.3}N_2$ Ceramics with Ion Implantation and Secondary Mass Spectroscopy. *Journal of Applied Physics*, 88:1827–1830, 2000.

[137] H. Schmidt, G. Borchardt, S. Weber, H. Scherrer, H. Baumann, A. Müller, and J. Bill. Comparison of ^{30}Si Diffusion in amorphous Si-C-N and Si-B-C-N Precursor-derived Ceramics. *Journal of Non-Crystalline Solids*, 298:232–240, 2002.

[138] H. Schober and C. Oligschleger. Low-frequency Vibrations in a Model Glass. *Physical Review B*, 53(17):11469–11480, 1996.

[139] J. Schön. *Two Mean-Field Thery Models of Phase Transitions: Staging in Intercalated Graphite and Melting*. Phd-thesis, Massachusetts Institute of Technology, July 1988.

[140] J. Schön. Energy Landscape of two-dimensional Lattice Polymers. *Journal of Physical Chemistry A*, pages 10886–10892, 2002.

[141] J. Schön, A. Hannemann, G. Sethi, M. Jansen, P. Salamon, R. Frost, and L. Kjeldgaard. Disordered Systems on Various Time Scales: a-$Si_3B_3N_7$ and Homogenous Sintering. cond-mat/0212279, 2002.

[142] J. C. Schön. *unpubl.*

[143] J. C. Schön. Preferential Trapping on Energy Landscapes in Regions Containing Deep-lying Minima - the Reason for the Success of Simulated Annealing? *J. Phys. A: Math. Gen.*, 30:2367–2389, 1997.

[144] J. C. Schön and M. Jansen. A First Step towards Planning of Syntheses in Solid State Chemistry: Determination of Promising Structure Candidates using Global Optimization. *Angew. Chem. Int. Ed.*, 35:1286–1304, 1996.

[145] J. C. Schön and P. Sibani. Properties of the energy landscape of network models for covalent glasses. *J. Phys. A: Math. Gen.*, 31:8165–8178, 1998.

[146] J. C. Schön and P. Sibani. Properties of the energy landscape of network models for covalent glasses. *JPA*, 31:8165–8178, 1998.

[147] J. C. Schön and P. Sibani. Energy and entropy of metastable states in glassy systems. *Europhys. Lett.*, 49:196–202, 2000.

[148] J. C. Schön, M. Wevers, and M. Jansen. Entropically Stabilized Region on the Energy Landscape of an Ionic Solid. *Journal of Physics: Condensed Matter*, 2003. accepted.

[149] S.D. Bembenek and B.B. Laird. Instantenous Normal Modes and the Glass Transition. *Physical Review Letters*, 74(6):936–939, 1996.

[150] G. Seeley and T. Keyes. Normal-Mode Analysis of Liquid State Dynamics. *Journal of Chemical Physics*, 91(9):5581–5586, 1989.

[151] P. Sibani and K. Hoffmann. Relaxation in Complex Systems. *Europhys. Lett.*, 16(5):423–428, 1991.

[152] P. Sibani and K.H. Hoffmann. Hierachical Models for Aging and Relaxation in Spin Glasses. *Physical Review Letters*, 63(26):2853–2857, 1989.

[153] R. Sinclair, J. Desa, G. Etherington, P. Johnson, and A. Wright. Neutron Diffraction Studies of Amorphous Solids. *Journal of Non-crystalline Solids*, 42:107–116, 1980.

[154] D. Stauffer. Gelation in Concentrated Critically Branched Polymer-Solutions - Percolation Scaling Theory of Intramolecular Bond Cycles. *Journal of the Chemical Society Faraday Transactions II*, 72:1354–1364, 1976.

[155] D. Stauffer. Gelation Theory - Failure of Cooperation between Physics and Chemistry. *Berichte Bunsengesellschaft Physikalische Chemie*, 102(11):1672–1678, 1998.

[156] R. Stephens. *Journal of Non-Crystalline Solids*, 20:75, 1976.

[157] F. Stillinger. Relaxation Behavior in Atomic and Molecular Glasses. *Physical Review B*, 41:2409–2416, 1990.

[158] F. Stillinger, P. Debenedetti, and T. Truskett. The Kauzmann Paradox Revisited. *Journal of Physical Chemistry B*, 105:11809–11816, 2001.

[159] F. Stillinger, K. Kornegay, and E. DiMarzio. Systematic Approach to Explanation of Rigid Disk Phase Transition. *Journal of Chemical Physics*, 40(6):1564–, 1964.

[160] F. Stillinger and T. Weber. Dynamics of Structural Transitions in Liquids. *Physical Review A*, 28(4):2408–2415, 1983.

[161] F. Stillinger and T. A. Weber. Hidden Structure in Liquids. *Physical Review A*, 25:978–989, 1982.

[162] W. Stockmayer. Theory of Molecular Size Distribution and Gel Formation in

Branched Chain Polymers. *Journal of Chemical Physics*, 11(2):45–55, 1943.

[163] W. Stockmayer. Theory of Molecular Size Distribution and Gel Formation in Branched Chain Polymers II. General Cross Linking. *Journal of Chemical Physics*, 12(1):125–131, 1944.

[164] A. Takada, C. R. A. Catlow, and G. D. Price. Computer modelling of B_2O_3: part I. New interatomic potentials, crystalline phases and predicted polymorphs. *J. Phys.: Cond. Mat.*, 7:8659–8692, 1995.

[165] W. van Megen and S. Underwood. Glass transition in colloidal hard spheres: Mode coupling theory analysis. *Physical Review Letters*, 70(18):2766–2769, 1993.

[166] L. van Wüllen , U.Müller, and M.Jansen. Intermediate-range Order in Amorphous Nitridic Ceramics: Lessons from Modern NMR-Spectroscopy. *Angew. Chem. Int.Ed.*, 39(14):2519–2521, 2000.

[167] L. van Wüllen, U. Müller, and M. Jansen. Understanding Intermediate-Range Order in amorphous nitridic ceramics: A ^{29}Si $\{\ ^{11}$B$\}$ REDOR/REAPDOR and ^{11}B $\{\ ^{29}Si\ \}$ REDOR Study. *Chemistry of Materials*, 12(8):2347–2352, 2000.

[168] L. Verlet. Computer "Experiments" on Classical Fluids. I. Thermodynamical Properties of Lennard-Jones Molecules. *Physical Review*, 159(1):98–103, 1967.

[169] K. Vollmayr, W. Kob, and K. Binder. Cooling-rate Effects in Amorphous Silica: A Computer Simulation Study. *Physical Review B*, 54:15808–15827, 1996.

[170] K. Vollmayr, W. Kob, and K. Binder. How do the Properties of a Glass Depend on the Cooling Rate? A Computer Simulation Study of a Lennard-Jones System. *Journal of Chemical Physics*, 105(11):4714–4728, 1996.

[171] O. Wagner. Molekular Precursoren für Bor-Siliciumnitrid-Mischkeramiken. Master's thesis, Universität Bonn, Gerhard-Domagk-Str 1, 1991.

[172] T. Weber and F. Stillinger. Local Order and Structural Transition in Amorphous Metal-Metalloid Alloys. *Physical Review B*, 31(4):1954–1963, 1985.

[173] S. Wefing. Modelling of Continous Random Networks: A Case Study for Vitreous GeO_2. *Journal of Non-Crystalline Solids*, 244:89–111, 1999.

[174] S. Wefing and H. Putz. private communication, 2000.

[175] W.H. Press, S.A. Teukolsky, W.T. Vetterling, and B.P. Flannery. *Numerical Recipes in FORTRAN. The Art of Scientific Computing*. Cambridge University Press, Cambridge, 2 edition, 1992.

[176] T. Williams and C. Kelley. Gnuplot linux version 3.7, 1999.

[177] A. Wright. Neutron Scattering from Vitreous Silica: IV. Time-of-flight Diffraction. *Journal of Non-Crystalline Solids*, 119(1):49–64, 1990.

[178] R. Zallen. *The Physics of Amorphous Solids*. Wiley, New York, 1983.

[179] G. Ziegler, J. Heinrich, and G. Wotting. *Jouernal of Materials Science*, 22:3041–3086, 1987.

[180] B. Zimm and W. Stockmayer. The Dimensions of Chain Molecules Containing Branches and Rings. *Journal of Chemical Physics*, 17(10):1301–1314, 1949.

Appendix C

Formalia

C.1 Software and technical resources

The following software packages were used in this thesis:

1. The GULP program[44] version 1.2, for conjugate gradient optimizations and the calculation of phonon and bulk properties.
2. The RMC-program *RMC* version 1.1 by Dr. H. Putz with bug fixes from C. M. Marian.
3. The GNUPLOT3.7 package for the generation of the plots of the data.[176]
4. The MOLDEN program package for the 3D display of structures.[134]
5. The LEDA library, Version 4.7. [108]
6. The Xfig package, Version 3.2.[37]
7. The GNU Fortran Compiler *g77*, Version 0.5.25, and the INTEL Fortran Compiler *ifc*, Version 6.0 .
8. The LaTeX-package, Version 3.14159.
9. If not stated otherwise, crystal structures were taken from the Inorganic Crystal Structure Database (ICSD), FIZ Karlruhe.

C.2 Eidesstattliche Versicherung

Ich versichere hiermit an Eides Statt, daß ich die vorliegende Arbeit selbstständig verfaßt und die verwendeten Hilfsmittel angegeben habe.